

学位論文

Theoretical Study of
Electron-Phonon Coupled Systems
in and out of Equilibrium

(平衡および非平衡における電子・フォノン系の理論的研究)

平成27年12月博士(理学)申請

東京大学大学院理学系研究科

物理学専攻

村上 雄太

Abstract

In this thesis, we have theoretically investigated electron-phonon coupled systems in and out of equilibrium. Our main interests are (1) competition of different orders in el-ph systems in equilibrium and (2) development of methodology for non-equilibrium el-ph systems and its application to dynamical properties of electron-phonon systems. Understanding of the point (1) is important, since competitions involving el-ph couplings can be observed in many interesting materials. Moreover, it provides promising situations for drastic optical controls out of equilibrium. The point (2) is necessary for understanding various optically induced phenomena in el-ph systems, since available theoretical approaches for non-equilibrium problems are still limited. Hence, these topics are potentially deeply related.

In the present thesis, we focus on the Holstein and Holstein-Hubbard models, which are the most fundamental models for el-ph coupled systems, and we employ the dynamical mean-field theory (DMFT), where the models are mapped onto effective impurity models.

In equilibrium, we perform systematic investigation of competition and possible microscopic coexistence of different orders emerging from the el-ph coupling. For this end, we newly extend a continuous-time quantum Monte Carlo impurity solver in DMFT for the Holstein(-Hubbard) model, so that we can directly deal with charge order (CO), antiferromagnetism (AF) and s-wave superconductivity (SC) on an equal footing. First, we study the competition in the half-filled Holstein-Hubbard model at finite temperatures when the electron-electron and electron-phonon interactions are comparable. There, we find AF and CO are separated by a regime of first-order phase transition for intermediate values of interactions. For small and large values of interactions, we find intervening paramagnetic metallic and insulating phases, respectively. Secondly, we investigate competition of SC and CO away from half-filling in the Holstein model. We argue that a *microscopic coexistence* of these orders is realized only in the intermediate-coupling regime and clarify its characteristic features. We also discuss that the origin of the stability of the coexisting phase in the intermediate-coupling regime is the effective long-range hopping and interactions of a composite particle, i.e., a bipolaron.

In non-equilibrium, we newly develop the non-equilibrium self-consistent Migdal theory as an impurity solver for the Holstein model, since numerically rigorous quantum Monte Carlo impurity solvers suffer from a sign problem in non-equilibrium. With this method we first examine relaxation dynamics after a sudden change of strength of the el-ph coupling (a quench problem), where we find change of qualitative characters of the thermalization process depending on the quenched el-ph coupling. We discuss the relation of this crossover behavior and the self-energies of electrons and phonons. Next, we apply the method to investigate collective oscillations in the strongly-coupled phonon-mediated SC in the Holstein model. We reveal that the coincidence of the energy of the amplitude Higgs mode and the SC gap persists beyond the weak-coupling regime, and effects of the phonon dynamics on the mode is also clarified. We also point out that a quasi-particle lifetime from the strong el-ph coupling leads to a crossover of decay of the amplitude Higgs mode from a power law to an exponential law depending on the temperature. Further, we find another amplitude mode that originates from phonon dynamics and involves a strong *electron-mediated phonon-phonon interaction*. We finally predict how these collective modes can be detected from time-resolved photoemission spectra.

Acknowledgment

I would like to express my sincerest gratitude to Prof. Hideo Aoki, whose patient supervision and advices coming from a wide range of knowledge of physics were very valuable. My heartfelt appreciation goes to Prof. Philipp Werner in Fribourg University for fruitful discussions with helpful advices, continuous encouragement and giving me many opportunities to visit his group. I would like to express my deep gratitude to Dr. Naoto Tsuji for motivating me to study non-equilibrium phenomena and having a number of illuminating discussions and advices. I am indebted to Dr. Denis Golez and Dr. Hugo Strand for constructive discussions and comments about various non-equilibrium problems. I am grateful to Dr. Ryusuke Matsunaga for fruitful discussions about his experiments on the amplitude Higgs mode. I wish to thank Prof. Takashi Oka and Dr. Shintaro Takayoshi for informing me of interesting topics about non-equilibrium phenomena in strongly correlated systems and spin systems. I would like to thank Dr. Toshikaze Kariyado and Dr. Yusuke Nomura for helpful discussions and information on carbon-based superconductors. I would like to appreciate interesting discussion with Dr. Takahiro Ohgoe about electron-phonon systems. I would like to acknowledge Prof. Yusuke Kato, Prof. Yasutami Takada, Prof. Naoki Kawashima, Prof. Shigi Shin, and Prof. Ryo Shimano for constructive comments and careful reading of the thesis.

During the course of the present study I have benefited from comments and encouragement from the previous and present members of the research group of Prof. H. Aoki, Prof. S. Tsuneyuki and Prof. P. Werner. In particular, I would like to thank Prof. P. Maksym, Dr. Y. Tatetsu, Dr. D. Hirai, Dr. L. Boehnke, S. Kitamura, M. Kitatani, A. Sugioka, K. Steiner and A. Herrmann.

Some computer simulations in this thesis have been performed with the ALPS libraries [1,2].

Last but not least I wish to express my deep appreciation to my family for their continuous support and encouragement, without which I could not have completed this thesis.

Contents

1	Introduction	1
1.1	Overview of the thesis	1
1.2	Topics of interest in electron-phonon coupled systems	5
1.2.1	Ordered phases in phonon-coupled correlated systems	5
1.2.2	Collective excitations in conventional superconductors	6
1.2.3	Photo-induced superconducting-like behavior	8
1.3	The Holstein-Hubbard and Holstein models	8
1.4	Structure of this thesis	12
2	Dynamical mean-field theory	15
2.1	General formalism	15
2.1.1	Green's functions in and out of equilibrium	16
2.1.2	Essence of DMFT	20
2.2	Equilibrium Formalism	21
2.2.1	DMFT for ordered states	21
2.2.2	Idea of continuous-time quantum Monte Carlo methods	23
2.2.3	CT-QMC method for ordered states in the Holstein-Hubbard model	24
2.3	Non-equilibrium formalism	33
2.3.1	Green's function for electrons	33
2.3.2	Green's function for phonons	35
2.3.3	The Dyson equation	38
2.3.4	Non-equilibrium dynamical mean-field theory for the Holstein model	40
2.3.5	Impurity solver	41
3	Competing orders in the Holstein-Hubbard and Holstein models in equilibrium	47
3.1	Half-filling: Competition between antiferromagnetism and charge order	47
3.1.1	Background: Electron-electron interaction vs electron-phonon interaction	47
3.1.2	Simplified descriptions	48
3.1.3	Phase diagrams	52
3.2	Away from half-filling: Supersolid state in the intermediate-coupling regime	56
3.2.1	Background: Charge order vs superconductivity	56
3.2.2	Predictions from approximations for the weak-coupling and strong-coupling regimes	57
3.2.3	Supersolid state in the intermediate-coupling regime	59

3.3	Summary of the chapter	67
4	Dynamical properties of the Holstein model	69
4.1	Thermalization crossover in normal states	69
4.1.1	Background: Feedback effects of phonon dynamics on non-equilibrium dynamics	69
4.1.2	Interaction quench: Results of DMFT + self-consistent Migdal approximation	70
4.1.3	Interaction quench: Results of DMFT + unrenormalized Migdal approximation	79
4.2	Collective excitations in strongly-coupled superconductors	81
4.2.1	Background: Collective amplitude mode in superconductors	81
4.2.2	Dynamical pair susceptibility and collective modes	83
4.2.3	Diagrammatic analysis	86
4.2.4	Experimental accessibility	93
4.2.5	Decay of the amplitude Higgs mode: Effect of quasiparticle lifetime	95
4.3	Conclusion of this chapter	100
5	Concluding remarks	103
5.1	Summary of the thesis: Equilibrium and non-equilibrium	103
5.2	Future perspectives: How do we connect insights obtained in this thesis?	104
A	Equilibrium part	107
A.1	CT-QMC	107
A.1.1	Evaluation of ω_{ph}	107
A.1.2	Derivation of the expression for g and f	108
A.2	Perturbative approaches for the Holstein model	109
A.3	Superconductivity in the Holstein-Hubbard model	113
B	Non-equilibrium part	123
B.1	Volterra equations for Dyson equations	123
B.2	Dimensionless electron-phonon coupling	124
B.3	Implementation of the pulse field	125

Chapter 1

Introduction

1.1 Overview of the thesis

Electron-phonon (el-ph) coupling is responsible for many interesting physical phenomena. Conventional pairing interaction for Cooper pairs in superconductivity (SC) is mediated by phonons, and other ordered phases such as charge ordered states can be driven by el-ph couplings. Study of electron-phonon problems has a long history. However, continuous experimental development has been revealing a lot of new phenomena both in equilibrium and out of equilibrium. They have been posing intriguing questions and keep the study of electron-phonon systems very attractive.

In equilibrium, for example, many materials in unconventional parameter regimes have been discovered. Carbon-based superconductors such as alkali-doped C_{60} fullerenes [3–7] and alkali-doped aromatic compounds [6, 8–12] are considered to involve strong Coulomb interactions and phonon modes whose energy scales are comparable to the electron bandwidth. In such cases, there is no guarantee for reliability of the conventional Migdal-Eliashberg theory [13–15], where a small phonon frequency as compared to the electron bandwidth is assumed. Indeed, an alkali-doped C_{60} compound shows a T_c dome structure along with competition between an s-wave SC state and an antiferromagnetic state [4, 5], both of which cannot be explained in the conventional theory. Even in the high T_c cuprates, evidence for a strong el-ph coupling in the angle-resolved photo-emission spectra has been reported [16], and phonon modes are thought to be involved in competition between d-wave SC and other orders such as a stripe phase.

Electron-phonon coupled systems also offer a fascinating field for physics out of equilibrium. Recent developments in strong THz/mid-infrared laser make it possible to manipulate coherent dynamics in conventional phonon-mediated superconductors [17, 18], and even to induce superconductivity-like optical behaviors above T_c through selective excitation of a certain phonon mode [19–22]. These experiments have demonstrated new possibilities of optical manipulation of superconductivity and are attracting much interests.

From a theoretical point of view, it is challenging to deal with such unconventional situations (unconventional parameter and non-equilibrium), and we have not yet reached a satisfactory understanding. For equilibrium cases, a question attracting us is competition/coexistence of different orders in such regimes, where el-ph couplings, the Coulomb interactions and/or phonon frequencies are comparable to the electron bandwidth. New understanding of this issue is not only necessary to understand potential effects of el-ph couplings on ordered states but also

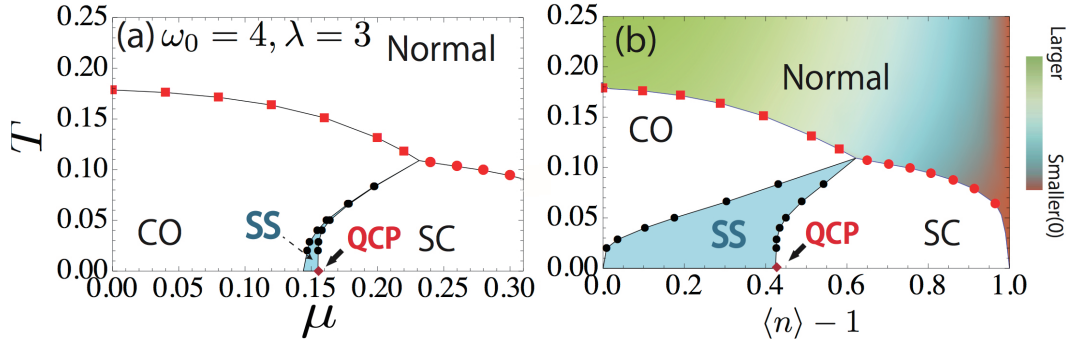


Figure 1.1: Phase diagrams of the Holstein model away from half-filling at the intermediate-coupling regime on the plain of the temperature and the chemical potential(μ) (a) and the temperature and the filling (b). Blue regions indicate the supersolid (SS) region, while red diamonds at $T = 0$ denote the quantum critical point (QCP) (From Ref. [27])

important in terms of future applications to non-equilibrium phenomena. If multiple orders are competing with each other, one can generally expect large responses for small external perturbations, and hence such a case is a promising situation for optical control of nature of materials. Indeed, in one of the experiments with selective phonon excitation, superconductivity is induced after melting a competing stripe order [19].

If we turn to non-equilibrium cases, theoretical methods for el-ph systems are limited as compared to purely electronic models, hence further developments of appropriate theoretical methods are highly required. With such methods we should understand the effect of non-equilibrium dynamics of phonons on relaxation dynamics and coherent dynamics in ordered states.

One important strategy to obtain insights into these issues is to focus on simple fundamental models and reveal physics involved, which we take in this thesis. The Holstein and Holstein-Hubbard models are such fundamental models for el-ph coupled systems. In order to investigate them, we employ the framework of the dynamical mean-field theory (DMFT) [23–26], which is a many-body theory and justified in the infinite-dimensional limit. In DMFT, a lattice problem is mapped onto an effective impurity problem, and one needs to solve it self-consistently. Developing impurity solvers depending on situations concerned, we investigate properties of the models in and out of equilibrium.

The main achievements of the present thesis are the following.

1. **Clarification of the competing orders in the Holstein(-Hubbard) model (Sec. 3, Ref. [27–29])**

Properties of the Holstein-Hubbard and Holstein models have been attracting interests for a long time and have been analyzed with various methods in various dimensions. Still, in terms of competition of different orders, systematic investigation and understanding are still required because of lack of methodology, except for in the one-dimensional case. Newly extending a numerically exact continuous-time quantum Monte Carlo impurity solver for ordered phases in the el-ph models, we have systematically studied competition of different orders to offer new insights into the case of higher dimensionality. In the

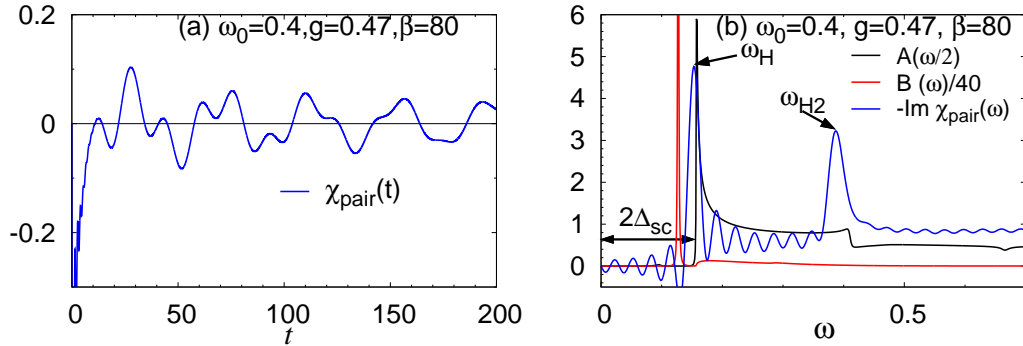


Figure 1.2: (a) Dynamical pair susceptibility against t , $\chi_{\text{pair}}(t)$, in the Holstein model with the strongly-coupled superconductivity. (b) Imaginary part of the dynamical susceptibility ($-\text{Im}\chi_{\text{pair}}(\omega)$), electron spectrum ($A(\omega)$) and phonon spectrum ($B(\omega)$) against ω . The self-consistent Migdal approximation is employed, where phonon dynamics taken into account.

half-filled Holstein-Hubbard model, we reveal the competition between the charge ordered phase (CO) and the antiferromagnetic phase (AF) at finite temperatures. In addition, we study phase diagrams of the Holstein model away from half-filling, to reveal the existence of a so-called *supersolid* state, where SC and CO microscopically coexist, in the intermediate-coupling regime, see Fig. 3.7. Stability of the supersolid state is evidenced by its finite region along the chemical potential, Fig. 3.7(a). We trace back the origin of the stable supersolid state by analyzing an effective model for composite particles of fermions, i.e. bipolarons.

2. Introduction of the self-consistent Migdal approximation for the impurity problem in non-equilibrium DMFT (Sec. 4.1, Ref. [30])

In the non-equilibrium DMFT, numerically exact QMC impurity solvers suffer from dynamical sign problem so that it is difficult to study long-time dynamics with them. Hence it is necessary to use proper approximations for solving effective impurity problems. As for the Hubbard model, many approximations have so far been developed and used to study its non-equilibrium problems [26]. However, as for the Holstein model, proper approximations are rather limited to the insulating (strong-coupling) regime, and development of such approximations for metallic regime has been highly required. In particular, effects of the non-equilibrium dynamics of phonons have been ignored there. To resolve this situation, we develop a non-equilibrium version of the self-consistent Migdal approximation, which is accurate when the phonon energy is small compared to the electron bandwidth.

3. Crossover in relaxation character in an isolated el-ph model (Sec. 4.1, Ref. [30])

As a first application of DMFT+ the non-equilibrium self-consistent Migdal approximation, we study relaxation dynamics of the Holstein model after a sudden change of the el-ph coupling (a quench problem). We reveal that qualitative character of the relaxation changes as the el-ph coupling after the quench is varied. Namely, in the weaker-coupling

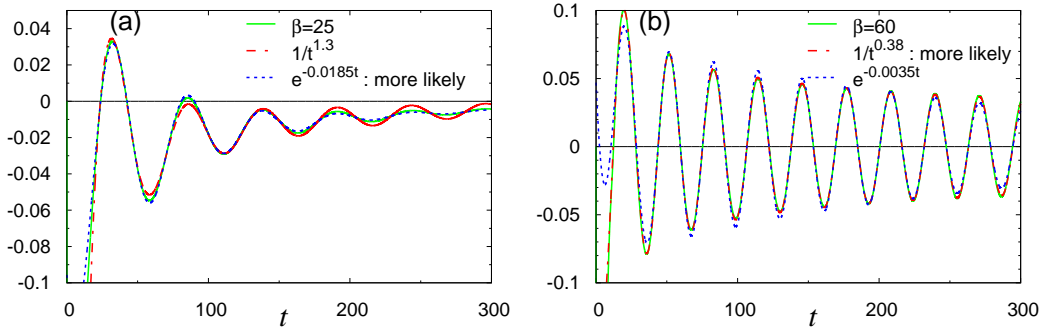


Figure 1.3: Temporal evolution of the order parameter with phonons fixed in equilibrium (a) near T_c and (b) far from T_c . The exponential and power-law fittings are shown.

regime, oscillation originated from phonon dynamics damps and the local quantities approach their thermal value, before thermalization of the momentum distribution of electrons. Conversely, in the stronger-coupling regime, the momentum distribution and local quantities approach their thermal values quickly, but they continue to oscillate. We trace back the origin of this phenomenon to different dependence of the electron and phonon self-energies on the el-ph coupling.

4. Collective amplitude modes in strongly-coupled superconductors (Sec. 4.2, Ref. [31])

Non-equilibrium DMFT also makes it possible to study collective excitations in strongly-coupled SCs. We study the dynamical pair susceptibility, which is a response of the SC order parameter against a SC pair potential, to reveal the properties of collective amplitude modes. Regarding the amplitude Higgs mode, we find that the BCS relation between the SC gap (Δ_{SC}) and the energy of the amplitude Higgs mode (ω_{Higgs}) holds even beyond the BCS regime, i.e. $2\Delta_{SC} \simeq \omega_{\text{Higgs}}$, see Fig. 1.2, and we discuss effects of the phonon dynamics on the Higgs mode. In addition, by fixing phonons in equilibrium to pinpoint the effect of a quasiparticle lifetime, we find that there occurs a crossover between a power-law decay and an exponential decay of the Higgs oscillations as the temperature is varied, see Fig. 1.3. Besides the Higgs mode, we also reveal that there emerges another collective amplitude mode in the strongly-coupled SCs described by the Holstein model, see Fig. 1.2. This mode involves the dynamics of phonons with a strong *electron-mediated phonon-phonon interaction*. We finally discuss how these collective modes can be observed in the time-resolved photoemission spectroscopy.

In the following sections, we briefly review recent topics of interest in electron-phonon coupled systems, and explain the models that we study in this thesis.

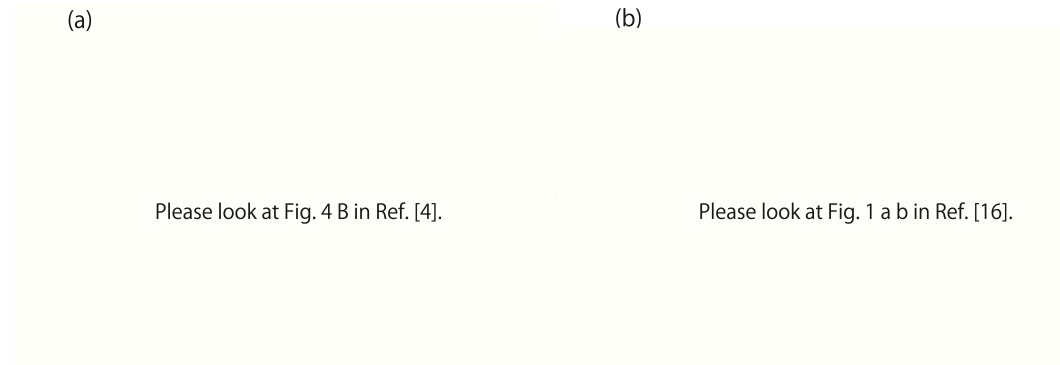


Figure 1.4: (a) Phase diagram of Cs_3C_{60} with the A15 crystal structure on the plane of temperature vs volume per C_{60} . Different markers represent different samples. Inset shows the crystal structure of this compound (From Ref. [4]). (b) ARPES spectra for various cuprates with kinks at a phonon energy scale (arrows) (From Ref. [16]).

1.2 Topics of interest in electron-phonon coupled systems

1.2.1 Ordered phases in phonon-coupled correlated systems

Electron-phonon couplings play crucial roles in various ordered states. Moreover, interplay with strong electron-electron Coulomb interactions makes physics richer, and unconventional parameter regimes beyond the conventional Migdal theory pose new questions.

One class of materials exemplifying such a situation is trivalent alkali fullerenes, A_3C_{60} . This family shows s-wave superconductivity (sSC), and it is usually believed that el-ph couplings play important roles. However in these compounds, intramolecular phonon frequencies are as high as $\omega_0 \sim 0.2$ eV while the electron bandwidth is $W \sim 0.5 - 0.6$ eV [3]. In addition, the Coulomb interactions are estimated to be as large as the bandwidth [6, 7]. In this situation, the Migdal theorem is no longer guaranteed, since it is justified when ω_0/W is small enough. Indeed, there have been some experimental results that cannot be explained by the conventional BCS theory or the Migdal-Eliashberg theory [4, 5]. (1) When the volume of a unit cell is modulated by pressure or chemical doping, there emerges a T_c dome for the SC phase, see Fig. 1.4(a). If the volume becomes large, overlapping of molecular orbitals decreases, the hopping parameter in the effective tight binding model decreases and then the density of states (DOS) at the Fermi level increases. In the conventional theories, an increased DOS leads to increase of T_c . (2) When the volume is large enough, the antiferromagnetic state or the Mott-insulating state is realized [4, 5, 7], see Fig. 1.4(a). In addition to this class of materials, aromatic superconductors are reported recently [8]. These compounds offer new examples to carbon based superconductors and are also considered to have the phonon frequency, the el-ph coupling and the Coulomb interaction that are comparable to the electron bandwidth.

Manifestation of a strong el-ph coupling is also observed in high T_c cuprates. Many properties of these compounds such as AF and d-wave SC are usually discussed without el-ph couplings. However, in an angle-resolved photoemission spectroscopy (ARPES) experiment, kinks in the band dispersion are observed and their origin is considered to be the el-ph coupling [16], see Fig. 1.4(b). In addition, cuprates accommodate ordered phases other than AF and d-wave

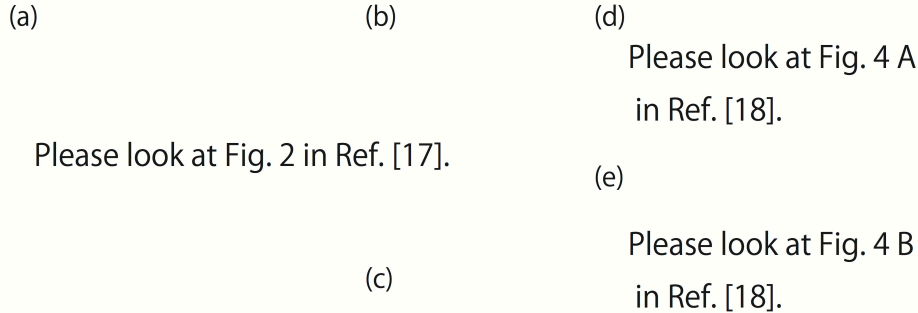


Figure 1.5: (a) Temporal evolutions of the change of the probe electric field after a THz monocycle pulse, (b) the oscillation frequency (f) and the asymptotic gap energy ($2\Delta_\infty$), and (c) the power of the decay of the oscillation (From Ref. [17]). (d) Temperature dependence of the SC gap, and (e) temperature dependence of the intensity of the third harmonic generation (From Ref. [18]).

SC such as a stripe phase around $1/8$ filling [19]. El-ph couplings in these compounds can be relevant to these orders as is exemplified by the light-induced superconducting-like behavior [19], which we shall discuss below.

These experiments motivate us to consider a question of how different orders compete with each other in el-ph coupled systems in unconventional regimes. We are going to discuss this issue in Chap. 3 for the case when the el-el interaction and the el-ph coupling are almost canceling each other, Sec. 3.1, and for the case when the phonon frequency and the el-ph coupling are comparable to the electron bandwidth, Sec. 3.2.

Besides these interests it is also important to understand properties of (s-wave) superconductivity in the unconventional regime, where the phonon frequency, the el-ph interaction and the Coulomb interaction are comparable to the bandwidth. Since this topic deviates from the main stream of the present thesis, we do not mention it in the main part, but we briefly discuss this in Appendix. A.3.

1.2.2 Collective excitations in conventional superconductors

Pump-probe experiments with strong laser pulses make it possible to gain access to new information or phenomena which cannot be observed in equilibrium. One typical example is the coherent dynamics of superconductivity with strong lasers in the THz regime [17, 18]. The main interest of these experiments is the amplitude Higgs mode in superconductors. Since the Higgs mode does not couple with the electromagnetic field in linear-response regime, it has not been observed except for a special cases in which a charge density wave and SC coexist [32–35].

In Ref. [17], the authors have reported the observation of the amplitude Higgs mode in conventional phonon-mediated superconductors ($\text{Nb}_{1-x}\text{Ti}_x\text{N}$). In this experiment, a strong monocycle THz pulse whose energy scale is slightly higher than that of superconducting gap is used to realize non-adiabatic excitations. After the pump pulse, coherent oscillations that

(a)	(b)	(c)
Please look at Fig. 4 A in Ref. [19].	Please look at Fig. 4 B in Ref. [19].	Please look at Fig. 3 C in Ref. [19].

Figure 1.6: (a) Temporal evolution of the imaginary part of optical conductivity, $\sigma_2(\omega)$, (b) temporal evolution of $\lim_{\omega \rightarrow 0} \omega \sigma_2(\omega)$, and (c) the light-induced Josephson plasma edge at 60cm^{-1} at 5 ps after a selective excitation of a mid-infrared phonon mode in $\text{La}_{1.675}\text{Eu}_{0.2}\text{Sr}_{0.125}\text{CuO}_4$ at 10K. (From Ref. [19]).

depend on the pump intensity are observed in the transmission of the probe pulse, see Fig. 1.5 (a). The frequency of the oscillation agrees well with the SC gap ($2\Delta_{\text{SC}}$), which is an indication of the amplitude Higgs mode from the BCS theory, see Fig. 1.5 (b).

In the other experiment [18] with a multicycle THz pulse with frequency ω , the authors have observed forced oscillations of the superconducting order parameter with 2ω . This can be understood with the BCS dynamics or, equivalently, the dynamics of Anderson pseudospin, in a spatially homogeneous field, where the leading term is $\sim \mathbf{A}^2$. Here \mathbf{A} is the vector potential. Important theoretical consequences are the non-linear current with third harmonics (3ω) and the fact that its intensity is enhanced at the resonance of the amplitude Higgs mode with the field ($2\Delta_{\text{SC}} = 2\omega$). These are indeed observed in the transmission of the pump pulse, see Fig. 1.5 (d) (e), indicating experimental realization of resonant excitations of the collective mode in conventional superconductors. Here, we have to note that, recently, contribution of quasi-particle excitations to the third harmonic generation is also theoretically discussed [36], and further investigations are required for better understanding of the third harmonic generation in SC.

With these experiments, the authors demonstrate novel possibilities of studying the collective amplitude mode, which has been difficult to observe, and of optical manipulation of superconductivity. As for theoretical study of coherent dynamics of a superconducting phase, even though it has begun just after the BCS theory, so far theoretical investigations are mainly limited to the mean-field description [32, 37–50]. Therefore there remain many points that have to be understood theoretically and experimentally. For example, it is obviously intriguing to understand effects of impurities and strong el-ph couplings on the lifetime of the amplitude mode and the nature of collective excitations in superconductors with multi-bands and/or unconventional pairing symmetry. In this thesis, among these interesting topics, we focus on effects of strong el-ph couplings on collective excitations, and we discuss the results in Sec.4.2.

1.2.3 Photo-induced superconducting-like behavior

In experiments a pump laser with a few eV is usually used, which is off-resonant from phonon excitations and excites electrons directly. Another way to excite a system is to use mid-infrared (or THz) laser to resonantly excite a certain phonon mode. This method is expected to be favorable for controlling ordered phases, since it avoids the direct excitation of electrons. With this strategy, the group of Cavalleri has reported a photo-induced superconducting-like behavior in cuprate superconductors as well as in C₆₀ SCs [19–22]. In Fig. 1.6, we show an example of their experiments [19]. In this experiment, they employ a special compound, La_{1.675}Eu_{0.2}Sr_{0.125}CuO₄, where the stripe-ordered phase and the superconductivity compete with each other. They resonantly excite a certain phonon mode with a strong mid-infrared pump pulse in the stripe phase to observe emergence of a Josephson plasma edge in reflectance, Fig. 1.6(c), as well as a 1/ω component in the imaginary part of the optical conductivity, Fig. 1.6(a)(b). Both of these properties are expected in a superconducting phase, and they conclude that this is a photo-induced superconducting phase. After this experiment, they have reported similar light-induced superconducting-like phenomena with selective excitation of a certain phonon mode in other materials such as YBCO [20, 21] and K₃C₆₀ [22].

Even though the interpretation of these phenomena as light-induced superconductivity is rather controversial at present, one important and seemingly relevant notion is "non-linear phononics", where a resonantly excited infrared phonon mode results in displacement of a Raman mode anharmonically coupled to the former [51, 52]. Indeed, this nonlinear lattice excitation is reported under the relevant conditions for enhanced superconductivity-like behavior [53]. It is discussed that the displaced Raman mode leads to a significant change in the electronic state [52, 53]. We note that, besides SC, there are many reports in which selective excitations of a certain phonon mode induce other phenomena, such as a transition between Mott-insulating and metallic states [54] and melting of orbital and magnetic orders [55]. In these cases, non-linear phononics is also considered to be crucial [52, 55, 56].

In this thesis, we do not deal with this problem directly. We only mention that this nonlinear phononics can be used for pumping a system to induce coherent oscillations in Sec. 4.2. However, at present, theoretical studies of non-linear phononics are limited to classical phonon dynamics, and effects of the phonon dynamics on electron properties are assessed assuming that electrons are in equilibrium under the induced phonon distortion [52]. Therefore, it will be important to extend our formalism that includes quantum phonon dynamics to the non-equilibrium problem involving non-linear phononics in future.

1.3 The Holstein-Hubbard and Holstein models

One of the simplest models of electron-phonon coupled systems is the Holstein-Hubbard model, whose Hamiltonian is

$$\begin{aligned} \mathcal{H}(t) = & - \sum_{i,j,\sigma} v_{i,j}(t) c_{i,\sigma}^\dagger c_{j,\sigma} - \mu \sum_i n_i + U \sum_i n_{i,\uparrow} n_{i,\downarrow} \\ & + \omega_0 \sum_i a_i^\dagger a_i + g(t) \sum_i (a_i^\dagger + a_i)(n_i - 1), \end{aligned} \quad (1.1)$$

where c_i^\dagger is a creation operator of an electron with spin σ at a site i , $n_i = n_{i,\uparrow} + n_{i,\downarrow}$ with $n_{i,\sigma} = c_{i,\sigma}^\dagger c_{i,\sigma}$, $v_{i,j}$ is the electron hopping, μ is the electron chemical potential and U is the

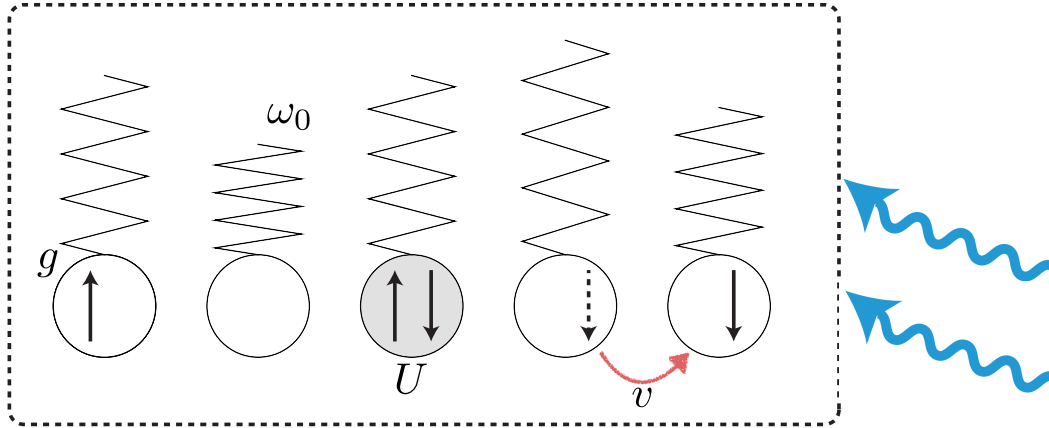


Figure 1.7: Schematic picture of the Holstein-Hubbard model. A circle stands for a site and arrows denote up and down spin electrons. U is the on-site electron-electron Coulomb interaction. A spring shows a phonon with frequency ω_0 , which is coupled to electrons with the el-ph coupling constant g . Electrons can hop between sites with the hopping amplitude v . Wavy lines indicate external perturbations.

Coulomb interaction. a_i^\dagger is a creation operator of a phonon, ω_0 is the bare frequency of an Einstein phonon and g is the el-ph coupling. When $U = 0$, the model is called the Holstein model. Here we also put time-dependence on the hopping term and the el-ph coupling, which we consider later in the thesis. Schematically the model is depicted in Fig. 1.7. We note that in a path-integral framework we can integrate out phonons to obtain an effective retarded electron-electron interaction,

$$U_{\text{eff}}(\omega) = U - \frac{2g^2\omega_0}{\omega_0^2 - \omega^2}. \quad (1.2)$$

The second term is the phonon-mediated retarded attractive interaction, whose strength is characterized by

$$\lambda \equiv \frac{2g^2}{\omega_0}, \quad (1.3)$$

in the $\omega \rightarrow 0$ limit. In the anti-adiabatic limit of $\omega_0 \rightarrow \infty$ with λ and U fixed, this model becomes the Hubbard model, a model without retarded interactions.

The Holstein and Holstein-Hubbard models have been studied to understand fundamental effects of the electron-phonon (el-ph) coupling in various spatial dimensions and with various methods. Here we briefly summarize these works. We start with equilibrium cases. In one spatial dimension, there are many kinds of useful methods, such as exact diagonalization for small chains [57, 58], a variational method [59], density-matrix renormalization group (DMRG) [60–62], and QMC methods [63–65]. Hence general features of the phase diagram of the ground state are understood better than those in other dimensions. At half-filling (one electron per site), it has been pointed out that there are three different phases, i.e. charge order (CO), spin density wave (SDW) and CDW/sSC, see Fig. 1.8(a). Here, CDW/sSC means that the coexistence of semi-long-range correlations (power-law decay of spatial correlations) of SC and CO is realized [60, 61]. In some literature [62], the authors call this phase a metallic state taking

<p>(a)</p> <p>Please look at Fig. 9 (a) in Ref. [61].</p>	<p>(b)</p> <p>Please look at Fig. 4 (d) in Ref. [66].</p>
---	---

Figure 1.8: (a) A phase diagram of the half-filled Holstein-Hubbard model in one dimension against U , λ and ω_0 derived with DMRG (From Ref. [61]). (b) A phase diagram in two dimensions derived with a determinant QMC method on the plane of λ and U (From Ref. [66]). The notation is the same as in the thesis.

account of the fact that the charge gap is zero there. At $\lambda > U$ the system tends to favor CO, while at $U > \lambda$ it favors SDW. The CDW/sSC phase is located in the region around $U \sim \lambda$ between CO and SDW. It is also suggested that, if U is large enough, the transition between CO and SDW is direct [65]. Even though the information about the competition between different orders are useful, ordered states considered in one-dimensional case are quasi-ordered states rather than long-ranged ones when the symmetry is continuous. Hence it is important to understand similarities and differences from the situation in other dimensions.

In two spatial dimensions, available methods become limited. Still, there have been many works for the Holstein model ($U=0$) with QMC or with the diagrammatic approximation based on the Migdal-Eliashberg theory [70–74]. In these works, susceptibilities for SC and CO are analyzed to reveal that a CO instability dominates at half-filling while away from half-filling a SC susceptibility becomes dominant. However, discussion on the boundary between CO and SC is lacking. As for the Holstein-Hubbard model, investigations are further limited compared to the Holstein model. So far, perturbative methods [75, 76] and QMC [66, 77] have been used for this model. Ref. [75] takes the adiabatic limit and treats the Coulomb repulsion U with the Hartree-Fock approximation. Existence of a CO+AF phase at quarter-filling is suggested there. However, the accuracy of the Hartree-Fock approximation should become degraded as U increases, and confirmation from more sophisticated methods are required. Ref. [66, 77] uses a determinant QMC method, which is an unbiased method, and suggests a possible metallic phase between AF and CO at half-filling as in the 1D case, see Fig. 1.8 (b). However, because of the sign problem, the authors could not reach low enough temperatures, and a question whether this metallic state remains towards $T = 0$ is still an open question. Therefore, there is much room for further investigation.

In dimensions higher than three, it is believed that physical properties are close to those in infinite dimensions, where the DMFT is exact. Therefore, we now review works with the DMFT for the Holstein and Holstein-Hubbard models. When we focus only on normal phases,

(a)	(b)	(c)
Please look at Fig. 1 in Ref. [67].	Please look at Fig. 2 in Ref. [68].	Please look at Fig. 1 in Ref. [69].

Figure 1.9: Phase diagrams obtained with DMFT. (a) A phase diagram of the Holstein-Hubbard model neglecting ordered states on the plane of μ and g at two indicated temperatures (From Ref. [67]). (b) A phase diagram of the Holstein model on the plane of μ and T for various values of g (From Ref. [68]). (c) A ground-state phase diagram of the Holstein-Hubbard model on the plane of U and λ (From Ref. [69]). PM stands for the paramagnetic metallic phase, MI the Mott insulating phase, and BP the bipolaronic phase. The other notation is the same as in the thesis.

the phase diagram is obtained, in which bipolaronic insulator, Mott insulator and metal compete with each other [67, 78], see Fig. 1.9 (a). As for ordered phases, the Holstein model has been investigated from the early stage of the DMFT [68, 79]. At half filling, CO is favored, and away from half filling SC is favored as in other dimensions, see Fig. 1.9(b). In those early works, they focus on the phase transition from the normal state by evaluating relevant susceptibilities. Hence direct studies of these ordered phases are missing and the information about the transition from CO to SC is not revealed. However, a phase with microscopic coexistence of SC (off-diagonal long range order; ODLRO) and CO (diagonal long range order; DLRO) is called a *supersolid state*, and has been attracting much interests in many fields including Bosonic systems [80–83], Boson-Fermion mixed systems [84] and spin systems [85–89]. Therefore, it is interesting to clarify possibility of coexistence of CO and SC in such a simple el-ph model along with its condition and mechanism. For the Holstein-Hubbard model, competition of phases around the $\lambda \sim U$ regime requires further investigation. As far as we are aware, the works by Bauer et al. [69, 90] are the only ones. They employ the numerical renormalization group (NRG) as an impurity solver, where the result is confined to $T = 0$, and they focus on half-filling. They conclude that AF and CO compete in this region and their boundary is located around $U \sim \lambda$ regardless of the strength of U and λ , see Fig. 1.9(c). They also point out that the order of transition changes. For weak couplings and high phonon frequencies, the phase transition tends to be continuous. On the other hand, for strong couplings and low phonon frequencies, the phase transition is discontinuous. Since the phase diagram around the $\lambda \sim U$ regime is attracting much interest in other dimensions [60, 61, 66], it is imperative to systematically study the competition of different orders and examine the fate of a possible intermediate metallic/SC phase ¹.

The Holstein and Holstein-Hubbard models have also been studied to explore non-equilibrium dynamics involving el-ph couplings. A time-dependent exact diagonalization (ED) method has

¹We note that properties of the superconducting state when ω_0 , λ and U are comparable to the band with is also important to understand. It is discussed in Appendix. A.3 since it slightly deviates from the stream of the thesis.

been applied to study dynamics of one or two polarons in the Holstein model [91–93], and the non-equilibrium DMFT [26] has been also applied to a single-electron problem [94]. As for many-electron problems, an ED analysis for the Holstein-Hubbard model [95] and weak-coupling perturbation analyses for the Holstein model with phonons in equilibrium [96–100] have been done so far in two dimensions. For higher dimensions, there have been analyses with the framework of DMFT for the strong-coupling regime [101,102]. Still, we must point out that effects of non-equilibrium phonon dynamics are taken into account only around the insulating regime [94,95,101,102], and development of methods taking account of the effect is required for the correlated metallic regime. In addition, studies of the dynamics of ordered states have just begun [99,100] and further investigation is necessary when we consider the present situation where non-equilibrium problems of ordered phases are experimentally a hot topic [17–22,55].

Taking account of above the situation, we study the Holstein and Holstein-Hubbard models with DMFT to obtain new understanding of competition of different orders and dynamical properties involving strong electron-phonon couplings. Briefly speaking, characteristic features of DMFT are

1. Existence of a well-defined limit :
DMFT becomes exact in the infinite spatial dimensions.
2. Rigorous implementation in equilibrium :
There are numerically reliable and feasible methods to solve the associated effective impurity problem, such as numerically exact CT-QMC and NRG.
3. Feasibility of extension to non-equilibrium problems :
Because the self-energy is independent of the momentum, implementation of the non-equilibrium DMFT is relatively easy as compared to other methods that take into account momentum dependence.

More detailed explanation of DMFT is in Chap. 2.

1.4 Structure of this thesis

This thesis is organized as follows: In Chap. 2, we explain the general idea of DMFT in and out of equilibrium. Then we formulate details of the hybridization expansion CT-QMC for the Holstein-Hubbard model (Sec. 2.2), which we newly extend in order to deal with ordered phases in the model. In Sec. 2.3, we discuss the non-equilibrium formalism and introduce the non-equilibrium self-consistent Migdal approximation, which is a new approximate impurity solver developed for the Holstein model. In Chap. 3, we investigate with DMFT+CT-QMC competition of different orders in the Holstein-Hubbard model at half-filling (Sec. 3.1) and in the Holstein model away from half-filling (Sec. 3.2). Chap. 4 is devoted to investigation of non-equilibrium situations using non-equilibrium DMFT with the impurity solver developed in Sec. 2.3. In Sec. 4.1 we study relaxation processes in the Holstein model to find a crossover of qualitative characters of relaxation processes. In Sec. 4.2 we reveal properties of collective excitations in strongly-coupled phonon-mediated superconductors. Finally, in Chap. 5, we conclude the thesis and explain future perspectives about how to relate the investigations of equilibrium and non-equilibrium states discussed in the thesis. We also pose several future problems there. The whole structure is illustrated in Fig. 1.10.

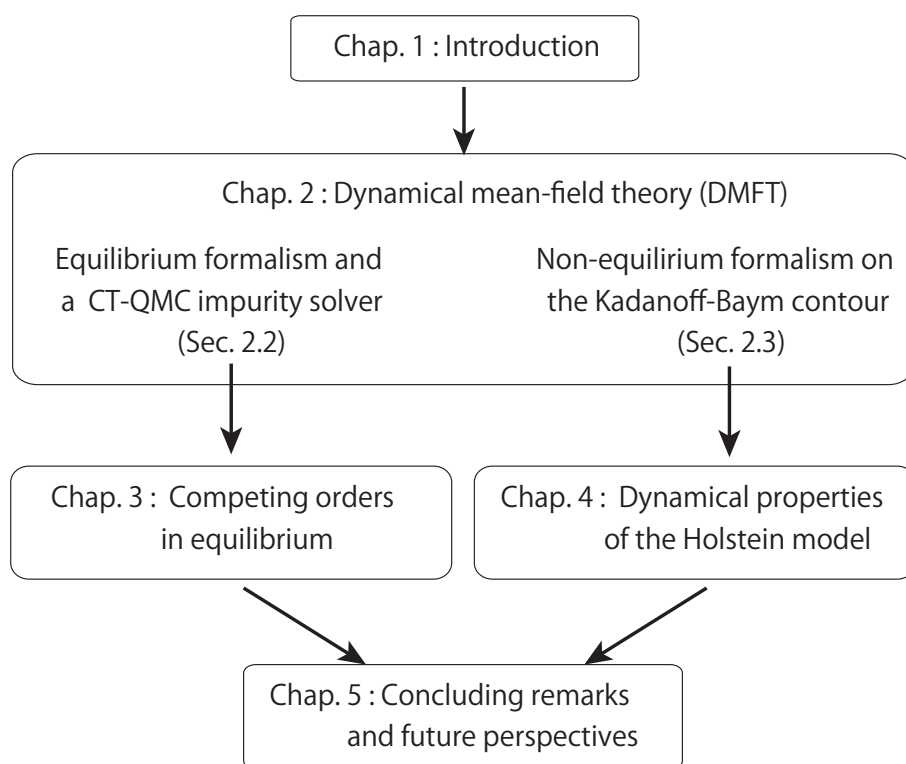


Figure 1.10: Organization of the thesis.

Chapter 2

Dynamical mean-field theory

In this chapter, we introduce the dynamical mean-field theory (DMFT) in [25] and out of equilibrium [26], which we employ to study the Holstein-Hubbard and Holstein models in this thesis. In Sec. 2.1, we introduce equilibrium and non-equilibrium Green's functions and explain the essential idea of DMFT, in which the original lattice model is mapped onto an effective impurity problem and how to solve the impurity model is important. In Sec. 2.2, we introduce a continuous time Quantum Monte Carlo (CT-QMC) impurity solver, which we have newly extend to deal with the s-wave superconductivity in the models mentioned above. In Sec. 2.3, we shall introduce the non-equilibrium DMFT for the Holstein model in detail and explain an approximate non-equilibrium impurity solver, which we have developed to take account of phonon dynamics.

2.1 General formalism

DMFT is one of the most successful Green's-function methods for strongly-correlated systems, and it is justified in the infinite dimensional limit [23–25, 103]. In this theory, the dynamical correlation is exactly taken into account for the spatially-local part, while non-local ones are neglected. Even though it is an approximation in finite spetial dimensions, it becomes a good approximation for large coordination numbers, and has successfully explained many important phenomena such as the Mott transition in strongly correlated materials [25, 104].

In DMFT, a lattice model is mapped onto an effective impurity problem and one needs to solve it in a self-consistent manner in order to obtain the Green's function and the self-energy. Hence how to solve the effective impurity problem is a crucial point in implementing DMFT. However, the effective impurity problem is still a many-body problem and is non-tribal, although it is easier than the original lattice model. In equilibrium, there are various reliable impurity solvers such as exact diagonalizations (ED), numerical renormalization group (NRG) and quantum Monte Carlo (QMC) methods. In particular, as for QMC methods, which we employ for equilibrium analyses, there has been continuous effort to develop new ones applicable to new situations (new phases, new type of interactions, etc) and to reduce sign problems. In non-equilibrium situations, development of impurity solvers is rather limited compared to the equilibrium cases. Since QMC methods suffer from a severe dynamical sign problem, one can only study short-time dynamics numerically accurately. Hence proper approximate solvers have often been developed and employed for the implementation.

2.1.1 Green's functions in and out of equilibrium

When we want to study properties of systems, we do not necessarily need to study the wave function or the density matrix, which include the full information. Instead, we can focus on certain functions that include sufficient information. Single-particle Green's functions are such functions, and DMFT is a theory for evaluating the Green's functions. Contours on which the Green's functions are defined depend on problems concerned. Hence we need to explain the Green's functions before we discuss DMFT. In equilibrium cases at finite temperatures, we usually use the Matsubara formalism, where the contour is located along the imaginary time axis, see Fig. 2.1 (a). With this formalism, real frequency data can be obtained by an analytical continuation from the imaginary axis after the Fourier transformation. On the other hand, when one is interested in the transient dynamics starting from an equilibrium state the L-shaped contour (the Kadanoff-Baym contour) illustrated in Fig. 2.1(b) is the proper choice. \mathcal{C}_3 in Fig. 2.1 (b) represents the initial state, and we follow the real time dynamics on \mathcal{C}_1 and \mathcal{C}_2 . We note in Fig. 2.1 that the contour in the Matsubara formalism is the same as \mathcal{C}_3 in the Kadanoff-Baym (KB) contour. Therefore, the Green's functions on \mathcal{C}_3 on the Matsubara contour are essentially the same. In the following, we introduce the Green's functions for electrons in both formalism briefly. For simplicity, here we suppress indices such as the momentum, spin, etc for electron operators. Detailed properties of the function in the KB formalism are given in Sec. 2.3.

Equilibrium

Let the Hamiltonian of the system be \mathcal{H} . In the Matsubara formalism, we define the Green's function as

$$G(\tau, \tau') = -\langle \mathcal{T} c(\tau) c^\dagger(\tau') \rangle, \quad (2.1)$$

where $c(\tau) = e^{\tau\mathcal{H}} c e^{-\tau\mathcal{H}}$ and $c^\dagger(\tau') = e^{\tau'\mathcal{H}} c^\dagger e^{-\tau'\mathcal{H}}$. Because of translational invariance against the imaginary time, we have $G(\tau, \tau') = G(\tau - \tau')$ in equilibrium. In addition, since $G(\tau) = G(\tau - \beta)$ for $\tau \in [0, \beta]$, we define the Fourier component of the Green's function as

$$G(i\omega_n) \equiv \int_0^\beta d\tau e^{i\omega_n \tau} G(\tau), \quad (2.2)$$

where $\omega_n = (2n + 1)\pi/\beta$ is the Matsubara frequency.

Non-equilibrium

For the KB formalism we fix the notation as follows:

1. \mathcal{C} indicates the KB contour (the L-shaped contour), Fig. 2.1(b). \mathcal{C}_1 stands for $[0, t_{\max}]$, \mathcal{C}_2 for $[t_{\max}, 0]$ and \mathcal{C}_3 for $[0, -i\beta]$.
2. $\nu \in \mathcal{C}$ denote points on the KB contour.
3. $s(\nu)$ is a function that takes $t \in [0, t_{\max}]$ when ν is at t or $\tau \in [0, \beta]$ when ν is at $-i\tau$.
4. Integral on \mathcal{C} : $\int_{\mathcal{C}} d\nu F(\nu) \equiv \int_0^{t_{\max}} dt F_1(t) - \int_0^{t_{\max}} dt F_2(t) - i \int_0^\beta d\tau F_3(\tau)$. Here $F(\nu)$ is a function on \mathcal{C} , and F_i corresponds to the part of $F(\nu)$ on \mathcal{C}_i .

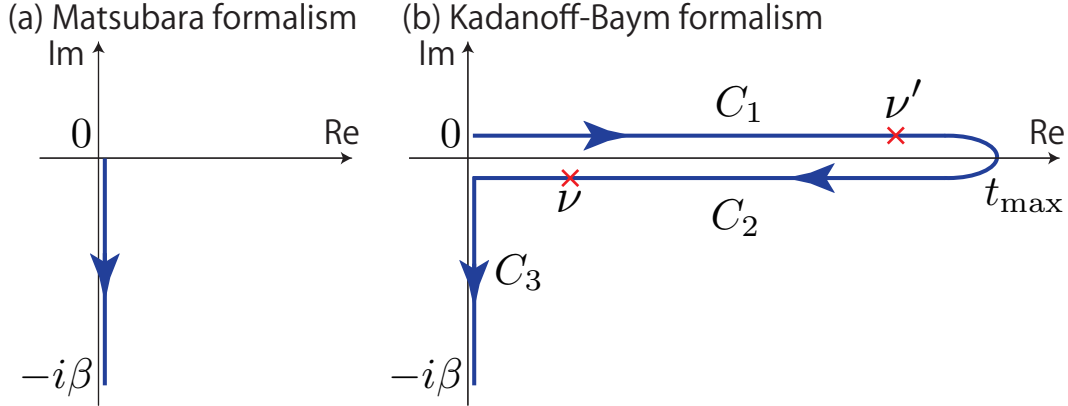


Figure 2.1: (a) A schematic picture for the contour in the Matsubara formalism. (b) A schematic picture for the contour in the Kadanoff-Baym formalism (the Kadanoff-Baym contour), $C = C_1 \cup C_2 \cup C_3$, where the arrows indicate the contour ordering.

5. Differential on C : $\partial_\nu g(\nu) \equiv \lim_{|\nu - \nu'| \rightarrow 0} \frac{g(\nu) - g(\nu')}{\nu - \nu'}$, where $\nu - \nu'$ means $s(\nu) - s(\nu')$ when $\nu, \nu' \in C_1$ or $\nu, \nu' \in C_2$ and $-i[s(\nu) - s(\nu')]$ when $\nu, \nu' \in C_3$.
6. We define the order on the contour as in Fig. 2.1. $\nu \succ \nu'$ means ν comes later than ν' .
7. $\theta_C(\nu, \nu')$ and $\delta_C(\nu, \nu')$ are the Heaviside function and the delta function respectively defined on the KB contour with the order defined above.

Now we introduce the contour-ordered Green's functions on the KB contour. Since these Green's functions are not so common as the equilibrium ones, we introduce them explaining the basic idea. In the present formalism, we consider situations described by a time-dependent Hamiltonian $\mathcal{H}(t) = H(t) - \mu N$, where the system is in equilibrium at $t = 0$ with a temperature T . Hence the initial state at $t = 0$ is characterized by the density matrix, $\rho(0) = \frac{1}{Z} e^{-\beta \mathcal{H}(0)}$ with $Z = \text{tr} e^{-\beta \mathcal{H}(0)}$. The time evolution of the the density matrix is expressed as $\rho(t) = \mathcal{U}(t, 0) \rho(0) \mathcal{U}(0, t)$. Here, $\mathcal{U}(t, t')$ satisfies $\mathcal{U}(t', t') = 1$ and obeys

$$i \frac{d}{dt} \mathcal{U}(t, t') = \mathcal{H}(t) \mathcal{U}(t, t'). \quad (2.3)$$

Hence we can express $\mathcal{U}(t, t')$ as

$$\begin{aligned} \mathcal{U}(t, t') &= \mathcal{U}(t', t') + \int_{t'}^t d\bar{t} \frac{d}{d\bar{t}} \mathcal{U}(\bar{t}, t') \\ &= 1 + \int_{t'}^t d\bar{t} (-i\mathcal{H}(\bar{t})) \mathcal{U}(\bar{t}, t') \\ &= 1 + \int_{t'}^t d\bar{t} (-i\mathcal{H}(\bar{t})) + \int_{t'}^t d\bar{t}_1 \int_{t'}^{\bar{t}_1} d\bar{t}_2 (-i\mathcal{H}(\bar{t}_1)) (-i\mathcal{H}(\bar{t}_2)) + \dots \\ &= \begin{cases} \mathcal{T} \exp(-i \int_{t'}^t d\bar{t} \mathcal{H}(\bar{t})) & t > t' \\ \bar{\mathcal{T}} \exp(-i \int_{t'}^t d\bar{t} \mathcal{H}(\bar{t})) & t < t' \end{cases}, \end{aligned} \quad (2.4)$$

where \mathcal{T} ($\bar{\mathcal{T}}$) is the time ordering (anti-time ordering) operator. Here we note that $\mathcal{U}(t, t')$ is a unitary operator, $\mathcal{U}(t, t')^\dagger = \mathcal{U}(t', t)$, and $\mathcal{U}(t, t'') = \mathcal{U}(t, t') \mathcal{U}(t', t'')$. Now, a physical quantity

$\langle \mathcal{O} \rangle$ is expressed as

$$\begin{aligned} \langle \mathcal{O} \rangle(t) &= \text{Tr}[\rho(t)\mathcal{O}_s] \\ &= \frac{1}{Z} \text{Tr}[e^{-\beta\mathcal{H}(0)}\mathcal{U}(0,t)\mathcal{O}_s\mathcal{U}(t,0)], \end{aligned} \quad (2.5)$$

where the subscript s indicates the operator is in the Schrödinger representation.

Our main interests are properties of interacting systems. Usual procedure to study quantities in interacting systems is to start with a solvable regime and take account of the interaction of the original problem. In the above expression, we need to take into account such corrections for both $\rho(0)$ and $\mathcal{U}(t,t')$. In order to do this, it is useful to extend the notion of the time-evolution operator $\mathcal{U}(t,t')$, so that it can express $\rho(0)$ and $\mathcal{U}(t,t')$ in a unified manner. For this, we now define the evolution operator on \mathcal{C} such that $\mathcal{U}_c(\nu,\nu) = 1$ and

$$i\partial_\nu \mathcal{U}_c(\nu,\nu') = \mathcal{H}(\nu)\mathcal{U}_c(\nu,\nu'). \quad (2.6)$$

From this definition, we obtain

$$\begin{aligned} \mathcal{U}_c(\nu,\nu') &= \mathcal{U}_c(\nu',\nu') + \int_{c,\nu'}^\nu d\bar{\nu} \frac{d}{d\bar{\nu}} \mathcal{U}_c(\bar{\nu},\nu'), \\ &= 1 + \int_{c,\nu'}^\nu d\bar{\nu} (-i\mathcal{H}(\bar{\nu}))\mathcal{U}_c(\bar{\nu},\nu'), \\ &= 1 + \int_{c,\nu'}^\nu d\bar{\nu} (-i\mathcal{H}(\bar{\nu})) + \int_{\nu'}^\nu d\bar{\nu}_1 \int_{\nu'}^{\bar{\nu}_1} d\bar{\nu}_2 (-i\mathcal{H}(\bar{\nu}_1))(-i\mathcal{H}(\bar{\nu}_2)) + \dots, \\ &= \begin{cases} \mathcal{T}_c \exp(-i \int_{\nu'}^\nu d\bar{\nu} \mathcal{H}(\bar{\nu})) & \nu \succ \nu' \\ \bar{\mathcal{T}}_c \exp(-i \int_{\nu'}^\nu d\bar{\nu} \mathcal{H}(\bar{\nu})) & \nu \prec \nu'. \end{cases} \end{aligned} \quad (2.7)$$

We note that, although the operator is no longer unitary, it satisfies

$$\mathcal{U}_c(\nu,\nu'') = \mathcal{U}_c(\nu,\nu')\mathcal{U}_c(\nu',\nu''). \quad (2.8)$$

As for the relation with $\rho(0)$ and $\mathcal{U}(t,t')$, one can show

1. $\mathcal{U}_c(\nu,\nu') = \mathcal{U}(s(\nu),s(\nu'))$ when $\nu,\nu' \in C_1, C_2$,
2. $\mathcal{U}_c(\nu,0) = \exp(-s(\nu)\mathcal{H}(0))$ when $\nu \in C_3$.

We also note that the partition function is expressed as $Z = \text{Tr} \exp(-\beta\mathcal{H}(0)) = \text{Tr}[\mathcal{T}_c \exp(-i \int_{\mathcal{C}} d\nu \mathcal{H}(\nu))]$.

Now, let us define the Heisenberg expression on \mathcal{C} ,

$$\mathcal{O}_c(\nu) = \mathcal{U}_c(0,\nu)\mathcal{O}_s(\nu)\mathcal{U}_c(\nu,0). \quad (2.9)$$

If we define as

$$\begin{aligned} \langle \mathcal{O} \rangle(\nu) &\equiv \frac{1}{Z} \text{Tr}[\exp(-\beta\mathcal{H}(0))\mathcal{O}_c(\nu)], \\ &= \frac{1}{Z} \text{Tr}[\mathcal{U}_c(-i\beta,0)\mathcal{U}_c(0,\nu)\mathcal{O}_s(\nu)\mathcal{U}_c(\nu,0)], \\ &= \frac{\text{Tr}[\mathcal{T}_c \exp(-i \int_{\mathcal{C}} d\bar{\nu} \mathcal{H}(\bar{\nu}))\mathcal{O}_s(\nu)]}{\text{Tr}[\mathcal{T}_c \exp(-i \int_{\mathcal{C}} d\bar{\nu} \mathcal{H}(\bar{\nu}))]}, \end{aligned} \quad (2.10)$$

then we find $\langle \mathcal{O} \rangle(\nu) = \langle \mathcal{O} \rangle(s(\nu))$ when $\nu \in C_1, C_2$. We can also consider higher-order correlation functions,

$$\begin{aligned}
 \langle \mathcal{T}_c A_c(\nu) B_c(\nu') \rangle &= \theta_C(\nu, \nu') \langle A_c(\nu) B_c(\nu') \rangle \pm \theta_C(\nu', \nu) \langle B_c(\nu') A_c(\nu) \rangle \\
 &= \theta_C(\nu, \nu') \frac{1}{Z} \text{Tr}[\mathcal{U}_c(-i\beta, 0) A_c(\nu) B_c(\nu')] \pm \theta_C(\nu', \nu) \frac{1}{Z} \text{Tr}[\mathcal{U}_c(-i\beta, 0) B_c(\nu') A_c(\nu)] \\
 &= \frac{\text{Tr}[\mathcal{T}_c \exp(-i \int_C d\bar{\nu} \mathcal{H}(\bar{\nu})) A_s(\nu) B_s(\nu')]}{\text{Tr}[\mathcal{T}_c \exp(-i \int_C d\bar{\nu} \mathcal{H}(\bar{\nu}))]}. \tag{2.11}
 \end{aligned}$$

Here + is for bosonic operators and – for fermionic ones.

Now, we define the contour-ordered Green's function for electrons on the KB contour,

$$\begin{aligned}
 G(\nu, \nu') &\equiv -i \langle T_c c(\nu) c(\nu') \rangle \\
 &= -\frac{i}{Z} \theta_C(\nu, \nu') \text{Tr}[\mathcal{U}_c(-i\beta, 0) c(\nu) c^\dagger(\nu')] + \frac{i}{Z} \theta_C(\nu', \nu) \text{Tr}[\mathcal{U}_c(-i\beta, 0) c^\dagger(\nu') c(\nu)]. \tag{2.12}
 \end{aligned}$$

Nambu formalism

In order to deal with superconducting states, we introduce the Nambu formalism. The Nambu spinor is

$$\hat{\Psi} \equiv \begin{bmatrix} c_1 \\ c_2 \end{bmatrix} \equiv \begin{bmatrix} c_\uparrow \\ c_\downarrow \end{bmatrix}. \tag{2.13}$$

For equilibrium cases, the Green's functions are defined as

$$\hat{G}(\tau - \tau') \equiv -\langle \mathcal{T} \hat{\Psi}(\tau) \hat{\Psi}^\dagger(\tau') \rangle, \tag{2.14}$$

or more explicitly

$$\begin{bmatrix} G_{11}(\tau - \tau') & G_{12}(\tau - \tau') \\ G_{21}(\tau - \tau') & G_{22}(\tau - \tau') \end{bmatrix} = \begin{bmatrix} -\langle \mathcal{T} c_1(\tau) c_1^\dagger(\tau') \rangle & -\langle \mathcal{T} c_1(\tau) c_2^\dagger(\tau') \rangle \\ -\langle \mathcal{T} c_2(\tau) c_1^\dagger(\tau') \rangle & -\langle \mathcal{T} c_2(\tau) c_2^\dagger(\tau') \rangle \end{bmatrix}. \tag{2.15}$$

For non-equilibrium cases, the 2×2 contour-ordered Green's function for electrons is defined as

$$\hat{G}(\nu, \nu') \equiv -i \langle \mathcal{T}_c \hat{\Psi}(\nu) \hat{\Psi}^\dagger(\nu') \rangle, \tag{2.16}$$

or more explicitly

$$\begin{bmatrix} G_{11}(\nu, \nu') & G_{12}(\nu, \nu') \\ G_{21}(\nu, \nu') & G_{22}(\nu, \nu') \end{bmatrix} = \begin{bmatrix} -i \langle \mathcal{T}_c c_1(\nu) c_1^\dagger(\nu') \rangle & -i \langle \mathcal{T}_c c_1(\nu) c_2^\dagger(\nu') \rangle \\ -i \langle \mathcal{T}_c c_2(\nu) c_1^\dagger(\nu') \rangle & -i \langle \mathcal{T}_c c_2(\nu) c_2^\dagger(\nu') \rangle \end{bmatrix}. \tag{2.17}$$

Here G_{12} and G_{21} are anomalous Green's functions.

2.1.2 Essence of DMFT

Here we explain the basic idea of DMFT. Since the KB formalism includes the Matsubara formalism we use the former for the explanation. The most general Hamiltonian considered in the thesis is

$$\begin{aligned}
 H(t) = & - \sum_{i,j,\sigma} v_{i,j}(t) c_{i,\sigma}^\dagger c_{j,\sigma} - \mu \sum_i n_i + \omega_0 \sum_i a_i^\dagger a_i + F_{\text{ex}}(t) \sum_i (c_{i\uparrow}^\dagger c_{i\downarrow}^\dagger + c_{i\downarrow} c_{i\uparrow}) \\
 & + g(t) \sum_i (a_i^\dagger + a_i)(n_{i,\uparrow} + n_{i,\downarrow} - 1) + U \sum_i n_{i,\uparrow} n_{i,\downarrow}.
 \end{aligned} \tag{2.18}$$

The notation is the same as in Eq. 1.1. The fourth term with $F_{\text{ex}}(t)$ is a pair potential field and is introduced here to evaluate the dynamical pair susceptibility, which detects the collective amplitude mode, see Sec. 4.2.

In DMFT, we map a lattice problem on an effective impurity model in a self-consistent manner. The corresponding Hamiltonian is

$$\begin{aligned}
 H_{\text{eff,imp}}(t) = & \sum_{\sigma,p} \epsilon_p(t) b_{p,\sigma}^\dagger b_{p,\sigma} + \sum_p \Delta_p(t) b_{p\uparrow}^\dagger b_{-p\downarrow}^\dagger + \sum_p \Delta_p^*(t) b_{-p\downarrow} b_{p\uparrow} \\
 & + \sum_{\sigma,p} [V_p^\sigma(t) c_\sigma^\dagger b_{p,\sigma} + \text{h.c.}] \\
 & - \mu(n_\uparrow + n_\downarrow) + F_{\text{ex}}(t)(c_\uparrow^\dagger c_\downarrow^\dagger + c_\downarrow c_\uparrow) \\
 & + U n_\uparrow n_\downarrow + g(t)(a^\dagger + a)(n_\uparrow + n_\downarrow - 1) + \omega_0 a^\dagger a.
 \end{aligned} \tag{2.19}$$

or, in the path integral form, the action is

$$\begin{aligned}
 S_{\text{imp}} = & i \int_{\mathcal{C}} d\nu d\nu' \hat{\Psi}^\dagger(\nu) \hat{\mathcal{G}}_{0,\sigma}^{-1}(\nu, \nu') \hat{\Psi}(\nu') + i \int_{\mathcal{C}} d\nu d\nu' a^\dagger(\nu) (i\partial_\nu - \omega_0) a(\nu) \\
 & - i \int_{\mathcal{C}} d\nu g(\nu) [a(\nu) + a^\dagger(\nu)] \hat{\Psi}^\dagger(\nu) \sigma_3 \hat{\Psi}(\nu) - iU \int_{\mathcal{C}} d\nu n_1(\nu) [1 - n_2(\nu)],
 \end{aligned} \tag{2.20}$$

where

$$\hat{\mathcal{G}}_0^{-1}(\nu, \nu') = [i\partial_\nu \hat{I} + \mu \hat{\sigma}_3 - F_{\text{ex}}(\nu) \hat{\sigma}_1] \delta_{\mathcal{C}}(\nu, \nu') - \hat{\Delta}(\nu, \nu'). \tag{2.21}$$

Here c is the annihilation operator of an electron on the impurity cite, n_σ is the number of electrons with spin σ on the impurity site, a is the annihilation operator of a local phonon connected to the impurity, and b is the annihilation operator of an electron in a fermionic bath. p represents a momentum, ϵ_p is the kinetic energy of the electron in the bath, where we assume $\epsilon_p = \epsilon_{-p}$. This model is the so-called Anderson-Holstein model. Since we consider SC states in this thesis, we have introduced Δ_p , a finite value of which indicates that the bath is in a SC phase. Hence this Hamiltonian expresses a single-site impurity connected to local phonons in a SC bath. $\hat{\Delta}(\nu, \nu')$ is the hybridization function that is obtained by tracing out the effective bath, \hat{I} is the identity matrix and $\hat{\sigma}_3$ is the Pauli matrix.

The Dyson equation for the impurity problem is

$$\hat{G}_{\text{imp}}(\nu, \nu') = \hat{\mathcal{G}}_0(\nu, \nu') + [\hat{\mathcal{G}}_0 * \hat{\Sigma}_{\text{imp}} * \hat{G}_{\text{imp}}](\nu, \nu'), \tag{2.22}$$

where \hat{G}_{imp} and $\hat{\Sigma}_{\text{imp}}$ are the full Green's function of the impurity problem and the self-energy, respectively, and $A * B(\nu, \nu')$ stands for $\int_{\mathcal{C}} A(\nu, \bar{\nu})B(\bar{\nu}, \nu')d\bar{\nu}$.

The effective impurity model, Eq. 2.19 or Eq. 2.20, is interpreted as an effective model for a focused site on the original lattice problem, and the bath part in $H_{\text{eff,imp}}$ and the hybridization function ($\hat{\Delta}$) in the action effectively represent the effect of the sites surrounding the focused one. These quantities are determined so that G_{imp} and Σ_{imp} are equal to the local Green's function $G_{\text{loc}} = G_{ii}$ and respectively the momentum independent self-energy, $\Sigma_{\mathbf{k}} = \Sigma_{\text{imp}}$, in the original lattice system. Precisely speaking, the effective model is required to satisfy

$$\hat{G}_{\text{imp}}(\nu, \nu') = \frac{1}{N} \sum_{\mathbf{k}} \hat{G}_{\mathbf{k}}(\nu, \nu'), \quad (2.23)$$

where $G_{\mathbf{k}}$ is the Green's function at a momentum, evaluated with

$$\hat{G}_{\mathbf{k}}(\nu, \nu') = \hat{G}_{0,\mathbf{k}}(\nu, \nu') + [\hat{G}_{0,\mathbf{k}} * \hat{\Sigma}_{\text{imp}} * \hat{G}_{\mathbf{k}}](\nu, \nu'), \quad (2.24a)$$

$$\hat{G}_{0,\mathbf{k}}^{-1}(\nu, \nu') = [i\partial_{\nu}\hat{I} - (\epsilon_{\mathbf{k}}(\nu) - \mu)\hat{\sigma}_3 - F_{\text{ex}}(\nu)\hat{\sigma}_1]\delta_{\mathcal{C}}(\nu, \nu'). \quad (2.24b)$$

Here N is the number of sites. From this expression, one can see that, although in DMFT the self-energy is momentum independent, $G_{\mathbf{k}}$ depends on momentum through $\hat{G}_{0,\mathbf{k}}$ and, in many cases $\hat{G}_{0,\mathbf{k}}$ depends only on the energy $\epsilon_{\mathbf{k}}$ of a time-independent free electron at \mathbf{k} . In these cases, one can express $G_{\mathbf{k}}$ as $G_{\epsilon(\mathbf{k})}$ and the summation in the momentum space is replaced by the energy integral with the density of states ($\rho(\epsilon)$) for a time-independent free system.

In other words, in DMFT, it is assumed that the electron self-energy, as a functional of the full Green's function (skeleton diagrams), has the same expression as in the single impurity Anderson model (SIAM),

$$\Sigma_{i,j}[G] = \delta_{i,j}\Sigma_{\text{SIAM}}[G_{i,i}]. \quad (2.25)$$

This expression for the self-energy becomes exact in the limit of infinite spatial dimensions, $d \rightarrow \infty$, with a scaling $1/d^{|i-j|/2}$ for the hopping v_{ij} .

To summarize, in DMFT, we seek the self-consistent solution of Eq. 2.22, Eq. 2.23 and Eq. 2.24, where we need to solve the effective impurity model in some way to relate \mathcal{G}_0 , Σ_{imp} and G_{imp} . The self-consistent solution is obtained by iteration processes.

Finally we comment on the Bethe lattice, which we employ in the thesis. This lattice has no loop (two nodes are connected by only one root) and each node is connected to z neighbors, see Fig. 2.2(a). In the limit of the infinite coordination number, $z \rightarrow \infty$, with the nearest-neighbor hopping scaled as $v_{ij} = v/\sqrt{z}$, the density of states of the free-electron system on the Bethe lattice becomes a semicircular $\rho(\epsilon) = \frac{1}{\pi v} \sqrt{1 - (\frac{\epsilon}{2v})^2}$. In particular, the self-consistency condition for a homogeneous state, Eq. 2.23 and Eq. 2.24, is reduced to

$$\hat{\Delta}(\nu, \nu') = v(\nu)v(\nu')\hat{\sigma}_3\hat{G}_{\text{loc}}(\nu, \nu')\hat{\sigma}_3. \quad (2.26)$$

2.2 Equilibrium Formalism

2.2.1 DMFT for ordered states

In this thesis we focus on three different orders: the s-wave superconductivity (SC), the staggered (commensurate) charge order (CO) and the staggered (commensurate) antiferromag-

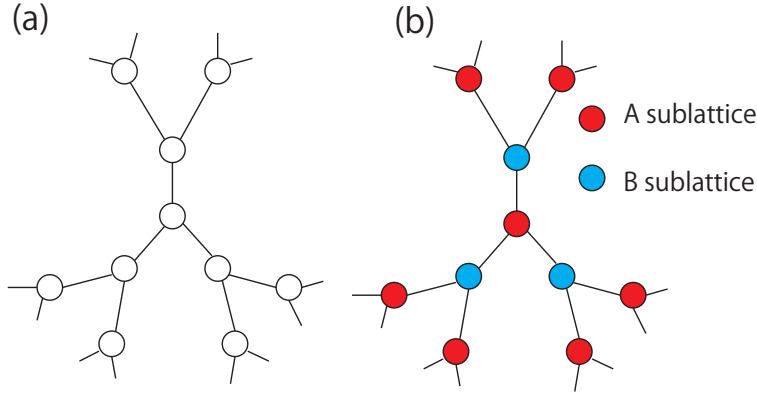


Figure 2.2: (a) The Bethe lattice with $z = 3$, where z is the number of the neighbors for each site. (b) shows how we set the sublattices in studying commensurate AF and CO.

netism (AF), which are considered on the Bethe lattice. The sublattices A and B is illustrated in Fig. 2.2(b). Order parameters for them are defined in Table. 2.1. In the case of a pure AF state ($\Phi_{\text{SC}} = 0, \Phi_{\text{CO}} = 0, \Phi_{\text{AF}} \neq 0$), the average number of the electrons for each sublattice is the same, but the average of the spin differs between sublattice. As for a pure CO state ($\Phi_{\text{SC}} = 0, \Phi_{\text{CO}} \neq 0, \Phi_{\text{AF}} = 0$), the average of the spin for each sublattice is 0, but the average number of the electrons differs between sublattices. In general, some of these can coexist.

Order	Order parameter
s-wave SC	$\Phi_{\text{SC}} = \frac{ \langle c_{A,\downarrow} c_{A,\uparrow} \rangle + \langle c_{B,\downarrow} c_{B,\uparrow} \rangle }{2}$
CO	$\Phi_{\text{CO}} = \frac{ (n_{A,\uparrow} + n_{A,\downarrow}) - (n_{B,\uparrow} + n_{B,\downarrow}) }{4}$
AF	$\Phi_{\text{AF}} = \frac{ (n_{A,\uparrow} - n_{A,\downarrow}) - (n_{B,\uparrow} - n_{B,\downarrow}) }{4}$

Table 2.1: Various order parameters. $n_{A,\sigma}$ and $n_{B,\sigma}$ indicate the density of electrons on the A and B sublattices with spin σ , respectively.

In order to deal with these orders without any bias, we need to allow the difference between A,B sublattices. In this case, the self-consistent condition, Eq. 2.26, is replaced with

$$\hat{G}_{0,A}^{-1}(i\omega_n) = i\omega_n \hat{I} + \mu \hat{\sigma}_3 - v^2 \hat{\sigma}_3 \hat{G}_{\text{loc},B}(i\omega_n) \hat{\sigma}_3, \quad (2.27a)$$

$$\hat{G}_{0,B}^{-1}(i\omega_n) = i\omega_n \hat{I} + \mu \hat{\sigma}_3 - v^2 \hat{\sigma}_3 \hat{G}_{\text{loc},A}(i\omega_n) \hat{\sigma}_3, \quad (2.27b)$$

or, with the hybridization function, it becomes

$$\hat{\Delta}_A(\tau) = v^2 \hat{\sigma}_3 \hat{G}_{\text{loc},B}(\tau) \hat{\sigma}_3, \quad (2.28a)$$

$$\hat{\Delta}_B(\tau) = v^2 \hat{\sigma}_3 \hat{G}_{\text{loc},A}(\tau) \hat{\sigma}_3. \quad (2.28b)$$

Following this general treatment for three different orders, we have implemented the code of DMFT that allows potential AF, CO, and SC orders. In Fig. 2.3, we show a schematic flow

of the DMFT iteration process to obtain the self-consistent solution:

1. Put some initial value to Δ_A ,
 2. solve the impurity problem with Δ_A and determine G_A ,
 3. using G_A , express Δ_B ,
 4. solve the impurity problem with Δ_B and determine G_B ,
 5. using G_B , express Δ_A ,
- and repeat 2~5, until the convergence is attained.

Now the remaining problem is how to solve the impurity problem. We explain this in the following sections.

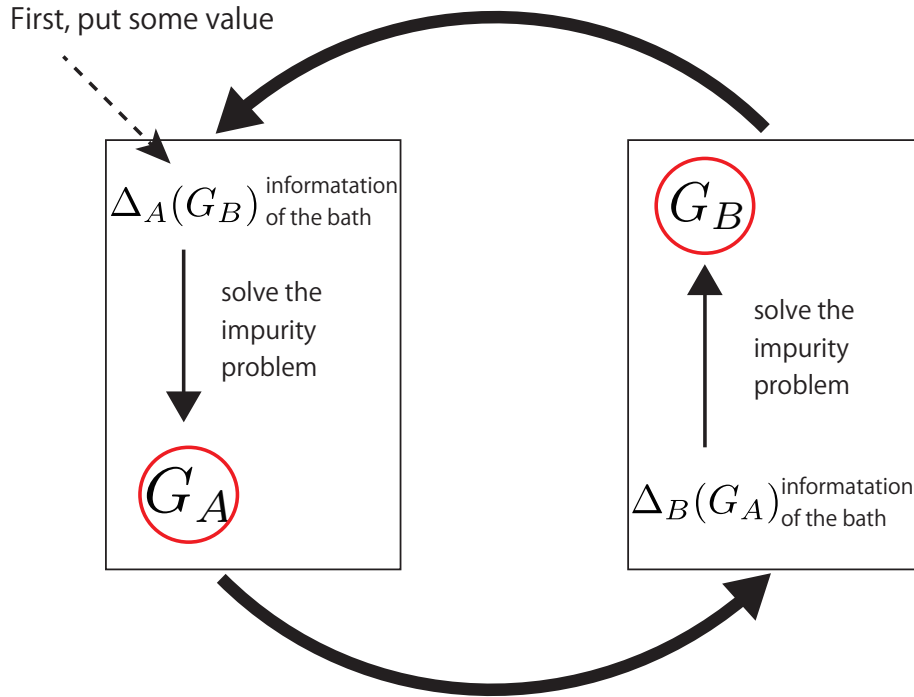


Figure 2.3: The flow of the iteration process. $\Delta_A(G_B)$ means that the hybridization function contains the information of G_B , see Eq. 2.28.

2.2.2 Idea of continuous-time quantum Monte Carlo methods

The basic idea is to make a stochastic sampling of perturbation terms in a partition function [105, 106]. A Hamiltonian is split into a non-perturbative part (H_1) and a perturbative part (H_2): $H = H_1 + H_2$. How to split the Hamiltonian can be decided depending on problems of interest. The interaction representation with respect to H_1 is defined as $O(\tau) = e^{\tau H_1} O e^{-\tau H_1}$. With this representation the partition function is expressed as $Z = \text{Tr}[e^{-\beta H_1} A(\beta)]$, where

$A(\beta) = e^{\beta H_1} e^{-\beta H}$. From the equation of motion, $A(\tau)$ can be expressed as

$$\begin{aligned} A(\beta) &= \mathcal{T} \exp \left[- \int_0^\beta d\tau H_2(\tau) \right] \\ &= 1 + \sum_{n=1}^{\infty} \int_0^\beta d\tau_1 \cdots \int_{\tau_{n-1}}^\beta d\tau_n (-H_2(\tau_n)) \cdots (-H_2(\tau_1)). \end{aligned} \quad (2.29)$$

From this, we obtain

$$\begin{aligned} Z &= \text{Tr} \left[e^{-\beta H_1} \mathcal{T} \exp \left[- \int_0^\beta d\tau H_2(\tau) \right] \right] \\ &= \sum_{n=0}^{\infty} \int_0^\beta d\tau_1 \cdots \int_{\tau_{n-1}}^\beta d\tau_n \text{Tr} \left[e^{-(\beta-\tau_n)H_1} (-H_2) \cdots e^{-(\tau_2-\tau_1)H_1} (-H_2) e^{-\tau_1 H_1} \right]. \end{aligned} \quad (2.30)$$

Now we regard $\theta \equiv \{\tau_1, \dots, \tau_n\}$ with $\tau_i \in [0, \beta]$, as a configuration. Then its weight (contribution to the partition function) is

$$\omega_\theta = \text{Tr} \left[e^{-(\beta-\tau_n)H_1} (-H_2) \cdots e^{-(\tau_2-\tau_1)H_1} (-H_2) e^{-\tau_1 H_1} \right] (d\tau)^n, \quad (2.31)$$

with which $Z = \sum_\theta \omega_\theta$. Here we note that \sum_θ corresponds to $\sum_{n=0}^{\infty} \int_0^\beta \cdots \int_0^\beta$.

In the CT-QMC method, we make a stochastic sampling over these configurations. For this, a random walk ($\theta_1 \rightarrow \theta_2 \rightarrow \dots$) in the configuration space is performed in such a way that the probability to encounter a certain configuration θ_0 in the random walk is equal to $|\omega_{\theta_0}|/Z$. In operating the random walk, one has to make sure that all the other configurations can be reached from each configuration in a finite number of steps (ergodicity) and that detailed balance be satisfied: $|\omega_{\theta_1}|p(\theta_1 \rightarrow \theta_2) = |\omega_{\theta_2}|p(\theta_2 \rightarrow \theta_1)$, where $p(\theta_i \rightarrow \theta_j)$ is the probability for moving from θ_i to θ_j in each step of the random walk.

It is not possible to directly calculate Z itself. Instead, we evaluate physical quantities by measuring contribution to the quantity from each configuration in the random walk. For example, for a Green's function (g), it becomes

$$g = \frac{\sum_i \omega_{\theta_i} g_{\theta_i}}{\sum_i \omega_{\theta_i}} = \frac{\sum_i |\omega_{\theta_i}| \text{sign}_{\theta_i} g_{\theta_i}}{\sum_i |\omega_{\theta_i}| \text{sign}_{\theta_i}} \simeq \frac{\langle \text{sign}_{\theta_i} \cdot g_{\theta_i} \rangle_{\text{MC}}}{\langle \text{sign}_{\theta_i} \rangle_{\text{MC}}}, \quad (2.32)$$

where g_{θ_i} represents the contribution from a configuration θ_i , sign_{θ_i} is the sign of ω_{θ_i} and $\langle \cdots \rangle_{\text{MC}}$ indicates the Monte Carlo sampling. If the sign changes from configuration by configuration, the weights of different configurations tend to cancel with each other. Because of this, one needs to execute large number of random walk steps in order to achieve enough accuracy. This is the so-called sign problem. In general, problems with a frustrated lattice configuration and/or fermions suffer from this problem. Fortunately, in the present case of the single-site Anderson-Holstein model, we did not encounter this problem.

2.2.3 CT-QMC method for ordered states in the Holstein-Hubbard model

In this section, we introduce a CT-QMC method that can deal with the Anderson-Holstein impurity model (AHIM) in a SC bath. Solving this type of Anderson impurity model (AIM) is essential to DMFT for the Holstein-Hubbard model in a SC phase. In the present work [27,28], we note newly extend this CT-QMC method for the present problem based on a previous work by Koga and Werner for the attractive Hubbard model in SC [107] and another by Werner and Millis for the Holstein-Hubbard model in normal phases [67].

The Anderson-Holstein model as an effective impurity model

For equilibrium cases, the Hamiltonian of AHIM in a SC bath is $H = H_{\text{loc}} + H_{\text{bath}} + H_{\text{mix}}$, where

$$H_{\text{loc}} = -\mu(n_{\uparrow} + n_{\downarrow}) + Un_{\uparrow}n_{\downarrow} + g(a^{\dagger} + a)(n_{\uparrow} + n_{\downarrow} - 1) + \omega_0 a^{\dagger} a, \quad (2.33a)$$

$$H_{\text{bath}} = \sum_{\sigma,p} \epsilon_p b_{p,\sigma}^{\dagger} b_{p,\sigma} + \sum_p \Delta_p b_{p\uparrow}^{\dagger} b_{-p\downarrow}^{\dagger} + \sum_p \Delta_p^* b_{-p\downarrow} b_{p\uparrow}, \quad (2.33b)$$

$$H_{\text{hyb}} = \sum_{\sigma,p} (V_p^{\sigma} c_{\sigma}^{\dagger} b_{p,\sigma} + \text{h.c.}). \quad (2.33c)$$

The notation is the same in as Eq. 2.19.

With the Nambu formalism, i.e.,

$$\begin{bmatrix} c_1 \\ c_2 \end{bmatrix} = \begin{bmatrix} c_{\uparrow} \\ c_{\downarrow} \end{bmatrix}, \quad \begin{bmatrix} b_{p,1} \\ b_{p,2} \end{bmatrix} = \begin{bmatrix} b_{p\uparrow} \\ b_{-p\downarrow} \end{bmatrix}, \quad (2.34)$$

, the Hamiltonian is expressed as

$$H_{\text{loc}} = \begin{bmatrix} c_1^{\dagger} & c_2^{\dagger} \end{bmatrix} \begin{bmatrix} -\mu & 0 \\ 0 & \mu \end{bmatrix} \begin{bmatrix} c_1 \\ c_2 \end{bmatrix} + Un_1(1 - n_2) + g(a^{\dagger} + a)(n_1 - n_2) + \omega_0 a^{\dagger} a \quad (2.35a)$$

$$H_{\text{bath}} = \sum_p \begin{bmatrix} b_{p,1}^{\dagger} & b_{p,2}^{\dagger} \end{bmatrix} \begin{bmatrix} \epsilon_p & \Delta_p \\ \Delta_p^* & -\epsilon_p \end{bmatrix} \begin{bmatrix} b_{p,1} \\ b_{p,2} \end{bmatrix}, \quad (2.35b)$$

$$H_{\text{hyb}} = \sum_p (V_p^1 c_1^{\dagger} b_{p,1} + V_p^2 c_2^{\dagger} b_{p,2} + \text{h.c.}), \quad (2.35c)$$

where $V_p^1 = V_p^{\uparrow}$, $V_p^2 = -V_p^{\downarrow*}$ and $n_{\alpha} = c_{\alpha}^{\dagger} c_{\alpha}$ ($\alpha = 1, 2$).

The action for AHIM is

$S_{\text{AHIM}} =$

$$\begin{aligned} & \int_0^{\beta} d\tau \sum_p \begin{bmatrix} b_{p,1}^{\dagger}(\tau) & b_{p,2}^{\dagger}(\tau) \end{bmatrix} \begin{bmatrix} \partial_{\tau} + \epsilon_p & \Delta_p \\ \Delta_p^* & \partial_{\tau} - \epsilon_p \end{bmatrix} \begin{bmatrix} b_{p,1}(\tau) \\ b_{p,2}(\tau) \end{bmatrix} + \int_0^{\beta} d\tau \begin{bmatrix} c_1^{\dagger}(\tau) & c_2^{\dagger}(\tau) \end{bmatrix} \begin{bmatrix} \partial_{\tau} - \mu & 0 \\ 0 & \partial_{\tau} + \mu \end{bmatrix} \begin{bmatrix} c_1(\tau) \\ c_2(\tau) \end{bmatrix} \\ & + \int_0^{\beta} d\tau \sum_p \begin{bmatrix} c_1^{\dagger}(\tau) & c_2^{\dagger}(\tau) \end{bmatrix} \begin{bmatrix} V_p^1 & 0 \\ 0 & V_p^2 \end{bmatrix} \begin{bmatrix} b_{p,1}(\tau) \\ b_{p,2}(\tau) \end{bmatrix} + \int_0^{\beta} d\tau \sum_p \begin{bmatrix} b_{p,1}^{\dagger}(\tau) & b_{p,2}^{\dagger}(\tau) \end{bmatrix} \begin{bmatrix} V_p^{1*} & 0 \\ 0 & V_p^{2*} \end{bmatrix} \begin{bmatrix} c_1(\tau) \\ c_2(\tau) \end{bmatrix} \\ & + S_{\text{loc,int}} \\ & = \text{quadratic part in } b \text{ and } b^{\dagger} \\ & + \sum_n \sum_p \begin{bmatrix} c_1^{\dagger}(i\omega_n) & c_2^{\dagger}(i\omega_n) \end{bmatrix} \begin{bmatrix} V_p^1 & 0 \\ 0 & V_p^2 \end{bmatrix} \hat{g}_{0,p}(i\omega_n) \begin{bmatrix} V_p^{1*} & 0 \\ 0 & V_p^{2*} \end{bmatrix} \begin{bmatrix} c_1(i\omega_n) \\ c_2(i\omega_n) \end{bmatrix} \\ & + \sum_n \begin{bmatrix} c_1^{\dagger}(i\omega_n) & c_2^{\dagger}(i\omega_n) \end{bmatrix} \begin{bmatrix} -i\omega_n - \mu & 0 \\ 0 & -i\omega_n + \mu \end{bmatrix} \begin{bmatrix} c_1(i\omega_n) \\ c_2(i\omega_n) \end{bmatrix} + S_{\text{loc,int}}, \end{aligned} \quad (2.36)$$

where the quadratic part means those obtained from the first equation after completing the

2.2. EQUILIBRIUM FORMALISM

square for b and b^\dagger , and

$$S_{\text{loc,int}} \equiv \int_0^\beta d\tau a^\dagger(\tau)(\partial_\tau + \omega_0)a(\tau) + g \int_0^\beta d\tau [a^\dagger(\tau) + a(\tau)][n_1(\tau) - n_2(\tau)] + U \int_0^\beta d\tau n_1(\tau)[1 - n_2(\tau)]. \quad (2.37)$$

Note that, in going from first to second equations, a Fourier transformation ($c(\tau) = 1/\sqrt{\beta} \sum_n e^{-i\omega_n \tau} c(i\omega_n)$) is performed. In the second term, $\hat{g}_{0,p}$ is

$$\hat{g}_{0,p}(i\omega_n) = -\frac{1}{\omega_n^2 + \epsilon_p^2 + |\Delta_p|^2} \begin{bmatrix} i\omega_n + \epsilon_p & \Delta_p \\ \Delta_p^* & i\omega_n - \epsilon_p \end{bmatrix}. \quad (2.38)$$

Then the action for the impurity problem after integrating out b and b^\dagger becomes

$$S'_{\text{AHIM}} = -\sum_n \left[c_1^\dagger(i\omega_n) c_2^\dagger(i\omega_n) \right] \hat{G}_0^{-1}(i\omega_n) \begin{bmatrix} c_1(i\omega_n) \\ c_2(i\omega_n) \end{bmatrix} + S_{\text{loc,int}}, \quad (2.39)$$

where $\hat{G}_0^{-1}(i\omega_n)$ is

$$\hat{G}_0^{-1}(i\omega_n) = i\omega_n \hat{I} + \mu \hat{\sigma}_3 + \sum_p \frac{1}{\omega_n^2 + \epsilon_p^2 + |\Delta_p|^2} \begin{bmatrix} (i\omega_n + \epsilon_p)|V_p^1|^2 & \Delta_p V_p^1 V_p^{2*} \\ \Delta_p^* V_p^2 V_p^{1*} & (i\omega_n - \epsilon_p)|V_p^2|^2 \end{bmatrix}. \quad (2.40)$$

The third term is called the hybridization function,

$$\hat{\Delta}(i\omega_n) \equiv -\sum_p \frac{1}{\omega_n^2 + \epsilon_p^2 + |\Delta_p|^2} \begin{bmatrix} (i\omega_n + \epsilon_p)|V_p^1|^2 & \Delta_p V_p^1 V_p^{2*} \\ \Delta_p^* V_p^2 V_p^{1*} & (i\omega_n - \epsilon_p)|V_p^2|^2 \end{bmatrix}. \quad (2.41)$$

This argument based on the action tells that, in order to obtain the information on the impurity site, we only need the hybridization function out of the full information of the bath part.

Relation between AIM and DMFT

In DMFT, the above effective action corresponds to the effective action for the focused site, and the bath or the hybridization function is determined to reflect the effect of other lattices. In the case of the Bethe lattice, this self-consistency condition is

$$v^2 \hat{\sigma}_3 \hat{G}_{\text{loc}}(i\omega_n) \hat{\sigma}_3 = \hat{\Delta}(i\omega_n), \quad (2.42)$$

where \hat{G}_{loc} is the Green's function in the DMFT calculation.

For the CT-QMC method introduced below, we define new operators for AIM as

$$B_\gamma = \sum_p V_p^\gamma b_{p,\gamma}, \quad (2.43)$$

where $\gamma=1,2$. Then we define their response functions as

$$\begin{aligned} F_{\alpha,\gamma}(\tau - \tau') &\equiv \langle \mathcal{T} B_\alpha^\dagger(\tau) B_\gamma(\tau') \rangle_{\text{bath}} \\ &= -\sum_p V_p^{\alpha*} V_p^\gamma \langle \mathcal{T} b_{p,\gamma}(\tau') b_{p,\alpha}^\dagger(\tau) \rangle_{\text{bath}}, \end{aligned} \quad (2.44)$$

where $\langle \cdots \rangle_{\text{bath}}$ means the thermal average with respect to H_{bath} . Therefore, $-\langle \mathcal{T} b_{p,j}(\tau') b_{p,i}^\dagger(\tau) \rangle_{\text{bath}}$ is the usual Green's function for a non-correlated system,

$$-\langle \mathcal{T} b_{p,\gamma}(\tau') b_{p,\alpha}^\dagger(\tau) \rangle_{\text{bath}} = [\hat{g}_{0,p}(\tau' - \tau)]_{\gamma,\alpha} = \frac{1}{\beta} \sum_n e^{-i\omega_n(\tau' - \tau)} [\hat{g}_{0,p}(i\omega_n)]_{\gamma,\alpha}. \quad (2.45)$$

Now we have

$$\begin{aligned} F_{\alpha,\gamma}(\tau - \tau') &= \frac{1}{\beta} \sum_{n,p} e^{-i\omega_n(\tau' - \tau)} V_p^{*\alpha} V_p^\gamma [\hat{g}_{0,p}(i\omega_n)]_{\gamma,\alpha} \\ &= \Delta_{\gamma,\alpha}(\tau' - \tau), \end{aligned} \quad (2.46)$$

where $\Delta_{\gamma,\alpha}$ indicates an element of the hybridization function $\hat{\Delta}$. For the equality in the second line, we have used Eq. 2.41. Therefore, $F_{\alpha,\gamma}$ is nothing but the hybridization function with the notation changed slightly. Hence for the Bethe lattice, it follows

$$F_{\alpha,\gamma}(\tau - \tau') = [v^2 \hat{\sigma}_3 \hat{G}_{\text{loc}}(\tau' - \tau) \hat{\sigma}_3]_{\gamma,\alpha}. \quad (2.47)$$

Configuration and its weight

Now we explain how to implement the idea described in Sec. 2.2.2 to AHIM in a SC bath. Even though we can use the expression for AHIM, Eq. 2.35, in the implementation, for simplicity we use the following expression for the Hamiltonian, where the Nambu formalism is only applied to the bath;

$$H_{\text{loc}} = -\mu(n_\uparrow + n_\downarrow) + U n_\uparrow n_\downarrow + g(a^\dagger + a)(n_\uparrow + n_\downarrow - 1) + \omega_0 a^\dagger a, \quad (2.48a)$$

$$H_{\text{bath}} = \sum_p \begin{bmatrix} b_{p,1}^\dagger & b_{p,2}^\dagger \end{bmatrix} \begin{bmatrix} \epsilon_p & \Delta_p \\ \Delta_p^* & -\epsilon_p \end{bmatrix} \begin{bmatrix} b_{p,1} \\ b_{p,2} \end{bmatrix}, \quad (2.48b)$$

$$H_{\text{hyb}} = (c_\uparrow^\dagger B_1 + c_\downarrow B_2 + B_1^\dagger c_\uparrow + B_2^\dagger c_\downarrow). \quad (2.48c)$$

In the present CT-QMC method, we set $H_1 = H_{\text{loc}} + H_{\text{bath}}$, $H_2 = H_{\text{hyb}}$, and we consider the interaction representation of H_1 . Therefore, the contribution from the hybridization part is expanded in the present method (hybridization expansion).

Since the number of spin-up and spin-down particles on the impurity site is conserved in H_1 , the number of times $c_\uparrow^\dagger B_1$ ($c_\downarrow B_2$) appears should be equal to that of $B_1^\dagger c_\uparrow$ ($B_2^\dagger c_\downarrow$). Therefore, we obtain

$$\begin{aligned} Z &= \sum_{n_\uparrow, n_\downarrow} \left(\prod_{\sigma=\uparrow, \downarrow} \int_0^\beta d\tau_1^\sigma \cdots \int_{\tau_{n_\sigma}^\sigma}^\beta d\tau_{n_\sigma}^\sigma \int_0^\beta d\tau_1'^\sigma \cdots \int_{\tau_{n_\sigma}'^\sigma}^\beta d\tau_{n_\sigma}'^\sigma \right) \\ &\times \text{Tr} \left\{ e^{-\beta H_1} \mathcal{T} \left[B_1^\dagger(\tau_{n_\uparrow}^\uparrow) c_\uparrow(\tau_{n_\uparrow}^\uparrow) c_\uparrow^\dagger(\tau_{n_\uparrow}'^\uparrow) B_1(\tau_{n_\uparrow}'^\uparrow) \cdots B_1^\dagger(\tau_1^\uparrow) c_\uparrow(\tau_1^\uparrow) c_\uparrow^\dagger(\tau_1'^\uparrow) B_1(\tau_1'^\uparrow) \right. \right. \\ &\quad \left. \left. \times B_2^\dagger(\tau_{n_\downarrow}'^\downarrow) c_\downarrow^\dagger(\tau_{n_\downarrow}'^\downarrow) c_\downarrow(\tau_{n_\downarrow}^\downarrow) B_2(\tau_{n_\downarrow}^\downarrow) \cdots B_2^\dagger(\tau_1'^\downarrow) c_\downarrow^\dagger(\tau_1'^\downarrow) c_\downarrow(\tau_1^\downarrow) B_2(\tau_1^\downarrow) \right] \right\}. \end{aligned} \quad (2.49)$$

2.2. EQUILIBRIUM FORMALISM

Since the bath part and the impurity part are completely separated in H_1 , we can separate the contents of the trace in the above equation into two parts as

$$\begin{aligned}
Z &= Z_{\text{bath}} \sum_{n_\uparrow, n_\downarrow} \left(\prod_{\sigma=\uparrow, \downarrow} \int_0^\beta d\tau_1^\sigma \cdots \int_{\tau_{n_\sigma-1}^\sigma}^\beta d\tau_{n_\sigma}^\sigma \int_0^\beta d\tau_1^{\prime\sigma} \cdots \int_{\tau_{n_\sigma-1}^{\prime\sigma}}^\beta d\tau_{n_\sigma}^{\prime\sigma} \right) \\
&\times \text{Tr}_{\text{loc}} \left\{ e^{-\beta H_{\text{loc}}} \mathcal{T} \left[c_\uparrow(\tau_{n_\uparrow}^\uparrow) c_\uparrow^\dagger(\tau_{n_\uparrow}^{\prime\uparrow}) \cdots c_\uparrow(\tau_1^\uparrow) c_\uparrow^\dagger(\tau_1^{\prime\uparrow}) \right. \right. \\
&\quad \left. \left. \times c_\downarrow^\dagger(\tau_{n_\downarrow}^{\prime\downarrow}) c_\downarrow(\tau_{n_\downarrow}^\downarrow) \cdots c_\downarrow^\dagger(\tau_1^{\prime\downarrow}) c_\downarrow(\tau_1^\downarrow) \right] \right\} \\
&\times \frac{1}{Z_{\text{bath}}} \text{Tr}_{\text{b}} \left\{ e^{-\beta H_{\text{bath}}} \mathcal{T} \left[B_1^\dagger(\tau_{n_\uparrow}^\uparrow) B_1(\tau_{n_\uparrow}^{\prime\uparrow}) \cdots B_1^\dagger(\tau_1^\uparrow) B_1(\tau_1^{\prime\uparrow}) \right. \right. \\
&\quad \left. \left. \times B_2^\dagger(\tau_{n_\downarrow}^{\prime\downarrow}) B_2(\tau_{n_\downarrow}^\downarrow) \cdots B_2^\dagger(\tau_1^{\prime\downarrow}) B_2(\tau_1^\downarrow) \right] \right\}, \tag{2.50}
\end{aligned}$$

where Tr_{loc} means the trace for the local part (the impurity electron and the local phonon), Tr_{b} means the trace for the bath part, and Z_{bath} is the partition function of the bath. The difference between a SC bath and a normal bath is that, in the former, the existence of Δ_p prevents us from separating the trace of the bath part into the spin-up part (B_1) and the spin-down part (B_2).

Now, with $F_{\alpha, \beta}(\tau - \tau')$ defined in Eq. 2.44, we define a matrix,

$$\begin{aligned}
&M^{-1}(\{\tau_1^\uparrow \cdots \tau_{n_\uparrow}^\uparrow\}, \{\tau_1^{\prime\downarrow} \cdots \tau_{n_\downarrow}^{\prime\downarrow}\}; \{\tau_1^{\prime\uparrow} \cdots \tau_{n_\uparrow}^{\prime\uparrow}\}, \{\tau_1^\downarrow \cdots \tau_{n_\downarrow}^\downarrow\}) \\
&\equiv \begin{bmatrix} F_{1,1}(\tau_1^\uparrow - \tau_1^{\prime\uparrow}) \cdots F_{1,1}(\tau_1^\uparrow - \tau_{n_\uparrow}^{\prime\uparrow}) & F_{1,2}(\tau_1^\uparrow - \tau_1^\downarrow) \cdots F_{1,2}(\tau_1^\uparrow - \tau_{n_\downarrow}^\downarrow) \\ \vdots & \vdots \\ F_{1,1}(\tau_{n_\uparrow}^\uparrow - \tau_1^{\prime\uparrow}) \cdots F_{1,1}(\tau_{n_\uparrow}^\uparrow - \tau_{n_\uparrow}^{\prime\uparrow}) & F_{1,2}(\tau_{n_\uparrow}^\uparrow - \tau_1^\downarrow) \cdots F_{1,2}(\tau_{n_\uparrow}^\uparrow - \tau_{n_\downarrow}^\downarrow) \\ \hline F_{2,1}(\tau_1^{\prime\downarrow} - \tau_1^{\prime\uparrow}) \cdots F_{2,1}(\tau_1^{\prime\downarrow} - \tau_{n_\uparrow}^{\prime\uparrow}) & F_{2,2}(\tau_1^{\prime\downarrow} - \tau_1^\downarrow) \cdots F_{2,2}(\tau_1^{\prime\downarrow} - \tau_{n_\downarrow}^\downarrow) \\ \vdots & \vdots \\ F_{2,1}(\tau_{n_\downarrow}^{\prime\downarrow} - \tau_1^{\prime\uparrow}) \cdots F_{2,1}(\tau_{n_\downarrow}^{\prime\downarrow} - \tau_{n_\uparrow}^{\prime\uparrow}) & F_{2,2}(\tau_{n_\downarrow}^{\prime\downarrow} - \tau_1^\downarrow) \cdots F_{2,2}(\tau_{n_\downarrow}^{\prime\downarrow} - \tau_{n_\downarrow}^\downarrow) \end{bmatrix}, \tag{2.51}
\end{aligned}$$

where $\{\tau_1^\uparrow \cdots \tau_{n_\uparrow}^\uparrow\}, \{\tau_1^{\prime\downarrow} \cdots \tau_{n_\downarrow}^{\prime\downarrow}\}$ is for the row index and $\{\tau_1^{\prime\uparrow} \cdots \tau_{n_\uparrow}^{\prime\uparrow}\}, \{\tau_1^\downarrow \cdots \tau_{n_\downarrow}^\downarrow\}$ is for the column index.

It turns out that

$$\begin{aligned}
&\frac{1}{Z_{\text{bath}}} \text{Tr}_{\text{b}} \left\{ e^{-\beta H_{\text{bath}}} \mathcal{T} \left[B_1^\dagger(\tau_{n_\uparrow}^\uparrow) B_1(\tau_{n_\uparrow}^{\prime\uparrow}) \cdots B_1^\dagger(\tau_1^\uparrow) B_1(\tau_1^{\prime\uparrow}) \right. \right. \\
&\quad \left. \left. \times B_2^\dagger(\tau_{n_\downarrow}^{\prime\downarrow}) B_2(\tau_{n_\downarrow}^\downarrow) \cdots B_2^\dagger(\tau_1^{\prime\downarrow}) B_2(\tau_1^\downarrow) \right] \right\} \\
&= \det M^{-1}(\{\tau_1^\uparrow \cdots \tau_{n_\uparrow}^\uparrow\}, \{\tau_1^{\prime\downarrow} \cdots \tau_{n_\downarrow}^{\prime\downarrow}\}; \{\tau_1^{\prime\uparrow} \cdots \tau_{n_\uparrow}^{\prime\uparrow}\}, \{\tau_1^\downarrow \cdots \tau_{n_\downarrow}^\downarrow\}). \tag{2.52}
\end{aligned}$$

We note that in Eq. 2.51 and Eq. 2.52 the order of time is irrelevant, i.e., $\{\tau_1^\uparrow \cdots \tau_{n_\uparrow}^\uparrow\}$ does not need to be time-ordered.

As for a configuration (θ) , it is expressed by $[\{\tau_1^\uparrow \cdots \tau_{n_\uparrow}^\uparrow\}, \{\tau_1^\downarrow \cdots \tau_{n_\downarrow}^\downarrow\}; \{\tau_1^{\prime\uparrow} \cdots \tau_{n_\uparrow}^{\prime\uparrow}\}, \{\tau_1^{\prime\downarrow} \cdots \tau_{n_\downarrow}^{\prime\downarrow}\}]$, which are time-ordered within each $\{\}$. Then its weight (ω_θ) is

$$\begin{aligned} \omega_\theta &= Z_{\text{bath}} \text{Tr}_{\text{loc}} \left\{ e^{-\beta H_{\text{loc}}} \mathcal{T} \left[c_\uparrow(\tau_{n_\uparrow}^\uparrow) c_\uparrow^\dagger(\tau_{n_\uparrow}^{\prime\uparrow}) \cdots c_\uparrow(\tau_1^\uparrow) c_\uparrow^\dagger(\tau_1^{\prime\uparrow}) \times c_\downarrow^\dagger(\tau_{n_\downarrow}^{\prime\downarrow}) c_\downarrow(\tau_{n_\downarrow}^\downarrow) \cdots c_\downarrow^\dagger(\tau_1^{\prime\downarrow}) c_\downarrow(\tau_1^\downarrow) \right] \right\} \\ &\times \det M^{-1}(\{\tau_1^\uparrow \cdots \tau_{n_\uparrow}^\uparrow\}, \{\tau_1^{\prime\downarrow} \cdots \tau_{n_\downarrow}^{\prime\downarrow}\}; \{\tau_1^{\prime\uparrow} \cdots \tau_{n_\uparrow}^{\prime\uparrow}\}, \{\tau_1^\downarrow \cdots \tau_{n_\downarrow}^\downarrow\}) (d\tau)^{2n_\uparrow + 2n_\downarrow}. \end{aligned} \quad (2.53)$$

The problem is how to evaluate $\text{Tr}_{\text{loc}}\{\}$. Here H_{loc} is nothing but the Hamiltonian for the one-site Holstein-Hubbard model, and the problem is translated into how to evaluate correlation functions for the one-site Holstein-Hubbard model. In order to do this, we employ the Lang-Firsov transformation [67]. This is because, after the transformation, the coupling between phonons and electrons vanishes and one obtains an analytical expression for $\text{Tr}_{\text{loc}}\{\}$. The Lang-Firsov transformation is a canonical transformation with e^{-S} , where $S = \frac{g}{\omega_0}(n_\uparrow + n_\downarrow - 1)(a^\dagger - a)$, and an operator (O) is transformed into $\tilde{O} \equiv e^S O e^{-S}$. Then the Hamiltonian H_{loc} is transformed into

$$\begin{aligned} \tilde{H}_{\text{loc}} &= e^S H_{\text{loc}} e^{-S} \\ &= -\tilde{\mu}(n_\uparrow + n_\downarrow) + \tilde{U} n_\uparrow n_\downarrow + \omega_0 a^\dagger a \\ &= H_{\text{eff,Hub}} + H_{\text{ph}}, \end{aligned} \quad (2.54)$$

where

$$\tilde{\mu} = \mu - \frac{g^2}{\omega_0}, \tilde{U} = U - \frac{2g^2}{\omega}. \quad (2.55)$$

As can be seen, there is no coupling between the fermion part ($H_{\text{eff,Hub}}$) and the phonon part (H_{ph}), and $H_{\text{eff,Hub}}$ is the Hamiltonian for the one-site Hubbard model and H_{ph} is that of a free-phonon system. We note that the electron creation and annihilation operators are transformed into $\tilde{c}_\sigma^\dagger = e^{\frac{g}{\omega_0}(a^\dagger - a)} c_\sigma^\dagger$ and $\tilde{c}_\sigma = e^{-\frac{g}{\omega_0}(a^\dagger - a)} c_\sigma$, respectively. Hence c^\dagger after the LF transformation creates an electron dressed with phonons (a polaron), see also Sec. 3.1.2.

With these relations, one can separate $\text{Tr}_{\text{loc}}\{\}$ in Eq. 2.53 into a polaron (electron) part and a phonon part,

$$\begin{aligned} &\text{Tr}_{\text{loc}} \left\{ e^{-\beta H_{\text{loc}}} \mathcal{T} \left[c_\uparrow(\tau_{n_\uparrow}^\uparrow) c_\uparrow^\dagger(\tau_{n_\uparrow}^{\prime\uparrow}) \cdots c_\uparrow(\tau_1^\uparrow) c_\uparrow^\dagger(\tau_1^{\prime\uparrow}) \times c_\downarrow^\dagger(\tau_{n_\downarrow}^{\prime\downarrow}) c_\downarrow(\tau_{n_\downarrow}^\downarrow) \cdots c_\downarrow^\dagger(\tau_1^{\prime\downarrow}) c_\downarrow(\tau_1^\downarrow) \right] \right\} \\ &= \text{Tr}_{\text{c}} \left\{ e^{-\beta H_{\text{eff,Hub}}} \mathcal{T} \left[c_\uparrow(\tau_{n_\uparrow}^\uparrow) c_\uparrow^\dagger(\tau_{n_\uparrow}^{\prime\uparrow}) \cdots c_\uparrow(\tau_1^\uparrow) c_\uparrow^\dagger(\tau_1^{\prime\uparrow}) \times c_\downarrow^\dagger(\tau_{n_\downarrow}^{\prime\downarrow}) c_\downarrow(\tau_{n_\downarrow}^\downarrow) \cdots c_\downarrow^\dagger(\tau_1^{\prime\downarrow}) c_\downarrow(\tau_1^\downarrow) \right] \right\} \\ &\times \text{Tr}_{\text{a}} \left\{ e^{-\beta H_{\text{ph}}} \mathcal{T} \left[e^{-A_b(\tau_{n_\uparrow}^\uparrow)} e^{A_b(\tau_{n_\uparrow}^{\prime\uparrow})} \cdots e^{-A_b(\tau_1^\uparrow)} e^{A_b(\tau_1^{\prime\uparrow})} \times e^{A_b(\tau_{n_\downarrow}^{\prime\downarrow})} e^{-A_b(\tau_{n_\downarrow}^\downarrow)} \cdots e^{A_b(\tau_1^{\prime\downarrow})} e^{-A_b(\tau_1^\downarrow)} \right] \right\} \end{aligned} \quad (2.56)$$

where $A_b(\tau) = \frac{g}{\omega_0}(e^{\omega_0 \tau} a^\dagger - e^{-\omega_0 \tau} a)$, and Tr_{a} and Tr_{c} mean the traces for the phonon part and the electron part, respectively. The electron part is nothing but the problem of the one-site Hubbard model, and it can be readily evaluated.

As for the phonon part,

$$\begin{aligned}
 \omega_{\text{ph}}(\theta) &\equiv \text{Tr}_{\text{a}} \left\{ e^{-\beta H_{\text{phonon}}} \mathcal{T} \left[e^{-A_b(\tau_{n_{\uparrow}}^{\uparrow})} e^{A_b(\tau_{n_{\uparrow}}^{\prime\uparrow})} \dots e^{-A_b(\tau_1^{\uparrow})} e^{A_b(\tau_1^{\prime\uparrow})} \right. \right. \\
 &\quad \left. \left. \times e^{A_b(\tau_{n_{\downarrow}}^{\prime\downarrow})} e^{-A_b(\tau_{n_{\downarrow}}^{\downarrow})} \dots e^{A_b(\tau_1^{\prime\downarrow})} e^{-A_b(\tau_1^{\downarrow})} \right] \right\} \\
 &= \text{Tr}_{\text{a}} \left\{ e^{-\beta H_{\text{ph}}} e^{s_{2n} A(\tau_{2n})} \dots e^{s_1 A(\tau_1)} \right\} \\
 &= \exp \left[-\frac{g^2/\omega_0^2}{e^{\beta\omega_0} - 1} \left\{ n(e^{\beta\omega_0} + 1) + \sum_{1 \leq j < i \leq 2n} s_i s_j [e^{\omega_0(\beta - (\tau_i - \tau_j))} + e^{\omega_0(\tau_i - \tau_j)}] \right\} \right],
 \end{aligned} \tag{2.57}$$

where $n = n_{\uparrow} + n_{\downarrow}$. Here $\{\tau_1 \dots \tau_{2n}\}$ is constrained to $0 \leq \tau_1 < \dots < \tau_{2n} < \beta$, and the elements are the same as those of $\theta = \{\{\tau_1^{\uparrow} \dots \tau_{n_{\uparrow}}^{\uparrow}\}, \{\tau_1^{\prime\downarrow} \dots \tau_{n_{\downarrow}}^{\prime\downarrow}\}; \{\tau_1^{\prime\uparrow} \dots \tau_{n_{\uparrow}}^{\prime\uparrow}\}, \{\tau_1^{\downarrow} \dots \tau_{n_{\downarrow}}^{\downarrow}\}\}$. In other words, we just change the order of elements of θ so that they are time-ordered. The sign s_i is 1 (-1) if τ_i is an argument for a creation (annihilation) operator. The derivation of Eq. 2.57 is given in Appendix. A.1.

Segment representation

So far, configurations (θ) are expressed as $[\{\tau_1^{\uparrow} \dots \tau_{n_{\uparrow}}^{\uparrow}\}, \{\tau_1^{\prime\downarrow} \dots \tau_{n_{\downarrow}}^{\prime\downarrow}\}; \{\tau_1^{\prime\uparrow} \dots \tau_{n_{\uparrow}}^{\prime\uparrow}\}, \{\tau_1^{\downarrow} \dots \tau_{n_{\downarrow}}^{\downarrow}\}]$, which are time-ordered within each $\{\}$. However, we can reduce the configuration space further by omitting configurations whose weight (ω_{θ}) is 0. This is possible because, for a certain configuration to have nonzero weight, the creation and annihilation operators for each spin must appear alternately since the time evolution with H_{loc} does not change the spin. We only need to consider configurations that satisfy this, and these configurations can be expressed as a collection of segments (see Fig. 2.4), where each segment represents a time interval during which the impurity site is occupied by a spin up or down electron (we call this the segment representation). Hereafter, when we regard a configuration (θ) as a collection of segments, we express θ as $[\{\tau_1^{e\uparrow} \dots \tau_{n_{\uparrow}}^{e\uparrow}\}, \{\tau_1^{s\downarrow} \dots \tau_{n_{\downarrow}}^{s\downarrow}\}; \{\tau_1^{s\uparrow} \dots \tau_{n_{\uparrow}}^{s\uparrow}\}, \{\tau_1^{e\downarrow} \dots \tau_{n_{\downarrow}}^{e\downarrow}\}]$. Here $\tau_i^{s\sigma}$ and $\tau_i^{e\sigma}$ respectively represent the starting point and the ending point of the i -th segment for spin σ . The order of the segments for each spin is determined by the order of starting points of the segments for that spin. We also note that the configurations of segments are categorized into two types, see Fig. 2.5. Type 1 is the configurations that have no segments at $\tau = 0$ and $\tau = \beta$, while, type 2 is the configurations where $\tau = 0$ and $\tau = \beta$ are on a segment.

Now, in order to evaluate the weight of a configuration (ω_{θ}), one has to evaluate the weight of the local part (ω_{loc}) and the weight of the bath part (ω_{bath}). Here, we can choose the order of time in such a way that ω_{loc} becomes always positive. In that case,

$$\omega_{\text{bath}} = (-)^x \det M^{-1}(\{\tau_{\uparrow}^e\}, \{\tau_{\downarrow}^s\}; \{\tau_{\uparrow}^s\}, \{\tau_{\downarrow}^e\}), \tag{2.58}$$

where x is a certain integer that depends on the configuration θ . The absolute value of $\text{Tr}_{\text{c}}\{\}$ in Eq. 2.56 is

$$|\text{Tr}_{\text{c}}\{\}| = \exp[\tilde{\mu}(l_{\uparrow} + l_{\downarrow}) - \tilde{U}l_{\text{overlap}}], \tag{2.59}$$

where l_{σ} is the total length of the segments for spin σ , and l_{overlap} is the total length of the overlaps between the segments for spin up and those for down. This and Eq. 2.57 determine ω_{loc} .

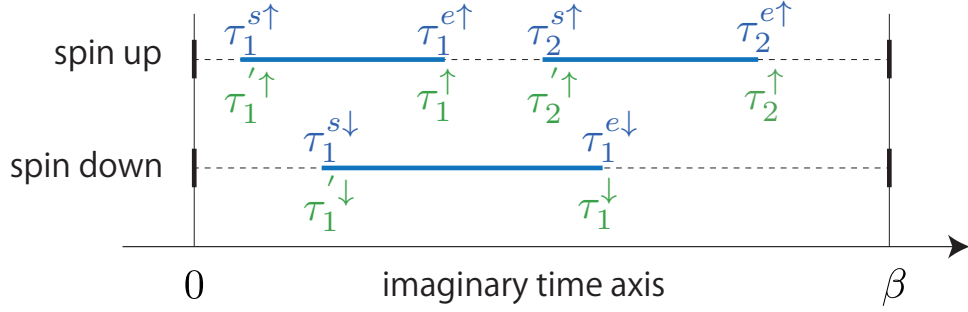


Figure 2.4: Configuration θ expressed in the segment representation. τ_i^s and τ_i^e respectively represent the starting point and the ending point of the i -th segment. The order of the segments follows the order of starting points of segments. Green letters represent the original time-ordered expression.

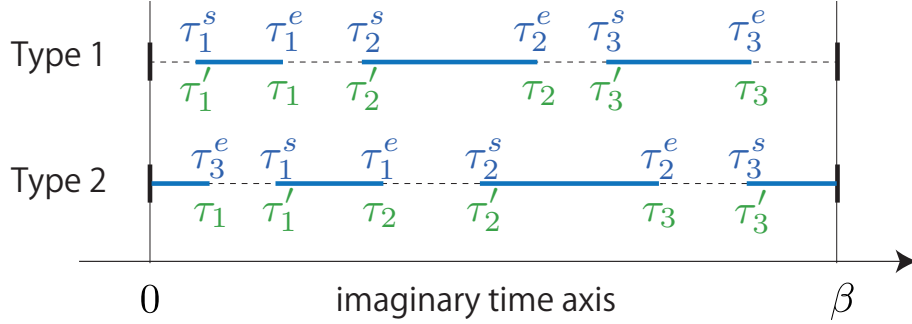


Figure 2.5: Two types of configurations of segments. τ_i^s and τ_i^e respectively represent the starting point and the ending point of the i -th segment. The order of segments follows the order of starting points of segments. Green letters represent the original time-ordered expression.

As for ω_{bath} , we show the value of x in Eq. 2.58 for various configurations in Table. 2.2. We shall illustrate the derivation for the case of (type 1,type 1), while the rest is obtained in a similar way. In that case,

$$\omega_{\text{loc}} = \text{Tr}_{\text{loc}} \left\{ e^{-\beta H_{\text{loc}}} \mathcal{T} \left[c_{\uparrow}(\tau_{n_{\uparrow}}^{e\uparrow}) c_{\uparrow}^{\dagger}(\tau_{n_{\uparrow}}^{s\uparrow}) \cdots c_{\uparrow}(\tau_1^{e\uparrow}) c_{\uparrow}^{\dagger}(\tau_1^{s\uparrow}) \right. \right. \\ \left. \left. \times c_{\downarrow}(\tau_{n_{\downarrow}}^{e\downarrow}) c_{\downarrow}^{\dagger}(\tau_{n_{\downarrow}}^{s\downarrow}) \cdots c_{\downarrow}(\tau_1^{e\downarrow}) c_{\downarrow}^{\dagger}(\tau_1^{s\downarrow}) \right] \right\}, \quad (2.60)$$

and

$$\omega_{\text{bath}} = \frac{1}{Z_{\text{bath}}} \text{Tr}_b \left\{ e^{-\beta H_{\text{bath}}} \mathcal{T} \left[B_1^{\dagger}(\tau_{n_{\uparrow}}^{e\uparrow}) B_1(\tau_{n_{\uparrow}}^{s\uparrow}) \cdots B_1^{\dagger}(\tau_1^{e\uparrow}) B_1(\tau_1^{s\uparrow}) \right. \right. \\ \left. \left. \times B_2(\tau_{n_{\downarrow}}^{e\downarrow}) B_2^{\dagger}(\tau_{n_{\downarrow}}^{s\downarrow}) \cdots B_2(\tau_1^{e\downarrow}) B_2^{\dagger}(\tau_1^{s\downarrow}) \right] \right\}. \quad (2.61)$$

Note that, in ω_{loc} , the order of creation and annihilation operators for each spin is time-ordered. It turns out that this type of ordering makes ω_{loc} positive, and this fact holds in the remaining

segment type of spin up	segment type of spin down	x
type 1	type 1	n_\downarrow
type 1	type 2	$n_\downarrow + 1$
type 2	type 1	$n_\downarrow + 1$
type 2	type 2	n_\downarrow

 Table 2.2: The coefficient x in Eq. 2.58 for the ω_{bath} for various segment configurations.

three cases as well. On the other hand, we have

$$\det M^{-1}(\{\tau_\uparrow^e\}, \{\tau_\downarrow^s\}; \{\tau_\uparrow^s\}, \{\tau_\downarrow^e\}) = \frac{1}{Z_{\text{bath}}} \text{Tr}_b \left\{ e^{-\beta H_{\text{bath}}} T \left[B_1^\dagger(\tau_{n_\uparrow}^{e\uparrow}) B_1(\tau_{n_\uparrow}^{s\uparrow}) \cdots B_1^\dagger(\tau_1^{e\uparrow}) B_1(\tau_1^{s\uparrow}) \right. \right. \\ \left. \left. \times B_2^\dagger(\tau_{n_\downarrow}^{s\downarrow}) B_2(\tau_{n_\downarrow}^{e\downarrow}) \cdots B_2^\dagger(\tau_1^{s\downarrow}) B_2(\tau_1^{e\downarrow}) \right] \right\}. \quad (2.62)$$

Then, comparing Eq. 2.61 and Eq. 2.62, one finds

$$\omega_{\text{bath}} = (-)^{n_\downarrow} \det M^{-1}(\{\tau_\uparrow^e\}, \{\tau_\downarrow^s\}; \{\tau_\uparrow^s\}, \{\tau_\downarrow^e\}). \quad (2.63)$$

Evaluation of the Green's function

The Green's functions such as $g(\tau) = \langle T c_\uparrow(\tau) c_\uparrow^\dagger(0) \rangle$ and $f(\tau) = \langle T c_\uparrow(\tau) c_\downarrow(0) \rangle$ can be measured as

$$g(\tau) = \frac{1}{Z} \sum_\theta \sum_{i,j=1}^{n_\uparrow} \frac{1}{\beta} \Delta(\tau, \tau_i^\uparrow - \tau_j^{\prime\uparrow}) M_{\theta,j,i} \omega_\theta \simeq \frac{\langle \sum_{i,j=1}^{n_\uparrow} \frac{1}{\beta} \Delta(\tau, \tau_i^\uparrow - \tau_j^{\prime\uparrow}) M_{\theta,j,i} \cdot \text{sign}_\theta \rangle_{\text{MC}}}{\langle \text{sign}_\theta \rangle_{\text{MC}}}, \quad (2.64a)$$

$$f(\tau) = \frac{1}{Z} \sum_\theta \sum_{i=1}^{n_\uparrow} \sum_{j=1}^{n_\downarrow} \frac{1}{\beta} \Delta(\tau, \tau_i^\uparrow - \tau_j^{\prime\downarrow}) M_{\theta,n_\uparrow+j,i} \omega_\theta \simeq \frac{\langle \sum_{i=1}^{n_\uparrow} \sum_{j=1}^{n_\downarrow} \frac{1}{\beta} \Delta(\tau, \tau_i^\uparrow - \tau_j^{\prime\downarrow}) M_{\theta,n_\uparrow+j,i} \cdot \text{sign}_\theta \rangle_{\text{MC}}}{\langle \text{sign}_\theta \rangle_{\text{MC}}}, \quad (2.64b)$$

where ω_θ is the weight of a configuration $\theta = \{\{\tau_1^\uparrow \cdots \tau_{n_\uparrow}^\uparrow\}, \{\tau_1^{\prime\downarrow} \cdots \tau_{n_\downarrow}^{\prime\downarrow}\}; \{\tau_1^{\prime\uparrow} \cdots \tau_{n_\uparrow}^{\prime\uparrow}\}, \{\tau_1^\downarrow \cdots \tau_{n_\downarrow}^\downarrow\}\}$, $M_\theta \equiv M(\{\tau_1^\uparrow \cdots \tau_{n_\uparrow}^\uparrow\}, \{\tau_1^{\prime\downarrow} \cdots \tau_{n_\downarrow}^{\prime\downarrow}\}; \{\tau_1^{\prime\uparrow} \cdots \tau_{n_\uparrow}^{\prime\uparrow}\}, \{\tau_1^\downarrow \cdots \tau_{n_\downarrow}^\downarrow\})$ and sign_θ is the sign of ω_θ . Here, τ is assumed to be positive, and $\Delta(\tau, \tau')$ is

$$\Delta(\tau, \tau') = \delta(\tau - \tau'), \quad (\tau' > 0) \\ - \delta(\tau - \tau' - \beta). \quad (\tau' < 0) \quad (2.65)$$

The derivation of Eq. 2.64 is given in Appendix. A.1.

Random walk

Here we briefly explain the random walk in the configuration space in our study, where configurations are expressed in the segment representation. The random walk consists of seven steps:

1. Adding a segment of random length for random spin at a random point.
2. Removing a randomly chosen segment.

3. Adding an anti-segment of random length for random spin at a random point.
4. Removing a randomly chosen anti-segment.
5. Shifting the end point of a randomly chosen segment.
6. Swapping segments for spin up and those for spin down.
7. Swapping segments and anti-segments for each spin.

Each step should be executed so that a probability for moving configuration θ_i to θ_j ($p(\theta_i \rightarrow \theta_j)$) satisfies the detailed balance. For this, we split $p(\theta_i \rightarrow \theta_j)$ into a probability of proposing a new configuration ($p^{\text{prop}}(\theta_i \rightarrow \theta_j)$) and a probability of accepting the proposal ($p^{\text{acc}}(\theta_i \rightarrow \theta_j)$). Then, we use the Metropolis algorithm,

$$p^{\text{acc}}(\theta_i \rightarrow \theta_j) = \min \left[1, \frac{p^{\text{acc}}(\theta_i \rightarrow \theta_j)}{p^{\text{acc}}(\theta_j \rightarrow \theta_i)} \right]. \quad (2.66)$$

In steps 1~5, segments for either spin up or down are modulated. Steps 1~4 are necessary for ergodicity, and 5~7 are for efficiency. During the random walk, we keep track of $M(\{\tau_{\uparrow}^e\}, \{\tau_{\downarrow}^s\}; \{\tau_{\uparrow}^s\}, \{\tau_{\downarrow}^e\})$ and $\det M$. As for a way to implement fast update of $M(\{\tau_{\uparrow}^e\}, \{\tau_{\downarrow}^s\}; \{\tau_{\uparrow}^s\}, \{\tau_{\downarrow}^e\})$ and $\det M$, see Ref. [106].

2.3 Non-equilibrium formalism

In this section, we explain the non-equilibrium DMFT formulated with the Green's function on the Kadanoff-Baym (KB) contour. This formalism enables us to study the situation where the system is in equilibrium at $t = 0$ and the system is excited at $t > 0$ into non-equilibrium state. This formalism has been applied mainly to the Hubbard model (the Coulomb interaction only). Our achievement is the extension of the theory that enables us to take into account phonon dynamics.

2.3.1 Green's function for electrons

We have introduced the contour ordered Green's function of the KB contour in Eq. 2.12. However, it has some redundancy, and in practice we do not need to deal with it directly. Instead, we introduce "physical" Green's functions, and select independent parts of the Green's functions that include the same amount of information as the original ones. Here we explain this point.

First let us separate $G(\nu, \nu')$ into nine components, since the KB contour, \mathcal{C} , can be separated into three parts. We can then define $G^{ij}(s(\nu), s(\nu')) = G(\nu, \nu')$ for $\nu \in C_i, \nu' \in C_j$. Then it is helpful to consider a 3×3 matrix assigned by the combination of the arguments (t, t', τ, τ') ,

$$\hat{G}(t, t', \tau, \tau') \equiv \begin{bmatrix} G^{11}(t, t') & G^{12}(t, t') & G^{13}(t, \tau') \\ G^{21}(t, t') & G^{22}(t, t') & G^{23}(t, \tau') \\ G^{31}(\tau, t') & G^{32}(\tau, t') & G^{33}(\tau, \tau') \end{bmatrix}. \quad (2.67)$$

2.3. NON-EQUILIBRIUM FORMALISM

Here one can see that G_{ij} has the following redundancy;

$$G^{11}(t, t') = G^{12}(t, t') \quad (\text{for } t \leq t'), \quad (2.68a)$$

$$G^{11}(t, t') = G^{21}(t, t') \quad (\text{for } t > t'), \quad (2.68b)$$

$$G^{22}(t, t') = G^{21}(t, t') \quad (\text{for } t < t'), \quad (2.68c)$$

$$G^{22}(t, t') = G^{12}(t, t') \quad (\text{for } t \geq t'), \quad (2.68d)$$

$$G^{13}(t, \tau') = G^{23}(t, \tau'), \quad (2.68e)$$

$$G^{32}(\tau, t') = G^{31}(\tau, t'). \quad (2.68f)$$

In particular these imply,

$$G^{11}(t, t') + G^{22}(t, t') = G^{12}(t, t') + G^{21}(t, t') \quad (\text{for } t \neq t'). \quad (2.69)$$

Now we introduce the "physical" Green's functions. First we define a 3×3 matrix \hat{L} as

$$\hat{L} = \frac{1}{\sqrt{2}} \begin{bmatrix} 1 & -1 & 0 \\ 1 & 1 & 0 \\ 0 & 0 & \sqrt{2} \end{bmatrix}, \quad (2.70)$$

and $\hat{\tau}_3 = \text{diag}(1, -1, -i)$. The "physical" Green's functions are obtained by rotating the matrix Eq. 2.67 as

$$\begin{aligned} & \begin{bmatrix} G^R(t, t') & G^K(t, t') & \sqrt{2}G^\neg(t, \tau') \\ 0 & G^A(t, t') & 0 \\ 0 & \sqrt{2}G^\neg(\tau, t') & G^M(\tau, \tau') \end{bmatrix} \equiv \hat{L}\hat{\tau}_3\hat{G}\hat{L}^\dagger \\ & = \frac{1}{2} \begin{bmatrix} G^{11} - G^{12} + G^{21} - G^{22} & G^{11} + G^{12} + G^{21} + G^{22} & \sqrt{2}(G^{13} + G^{23}) \\ G^{11} - G^{12} - G^{21} + G^{22} & G^{11} + G^{12} - G^{21} - G^{22} & \sqrt{2}(G^{13} - G^{23}) \\ -\sqrt{2}i(G^{31} - G^{32}) & -\sqrt{2}i(G^{31} + G^{32}) & -2iG^{33} \end{bmatrix}. \end{aligned} \quad (2.71)$$

The explicit form of the "physical" Green's functions is

$$G^R(t, t') = -i\theta(t - t')\langle [c(t), c^\dagger(t')]_+ \rangle, \quad (2.72a)$$

$$G^A(t, t') = i\theta(t' - t)\langle [c(t), c^\dagger(t')]_+ \rangle, \quad (2.72b)$$

$$G^K(t, t') = -i\langle [c(t), c^\dagger(t')]_- \rangle, \quad (2.72c)$$

$$G^\neg(t, \tau') = i\langle c^\dagger(\tau')c(t) \rangle, \quad (2.72d)$$

$$G^\neg(\tau, t') = -i\langle c(\tau)c^\dagger(t) \rangle, \quad (2.72e)$$

$$G^M(\tau, \tau') = -\langle \mathcal{T}_\tau c(\tau)c^\dagger(\tau') \rangle, \quad (2.72f)$$

where $[\cdot]_{-(+)}$ is the (anti-)commutator, and R , A , K , \neg , \neg and M respectively stand for the retarded, advanced, Keldysh, left-mixing, right-mixing and Matsubara components. Other important Green's functions are

$$G^<(t, t') = G^{12}(t, t') = i\langle c^\dagger(t')c(t) \rangle, \quad (2.73a)$$

$$G^>(t, t') = G^{21}(t, t') = -i\langle c(t)c^\dagger(t') \rangle. \quad (2.73b)$$

These Green's functions are not independent of each other but satisfies the relations;

$$G^K(t, t') = G^<(t, t') + G^>(t, t'), \quad (2.74a)$$

$$G^A(t, t') = G^R(t', t)^*, \quad (2.74b)$$

$$G^>(t, t') = G^<(t, t') + G^R(t, t') - G^R(t', t)^*, \quad (2.74c)$$

$$G^\Gamma(\tau, t') = G^\Gamma(t', \beta - \tau)^*. \quad (2.74d)$$

From these, we find that the set of $G^M, G^<, G^R$ and G^Γ has the full information, and we can construct the non-equilibrium DMFT focusing on this set. We note that a relation,

$$G^{<, >}(t, t')^* = -G^{<, >}(t', t), \quad (2.75)$$

is also important in the implementation.

Nambu formalism

In the Nambu formalism Eq. 2.17, each of the four components satisfies the relation Eq. 2.68. Hence we can define the "physical" Green's functions and the lesser and the greater Green's functions for each component in the same manner as in the normal state described above. As a counterpart to Eq. 2.74, we obtain

$$G_{\alpha, \gamma}^K(t, t') = G_{\alpha, \gamma}^<(t, t') + G_{\alpha, \gamma}^>(t, t'), \quad (2.76a)$$

$$G_{\gamma, \alpha}^A(t, t') = G_{\alpha, \gamma}^R(t', t)^*, \quad (2.76b)$$

$$G_{\alpha, \gamma}^>(t, t') = G_{\alpha, \gamma}^<(t, t') + G_{\alpha, \gamma}^R(t, t') - G_{\gamma, \alpha}^R(t', t)^*, \quad (2.76c)$$

$$G_{\gamma, \alpha}^\Gamma(\tau, t') = G_{\alpha, \gamma}^\Gamma(t', \beta - \tau)^*, \quad (2.76d)$$

where $\alpha, \gamma = 1, 2$ are Nambu indices.

Hence we only need to focus on G^M, G^Γ, G^R and $G^<$ again. For Eq. 2.75, we have

$$G_{\gamma, \alpha}^{<, >}(t, t')^* = -G_{\alpha, \gamma}^{<, >}(t', t). \quad (2.77)$$

In the following, we are going to use the Nambu formalism, since this is more general than the previous formalism.

2.3.2 Green's function for phonons

In principle, we can also define the Green's function for a phonon part as in the fermionic case, Eq. 2.12. However, if the Hamiltonian concerned has a structure of,

$$H(t) = \omega_0 a^\dagger a + \hat{F}(X, t), \quad (2.78)$$

it is simpler to consider the phonon Green's function with the form of

$$D(\nu, \nu') \equiv -i \langle \mathcal{T}_c X_c(\nu) X_c(\nu') \rangle. \quad (2.79)$$

Here a^\dagger again denotes a creation operator of a phonon, $X = a + a^\dagger$, and \hat{F} is a time-dependent operator expressed only with X (without $a - a^\dagger$) but can involve other degrees of freedom such as electrons. The Holstein model and its effective impurity problem have this structure. Since

2.3. NON-EQUILIBRIUM FORMALISM

we can integrate out the contribution from $P = (a - a^\dagger)/i$ in the action, we do not need to consider the propagator such as $-i\langle \mathcal{T}_c X_c(\nu) P_c(\nu') \rangle$, $-i\langle \mathcal{T}_c P_c(\nu) X_c(\nu') \rangle$ and $-i\langle \mathcal{T}_c P_c(\nu) P_c(\nu') \rangle$ in the diagrammatic expansion for $D(\nu, \nu')$ and $G(\nu, \nu')$.

For example, when the system is free ($\hat{F} = 0$), the phonon Green's function becomes

$$D_0(\nu, \nu') = G_0^B(\nu', \nu) + G_0^B(\nu, \nu'), \quad (2.80)$$

where $G_0^B(\nu, \nu') \equiv -i[\theta_C(\nu, \nu') + f_B(\omega_0)] \exp(-i \int_{c, \nu'}^\nu d\bar{\nu} \omega_0)$. $f_B(\omega) = 1/(e^{\beta\omega} - 1)$ is the Bose occupation function at an inverse temperature β . The inverse of $D_0(\nu, \nu')$ is defined by $[D_0^{-1} * D_0](\nu, \nu') = \delta_C(\nu, \nu')$ and given as

$$D_0^{-1}(\nu, \nu') = \frac{-\partial_\nu^2 - \omega_0^2}{2\omega_0} \delta_C(\nu, \nu'). \quad (2.81)$$

Now we can define nine Green's functions in the same way as for $G(\nu, \nu')$, and we obtain the relation,

$$D^{11}(t, t') = D^{12}(t, t') \quad (\text{for } t \leq t'), \quad (2.82a)$$

$$D^{11}(t, t') = D^{21}(t, t') \quad (\text{for } t > t'), \quad (2.82b)$$

$$D^{22}(t, t') = D^{21}(t, t') \quad (\text{for } t < t'), \quad (2.82c)$$

$$D^{22}(t, t') = D^{12}(t, t') \quad (\text{for } t \geq t'), \quad (2.82d)$$

$$D^{13}(t, \tau') = D^{23}(t, \tau'), \quad (2.82e)$$

$$D^{32}(\tau, t') = D^{31}(\tau, t'). \quad (2.82f)$$

From the definition of D , we find

$$D^{11}(t, t) = D^{12}(t, t) = D^{21}(t, t) = D^{22}(t, t), \quad (2.83)$$

and, from Eq. 2.82,

$$D^{11}(t, t') + D^{22}(t, t') = D^{12}(t, t') + D^{21}(t, t') \quad (\text{for any } t, t'). \quad (2.84)$$

Now we introduce the "physical" Green's functions as in the electron case,

$$\begin{bmatrix} D^R & D^K & \sqrt{2}D^\neg \\ 0 & D^A & 0 \\ 0 & \sqrt{2}D^\neg & D^M \end{bmatrix} \equiv \hat{L} \hat{\tau}_3 \hat{D} \hat{L}^\dagger, \quad (2.85)$$

where

$$\begin{aligned} D^R(t, t') &= -i\theta(t - t') \langle [X(t), X(t')]_- \rangle, \\ D^A(t, t') &= i\theta(t' - t) \langle [X(t), X(t')]_- \rangle, \\ D^K(t, t') &= -i \langle [X(t), X(t')]_+ \rangle, \\ D^\neg(t, \tau') &= -i \langle X(\tau') X(t) \rangle, \\ D^\neg(\tau, t') &= -i \langle X(\tau) X(t') \rangle, \\ D^M(\tau, \tau') &= -\langle T_\tau X(\tau) X(\tau') \rangle. \end{aligned} \quad (2.86)$$

We note that D^R and D^A are real, while D^K is purely imaginary. We also introduce the lesser and greater Green's functions as

$$D^<(t, t') = D^{12}(t, t') = -i\langle X(t')X(t) \rangle, \quad (2.87a)$$

$$D^>(t, t') = D^{21}(t, t') = -i\langle X(t)X(t') \rangle. \quad (2.87b)$$

Now we note the phonon Green's function satisfies

$$D(\nu, \nu') = D(\nu', \nu). \quad (2.88)$$

This leads to the relations,

$$D^>(t, t') = D^<(t', t), \quad (2.89a)$$

$$D^K(t, t') = D^<(t, t') + D^>(t', t), \quad (2.89b)$$

$$D^A(t, t') = D^R(t', t), \quad (2.89c)$$

$$D^\Gamma(\tau, t') = D^\Gamma(t', \tau). \quad (2.89d)$$

Hence one finds that the set of D^M , D^Γ , $D^<$ and D^R is enough. We also point out other important relations for the implementation,

$$\begin{aligned} D^{<, >}(t, t')^* &= -D^{<, >}(t', t), \\ D^R(t + 0^+, t) &= -i\langle [X(t + 0^+), X(t)] \rangle = 0, \\ \partial_t D^R(t, t')|_{t'=t-0^+} &= -2\omega_0. \end{aligned} \quad (2.90a)$$

Although we have mentioned that the other types of Green's functions for phonons are not necessary for the diagrammatic expansion for $D(\nu, \nu')$ and $G(\nu, \nu')$, we need them when we are interested in quantities related to phonons such as the phonon density, $\langle a^\dagger(t)a(t) \rangle$. Here we explain that the other Green's functions for phonons ($-i\langle \mathcal{T}_c X_c(\nu)P_c(\nu') \rangle$, $-i\langle \mathcal{T}_c P_c(\nu)X_c(\nu') \rangle$ and $-i\langle \mathcal{T}_c P_c(\nu)P_c(\nu') \rangle$) can be obtained from the derivatives of D . From Eq. 2.78, we find

$$\begin{aligned} i\partial_\nu X_c(\nu) &= \mathcal{U}_c(0, \nu)[X, H(\nu)]\mathcal{U}_c(\nu, 0) \\ &= \omega_0[-a^\dagger(\nu) + a(\nu)], \end{aligned} \quad (2.91)$$

where \mathcal{U}_c is defined in Eq. 2.7. From this we have

$$D_{d1}(\nu, \nu') \equiv \frac{\partial_\nu D(\nu, \nu')}{\omega_0} = -i\langle \mathcal{T}_c P(\nu)X(\nu') \rangle, \quad (2.92a)$$

$$D_{d2}(\nu, \nu') \equiv \frac{\partial_{\nu'} D(\nu, \nu')}{\omega_0} = -i\langle \mathcal{T}_c X(\nu)P(\nu') \rangle, \quad (2.92b)$$

$$D_{d1, d2}(\nu, \nu') \equiv \frac{\partial_\nu \partial_{\nu'} D(\nu, \nu')}{\omega_0^2} = \frac{2}{\omega_0} \delta_C(\nu, \nu') - i\langle \mathcal{T}_c P(\nu)P(\nu') \rangle. \quad (2.92c)$$

We note that, since $D_{d1}(\nu, \nu')$, $D_{d2}(\nu, \nu')$ and $D_{d1, d2}(\nu, \nu') - \frac{2}{\omega_0} \delta_C(\nu, \nu')$ satisfy the same relation as $D(\nu, \nu')$ (Eq. 2.82), we can define physical parts for them (retarded part, etc) in the same manner. For example,

$$D_{d2}^R(t, t') = -i\theta(t - t')\langle [X(t), P(t')] \rangle, \quad (2.93)$$

$$D_{d2}^A(t, t') = i\theta(t' - t)\langle [X(t), P(t')] \rangle. \quad (2.94)$$

2.3.3 The Dyson equation

In non-equilibrium cases, solving the Dyson equation is not so simple as in equilibrium cases, where each frequency component is independent of the rest because of the translational invariance along time. The integral form of the Dyson equation has a form of the Volterra integral equation, and the differential form of the Dyson equation has a form of the integral-differential equation [26], which we solve numerically, see Appendix. B.1. Here we explicitly show the form of the Dyson equations for the retarded (R), lesser ($<$) and left-mixing (\neg) parts. We note that the Matsubara component is prepared in the usual procedure and sets the initial conditions for these components. Technically speaking, the equations represent a non-Markovian time-propagation, hence we need to preserve all the Green's function with two arguments. This leads to a required memory scaling as $\mathcal{O}(M^2)$, where M is the number of grids along time. In addition, since the Dyson equation is nothing but evaluating an inversion of a $M \times M$ matrix, it requires $\mathcal{O}(M^3)$ calculation time. In general, the integral-differential form requires less memory and less calculation time than the integral form in the implementation of DMFT.

Electrons

The integral form of the Dyson equation for the electron Green's function is expressed as

$$\hat{G}(\nu, \nu') = \hat{G}_0(\nu, \nu') + [\hat{G}_0 * \hat{\Sigma} * \hat{G}](\nu, \nu'), \quad (2.95)$$

where $\hat{\Sigma}$ is the self-energy in the Nambu formalism. The explicit expression for G^R , G^\neg and $G^<$ are

$$\hat{G}^R(t, t') - \int_{t'}^t d\bar{t} [\hat{G}_0 * \hat{\Sigma}]^R(t, \bar{t}) \hat{G}^R(\bar{t}, t') = \hat{G}_0^R(t, t') \quad (\text{for } t > t'), \quad (2.96a)$$

$$\hat{G}^\neg(t, \tau') - \int_0^t d\bar{t} [\hat{G}_0 * \hat{\Sigma}]^R(t, \bar{t}) \hat{G}^\neg(\bar{t}, \tau') = \hat{Q}^\neg(t, \tau'), \quad (2.96b)$$

$$\hat{G}^<(t, t') - \int_0^t d\bar{t} [\hat{G}_0 * \hat{\Sigma}]^R(t, \bar{t}) \hat{G}^<(\bar{t}, t') = \hat{Q}^<(t, t'), \quad (2.96c)$$

where

$$\hat{Q}^\neg(t, \tau') = \hat{G}_0^\neg(t, \tau') + \int_0^\beta d\bar{\tau} [\hat{G}_0 * \hat{\Sigma}]^\neg(t, \bar{\tau}) \hat{G}^M(\bar{\tau}, \tau'), \quad (2.97a)$$

$$\hat{Q}^<(t, t') = \hat{G}_0^<(t, t') + \int_0^{t'} d\bar{t} [\hat{G}_0 * \hat{\Sigma}]^<(t, \bar{t}) \hat{G}^A(\bar{t}, t') - i \int_0^\beta d\bar{\tau} [\hat{G}_0 * \hat{\Sigma}]^\neg(t, \bar{\tau}) \hat{G}^\neg(\bar{\tau}, t'). \quad (2.97b)$$

We note that, since \hat{G}^\neg and \hat{G}^A can be expressed in terms of \hat{G}^R and \hat{G}^\neg using Eq. 2.76, these equations are closed for a given $\hat{\Sigma}$. The Dyson equation can also be expressed in a differential form,

$$\begin{bmatrix} i\partial_\nu - h(\nu) & -F_{\text{ex}}(\nu) \\ -F_{\text{ex}}(\nu) & i\partial_\nu + h(\nu) \end{bmatrix} \hat{G}(\nu, \nu') - \int_{\mathcal{C}} d\bar{\nu} \hat{\Sigma}(\nu, \bar{\nu}) \hat{G}(\bar{\nu}, \nu') = \hat{I} \delta_{\mathcal{C}}(\nu, \nu'). \quad (2.98)$$

The explicit form for G^R , G^\neg and $G^<$ are

$$[i\partial_t \hat{I} - h(t)\hat{\sigma}_3 - F_{\text{ex}}(t)\hat{\sigma}_1]\hat{G}^R(t, t') - \int_{t'}^t d\bar{t} \hat{\Sigma}^R(t, \bar{t})\hat{G}^R(\bar{t}, t') = \delta(t - t')\hat{I} \quad (\text{for } t > t'), \quad (2.99a)$$

$$[i\partial_t \hat{I} - h(t)\hat{\sigma}_3 - F_{\text{ex}}(t)\hat{\sigma}_1]\hat{G}^\square(t, \tau') - \int_0^t d\bar{t} \hat{\Sigma}^R(t, \bar{t})\hat{G}^\square(\bar{t}, \tau') = \hat{Q}^\square(t, \tau'), \quad (2.99b)$$

$$[i\partial_t \hat{I} - h(t)\hat{\sigma}_3 - F_{\text{ex}}(t)\hat{\sigma}_1]\hat{G}^<(t, t') - \int_0^t d\bar{t} \hat{\Sigma}^R(t, \bar{t})\hat{G}^<(\bar{t}, t') = \hat{Q}^<(t, t'), \quad (2.99c)$$

where

$$\hat{Q}^\square(t, \tau') = \int_0^\beta d\bar{\tau} \hat{\Sigma}^\square(t, \bar{\tau})\hat{G}^M(\bar{\tau}, \tau'), \quad (2.100a)$$

$$\hat{Q}^<(t, t') = \int_0^{t'} d\bar{t} \hat{\Sigma}^<(t, \bar{t})\hat{G}^A(\bar{t}, t') - i \int_0^\beta d\bar{\tau} \hat{\Sigma}^\square(t, \bar{\tau})\hat{G}^\square(\bar{\tau}, t'). \quad (2.100b)$$

Phonons

The Dyson equation for the phonon Green's function is

$$\begin{aligned} D(\nu, \nu') &= D_0(\nu, \nu') + [D_0 * \Pi * D](\nu, \nu') \\ &= D_0(\nu, \nu') + [D * \Pi * D_0](\nu, \nu'), \end{aligned} \quad (2.101)$$

where Π is the phonon self-energy. The explicit forms of the equations for D^R , D^\square and $D^<$ are

$$D^R(t, t') - \int_{t'}^t d\bar{t} [D_0 * \Pi]^R(t, \bar{t})D^R(\bar{t}, t') = D_0^R(t, t') \quad (\text{for } t > t'), \quad (2.102a)$$

$$D^\square(t, \tau') - \int_0^t d\bar{t} [D_0 * \Pi]^R(t, \bar{t})D^\square(\bar{t}, \tau') = \mathcal{R}^\square(t, \tau'), \quad (2.102b)$$

$$D^<(t, t') - \int_0^t d\bar{t} [D_0 * \Pi]^R(t, \bar{t})D^<(\bar{t}, t') = \mathcal{R}^<(t, t'),$$

where

$$\mathcal{R}^\square(t, \tau') = D_0^\square(t, \tau') + \int_0^\beta d\bar{\tau} [D_0 * \Pi]^\square(t, \bar{\tau})D^M(\bar{\tau}, \tau'), \quad (2.103a)$$

$$\mathcal{R}^<(t, t') = D_0^<(t, t') + \int_0^{t'} d\bar{t} [D_0 * \Pi]^<(t, \bar{t})D^A(\bar{t}, t') - i \int_0^\beta d\bar{\tau} [D_0 * \Pi]^\square(t, \bar{\tau})D^\square(\bar{\tau}, t'). \quad (2.103b)$$

We note that, since D^\square and D^A can be expressed with D^R and D^\square through Eq. 2.89, these equations are closed for a given Π .

The Dyson equation for the phonon Green's function can also be written with a differential form as

$$\left[\frac{-\partial_\nu^2 - \omega_0^2}{2\omega_0} \right] D(\nu, \nu') - \int_{\mathcal{C}} \Pi(\nu, \bar{\nu})D(\bar{\nu}, \nu')d\bar{\nu} = \delta_{\mathcal{C}}(\nu, \nu'), \quad (2.104)$$

2.3. NON-EQUILIBRIUM FORMALISM

where $\frac{-\partial_\nu^2 - \omega_0^2}{2\omega_0} = \frac{-\partial_t^2 - \omega_0^2}{2\omega_0}$ for $\nu \in C_1, C_2$ and $\frac{-\partial_\nu^2 - \omega_0^2}{2\omega_0} = \frac{\partial_\tau^2 - \omega_0^2}{2\omega_0}$ for $\nu \in C_3$.

From this we can explicitly write the equations for D^R , D^Γ and $D^<$ as

$$\left[\frac{-\partial_t^2 - \omega_0^2}{2\omega_0} \right] D^R(t, t') - \int_{t'}^t d\bar{t} \Pi^R(t, \bar{t}) D^R(\bar{t}, t') = \delta(t - t'), \quad (2.105a)$$

$$\left[\frac{-\partial_t^2 - \omega_0^2}{2\omega_0} \right] D^\Gamma(t, \tau') - \int_0^t d\bar{t} \Pi^R(t, \bar{t}) D^\Gamma(\bar{t}, \tau') = R^\Gamma(t, \tau'), \quad (2.105b)$$

$$\left[\frac{-\partial_t^2 - \omega_0^2}{2\omega_0} \right] D^<(t, t') - \int_0^t d\bar{t} \Pi^R(t, \bar{t}) D^<(\bar{t}, t') = R^<(t, t'), \quad (2.105c)$$

where

$$R^\Gamma(t, \tau') = \int_0^\beta d\bar{\tau} \Pi^\Gamma(t, \bar{\tau}) D^M(\bar{\tau}, \tau'), \quad (2.106a)$$

$$R^<(t, t') = \int_0^{t'} d\bar{t} \Pi^<(t, \bar{t}) D^A(\bar{t}, t') - i \int_0^\beta d\bar{\tau} \Pi^\Gamma(t, \bar{\tau}) D^\Gamma(\bar{\tau}, t'). \quad (2.106b)$$

Since these equations are 2nd derivative-integral equations, we need the information of $\partial_\nu D(\nu, \nu')|_{\nu=0}$ ($= \omega_0 D_{d1}(0, \nu')$) as well as that of $D(0, \nu')$.

Differentiating the Dyson equation Eq. 2.101, we obtain

$$D_{d1}(t, t') = D_{0,d1}(t, t') + [D_{0,d1} * \Pi * D](t, t'), \quad (2.107a)$$

$$D_{d2}(t, t') = D_{0,d2}(t, t') + [D * \Pi * D_{0,d2}](t, t'), \quad (2.107b)$$

$$D_{d1,d2}(t, t') = D_{0,d1,d2}(t, t') + [D_{0,d1} * \Pi * D_{d2}](t, t'). \quad (2.107c)$$

Technically speaking, even though D_{d1}, D_{d1} and $D_{d1,d2}$ can be obtained by differentiating D , it is not easy to keep the same scaling for the accuracy in the implementation as for D . With regards to this point, it is much easier to use Eq. 2.107 for evaluating D_{d1}, D_{d1} and $D_{d1,d2}$.

2.3.4 Non-equilibrium dynamical mean-field theory for the Holstein model

In DMFT, the lattice problem is mapped onto an effective impurity problem. For the Holstein model, the effective impurity model is Eq. 2.20 with $U = 0$. The action for the impurity model is simplified by integrating out P , and we obtain

$$\begin{aligned} S'_{\text{imp}} &= i \int_{\mathcal{C}} d\nu d\nu' \hat{\Psi}^\dagger(\nu) \hat{G}_{0,\sigma}^{-1}(\nu, \nu') \hat{\Psi}(\nu') + i \int_{\mathcal{C}} d\nu d\nu' X(\nu) \frac{D_0^{-1}(\nu, \nu')}{2} X(\nu') \\ &\quad - i \int_{\mathcal{C}} d\nu g(\nu) X(\nu) \hat{\Psi}^\dagger(\nu) \hat{\sigma}_3 \hat{\Psi}(\nu). \end{aligned} \quad (2.108)$$

From this expression, we can confirm that when we consider an expansion of G and D we do not need to consider other types of phonon Green's functions ($-i\langle \mathcal{T}_c X_c(\nu) P_c(\nu') \rangle$, $-i\langle \mathcal{T}_c P_c(\nu) X_c(\nu') \rangle$ and $-i\langle \mathcal{T}_c P_c(\nu) P_c(\nu') \rangle$). We only have to solve this impurity problem in some way and find a self-consistent solution as explained in Sec. 2.1.2. We again note that the self-consistent solution has the following relation,

$$\hat{G}_{\text{loc}}(t, t') \equiv -i\langle \mathcal{T}_c \Psi_i(t) \Psi_i^\dagger(t') \rangle = \hat{G}_{\text{imp}}(t, t') \quad (2.109a)$$

$$D_{\text{loc}}(t, t') \equiv -i\langle \mathcal{T}_c X_i(t) X_i(t') \rangle = D_{\text{imp}}(t, t'). \quad (2.109b)$$

Observables

In DMFT one can derive the following expressions for various physical quantities using the Dyson equations for the lattice and the effective impurity problem ¹.

1. *Kinetic energy:*

$$E_{\text{kin}}(t) = -\frac{1}{N} \sum_{i,j,\sigma} v_{i,j}(t) \langle c_{i,\sigma}^\dagger(t) c_{j,\sigma}(t) \rangle = -i \sum_{\alpha} [\hat{\Delta} \circledast \hat{G}_{\text{loc}}]_{\alpha,\alpha}^<(t,t), \quad (2.110)$$

where \circledast means to operate multiplication of 2×2 matrices and integration along the KB contour \mathcal{C} , i.e., $[\hat{A} \circledast \hat{B}]_{\alpha,\alpha'}(\nu,\nu') = \sum_{\gamma} \int_{\mathcal{C}} d\bar{\nu} A_{\alpha,\gamma}(\nu,\bar{\nu}) B_{\gamma,\alpha'}(\bar{\nu},\nu')$

2. *Correlation between lattice distortion and electron density:*

$$\frac{1}{N} \sum_i \langle X_i(t) \hat{\Psi}_i^\dagger \hat{\sigma}_3 \hat{\Psi}_i(t) \rangle = \frac{1}{ig(t)} \sum_{\alpha} [\hat{\Sigma} \circledast \hat{G}_{\text{loc}}]_{\alpha,\alpha}^<(t,t). \quad (2.111)$$

3. *Phonon density:*

$$\langle a_i^\dagger(t) a_i(t) \rangle = \frac{1}{4} [\langle X_i(t) X_i(t) \rangle + \langle P_i(t) P_i(t) \rangle] - \frac{1}{2}. \quad (2.112)$$

4. *Total energy per site:*

$$\begin{aligned} E_{\text{tot}}(t) &= E_{\text{kin}}(t) - \mu \frac{1}{N} \sum_i \langle n_i(t) \rangle + \frac{1}{N} \omega_0 \sum_i \langle a_i^\dagger(t) a_i(t) \rangle \\ &\quad + \frac{1}{N} \sum_i g(t) \langle X_i(t) \hat{\Psi}_i^\dagger(t) \hat{\sigma}_3 \hat{\Psi}_i(t) \rangle. \end{aligned} \quad (2.113)$$

2.3.5 Impurity solver

The most important step in the DMFT self-consistency loop is to solve the effective impurity problem. In principle, a numerically exact solution can be obtained with real-time CT-QMC methods [108–110]. However, QMC methods suffer from a dynamical sign problem when they are implemented on the real-time axis. This makes it difficult to reach long times required to investigate dynamics of phonons and/or some order parameters in symmetry-broken states. What is often done to deal with this difficulty is to use proper approximate solvers for effective impurity models. Compared to the situation in the Hubbard model, such approximations remain to be developed for electron-phonon systems. Here we have newly extended the Migdal approximation, which has been a successful method in describing conventional superconductors in the strongly-coupled regime [14, 15], to solve the effective non-equilibrium impurity problem. The basic idea of this approximation is that the vertex corrections for self-energies can be neglected when ω_0/W is small, which is usually the case in many materials [13].

¹Here we assume that $F_{\text{ex}} \equiv 0$ and the system does not break the spatial translational symmetry.

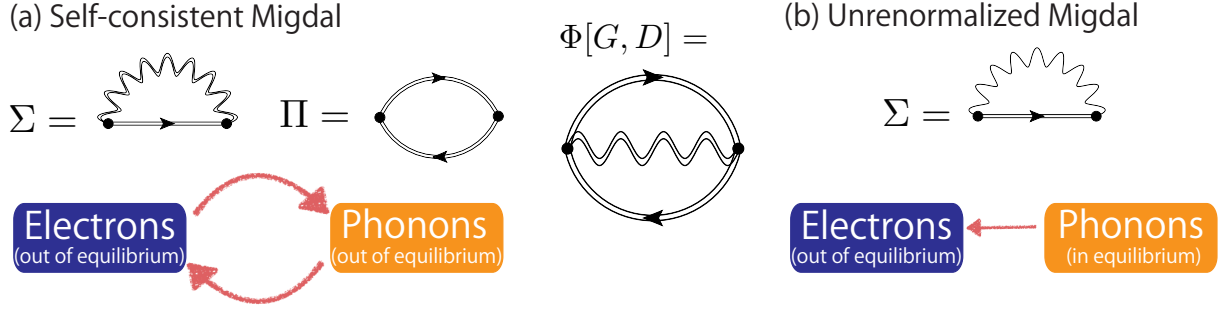


Figure 2.6: (a) The electron self-energy (Σ), phonon self-energy (Π) diagrams and the Luttinger-Ward functional $\Phi[G, D]$ in the self-consistent Migdal approximation. Here, double straight lines represent the dressed electron Green's functions, while double wiggly lines the dressed phonon Green's function. (b) The electron self-energy in the unrenormalized Migdal approximation, where the single wiggly line indicate the bare (equilibrium) phonon Green's function. In both cases, the Hartree terms are neglected since we consider homogeneous excitations with no change in the electron number at half-filling. Schematic pictures at lower parts of both panels show that electrons and phonons make time-evolution affecting each other in the self-consistent Migdal approximation, while in the unrenormalized Migdal approximation only electrons make time-evolution with phonons remaining in equilibrium.

First of all, we have to note that the term “Migdal approximation” is used for two distinct types of approximations in the literature on the Holstein model, i.e., the *self-consistent* Migdal approximation and the *unrenormalized* Migdal approximation. Prior to the present work, only the latter type of approximation is extended to non-equilibrium [96–100]. However, in the approximation, phonon dynamics is neglected and its effect has not been clear. In addition, as we show below, the self-consistent Migdal approximation, as impurity solvers, is quantitatively more accurate than the other. Our main contribution here in terms of development of methodology is the extension of the self-consistent Migdal approximation to non-equilibrium situations and clarification of effects of phonon dynamics.

Now, let us start with a comparison between the self-consistent and un-renormalized Migdal approximations.

1. Self-consistent Migdal approximation (sMig)

The self-energies for electrons and phonons are expressed as

$$\hat{\Sigma}(\nu, \nu') = -\hat{\sigma}_3 \delta_{\mathcal{C}}(\nu, \nu') g(\nu) \int_{\mathcal{C}} d\nu_1 \text{tr}[i\hat{G}_{\text{imp}}(\nu_1, \nu_1 + 0_{\mathcal{C}}^+) \hat{\sigma}_3] D_0(\nu_1, \nu) g(\nu_1) + ig^2 D_{\text{imp}}(\nu, \nu') \hat{\sigma}_3 \hat{G}_{\text{imp}}(\nu, \nu') \hat{\sigma}_3, \quad (2.114a)$$

$$\Pi(\nu, \nu') = -ig^2 \text{tr}[\hat{\sigma}_3 \hat{G}_{\text{imp}}(\nu, \nu') \hat{\sigma}_3 \hat{G}_{\text{imp}}(\nu', \nu)]. \quad (2.114b)$$

Here the first term in Σ is the Hartree term. In this thesis, we focus on homogeneous phases at half-filling and homogeneous external fields with no change in the number of electrons. In this case, the Hartree term is always zero and we do not need to think of it explicitly. The Feynman diagrams for self-energies of electrons (without the Hartree term) and of phonons are shown in Fig. 2.6(a). This approximation has been used to study the Holstein model in equilibrium, and its accuracy has been discussed in a number of

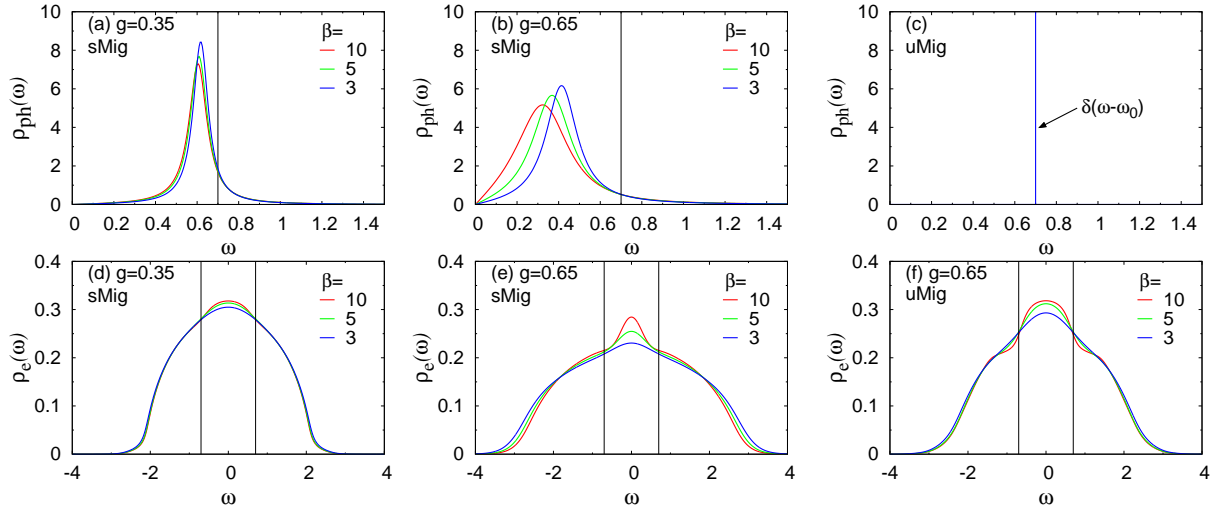


Figure 2.7: (a)(b) The phonon spectral functions $\rho_{\text{ph}}(\omega)$ and (d)(e) the electron spectral functions $\rho_e(\omega)$ computed with the self-consistent Migdal approximation at half filling with $\omega_0 = 0.7$ for $g = 0.35$ (a,d) or $g = 0.65$ (b,e) at various values of $T = 1/\beta$. (c)(f) are corresponding results in the unrenormalized Migdal approximation at half filling for $g = 0.65$. Vertical lines in each panel show the bare phonon frequency, $|\omega| = \omega_0$.

papers [111–116]. As long as g is not close to the critical value g_c for the transition to the bipolaronic insulating phase and ω_0 is small enough compared to the electron bandwidth, it provides a quantitatively accurate description [112, 115, 116]. Since the self-energies of the electrons and phonons involve dressed propagators (as represented by double lines in Fig. 2.6(a)), we can take account of the interplay between the electrons and phonons in non-equilibrium dynamics. In particular, we can construct a Luttinger-Ward functional $\Phi[G, D]$ for this approximation as displayed in Fig. 2.6(a). Hence this approximation is a conserving one, and we have numerically confirmed that number of electrons and total energies are indeed conserved.

2. Unrenormalized Migdal approximation (uMig)

The unrenormalized Migdal approximation is sometimes called the Hartree-Fock approximation [68]. In this approximation, we ignore the phonon self-energy, and the electron self-energy is given by

$$\begin{aligned} \hat{\Sigma}(\nu, \nu') = & -\hat{\sigma}_3 \delta_{\mathcal{C}}(\nu, \nu') g(\nu) \int_{\mathcal{C}} d\nu_1 \text{tr}[i\hat{G}_{\text{imp}}(\nu_1, \nu_1 + 0_{\mathcal{C}}^+) \hat{\sigma}_3] D_0(\nu_1, \nu) g(\nu_1) \\ & + ig^2 D_0(\nu, \nu') \hat{\sigma}_3 \hat{G}_{\text{imp}}(\nu, \nu') \hat{\sigma}_3. \end{aligned} \quad (2.115)$$

The corresponding Feynman diagram for the self-energy is shown in Fig. 2.6(b), where the Hartree term is again neglected. We note that the electron self-energy has the same structure as the self-consistent Migdal approximation, Fig. 2.6(a), but that the dressed phonon propagator is replaced with the bare equilibrium propagator. Hence the phonon dynamics is not considered in this scheme, and its effect on electron dynamics is also

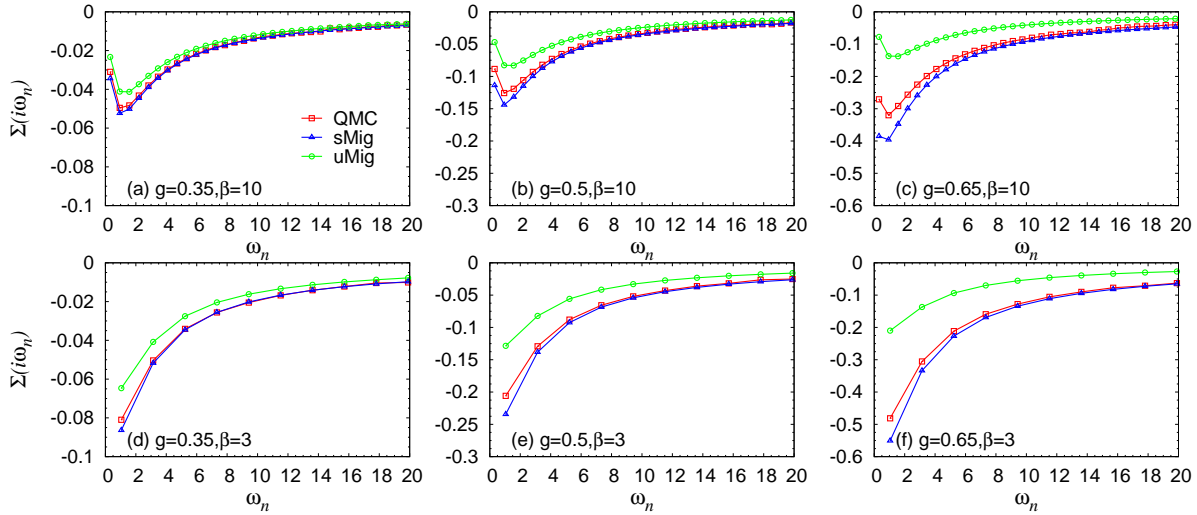


Figure 2.8: The electron self-energies on the Matsubara axis calculated in DMFT with the Migdal approximation, HF approximation, and CT-QMC impurity solvers for $\omega_0 = 0.7$ and indicated values of g and β .

neglected, see Fig. 2.6(b). In addition, this approximation cannot be derived from a Luttinger-Ward functional and is thus not conserving. The uMig approximation has been used to study equilibrium states [68] and nonequilibrium dynamics [98–100] of the Holstein model. In addition, the uMig self-energy for small g has been added in some DMFT studies to describe an effect of a bosonic heat bath on the electrons [117, 118], and we also see that phonons indeed act as a heat bath in this approximation in Sec. 4.1.3.

In the following, we shall show that the sMig approximation is definitely more reliable than the unrenormalized one, by benchmarking equilibrium results against DMFT data obtained with the CT-QMC impurity solver [28, 67]. We also demonstrate how the sMig approximation quantitatively is improved as we decrease the phonon frequency by comparing the results for the transition temperatures to the SC phase with those from DMFT+CT-QMC's [28, 112].

First, we compare spectral functions for electrons and phonons in the sMig approximation and the uMig approximation. The spectral functions are defined by

$$\rho_{\text{ph}}(\omega) = -\text{Im}D_{\text{loc}}^R(\omega)/\pi, \quad (2.116a)$$

$$\rho_e(\omega) = -\text{Im}G_{\text{loc}}^R(\omega)/\pi \quad (2.116b)$$

for phonons and electrons, respectively, and the superscript R denotes retarded components. We obtain these spectral functions by calculating the equilibrium propagators on the real-time axis and performing Fourier transformations.

We show $\rho_{\text{ph}}(\omega)$ in the sMig approximation at half filling for $\omega_0 = 0.7$ and indicated values of $T = 1/\beta$ and g in Fig. 2.7 (a)(b). It exhibits a single peak at a renormalized phonon frequency, which we call ω_0^r and shifts from $\omega = \omega_0$ (vertical lines) with increasing electron-phonon coupling g . This result is consistent with previous $T = 0$ calculations based on DMFT+ numerical renormalization group (NRG) [114], whose results can be regarded as a benchmark. In addition,

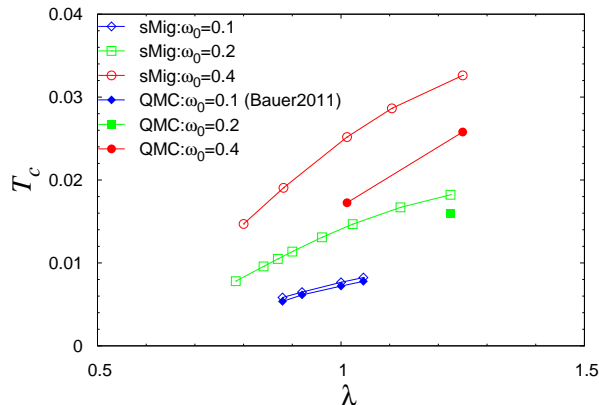


Figure 2.9: Comparison of the DMFT transition temperatures for the SC phase against the el-ph coupling λ evaluated from DMFT+CT-QMC (solid symbols) and from DMFT+ self-consistent Migdal approximation (open symbols) for various phonon frequencies. The data for $\omega_0 = 0.1$ is extracted from Fig. 2(a) and Fig. 3(b) in Ref. [112].

we find that the phonon frequency becomes less renormalized with increasing temperature, and that the temperature dependence becomes more significant for larger g . By contrast, in the uMig approximation, $\rho_{\text{ph}}(\omega)$ has a delta-function peak at $\omega = \pm\omega_0$ [Fig. 2.7(c)], since the phonons are assumed to have no self-energy.

The electron spectral function $\rho_e(\omega)$ is shown in Fig. 2.7(d)(e) for the sMig approximation and in Fig. 2.7(f) for the unrenormalized one. In both cases, there emerges a peak in the spectrum in the energy interval $|\omega| \lesssim \omega_0$ as the temperature is lowered. This peak represents quasiparticles (polarons) and becomes more pronounced for stronger g . In the sMig approximation, the peak becomes narrower with increasing g , which reflects the renormalization of the phonon frequency (ω_0^r), while in the uMig approximation the width is determined by the bare phonon frequency ω_0 . Again, the former behavior is consistent with the results from DMFT+NRG [113, 114].

Now, we compare self-energies on the Matsubara axis derived from the sMig, the uMig and CT-QMC in Fig. 2.8. Clearly, the sMig approximation is much closer to the CT-QMC results in the parameter regime considered here, where the uMig approximation underestimates the electron self-energy, while the sMig approximation slightly overestimates it. The quantitative difference becomes more pronounced as the interaction g is increased.

From these analyses, we conclude that the sMig approximation is significantly more reliable than the unrenormalized one in a wide parameter regime when the system is not too close to the transition to a bipolaronic phase. Hence it is natural to expect that even in the non-equilibrium dynamics the sMig approximation provides a better description of the isolated Holstein model.

Finally, we demonstrate that quantitative accuracy of the self-consistent Migdal approximation is improved as the phonon frequency is decreased. In Fig. 2.9, we show the transition temperatures of the SC phase evaluated with the self-consistent Migdal approximation and CT-QMC's. We note that our CT-QMC is the hybridization expansion method so that it is difficult to study weak-coupling and low-temperature regimes. Therefore, for $\omega_0 = 0.1$, we have extracted the data from Fig. 2(a) and Fig. 3(b) in Ref. [112], where the authors evaluate the

2.3. NON-EQUILIBRIUM FORMALISM

transition temperature with a CT-QMC in a weak-coupling expansion. We can see that sMig results approach the QMC results as ω_0 is decreased and, at $\omega_0 = 0.1$ the deviation becomes less than 10%.

Chapter 3

Competing orders in the Holstein-Hubbard and Holstein models in equilibrium

In this chapter, we discuss competing orders in the Holstein-Hubbard model and the Holstein model using DMFT with the hybridization expansion CT-QMC as an impurity solver. In Sec. 3.1, we study the competition of ordered phases in the Holstein-Hubbard model at half-filling determining the phase diagrams at finite temperatures. In Sec. 3.2, we investigate the competition and coexistence of the charge order (CO) and the superconductivity (SC) in the Holstein model away from half-filling. There, we find a so-called supersolid state characterized by a microscopic coexistence of CO and SC, which is stable only in the intermediate-coupling regime. We reveal the reason why the supersolid state is stabilized using an effective bipolaron model. The results of this chapter have been published in Refs. [27–29]

3.1 Half-filling: Competition between antiferromagnetism and charge order

3.1.1 Background: Electron-electron interaction vs electron-phonon interaction

The interplay of electron-electron (el-el) Coulomb interactions and electron-phonon (el-ph) interactions brings about rich physics in various classes of materials of interest. For example, alkali-doped fullerenes show an s-wave superconducting (SC) phase with a T_c dome and competition between SC and an antiferromagnetic (AF) state. It has been discussed that in this material both the Coulomb interaction and the el-ph coupling are strong and play significant roles [3–7]. In addition, even in the high- T_c cuprates, coupling to phonons is significant as is evidenced by the kinks observed in the angle-resolved photoemission spectrum, although usually properties of cuprates are discussed only with the el-el Coulomb interactions [16].

In order to theoretically explore the interplay of different interactions, the Holstein-Hubbard model, which is one of the simplest models for such situations, has been investigated. In particular, our interests are competition of different ordered phases when both the Coulomb interaction and the phonon-mediated effective retarded attractive interaction are comparable.

3.1. HALF-FILLING: COMPETITION BETWEEN ANTIFERROMAGNETISM AND CHARGE ORDER

In such a situation, it is expected that the AF state, the CO state and the s-wave SC state can appear and compete with each other. Competition and evolution of different orders in the coexistence of the Coulomb interaction and the el-ph coupling have indeed been attracting much interests, and have been discussed in the one-dimensional case including small-size chains [57–62, 64, 65, 119], in the two-dimensional case [66, 77] and in the infinite-dimensional case [69, 90]. In one-dimensional case, various numerical analyses have revealed that the ground-state phase diagram includes AF, CO and an intermediate metallic phase between them in the small U regime [57–62, 65]. In two-dimensional case [66, 77], the authors have employed the numerically exact determinant QMC, and they have shown that there exists an intermediate metallic regime between CO and AF when U and λ are small, which is similar to the ground state of the 1D case. However, they could not go to low temperatures because of a sign problem, and whether this metallic phase remains at $T = 0$ is still an open question. In the infinite-dimensional case, the dynamical mean-field theory (DMFT) is used [28, 69, 90]. Before the present study, investigation of the ordered phases of the Holstein-Hubbard model is limited to that for the ground state with DMFT + numerical renormalization group (NRG) impurity solver. The ground state phase diagrams show that a second-order transition between CO and AF with no intermediate metallic phase in the weak-coupling regime, while in the strong-coupling a first-order transition occurs between them. However, how different orders compete with each other at finite temperatures remains an open question.

Motivated by these, in order to investigate the competition of ordered phases around $U_{\text{eff}} (= U - \lambda) = 0$, we have determined phase diagrams of the half-filled Holstein-Hubbard model at finite temperatures on the infinitely connected Bethe lattice, which is a bipartite lattice and has no lattice frustration, with DMFT + CT-QMC and without any constraint (i.e., we allow all of commensurate CO, commensurate AF and s-wave SC to emerge.). The order parameters for these orders are defined in Table. 2.1 in Sec. 2.2. When we study the hysteresis at the phase transition between CO and AF, we use the hybridization functions for $U_{\text{eff}} = U - \lambda$ as an input for the next step $U_{\text{eff}} = U - \lambda - \delta\lambda$, where $\delta\lambda$ denotes a small change in λ .

3.1.2 Simplified descriptions

Before we show the phase diagrams of the Holstein-Hubbard model and discuss the competition of different orders, here we introduce some simplified descriptions for heuristic purposes. We are going to clarify the reliability of these descriptions by comparing their prediction with the results of DMFT+CT-QMC.

1. The anti-adiabatic limit: the Hubbard model

As is mentioned in the introduction, we can integrate out the phonon degrees of freedom in a path-integral framework to obtain an effective retarded el-el interaction, Eq. 1.2. In the anti-adiabatic limit of $\omega_0 \rightarrow \infty$ with $\lambda \equiv \frac{2g^2}{\omega_0}$ and U fixed, we can neglect the frequency dependence of $U_{\text{eff}}(\omega)$, and the HH model is reduced to the Hubbard model,

$$H = -v \sum_{\langle i,j \rangle, \sigma} (c_{i,\sigma}^\dagger c_{j,\sigma} + \text{H.c.}) + U_{\text{eff}} \sum_i n_{i,\uparrow} n_{i,\downarrow} - \mu_{\text{eff}} \sum_i n_i, \quad (3.1)$$

with $U_{\text{eff}} = U - \lambda$ and $\mu_{\text{eff}} = \mu - g^2/\omega_0$. If we discuss the phase diagram of the HH model at half-filling with this picture, it follows that

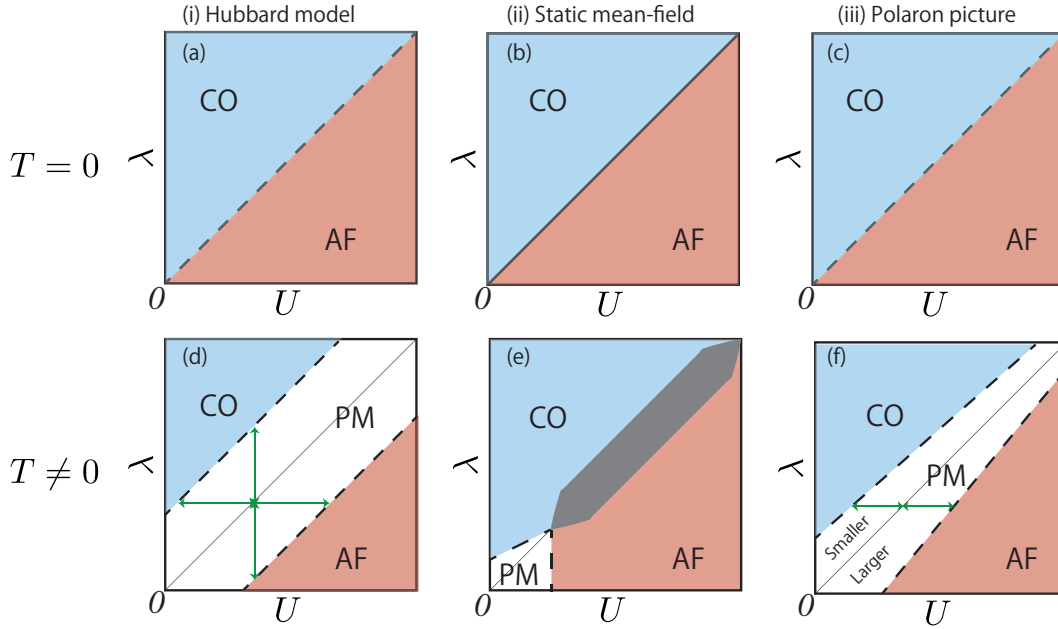


Figure 3.1: Schematic phase diagrams around $U_{\text{eff}} = 0$ in the Hubbard model (i), the static mean-field approximation (ii) and the polaron picture (iii). CO indicates the charge ordered phase, AF the antiferromagnetic phase and PM the paramagnetic metallic phase. Dashed lines indicate continuous phase transitions, while solid lines first-order transitions. Green arrows show the same length in each panel. We note that in (i) and (iii), transition temperatures show a dome structure against, for example, U . Therefore, if we go away from the $U_{\text{eff}} = 0$ line there are other boundaries between AF-normal states or CO-normal states, which we do not consider here. The gray area in panel (e) means that we have not yet clarified the phase boundary at finite temperatures.

1. The ground-state phase diagram shows no paramagnetic state and the direct phase transition between AF and CO is of second order, Fig. 3.1(a).
2. At finite temperatures, there emerges a paramagnetic metallic (PM) phase between AF and CO. The PM region is symmetric about $U = \lambda$ and the boundary is parallel to the $U = \lambda$ line, Fig. 3.1(d).

Comparison between this picture and the direct calculation of the HH model has been done in previous works [66, 69], and indeed some aspects can be described with this picture [69].

2. The static mean-field description

When the phonon frequency (ω_0), the el-ph interaction (λ) and the el-el interaction (U) are all small compared to the electron bandwidth, it is justified to introduce a static mean-field approximation by introducing the average of the lattice displacement $\langle a_i^\dagger + a_i \rangle / \sqrt{2\omega_0}$ and the averaged number of electrons $\langle n_{i,\sigma} \rangle$. The resultant static mean-field Hamiltonian is

$$H_{\text{MF}} \equiv H_{\text{MF}}^{\text{el}} + H_{\text{MF}}^{\text{ph}}, \quad (3.2)$$

3.1. HALF-FILLING: COMPETITION BETWEEN ANTIFERROMAGNETISM AND CHARGE ORDER

where

$$H_{\text{MF}}^{\text{el}} = -v \sum_{\langle i,j \rangle, \sigma} (c_{j,\sigma}^\dagger c_{i,\sigma} + \text{H.c.}) + \sum_i [U(\langle n_{i\uparrow} \rangle n_{i\downarrow} + \langle n_{i\downarrow} \rangle n_{i\uparrow}) - \mu n_i + g(a_i^\dagger + a_i) n_i], \quad (3.3)$$

where $n_i = n_{i\uparrow} + n_{i\downarrow}$, and

$$H_{\text{MF}}^{\text{ph}} = g \sum_i (a_i^\dagger + a_i) (\langle n_i \rangle - 1) + \omega_0 \sum_i a_i^\dagger a_i. \quad (3.4)$$

From $H_{\text{MF}}^{\text{ph}}$, we find $\langle a_i \rangle = \langle a_i^\dagger \rangle = -\frac{g}{\omega_0} (\langle n_i \rangle - 1)$. Then we obtain

$$H_{\text{MF}}^{\text{el}} = -v \sum_{\langle i,j \rangle, \sigma} (c_{j,\sigma}^\dagger c_{i,\sigma} + \text{H.c.}) - \sum_i (\mu - \lambda) n_i + \sum_{i,\sigma} n_{i\sigma} (U \langle n_{i\bar{\sigma}} \rangle - \lambda \langle n_i \rangle). \quad (3.5)$$

This mean-field Hamiltonian suggests that the driving force for CO, $-\sum_\sigma \lambda \langle n_i \rangle n_{i\sigma}$, comes from electrons of both spins, i.e. σ and $\bar{\sigma}$. This is different from the case of the anti-adiabatic limit, i.e. the Hubbard interaction, where an electron with spin σ feels interaction only from those with $\bar{\sigma}$ in the static mean-field description.

When we assume a pure CO phase or a pure AF phase, we can derive a self-consistent equation,

$$1 = V \int d\xi \rho(\xi) \frac{\tanh(\beta E(\xi, \Phi, V)/2)}{2E(\xi, \Phi, V)}, \quad (3.6)$$

where $\rho(\xi)$ is the density of states for bare electrons and $E(\xi, \Phi, V) = \sqrt{V^2 \Phi^2 + \xi^2}$. For CO we put $\Phi = \Phi_{\text{CO}}, V = 2\lambda - U$ and for AF, $\Phi = \Phi_{\text{AF}}, V = U$. Here we note that when we consider CO and SC in the attractive Hubbard model within the static mean-field approximation, we use $V = -U = -U_{\text{eff}}$ in Eq. 3.6. In the present description for the adiabatic limit, we put $V = 2\lambda = -2U_{\text{eff}}$ (in the Holstein model), where the factor 2 comes from spin up and down. Here we list up several consequences from the mean-field description [28, 69].

1. A first-order phase transition between CO and AF in the ground-state phase diagram occurs, Fig. 3.1(b).
2. There exists a paramagnetic metallic region at finite temperatures when λ and U are small, where the region is larger on the $U > \lambda$ side than on the $U < \lambda$ side. This is explained by considering dependence of AF and CO on U and λ . At a given temperature T , let $V_0 > 0$ satisfy

$$1 = V_0 \int d\xi \rho(\xi) \frac{\tanh(\beta E(\xi, 0, V_0)/2)}{2E(\xi, 0, V_0)}. \quad (3.7)$$

The mean-field analysis then dictates that the boundary of CO and PM is located at $\lambda = (V_0 + U)/2$, while the boundary of AF and PM is at $U = V_0$. The two boundaries cross at $U = \lambda = V_0$, see Fig. 3.1(e).

3. The polaron picture

When the el-ph coupling is strong enough and phonons move fast enough, it is better to change the basic particle from an electron to a so-called polaron, which represents an electron dressed

with phonons. For this, we perform a Lang-Firsov (LF) canonical transformation for the HH model, $H_{\text{LF}} = e^S H e^{-S}$ with $S = \frac{g}{\omega_0} \sum_i (n_i - 1)(a_i^\dagger - a_i)$. The expression for H_{LF} is

$$H_{\text{LF}} = -v \sum_{\langle i,j \rangle, \sigma} \left[e^{\frac{g}{\omega_0}(a_i^\dagger - a_i)} e^{-\frac{g}{\omega_0}(a_j^\dagger - a_j)} c_{i,\sigma}^\dagger c_{j,\sigma} + \text{H.c.} \right] + U_{\text{eff}} \sum_i n_{i,\uparrow} n_{i,\downarrow} - \mu_{\text{eff}} \sum_i n_i + \omega_0 \sum_i a_i^\dagger a_i. \quad (3.8)$$

We note that c^\dagger , after the LF transformation, creates a polaron (a phonon-dressed electron), since in the original representation it is expressed as $e^{-S} c^\dagger e^S = e^{-\frac{g}{\omega_0}(a^\dagger - a)} c^\dagger$. Up to this point there is no approximation and it is just a unitary transformation. Now we consider the situation when the phonon frequency is very large, hence phonons are not much excited. In this case, we can obtain an effective low-energy model for polarons with a projection onto the subspace of zero phonons, $H_{\text{eff}} = \langle 0 | H_{\text{LF}} | 0 \rangle$, where $|0\rangle$ is the phonon vacuum. Namely, we are thinking of the limit $\omega_0 \rightarrow \infty$ with g/ω_0 and U_{eff} fixed to take the lowest-order perturbation theory. We note that this is a different type of anti-adiabatic limit of the Holstein-Hubbard model from the case mentioned in Eq.3.1 above. The Hamiltonian resulting from the projection is [120]

$$H_{\text{eff}} = -Z_B v \sum_{\langle i,j \rangle, \sigma} (c_{i,\sigma}^\dagger c_{j,\sigma} + \text{H.c.}) + U_{\text{eff}} \sum_i n_{i,\uparrow} n_{i,\downarrow} - \mu_{\text{eff}} \sum_i n_i, \\ Z_B = \exp(-g^2/\omega_0^2). \quad (3.9)$$

Even though this has the form of the usual Hubbard model with the non-retarded interaction U_{eff} , the hopping parameter is renormalized by Z_B unlike the anti-adiabatic limit, Eq. 3.1¹. Since we can evaluate physical quantities of the Hubbard model such as transition temperatures and order parameters with DMFT+CT-QMC, we can evaluate physical quantities of the Holstein-Hubbard model thorough the polaron picture. For example, the transition temperature ($T_c[U, U_{\text{eff}}, Z_B]$) for the Holstein-Hubbard model with U , U_{eff} and Z_B is given by,

$$T_c[U, U_{\text{eff}}, Z_B] \approx Z_B T_c^0[U_{\text{eff}}/Z_B] \\ \equiv T_{c,\text{eff}}[Z_B, U_{\text{eff}}], \quad (3.10)$$

where $T_c^0[U]$ is the transition temperature for the corresponding order in the Hubbard model with the unrenormalized hopping v .

Here we list up several consequences from the polaron description.

1. The boundary of CO and AF in the phase diagram at $T = 0$ is located along $\lambda = U$ and the transition is continuous, Fig. 3.1 (c).
2. At finite temperatures, there exists PM between CO and AF, in particular, at $U_{\text{eff}} = 0$. The boundaries between CO and PM and between AF and PM are continuous. The PM regime shrinks first as we increase U and λ from zero and the region is wider on the $U > \lambda$ side, Fig. 3.1 (f). If U and λ are large, Z_B becomes exponentially small and there emerges a paramagnetic insulating state for small but nonzero U_{eff} .

3.1. HALF-FILLING: COMPETITION BETWEEN ANTIFERROMAGNETISM AND CHARGE ORDER

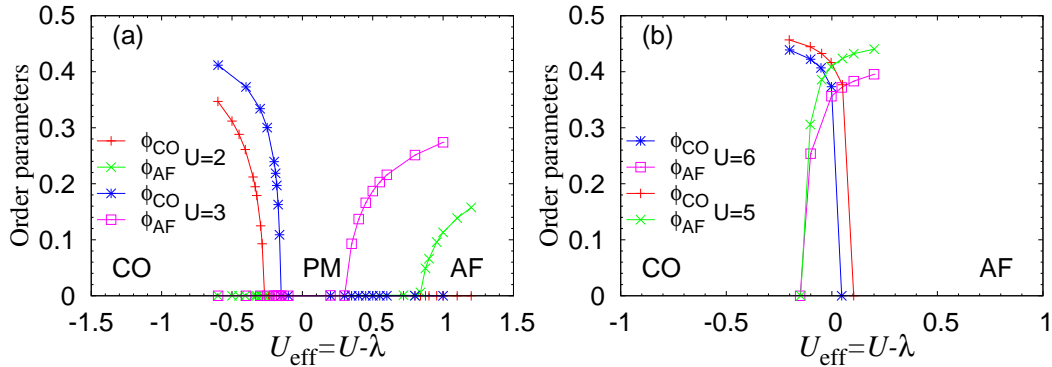


Figure 3.2: Order parameters against $U_{\text{eff}} = U - \lambda$ around $U \sim \lambda$ for a fixed $\omega_0 = 0.6$ at half-filling. In panel (a), the results for $U = 2$ and 3 are shown, while (b) shows the results for $U = 5$ and 6 (both at $\beta = 20$). For smaller U in (a), the charge ordered state (CO) and the antiferromagnetic phase (AF) are separated by a paramagnetic metallic phase (PM).

3.1.3 Phase diagrams

First we have to note that we find no evidence for SC around $U_{\text{eff}} = 0$ within our investigation, although both of competing orders, CO and AF, become weak in this regime. This behavior is consistent with the absence of SC in the ground state, where only CO and AF appear [69, 90]. Hence we focus on the competition between AF and CO hereafter.

In Figure 3.2, we show the behavior of the order parameters around $U_{\text{eff}} = 0$ obtained by varying λ to change U_{eff} for each value of U . Here we fix $\omega_0 = 0.6$ and $\beta = 20$. When the Coulomb interaction U is small ($U = 2, 3$ in Fig. 3.2(a)), there emerges a paramagnetic metallic phase (PM) between the CO and AF phases. The transitions to PM from ordered phases are of second-order, as is evidenced by the continuous disappearance of the order parameter toward the boundary in Fig. 3.2(a). This PM phase has also been pointed out in a QMC analysis of the two-dimensional Holstein-Hubbard model [66]. When the interaction U is stronger ($U = 5, 6$ in Fig. 3.2(b)), there occurs a direct phase transition between CO and AF just around $U_{\text{eff}} = 0$. This transition is of first-order, since the order parameters show a hysteresis around the phase boundary and we find no solution with microscopic mixing of CO and AF. Here hysteresis means that gradual increase and gradual decrease of λ give different DMFT self-consistent solutions. Namely, there is a region around $U_{\text{eff}} = 0$, where both an AF solution and a CO solution of the DMFT equations exist. Beyond this regime one of the CO and AF states becomes unstable, and the iterations around it converge to the other. In order to identify the most stable solution in the hysteretic regime, one needs to compute the free energies, which is beyond the scope of the present study.

From the results for the order parameters, we have obtained the phase boundaries. In Fig. 3.3, we show phase diagrams for different values of the phonon frequency. In Fig. 3.4, we show phase diagrams for a fixed $\omega_0 = 0.2$ at different temperatures. In Fig. 3.5(a), we show a phase diagram on the plane of T and $-U_{\text{eff}}$ in the small U regime to see how the PM phase

¹We note that this effective description is useful for the SC phases themselves when λ , U and ω_0 are comparable to the bandwidth. For details, see Appendix. A.3.

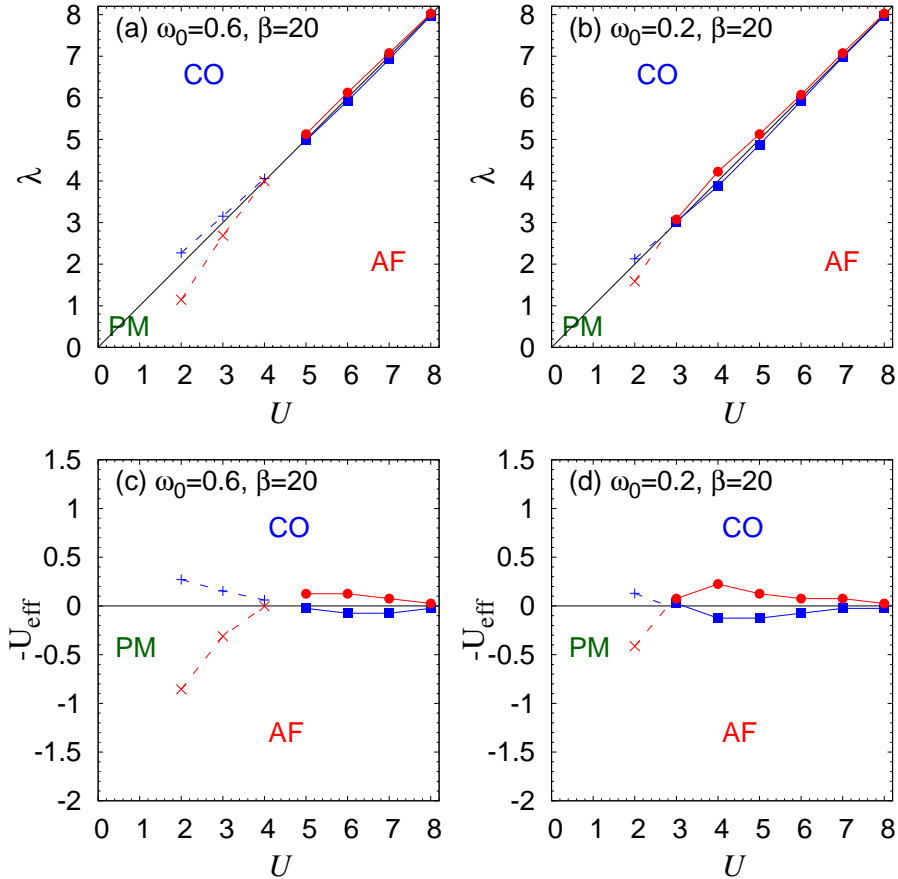


Figure 3.3: (a) (b) Phase diagrams on the U - λ plane at a fixed $\beta = 20$ for $\omega_0 = 0.6$ (a) and $\omega_0 = 0.2$ (b). (c) (d) Phase diagrams on the plane of U and $-U_{\text{eff}}$ for the same conditions. Colored dashed lines represent the boundaries between a paramagnetic phase and ordered phases, which are continuous. Red solid lines show the boundaries of the region where the stable AF solution exists, while blue lines are the boundaries for CO.

shrinks towards $T = 0$.

When both U and λ are small, there is a PM phase around $U_{\text{eff}} = 0$ as pointed out above. This PM region becomes wider as the temperature increases (Fig. 3.4) or ω_0 increases (Fig. 3.3). The latter can be attributed to the cancellation between the instantaneous repulsive interaction and the retarded interaction that tends to become more direct for larger ω_0 . In addition, the PM regime is wider on the $U > \lambda$ side than on the opposite side. As discussed in the previous section, the existence of the PM phase in the small- U and small- λ regime is predicted from all of the three descriptions. Asymmetric development of the PM regime between the $U > \lambda$ side and the $U < \lambda$ side cannot be captured by the Hubbard model, but both the static mean-field and polaron pictures can capture this asymmetry. In the former, this phenomenon comes from asymmetric form of the driving force of AF and CO, i.e. V in Eq. 3.6. On the other hand, in the polaron picture this asymmetry comes from the fact that the band renormalization due to the el-ph coupling is stronger in the $\lambda > U$ regime. We note that, when $|U_{\text{eff}}|$ and $1 - Z_B$

3.1. HALF-FILLING: COMPETITION BETWEEN ANTIFERROMAGNETISM AND CHARGE ORDER

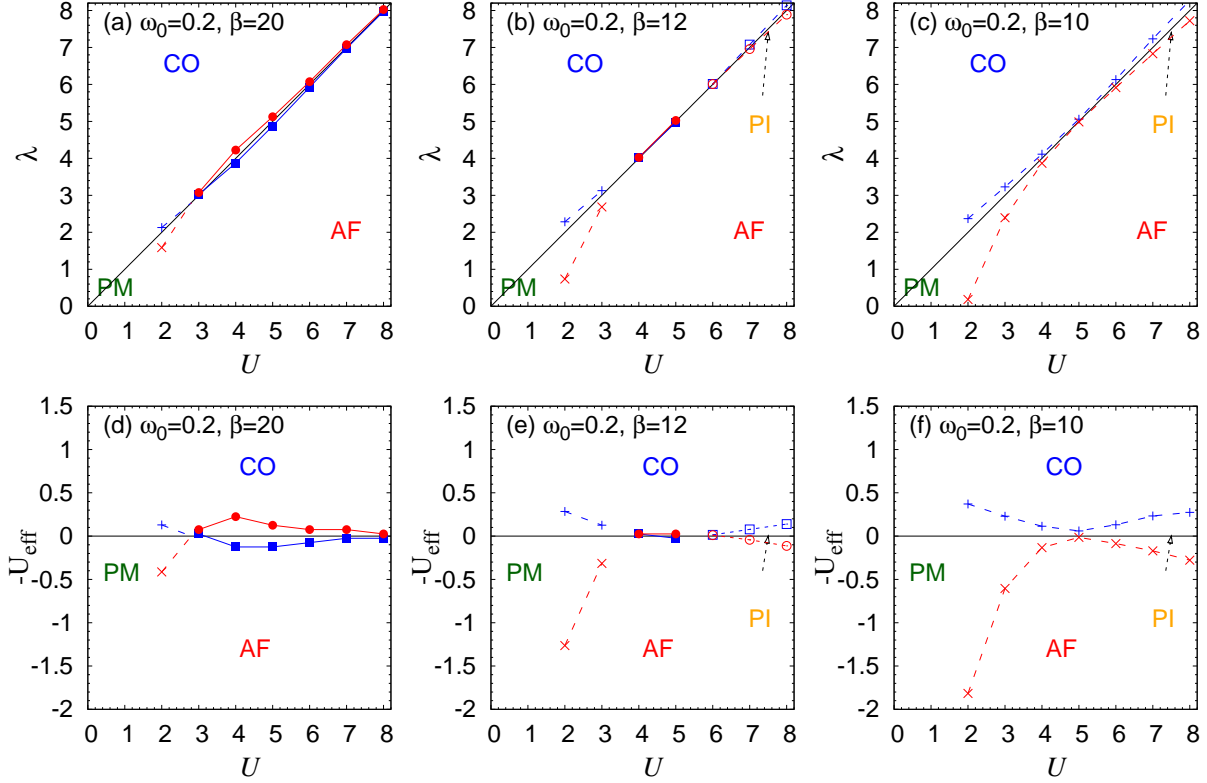


Figure 3.4: (a)(b)(c) Phase diagrams on the U - λ plane for a fixed $\omega_0 = 0.2$ at various temperatures. (d)(e)(f) Phase diagrams on the plane of U and $-U_{\text{eff}}$ for the same conditions. PI stands for a paramagnetic insulating state. Colored dashed lines represent the boundaries between a paramagnetic phase and ordered phases, which are continuous. Solid lines show the boundaries of the region where the stable solution for CO or AF exists. Red lines show the boundaries of AF and blue lines the boundaries for CO.

are small enough, $T_{c,\text{eff}}$ becomes larger with decreasing Z_B because of the downward convex structure of $T_c^0[U]$ against U . While the static mean-field cannot describe the dependence on the phonon frequency, the polaron picture can explain the enhancement of the PM regime as the phonon frequency is increased.

When U and λ take intermediate values, the transition between AF and CO is of first-order and takes place within the hysteretic region, which is shown as the region surrounded by red and blue solid lines in Fig. 3.3 and Fig. 3.4. We note that previous studies [69, 90] show that if U and λ are strong enough there occurs a first-order transition between AF and CO almost at $U \sim \lambda$. Our analysis reveals that the coexistence region of the two stable solutions (AF and CO) remains located around $U \sim \lambda$ at finite temperatures and shrinks as the temperature increases. If one increases the interactions further, the hysteretic region becomes narrower (Fig. 3.3, Fig. 3.4(a)(d)). When U and λ are large, the CO and AF solutions are separated by a paramagnetic insulating (PI) phase (Fig. 3.4(b)(e)). Here, we note that only the static mean-field description can explain the disappearance of the PM phase with increasing U and λ . As for the PI phase, only the polaron picture predicts such a phase around $U_{\text{eff}} = 0$ (but not

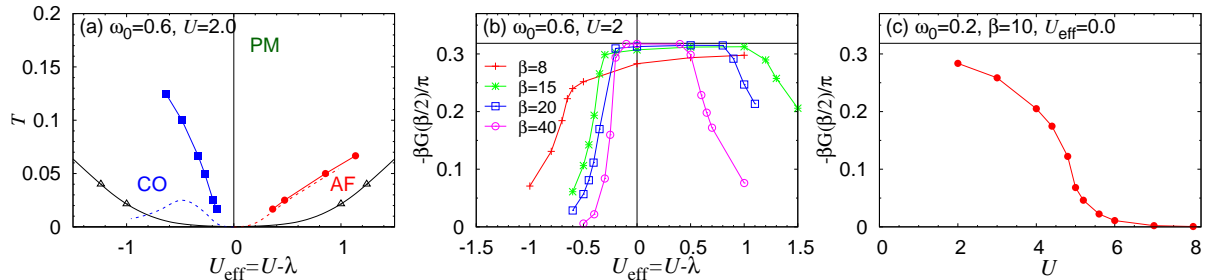


Figure 3.5: (a) Phase diagram for $U = 2$, $\omega_0 = 0.6$ on the plane of U_{eff} and T . Open markers show transition temperatures of the Hubbard model, and the solid black curve is a guide for the eye. Blue and red dashed curves represent transition temperatures predicted from the polaron picture for CO and AF, respectively. (b) $-\frac{\beta}{\pi}G(\tau = \beta/2)$ (an approximate spectral function $A(\omega = 0)$) against U_{eff} at several temperatures with fixed $U = 2$, $\omega_0 = 0.6$. (c) $-\frac{\beta}{\pi}G(\tau = \beta/2)$ against U along $U_{\text{eff}} = 0$ for $\omega_0 = 0.2$, $\beta = 10$. In (b) (c), the black horizontal line indicates the bare density of states, $1/\pi$.

at $U_{\text{eff}} = 0$) when U and λ are large enough. If we further increase the temperature, the direct phase transition between CO and AF vanishes and PM and PI intervene along the $U_{\text{eff}} = 0$ line, Fig. 3.4(c)(f).

Now we study the paramagnetic regime in more detail. Figure 3.5(a) displays the phase diagram on the plane of T and U_{eff} when U and λ are small, which shows how the PM state between AF and CO behaves towards $T = 0$. Previous study of the HH model with DMFT+NRG has pointed out that with a finite phonon frequency there emerges a direct continuous transition between AF and CO when U and λ are both small, and that this is a manifestation of a phenomenon of the Hubbard model (anti-adiabatic limit with λ, U fixed). Here we point out that the polaron picture is also consistent with the continuous phase transition at $T = 0$. When we look at the transition temperatures of CO and AF in Fig. 3.5(a), we find that they rise much faster than the prediction from the Hubbard model as a function of $|U_{\text{eff}}|$. Compared to this, the polaron picture much improves the development of the transition temperature around $U_{\text{eff}} = 0$. In addition, it also shows the asymmetric behavior of CO and AF, where T_c for CO develops faster when λ is changed. These indicate, quantitatively, that the polaron picture is a better description around $U_{\text{eff}} = 0$ in the small U and λ regime. Now we comment on the results of the previous works. In 1D [60,61], it has been claimed that there is an intermediate metallic region between CO and AF in the small U and λ regime. On the other hand, the DMFT+NRG analysis claims that there is no such region in the ground state. Unfortunately, we cannot say anything rigorous about this issue from our results mainly because of the limit in accessible temperatures. At least, our results seem to suggest that a discontinuous direct transition between CO and AF is unlikely to occur at $T \rightarrow 0$ and that the behavior of the ground state should be qualitatively different from that in the stronger-coupling regime. How the possible metallic phase depends on the dimensionality is an interesting open question. The first step would be the confirmation of the existence of the metallic phase suggested in the two dimension [66], and recently developed variational Monte Carlo method for electron-phonon coupled systems would be a promising method [121].

We now study the behavior of the density of states at the Fermi level to discriminate metallic

or insulating behavior of the paramagnetic phases. For this we use the relation between the Green's function on the imaginary axis and the spectral function ($A(\omega) = -(1/\pi)\text{Im}G_{\text{loc}}(\omega)$),

$$G(\tau = \beta/2) = - \int d\omega \frac{1}{2 \cosh(\beta\omega/2)} A(\omega). \quad (3.11)$$

When the temperature is low enough, $1/\cosh(\beta\omega/2)$ has a sharp peak at $\omega = 0$ and the value of $-(\beta/\pi)G(\tau = \beta/2)$ gives a good estimate for the value of the spectral function $A(\omega = 0)$. In Fig. 3.5(b), we show the results for $U = 2$, $\mu = 1$, $\omega_0 = 0.6$ (in the small U and λ regime). There is a significant density of states at the Fermi level in the paramagnetic phase, which indeed indicates a metallic behavior there. The value of $-(\beta/\pi)G(\tau = \beta/2)$ monotonically increases and saturates towards the bare density of state, $\rho_0(\omega = 0) = 1/\pi v$, at low enough temperatures, even though the region of PM itself is strongly suppressed. When U and λ are large, we can only observe a small value of $-(\beta/\pi)G(\tau = \beta/2)$ in the paramagnetic state, which indicates an insulating behavior. In Fig. 3.5(c), we show a crossover between these two regimes along the $U_{\text{eff}} = 0$ line for $\omega_0 = 0.2$, $\beta = 10$, cf Fig. 3.4(c).

3.2 Away from half-filling: Supersolid state in the intermediate-coupling regime

3.2.1 Background: Charge order vs superconductivity

In this section, we turn to focus on the Holstein model and investigate competition of different orders away from half-filling. This model has been studied for a long time [28, 60, 61, 68, 70, 71, 71–74, 79, 111, 112, 122–124]. Before our study it had been pointed out that, at half-filling, CO is favorable, while, away from half-filling, s-wave SC becomes more favorable. We can easily expect this from a weak-coupling picture, since away from half-filling the nesting of the Fermi surface becomes worse, while this is not important for s-wave SC. Now, interesting questions are whether the microscopic coexistence of CO and SC can be realized, in what condition it would be enhanced if any and what the mechanism would be. Even though there is a long history of studies on the Holstein model, answers to these questions had not been well established before our work [27]. In Ref. [60], the authors studied the model in one dimension and showed that there occurs coexistence of quasi-orders of SC and CO, which are characterized by power-law decay of correlations. In two-dimensional cases [71, 72], the authors mainly focused on susceptibilities for SC and CO and do not study the phase boundary in detail. Previous works with DMFT [68, 79, 111, 122, 123] also focused on susceptibilities for SC and CO in normal states to decide the phase boundary between normal phases and ordered phases. In Ref. [124], ordered states were investigated in the strong-coupling limit with a static mean-field theory and existence of a coexisting phase of SC and CO is claimed. However, we note that possibility of a phase separation was not considered in Ref. [124], and it turns out that the coexisting phase pointed out there becomes fragile if the possibility is taken into account.

We note that the present study is related to a wide range of other models and systems. CO is one example of diagonal long-range orders (DLRO), while SC belongs to off-diagonal long-range orders (ODLRO). How these different types of orders compete with each other has been attracting interests in various systems [80–89, 125–130]. In particular, a phase with microscopic coexistence of a charge order and superfluidity (or superconductivity) is named a *supersolid* (SS) phase, and its existence has been investigated in bosonic systems [80–83, 125], typically

liquid helium, but also in boson-fermion mixtures [84] and spin systems [85–89]. In addition, even though types of involved DLRO and ODLRO are different, in unconventional superconductors, the relation between magnetic orders and superconducting phases is often discussed and coexistences of them are reported. For instance, a compound in the iron-based superconductor family, $\text{BaFe}_2(\text{As}_{1-x}\text{P}_x)_2$, exhibits a quantum critical point (QCP) accompanied by a non-Fermi liquid behavior, which separates SC and a phase in which SC and antiferromagnetism (AF) coexist [127].

Motivated by above situations, in this section we operate a systematic investigation of the Holstein model on the Bethe lattice with infinite coordination number employing DMFT with the CT-QMC impurity solver developed in Sec. 2.2. We note that we are focusing on a simplest setup, and we do not impose further complications such as lattice frustrations and long-range interactions, which would favor the SS phase. In the present study, we focus on an intriguing regime where ω_0 is comparable to the electronic bandwidth $W(=4)$. Our main analysis is for $\omega_0 = W(=4)$, but we also discuss dependence on the phonon frequency. We note that this situation ($\omega_0 \sim W$) is realized in carbon-based compounds such as alkali-doped fullerenes [3–7] or the recently found aromatic superconductors [6, 8–12], and hence it is interesting to study this situation. We focus on s-wave SC and staggered (commensurate) CO as possible orders and do not consider incommensurate charge orderings². The order parameters for them are, respectively, $\Phi_{\text{SC}} = \frac{1}{N} \sum_i \langle c_{i\downarrow} c_{i\uparrow} \rangle$ and $\Phi_{\text{CO}} = |n_A - n_B|/4$, where N is the total number of lattice sites, and A and B label sublattices. The phase boundaries are determined from onsets of these order parameters. We also note that, although we focus on $\mu > 0$ (electron doping), phase diagrams for $\mu < 0$ (hole doping) has the same structure because of a symmetry in the Hamiltonian.

3.2.2 Predictions from approximations for the weak-coupling and strong-coupling regimes

Before we show the results of DMFT+CT-QMC, we explain predictions from perturbative approximations in the weak-coupling and strong-coupling regimes. For the weak-coupling regime, we can analyze the Holstein model using diagrammatic approximations. To be more specific, we use the diagrammatic approximations in order to solve the effective impurity problem in the DMFT iteration. In Ref. [68, 111, 123], Freericks et al showed several types of weak-coupling approximations according as how they expand the diagrams for the self-energy of electrons. In our analysis we use the second-order weak-coupling expansion (iterative perturbation theory, IPT) [123], the unrenormalized Migdal approximation (the Hartree-Fock approximation) [68] and the second-order conserving approximation [111]. Since all of these approximations give quantitatively similar results, here we show, as a representative example, the results of IPT, where we expand all the self-energy diagrams including the Hartree term up to second order in λ (fourth order in g) [133], see Appendix. A.2. Figure 3.6 displays the IPT phase diagram on the plane of T and μ for $\omega_0 = 4$, $\lambda = 1.5$ (a) and the variation of $\langle n \rangle$ with μ at $\beta = 80$ (b). Between SC and CO, there is a hysteretic region, where both CO and SC are stable DMFT solutions, and we have found no stable self-consistent SS solution even when we choose the initial input of

²In the iteration process for DMFT, we encountered difficulties in the convergence when ω_0 is smaller than 2 such as $\omega_0 = 1$. There, the solution for consecutive iterations oscillates. Similar behaviors have been reported and attributed to the tendency to ordered phases with longer spatial periods [131, 132]. Conversely, the absence of such a difficulty for $\omega_0 \geq 2$ indicates that a tendency to ordered phase with longer period is small.

3.2. AWAY FROM HALF-FILLING: SUPERSOLID STATE IN THE INTERMEDIATE-COUPLING REGIME

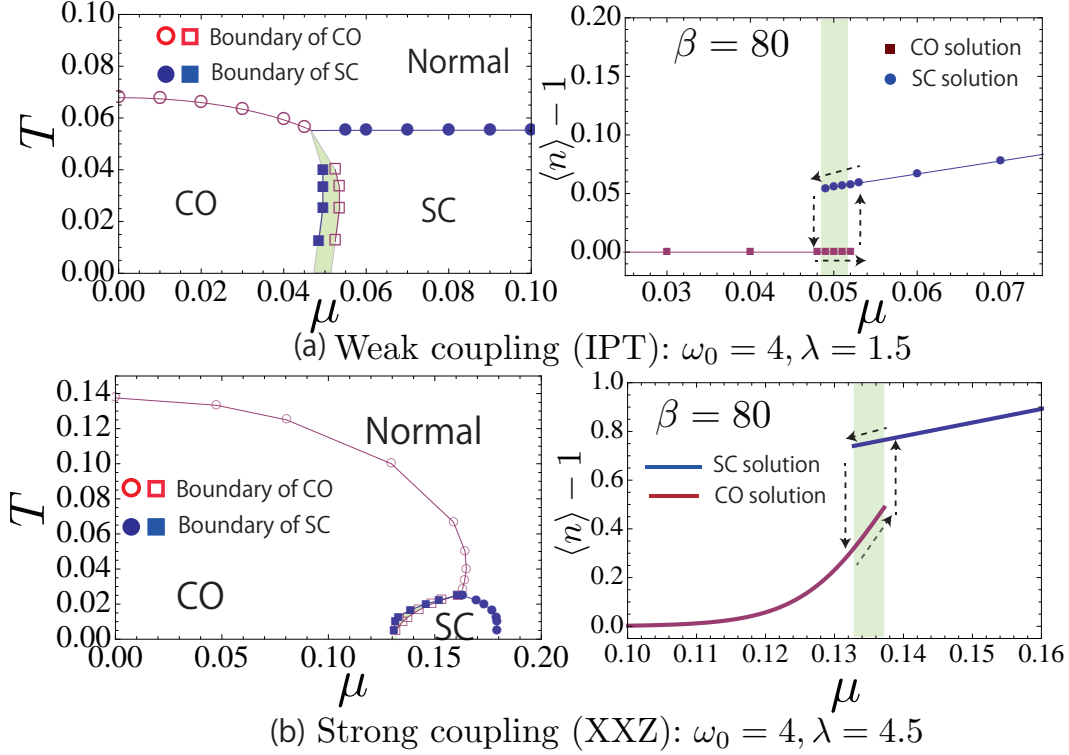


Figure 3.6: (a)(b) Results of IPT + DMFT for $\omega_0 = 4, \lambda = 1.5$. Panel (a) shows the T vs μ phase diagram, and panel (b) the μ -dependence of $\langle n \rangle - 1$ at $\beta = 80$. (c)(d) Results of the static mean-field solution for the leading-order effective spin model [Eq. (3.12)] for $\omega_0 = 4, \lambda = 4.5$. Panel (c) shows the T vs μ phase diagram, and panel (d) the μ -dependence of $\langle n \rangle - 1$ at $\beta = 80$. The green area in each panel indicates a hysteretic region for CO and SC.

the Green's function that includes significant amount of SC and CO. Here, the hysteretic region for the two solutions has been determined in the following manner. For CO, a CO solution is derived by suppressing SC, and we then add a small anomalous part ($\Phi_{\text{SC}} \simeq 0.002$) to see whether it grows or vanishes. For SC, we use the local Green's function for μ as an initial input for $\mu - \delta\mu$ ($\delta\mu = 0.001$ here). Hence these results mean that the phase boundary between SC and CO is of first-order and that a phase separation occurs there. We note that we have checked that the same conclusion holds for even smaller interactions (e.g., $\lambda = 1$) and that the absence of a SS phase is also predicted with the HF approximation and the second-order conserving approximation. These analyses predict that the weak-coupling regime does not accommodate an intervening SS phase. We also note that there are phenomenological arguments for explaining coexistence of different phases [126, 134]. In this theory, when a charge density wave is created, there remains the Fermi surface because of imperfect nesting of the Fermi surface in normal states, and instability to SC of the remaining Fermi surface occurs with decreasing temperature. Since this argument is for the weak-coupling regime, the absence of the coexistence in the weak-coupling regime indicates that this scenario is not applicable to the present situation.

As for the strong-coupling regime, we consider $1/\lambda$ expansions [63, 122]. With a large value of λ , only a bound state of two electrons (a bipolaron) or an empty hole is energetically allowed for

each site. Hence by regarding a state with a bipolaron as $|\uparrow\rangle$ and a state without a bipolaron as $|\downarrow\rangle$, we can map the Holstein model to effective pseudospin models. Here we consider the lowest order in the $1/\lambda$ expansion, where the Holstein model is reduced to an effective (pseudo)spin- $\frac{1}{2}$ XXZ model with only nearest-neighbor exchange interactions [63, 122],

$$H_{\text{xxz}} = -2\mu \sum_i S_i^z - J_{\perp} \sum_{\langle i,j \rangle} (S_i^x S_j^x + S_i^y S_j^y) + J_{\parallel} \sum_{\langle i,j \rangle} S_i^z S_j^z, \quad (3.12)$$

where $\langle \rangle$ indicates the nearest-neighbor and

$$J_{\perp} = 4 \frac{v^2}{\lambda} \sum_{n_i^b, n_j^b=0}^{\infty} \frac{e^{-\frac{2g^2}{\omega_0^2}}}{n_i^b! n_j^b!} \frac{(-g^2/\omega_0^2)^{n_i^b+n_j^b}}{1 + \frac{\omega_0^2}{2g^2} (n_i^b + n_j^b)}, \quad (3.13)$$

$$J_{\parallel} = 4 \frac{v^2}{\lambda} \sum_{n_i^b, n_j^b=0}^{\infty} \frac{e^{-\frac{2g^2}{\omega_0^2}}}{n_i^b! n_j^b!} \frac{(g^2/\omega_0^2)^{n_i^b+n_j^b}}{1 + \frac{\omega_0^2}{2g^2} (n_i^b + n_j^b)}. \quad (3.14)$$

Here $S^+ \equiv S^x + iS^y$ and S^z are regarded as a creation operator of a bipolaron and its density, respectively. We note that in effective pseudospin models, CO, SC and SS correspond to the following situations:

1. CO : $\langle S_A^z \rangle - \langle S_B^z \rangle \neq 0$, $\langle S_A^+ \rangle = 0$, $\langle S_B^+ \rangle = 0$.
2. SC : $\langle S_A^z \rangle - \langle S_B^z \rangle = 0$, $\langle S_A^+ \rangle = \langle S_B^+ \rangle \neq 0$.
3. SS : $\langle S_A^z \rangle - \langle S_B^z \rangle \neq 0$, $\langle S_A^+ \rangle \neq 0$ and/or $\langle S_B^+ \rangle \neq 0$.

In the limit of infinite spatial dimensions ($d \rightarrow \infty$), J_{\perp} and J_{\parallel} scale as $1/d$ since v scales as $1/\sqrt{d}$. Hence the static mean-field treatment for the effective pseudospin model is justified. In Fig. 3.6(c)(d), we show the results of the mean-field analysis. At $T = 0$, there is no extended SS region along μ (an external field in the spin model), and the SC, CO and SS phases become all energetically degenerate just at $\mu_c = (zJ_{\parallel}/4)\sqrt{1 - (J_{\perp}/J_{\parallel})^2}$. Here z is the coordination number. This result is already shown in Ref. [124, 135], and if the phase diagram is plotted against $\langle n \rangle$ this result may seem to indicate existence of a SS phase. However, we have to note that a SS state is only realized at a single point on the μ -axis ($\mu = \mu_c$), hence is expected to be fragile against external perturbations and against the phase separation into SC and CO. At non-zero temperatures, a SS region on the μ -axis vanishes, and there emerges a finite hysteretic region where the solutions always converge to either SC or CO, see the green shaded regimes in Fig. 3.6(a)(b). Hence the lowest-order pseudospin model, Eq. 3.12, predicts a first-order phase transition with no SS phase in the strong-coupling regime.

These analyses indicate that a stable supersolid phase cannot be expected both in the weak-coupling regime and in the strong-coupling regime, so that the SS phase, if any, should be sought in the intermediate-coupling regime.

3.2.3 Supersolid state in the intermediate-coupling regime

Now we show phase diagrams determined with DMFT+CT-QMC. In order to make the discussion clear, we first focus on a specific phonon frequency, $\omega_0 = W (= 4)$, and later we discuss dependence on the phonon frequency.

3.2. AWAY FROM HALF-FILLING: SUPERSOLID STATE IN THE INTERMEDIATE-COUPLING REGIME

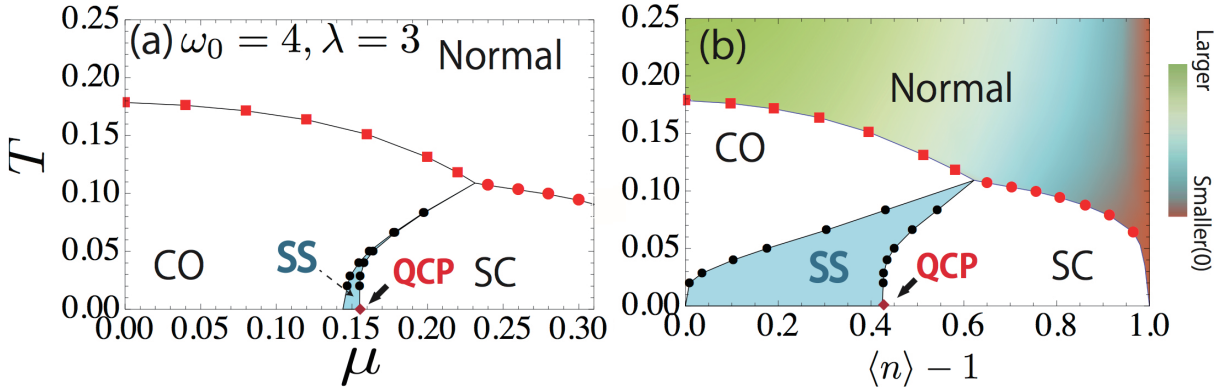


Figure 3.7: A phase diagram of the Holstein model in the intermediate-coupling regime plotted against (a) the chemical potential μ , and (b) the electron band filling $\langle n \rangle$ for $\omega_0 = 4, \lambda = 3$. Blue regions indicate the supersolid (SS) phase, while red diamonds at $T = 0$ denote the quantum critical point (QCP). In the normal state, the dc conductivity is displayed with color coding.

Results at $\omega_0 = 4$

In Fig. 3.7, we show the DMFT+CT-QMC phase diagram away from half filling for $\lambda = 3$ and $\omega_0 = 4$, which is around the peak of the transition temperatures for CO and SC and hence belongs to the intermediate-coupling regime, as discussed later. Panel (a) plots the phase diagram against the chemical potential μ and the temperature T , while panel (b) is against the electron filling $\langle n \rangle$ and T . In both panels, we find an intervening SS region between SC and CO, in which two different types of order parameters, Φ_{SC} (ODLRO) and Φ_{CO} (DLRO), are both nonzero. We note that, in contrast to the predictions from perturbation theories explained in the previous section, this SS phase appears in an extended region even on the μ -axis. Therefore, it should be robust against external field and phase separation into SC and CO. As is discussed below, the phase boundaries of SS/SC and SS/CO are continuous. The SS region widens against both μ and $\langle n \rangle$ with decreasing temperature. When we look at the SS/CO boundary, we find that the SS phase appears at a nonzero value of μ (≈ 0.145) and that this should correspond to $\langle n \rangle = 1$ (half filling), see Fig. 3.7(b). Therefore, the SS phase is expected to show up immediately upon doping at low enough temperatures. As for the SS/SC boundary, since it is continuous at low temperatures, the boundary is expected to end at a quantum critical point (QCP) at $T = 0$. In addition, in the filling range $0.43 \lesssim \langle n \rangle - 1 \lesssim 0.6$, SS changes into pure SC and Z_2 -symmetry (symmetry between sublattices) recovers as temperature is lowered (a reentrant behavior). Hence QCP is characterized by this reentrant behavior around it and SS is located only below CO. We note that this situation is qualitatively different from the phase diagram of $\text{BaFe}_2(\text{As}_{1-x}\text{P}_x)_2$ [127], where the SC+AF phase appears below both SC and AF and there is no reentrant behavior.

In order to closely look at the behavior of the SS region, in Fig. 3.8 we plot the order parameters against μ (panel (a)) and against $\langle n \rangle$ (panel (b)), along with $\langle n \rangle$ vs μ (panel (c)) for $\lambda = 3, \omega_0 = 4$, and $\beta = 35$. As Fig. 3.8(a)(b) indicate, in the SS phase between SC and CO ($0.149 \lesssim \mu \lesssim 0.156$, $0.04 \lesssim \langle n \rangle - 1 \lesssim 0.43$), both Φ_{SC} and Φ_{CO} are indeed nonzero. Panel (c) shows that the compressibility, $\partial n / \partial \mu$, is strongly enhanced but still positive in the SS. Continuous changes of order parameters (Fig. 3.8(a)(b)) and density (Fig. 3.8(c)) indicates that

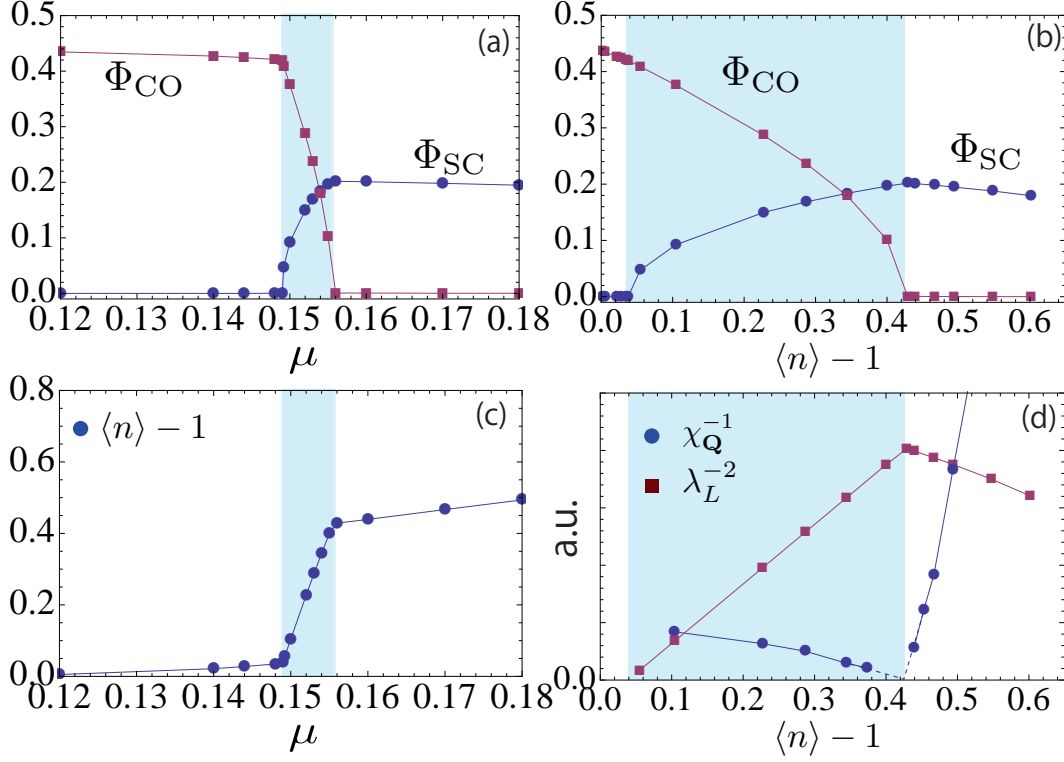


Figure 3.8: SC and CO order parameters against μ (a) and against $\langle n \rangle$ (b). Blue regions indicate the SS phase. (c) Evolution of the filling as a function of μ . (d) Inverse of the static charge susceptibility, $\chi_{\mathbf{Q}}$ at $\mathbf{Q} = (\pi, \pi)$, and the inverse of the squared London penetration depth λ_L , against the electron band filling. The parameters are $\omega_0 = 4, \lambda = 3, \beta = 35$. Dashed lines are extrapolations of the two points closest to the boundary.

the phase boundaries of SS is of second order. This is also supported by the divergence of the static charge susceptibility $\chi_{\mathbf{Q}}$ at $\mathbf{Q} = (\pi, \pi)$. Inverse of this quantity is plotted in Fig. 3.8(d) and we can see that it diverges from both sides like $1/(\langle n \rangle - n_c)$ at the critical value n_c for the SC/SS boundary. Here, susceptibilities are computed by directly applying a small staggered external field $H_{\text{ext}} = \delta\mu(N_A - N_B)$, where $N_{A,B} = \sum_{i \in A,B} n_i$, with a tiny $\delta\mu = 2 \times 10^{-4}$ for SS and $\delta\mu = 5 \times 10^{-4}$ for SC.

Now we discuss how the SS/SC boundary is characterized by the superfluid density. For this, we introduce the expression for the (dc and ac) conductivity, since the superfluid density is characterized by the coefficient of $1/\omega$ component in the imaginary part of the optical conductivity. The conductivity can be expressed as [25]

$$\sigma_{xx}(\omega) = \frac{1}{i\omega} \left[\chi_{J_x, J_x}(\omega) - \sum_{\mathbf{k}, \sigma} e^2 \frac{\partial^2 \epsilon(\mathbf{k})}{\partial k_x^2} \langle c_{\mathbf{k}, \sigma}^\dagger c_{\mathbf{k}, \sigma} \rangle \right]. \quad (3.15)$$

Here χ_{J_x, J_x} is the current-current correlation function for a certain direction, which we denote as x , e is the elementary charge and the lattice constant is set to unity. In order to evaluate this quantity on the Bethe lattice, we adopt the formulas for the d -dimensional hypercubic lattice

3.2. AWAY FROM HALF-FILLING: SUPERSOLID STATE IN THE INTERMEDIATE-COUPPLING REGIME

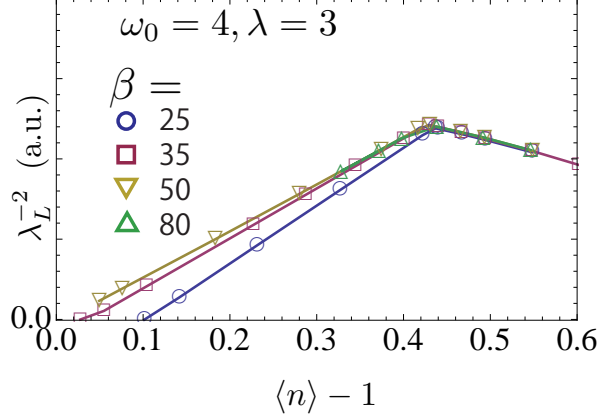


Figure 3.9: Temperature dependence of λ_L^{-2} for $\omega_0 = 4, \lambda = 3$ around the boundary of SC and SS.

and substitute a semi-circular density of states as in Ref. [136]. By extending Ref. [136], we obtain the general expression for χ_{J_x, J_x} applicable to normal, CO, SC and SS states,

$$\begin{aligned} \chi_{J_x, J_x}(i\nu_m) = & \\ & - \frac{e^2}{\beta} \sum_{\omega_n, \alpha, \alpha'} \int d\epsilon \Phi_{x,x}(\epsilon) \left[G_{\mathbf{0}}^{\alpha', \alpha}(\epsilon, i\omega_n) G_{\mathbf{0}}^{\alpha, \alpha'}(\epsilon, i\omega_n + i\nu_m) \right. \\ & \left. - G_{\mathbf{Q}}^{\alpha', \alpha}(\epsilon, i\omega_n) G_{\mathbf{Q}}^{\alpha, \alpha'}(-\epsilon, i\omega_n + i\nu_m) \right]. \end{aligned} \quad (3.16)$$

Here $\omega_n = \frac{\pi}{\beta}(2n + 1)$, $\nu_m = \frac{\pi}{\beta}2m$, $\Phi_{x,x}(\epsilon) \equiv \sum_{\mathbf{k}} (\partial \epsilon_{\mathbf{k}} / \partial k_x)^2 \delta(\epsilon - \epsilon_{\mathbf{k}})$, $\epsilon_{\mathbf{k}}$ is the energy of a free electron with momentum \mathbf{k} , $G_{\mathbf{q}}^{\alpha, \alpha'}(\epsilon_{\mathbf{k}}, i\omega_n) = -\int_0^\beta \langle T_\tau c_{\mathbf{k}, \alpha}(\tau) c_{\mathbf{k}+\mathbf{q}, \alpha'}^\dagger(0) \rangle e^{i\omega_n \tau}$ with $\alpha, \alpha' = \uparrow, \downarrow$. We note that the vertex correction vanishes due to the parity symmetry within DMFT. For the Bethe lattice $\Phi_{x,x}(\epsilon) = (N/3d)[(W/2)^2 - \epsilon^2] \rho_0(\epsilon)$ [136], where N is the system size and $2d$ the coordination number.

As for the superfluid density, it is proportional to [137]

$$\lambda_L^{-2} = - \frac{c^2}{4\pi N} \left[\chi_{J_x, J_x}(i0^+) - e^2 \sum_{\mathbf{k}, \sigma} \frac{\partial^2 \epsilon(\mathbf{k})}{\partial k_x^2} \langle c_{\mathbf{k}, \sigma}^\dagger c_{\mathbf{k}, \sigma} \rangle \right], \quad (3.17)$$

where λ_L represents the London penetration depth, and c is the speed of light. In order to evaluate this quantity, we use a relation, $\sum_{\mathbf{k}} (\partial^2 \epsilon_{\mathbf{k}} / \partial k_x^2) \delta(\epsilon - \epsilon_{\mathbf{k}}) = d\Phi_{x,x}(\epsilon)/d\epsilon$. We note that $\chi_{J_x, J_x}(i0^+)$ can be evaluated from Eq. 3.16 with $\nu_m = 0$.

In Fig. 3.8(d), we show the behavior of λ_L^{-2} in the SC and SS phases for $\omega_0 = 4$, $\lambda = 3$, $\beta = 35$. λ_L^{-2} shows a kink (maximum) at the boundary of SC and SS. Figure 3.9 illustrates temperature dependence of λ_L^{-2} for $\omega_0 = 4$, $\lambda = 3$. A kink (maximum) in λ_L^{-2} at the boundary of SC and SS shows up for all the temperatures investigated, and there is no significant temperature dependence around the boundary of SC and SS at temperatures lower than $T = 1/\beta = 1/50$ (Fig. 3.9). This observation suggests that the kink (maximum) is a characteristic feature of the phase boundary of SC and SS at low temperatures, including the $T = 0$, i.e. QCP, in the present model.

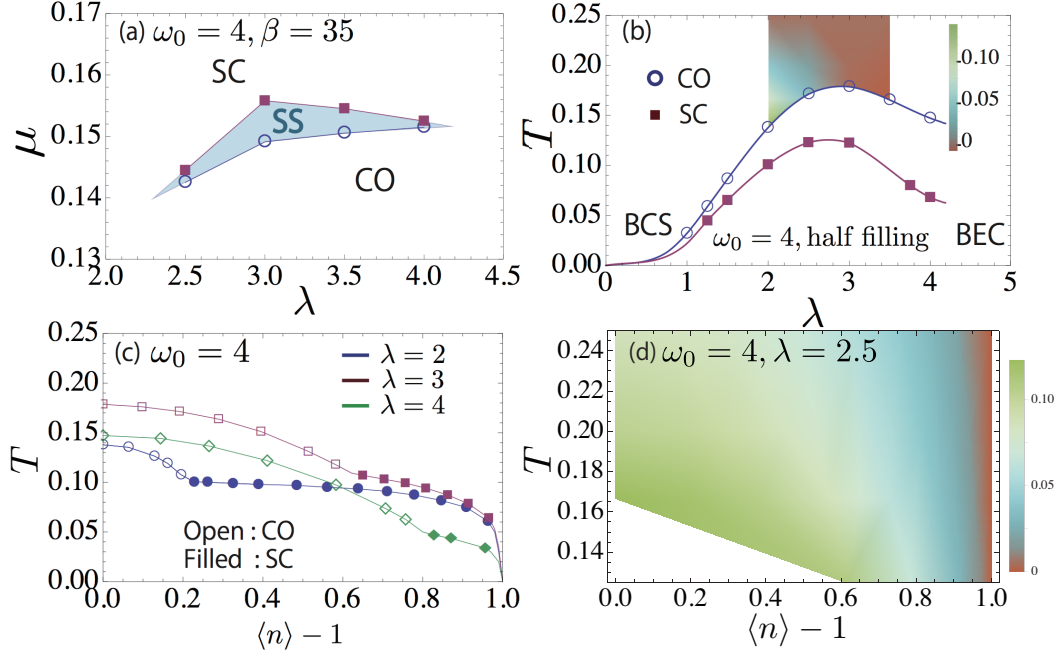


Figure 3.10: (a) $\lambda - \mu$ phase diagram (μ : chemical potential, λ : phonon-mediated attraction) for the SS region for $\omega_0 = 4, \beta = 35$. (b) Transition temperatures for CO and SC against λ at half filling for $\omega_0 = 4$. CO is suppressed to obtain the T_c for SC. In the normal state, the dc conductivity (difference from its value at $T = 0.25$ for each λ) is shown with color coding. (c) Transition temperatures for CO and SC as a function of filling for $\omega_0 = 4$ without any restriction on the type of order. (d) Color-coded dc conductivity in the normal state for $\omega_0 = 4, \lambda = 2.5$.

Now an important question is where the stable SS phase exists. Fig. 3.10(a) displays the region of the SS phase on the plane of μ and the phonon-induced attractive interaction λ for $\omega_0 = 4, \beta = 35$. The SS region is widest around $\lambda = 3$. On the other hand, we find no SS phase for $\lambda = 2$ nor for $\lambda = 4.5$, where a first-order transition (i.e., phase separation) occurs between SC and CO. The absence of the SS phase in the weak-coupling and strong-coupling regimes is consistent with the predictions from the perturbation theories discussed in the previous section. Now we point out that the SS phase with an associated QCP emerges in the intermediate-coupling regime characterized by the peak in the T_c dome. In Fig. 3.10(b) we show the λ -dependence of the transition temperatures for SC and CO at half filling, both of which show peaks around $\lambda \simeq 3$. In Fig. 3.10(c) we plot the transition temperatures against the electron band filling for $\lambda = 2, 3$ and 4 . We can see that $\lambda = 3$ has indeed the highest transition temperatures for both SC and CO among the three values of λ , independent of filling. Hence the SS phase develops below the T_c dome of ordered phases (see Fig. 3.10(a)(b)(c)). In addition to this, we also point out that a metal-insulator crossover occurs in the normal phase as one changes λ around this intermediate-coupling ($\lambda \sim 3$). Here we employ a criterion for a metallic and insulating phases, where the former phase is characterized by decrease of the dc conductivity with increasing temperature and in the latter phase the situation is opposite. The dc conductivity in normal states is expressed as $\text{Re } \sigma(0) = -\lim_{\nu \rightarrow 0^+} [\chi_{J_x, J_x}(i\nu) - \chi_{J_x, J_x}(i0^+)]/\nu$. In order to evaluate this quantity from information on the Matsubara axis, we interpolate $\chi_{J_x, J_x}(i\nu_n)$ for $n = 0, 1, \dots$

3.2. AWAY FROM HALF-FILLING: SUPERSOLID STATE IN THE INTERMEDIATE-COUPPLING REGIME

with polynomials of second-order, third-order or Pade approximations. Since quantitatively all give the same conclusion about whether the phase is metallic or insulating, we show the results of the second-order interpolation here. The resultant dc conductivities are shown in Fig. 3.7(b) and Fig. 3.10 (b)(d). Figure 3.7(b) illustrates that the dc conductivity ($\text{Re}\sigma(0)$) increases with temperature for $\lambda = 3$. Therefore, normal states are insulating in the whole doping range. On the other hand, it turns out that normal states for $\lambda = 2.5$ is metallic as is shown in Fig. 3.10 (b)(d). Hence we can conclude that a metal-insulator crossover occurs between $\lambda = 2.5$ and $\lambda = 3$ for $\omega_0 = 4$, independent of doping. We note that the SS region, the peak of the T_c dome and the metal-insulator crossover point all shift in a correlated manner when ω_0 is varied as will be shown later. Therefore, our finding that all these three occur at almost the same coupling regime is not limited to the present choice of ω_0 .

Now we explain the origin of the stable SS phase in the intermediate regime with the strong-coupling expansion, i.e. the bipolaron picture. We note that the lowest-order expansion, Eq. 3.12, cannot explain the stable SS phase even when it is applied to the intermediate-coupling regime. At $T = 0$, as we explained in the previous section, the phase transition between SC and CO occurs at $\mu = (zJ_{\parallel}/4)\sqrt{1 - (J_{\perp}/J_{\parallel})^2}$, where all of SC, CO and SS are energetically degenerated, see the dashed line Fig. 3.11(b). For $T > 0$, the absence of SS is numerically checked. On the other hand, when we consider higher-order processes than in Eq. 3.12, we can obtain long-range exchange interactions. Here we argue that these long-range exchange interactions are responsible for the SS phase. In order to see this, we expand the Holstein model on the Bethe lattice up to fourth-order in $1/\lambda$ [122] to obtain additional terms for Eq. 3.12,

$$H'_{\text{xxz}} = J'_{\perp} \sum_{\langle\langle i,j \rangle\rangle} (S_i^x S_j^x + S_i^y S_j^y) + J'_{\parallel} \sum_{\langle\langle i,j \rangle\rangle} S_i^z S_j^z, \quad (3.18)$$

where $\langle\langle \rangle\rangle$ denotes the next-nearest neighbor sites. In addition, there are some correction to the nearest neighbor exchange interactions in Eq. 3.12. The expression for these terms are described in Appendix A.2. Results for a numerical evaluation is shown in Fig. 3.11(a), which tells that J'_{\perp} and J'_{\parallel} develop as we move from the strong-coupling regime to the intermediate-coupling regime. More importantly, J'_{\perp} and J'_{\parallel} are negative and positive, respectively. Intuitively, the J'_{\perp} term enables bipolarons to move around on the A sublattice while avoiding those on the B sublattice forming a CO pattern, thus establishing a phase coherence within the less occupied sublattice in the CO background, see Fig. 3.11(c). We note that negative value of J'_{\perp} is necessary to keep the same phase within the same sublattice ($\langle S_i^+ \rangle = \langle S_j^+ \rangle$ for $i, j \in A$). Since $z'J'_{\perp}$ and $z'J'_{\parallel}$ are constant in the infinite-dimensional limit (z' is the coordination number of the next-nearest neighbor sites), it is justified to use the static mean-field analysis to study this model [125]. For the mean-field theory, we define

$$J_0 = zJ_{\parallel}, \quad J_1 = zJ_{\perp}, \quad J'_0 = z'J'_{\parallel}, \quad J'_1 = z'J'_{\perp}, \quad (3.19)$$

where z is the coordination number of the nearest-neighbor sites and $z' = z^2$ for the Bethe lattice. The mean-field analysis amounts to considering the variational wavefunction,

$$|\Psi\rangle = \bigotimes_{i_A \in A} |A\rangle_{i_A} \bigotimes_{i_B \in B} |B\rangle_{i_B}, \quad (3.20)$$

$$|A\rangle = \cos(\theta_{\alpha}/2)|\uparrow\rangle + \sin(\theta_{\alpha}/2)|\downarrow\rangle, \quad (3.21)$$

$$|B\rangle = \cos(\theta_{\beta}/2)|\uparrow\rangle + \sin(\theta_{\beta}/2)|\downarrow\rangle. \quad (3.22)$$

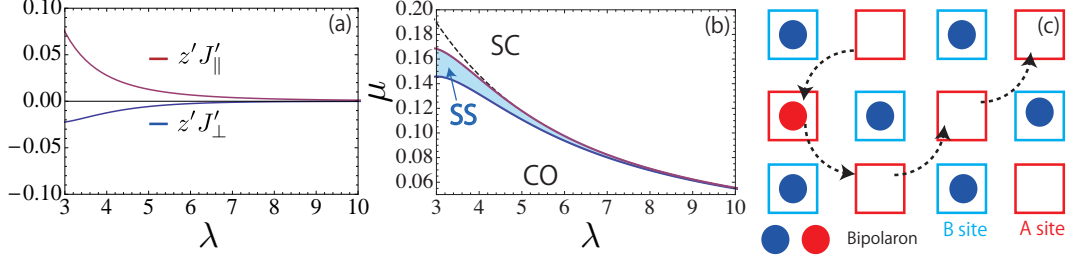


Figure 3.11: (a) shows the dependence of the next-nearest neighbor exchange interaction on λ . (b) The phase diagram at $T = 0$ of the fourth-order effective spin model. The blue region represents the supersolid state, and the dashed line the phase boundary of SC and CO in the leading-order effective spin model. (c) Schematic picture of the motion of bipolarons (circles) on the A sublattice (red squares) with those on the B sublattice (blue) forming a CO pattern. Dotted arrows represent next-nearest neighbor hoppings arising from the higher-order terms in the effective spin model.

To obtain the mean-field ground state, we need to find θ_α and θ_β that minimize the energy,

$$E = \langle H_{\text{xxz}} + H'_{\text{xxz}} \rangle / N = \frac{J'_1}{8} + \frac{1}{8} \times [-2B(\cos \theta_\alpha + \cos \theta_\beta) - J_1 \sin \theta_\alpha \sin \theta_\beta + J_0 \cos \theta_\alpha \cos \theta_\beta + \frac{J'}{2}(\cos^2 \theta_\alpha + \cos^2 \theta_\beta)], \quad (3.23)$$

where $J' = J'_0 - J'_1$. From this expression we can see that the effect of the J'_\parallel term can be translated to that of a J'_\perp term with $J'_\perp = -J'_\parallel$. Hence both of $J'_\perp (< 0)$ and $J'_\parallel (> 0)$ cooperatively stabilize the SS phase in the intermediate-coupling regime, where these terms become significant.

As shown in Fig. 3.11(b), the resultant mean-field phase diagram for the fourth-order effective pseudo-spin model indeed exhibits a SS region that widens toward the intermediate-coupling regime. We note that the position of the SS region agrees well with that estimated from the result for finite temperatures with DMFT+CT-QMC ($\lambda = 3, \omega_0 = 4$), although the effective model overestimates the size of the region. From these arguments, we conclude that the stable SS phase in the intermediate-coupling regime is attributed to the long-range hopping (J'_\perp) and interaction (J'_\parallel) of bipolarons from high-order processes, which become significant in the intermediate-coupling regime.

Dependence of phase diagrams on the phonon frequency ω_0

Now we discuss the effect of the phonon frequency ω_0 on phase diagrams. First we show what happens for a phonon frequency smaller than the electron bandwidth, i.e. $\omega_0 < W = 4$. In Fig. 3.12, we show phase diagrams for $\omega_0 = 2$. The panel (a) plots transition temperatures of CO and SC at half-filling, where we suppress CO to obtain SC, see Appendix. A.3. We can see that the positions of the peaks of the T_c domes for both CO and SC move to smaller values of λ as we decrease ω_0 . We note that the peaks are around $\lambda = 2.5$ for $\omega_0 = 2$, while for $\omega_0 = 4$ they are around $\lambda = 3$. In Fig. 3.12(a), we also display the dc conductivity in normal states, which reveals that the metal-insulator crossover occurs at some point between $\lambda = 2.25$ and $\lambda = 2.5$. Thus, the position of the metal-insulator crossover also shifts to smaller λ and sticks around the shifted peaks of the T_c domes. Concomitantly the SS region shifts to smaller λ , as

3.2. AWAY FROM HALF-FILLING: SUPERSOLID STATE IN THE INTERMEDIATE-COUPLING REGIME

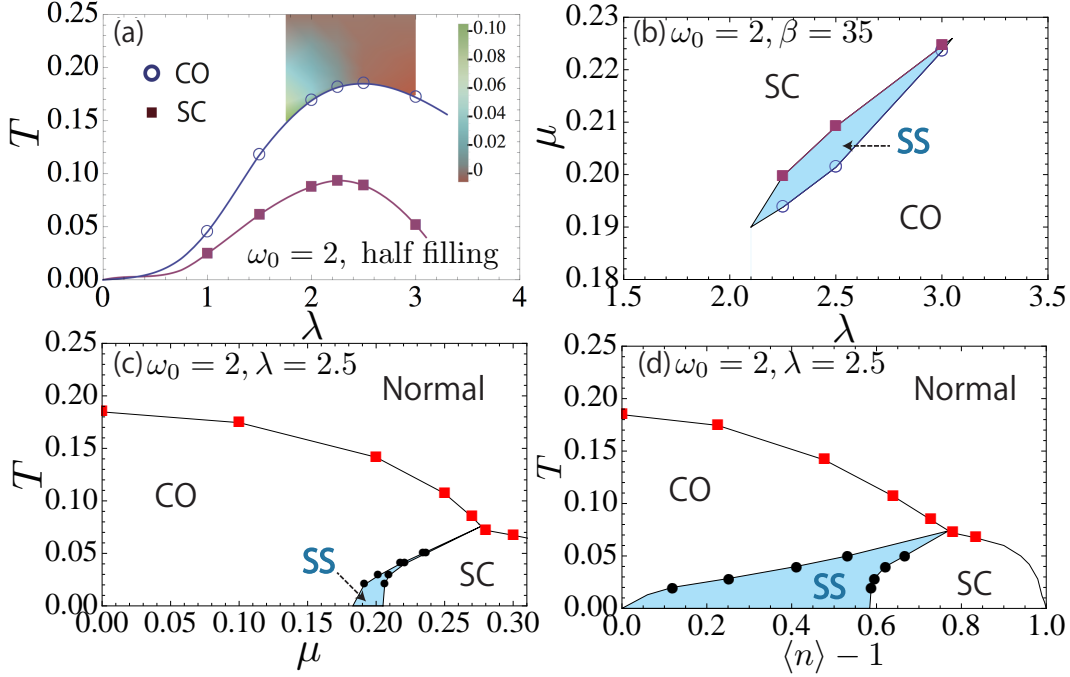


Figure 3.12: For a smaller $\omega_0 = 2$, (a) Transition temperatures for CO and SC against λ at half filling. Here the T_c for SC is obtained by suppressing CO. In the normal state, the dc conductivity (difference from its value at $T = 0.25$ for each λ) is shown by color coding. (b) $\lambda - \mu$ phase diagram for the SS region for $\omega_0 = 2, \beta = 35$. (c,d) Phase diagram of the Holstein model plotted against (c) the chemical potential μ , and (d) the band filling $\langle n \rangle$ for $\omega_0 = 2, \lambda = 2.5$. Blue areas indicate the supersolid (SS) region.

shown in Fig. 3.12(b) which describes the SS region on the plane of λ and μ for $\omega_0 = 2, \beta = 35$. We note that the SS region becomes widest at $\lambda = 2.5$ and disappears around $\lambda = 2$ for this set of parameter (cf Fig. 3.10 for $\omega_0 = 4, \beta = 35$). Hence we can see from these results that as we change ω_0 , the SS phase, the peak of the T_c dome and the metal-insulator crossover all move in a correlated manner.

We also argue that the characteristic features discussed in the previous section for the phase diagram of the Holstein model in the intermediate-coupling regime are robust against the change of the phonon frequency. Figures 3.12(c) and (d) illustrate the phase diagrams on the plain of μ - T (c) and $\langle n \rangle$ - T (d), respectively, for $\lambda = 2.5$ as representing phase diagrams in the intermediate-coupling regime for $\omega_0 = 2$. The SS region becomes wider as we decrease temperature, and the phase transition of SS is continuous, which suggests the existence of a QCP between SC and SS at $T = 0$. Moreover, we note that the characteristic reentrant behavior around the QCP is also observed. Here we note again, as we have explained in the introduction of this section, that we encounter non-converging oscillations in the DMFT self-consistency iteration loop for an even smaller ω_0 than $W/2$ such as $\omega_0 = 1$. Similar behaviors have also been observed in previous works and interpreted as tendency to ordered states with longer spatial periods (including incommensurate ones) [131, 132], which we do not consider here. We consider that this tendency is also the reason here, but study of such phases is beyond the

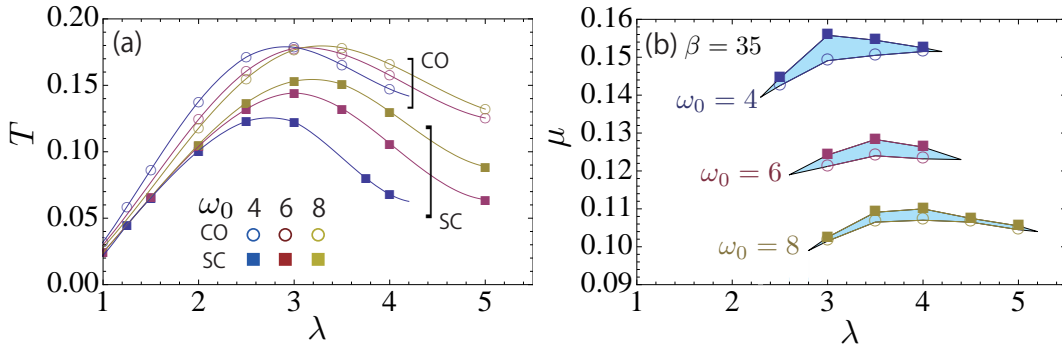


Figure 3.13: (a) Transition temperatures for CO and SC against λ for various values of ω_0 at half-filling. (b) λ vs μ phase diagram for the SS region (shaded) at $\beta = 35$ for various values of ω_0 .

present scope.

Next we discuss phase diagrams for $\omega_0 \geq W = 4$. In Fig. 3.13(a), we show transition temperatures for CO and SC at half-filling for various values of $\omega_0 \geq 4$. The position of the peak of the dome shifts to larger λ with increasing the phonon frequency. In Fig. 3.13(b), we show the SS region on the plane of λ and μ for various values of ω_0 . The location of the SS phase also moves to the larger λ side and sticks around the position of the T_c dome³. Moreover, the position of the SS phase on the chemical potential (μ) axis shifts to smaller μ with increasing ω_0 , while its width along μ gradually decreases. These behaviors are consistent with what is expected from the attractive Hubbard model ($\omega_0 \rightarrow \infty$), where the degeneracy among CO, SC and SS is lifted for nonzero μ and finite doping favors SC [138, 139].

3.3 Summary of the chapter

In this chapter, we have studied the competition between different orders in the Holstein and Holstein-Hubbard models on the Bethe lattice, which is a bipartite lattice and is not frustrated, using DMFT with the CT-QMC impurity solver, which is newly developed in Sec. 2.2 to deal with SC, CO and AF at the same time.

In the former half of this chapter, Sec. 3.1, we have investigated the half-filled Holstein-Hubbard model at $T > 0$ around $U_{\text{eff}} = 0$, allowing the system to have SC, AF and CO orders. A PM phase appears between CO and AF when U and λ are small, and a PI phase when U and λ are large. On the other hand, in the intermediate regime, the transition between CO and AF is direct and discontinuous, and a hysteresis region of AF and CO is located just around $U_{\text{eff}} = 0$ even at non-zero temperatures. We have also clarified reliability of three different simplified descriptions for the Holstein-Hubbard model.

In the latter half of this chapter, Sec. 3.2, we have investigated competition between CO and SC in the Holstein model away from half filling. We have focused on the unconventional region where ω_0 and λ are comparable to the electron bandwidth W . We have revealed that the intermediate-coupling regime characterized by the peak of the T_c dome and the metal-insulator

³The end points of the SS region (shaded area) in Fig. 3.13 have been established numerically, except for the end point on the low- λ side for $\omega_0 = 8$, where DMFT calculations for $\lambda = 2.5$ converge very slowly. As for the other end points of the SS regime, we have checked the absence of SS at $(\lambda, \omega_0) = (5.5, 8), (4.5, 6)$ and $(2.5, 6)$.

3.3. SUMMARY OF THE CHAPTER

crossover is favorable for a stable SS phase and an associated QCP. Conversely, the observed absence of SS in the weak- and strong-coupling regimes is consistent with simple perturbative analyses. As characteristic behaviors of the SS phase and the associated QCP, we have found a downward kink in the London penetration depth (\propto (superfluid density)^{-0.5}) between the continuous SC/SS transition and the reentrant behavior (lower symmetry with increasing temperature) around the QCP. The stable SS phase is attributed to long-range exchange interactions from high-order processes in the bipolaron picture. Since some of carbon-based compounds belong to the unconventional parameter regime considered here, we consider that these materials are potential candidates for application of the present discussion. Further more, it has been reported that Ba(Bi,Pb)O₃ and (Ba,K)BiO₃ can accommodate a coexistence of *s*-wave SC and CO [126]. We note that these compounds are known to be represented well by the Holstein model. They have relatively large phonon energies compared to other phonon-mediated superconductors even though the phonon frequencies are still not comparable to the electron band width, and the strength of the el-ph coupling is estimated to be strong ($\lambda_{\text{eff}} \sim 1.0$) [140, 141]. Hence the present study might be related to the emergence of the coexistence, which we need to clarify in future. We also note that coexisting states in various superconductors [126, 127, 130] show different behaviors, and it would be important to clarify their relation to types of orders involved, which is another future problem.

Chapter 4

Dynamical properties of the Holstein model

In this chapter, we investigate dynamical properties of the Holstein model using the framework of the non-equilibrium DMFT. In Sec. 4.1, we focus on normal states and study their dynamics after a sudden change of a parameter of the system (a quench problem). There we find a qualitative change of the relaxation process as the el-ph coupling is varied. In Sec. 4.2, we apply the method to study collective amplitude modes in strongly-coupled phonon-mediated superconductors. There we discuss similarities and differences from the BCS predictions and effects of phonon dynamics on the amplitude Higgs mode. We also reveal that there exists a new collective amplitude mode, which involves phonon dynamics as well as electron-mediated phonon-phonon interaction.

4.1 Thermalization crossover in normal states

4.1.1 Background: Feedback effects of phonon dynamics on non-equilibrium dynamics

The purpose of this section is to study relaxation dynamics of electron-phonon systems beyond conventional approaches that are based on the Boltzmann equation [142–144], where the time scale of the dynamics is restricted from the gradient approximation used there. The non-equilibrium dynamics of el-ph systems beyond the Boltzmann equation has been studied recently with various methods. Time-dependent exact diagonalization (ED) method and DMFT have been applied to study the dynamics of one or two polarons in the Holstein model [91–94]. As for many-electron problems, previous works have investigated systems with classical phonons [145] or quantum phonons [146] in one-dimension. For two-dimensional system, an ED analysis for the Holstein-Hubbard model [95] and weak-coupling perturbation analysis for the Holstein model with phonons fixed in equilibrium [96–98] have been done so far. For higher dimensions, there have been analyses using the framework of DMFT for the insulating cases [101, 102].

Despite these advances, studies treating dynamics of quantum phonons in many-electron systems are mostly limited to cases in or near the Mott insulating phase [95, 101, 102, 146]. Hence this section is devoted to understand non-equilibrium dynamics in the complementary regime, i.e. the weakly to moderately correlated metallic regime. Our interests are effects of the phonon dynamics and the retarded interaction on the dynamics. We again note that

the relaxation dynamics without phonon dynamics beyond the Boltzmann equation has been recently investigated by Sentef et al [96–98]. Their assumption is that phonons coupled to electrons stay in equilibrium due to some coupling to other degrees of freedom. However if such a coupling is not strong enough (as in an isolated system), the electron degrees of freedom should be affected by feedback from non-equilibrium dynamics of phonons. In addition, phonon degrees of freedom should relax towards its equilibrium through the el-ph coupling. We want to understand consequence of the phonon dynamics and clarify the difference from the picture used in previous works [96–98]. Moreover, it is interesting to understand the difference from the phenomena observed in the Hubbard model, which only includes electrons. One important question in this context is whether or not the so-called prethermalization phenomena [109, 110, 147, 148] and dynamical phase transitions [109, 110, 149–151] occur in electron-phonon systems.

To address the above issues, we focus on the quench problem of the half-filled Holstein model, i.e. a sudden change of the electron-phonon coupling from $g = 0$ at $t = 0$ to $g_f \neq 0$ at $t = 0_+$, and we investigate subsequent relaxation processes. The system is initially set to be noninteracting and in equilibrium at $T = 0$, and we do not consider any broken symmetry. Even though the setup seems a bit artificial, it can be realized in cold-atom systems in optical lattices [152–155], and expected to be closely related to the phonon frequency quench, which has been studied experimentally in bismuth [156]. As an impurity solver for non-equilibrium DMFT we mainly employ the self-consistent Migdal approximation, which is justified when the phonon frequency is small compared to the electron bandwidth. As we discussed in Sec. 2.3.5, this approximation is a conserving approximation, includes the feedback from the phonon dynamics and gives a better description of equilibrium states than the unrenormalized Migdal approximation used in previous papers [96–98].

At the end of this section, we shall compare the results of the self-consistent Migdal approximation with those of the unrenormalized Migdal approximation to clarify the effect of the feedback from the phonon dynamics. It turns out that the latter gives a totally different relaxation dynamics than the self-consistent one and that phonons effectively act as a thermal bath in the unrenormalized Migdal approximation. Before we proceed, let us mention about the choice of parameters. In this section, we use a relatively high phonon frequency, $\omega_0 = 0.7$, because of the limit of the computational time and the memory of the machine used. However, it is still small compared to the electron bandwidth $W = 4$, and hence we consider that results discussed here with the self-consistent Migdal approximation should be qualitatively correct and the discussions involved are applicable to lower phonon frequencies. Indeed, we have checked that choice of lower phonon frequencies such as $\omega_0 = 0.4, 0.2$ gives qualitatively the same results and discussions involved do not change, although the study for these cases is less systematic since the calculation is more demanding. The results discussed in this section has been published in Ref. [30].

4.1.2 Interaction quench: Results of DMFT + self-consistent Migdal approximation

Since we consider isolated systems, the total energy is conserved after a quench. Hence if the system becomes thermalized, the temperature of the system T_{th} should satisfy the relation

$$E_{\text{tot}}(t > 0) = \frac{\text{Tr}e^{-\mathcal{H}_f/T_{\text{th}}}\mathcal{H}_f}{\text{Tr}e^{-\mathcal{H}_f/T_{\text{th}}}}, \quad (4.1)$$

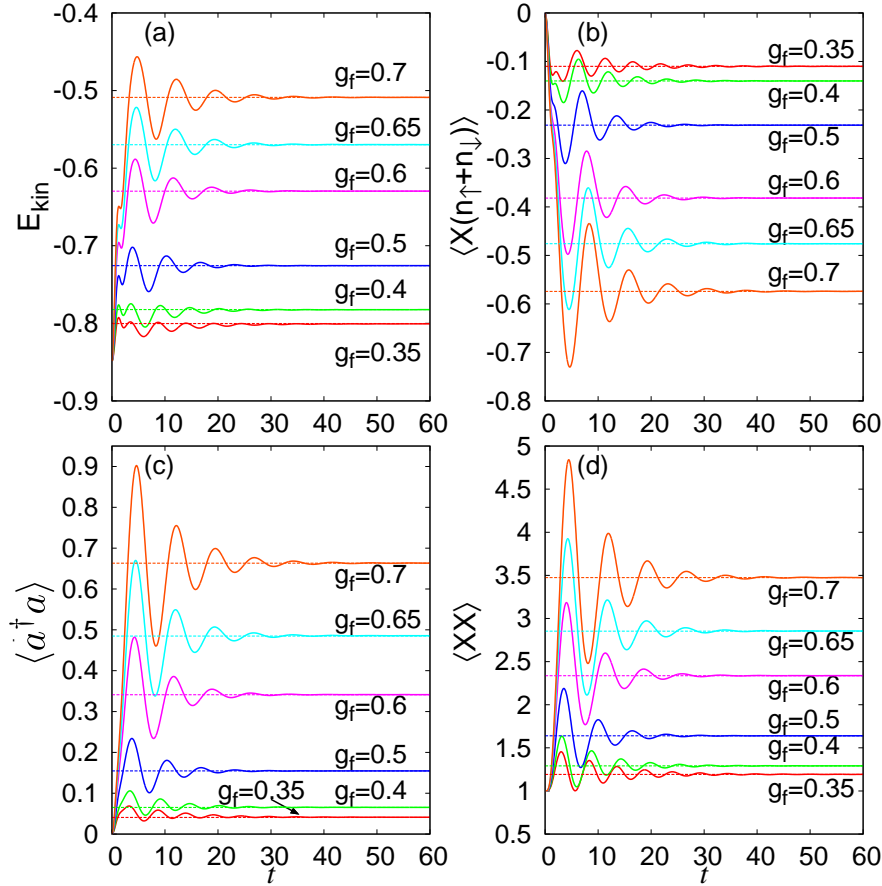


Figure 4.1: Time evolution of local quantities after an interaction quench at $t = 0$ from $g = 0$ at $T = 0$ to indicated values of g_f for $\omega_0 = 0.7$: (a) E_{kin} , (b) $\langle X(n_\uparrow + n_\downarrow) \rangle$, (c) $\langle a^\dagger a \rangle$, and (d) $\langle XX \rangle$. Dashed lines in each panel indicate the expected thermal values for each value of g_f determined from the conserved total energy.

where $\mathcal{H}_f = \mathcal{H}(t > 0)$. Since the present model is not an integrable one, it is natural to expect that thermalization takes place after a long time. The question is how the system thermalizes. Here we keep track of relaxation of local observables and the momentum distribution $n(\epsilon_{\mathbf{k}}, t) = -iG_{\mathbf{k}}^<(t, t)$. Since we start from the free state at $T = 0$, the momentum distribution exhibits a jump at $\epsilon = 0$ (i.e., the Fermi surface) for short times, while the jump is expected to vanish once the system is thermalized at $T_{\text{th}} > 0$. We note that a similar quench problem has been studied in the Hubbard model with DMFT+QMC [109, 110] and our setup in the limit of $\omega_0 \rightarrow \infty$ becomes identical to them.

Local observables

We start with looking at temporal evolution of local quantities. Here we call quantities evaluated by momentum integral and with no momentum index as local quantities. In Fig. 4.1, we show the results for the kinetic energy, the correlation between the phonon displacement and the density of electrons $\langle X(n_\uparrow + n_\downarrow) \rangle$, the phonon density $\langle a^\dagger a \rangle$, and the variance of the phonon displacement

4.1. THERMALIZATION CROSSOVER IN NORMAL STATES

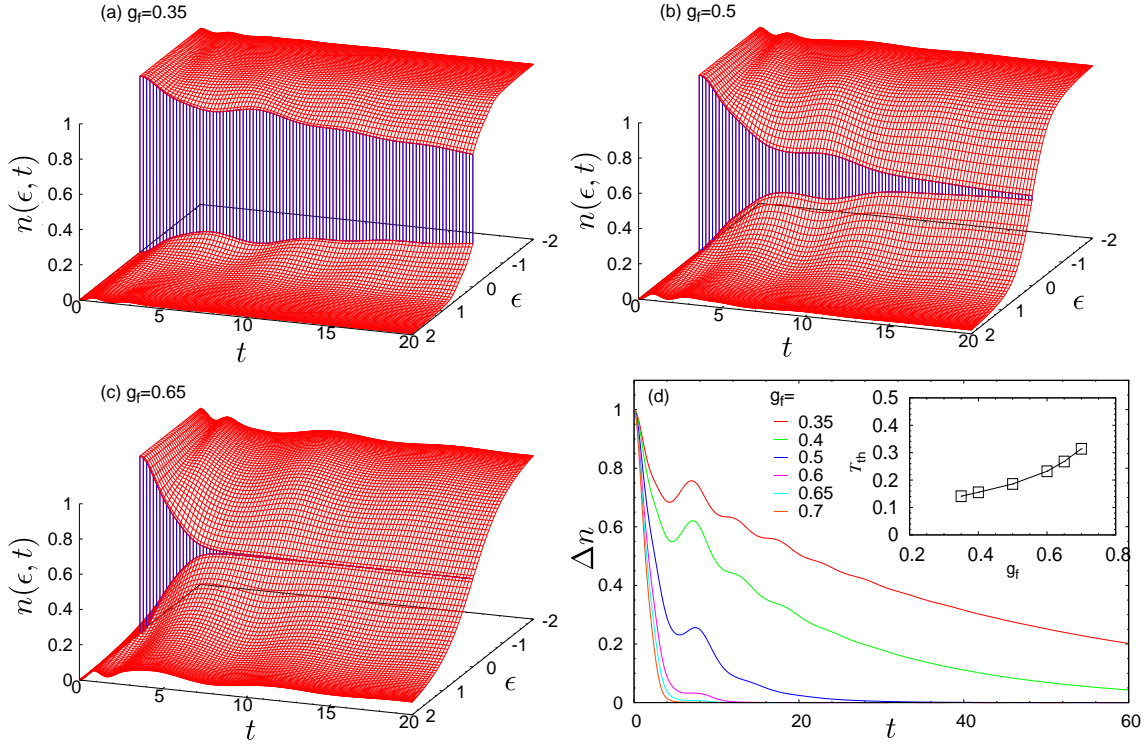


Figure 4.2: (a)-(c) Temporal evolution of the momentum distribution, $n(\epsilon, t)$, for $\omega_0 = 0.7$ after quenches to indicated values of g_f . Blue regions represent the jump in the momentum distribution around $\epsilon = 0$. (d) Temporal evolution of the jump in the momentum distribution, $\Delta n(t)$, for various values of g_f at $\omega_0 = 0.7$. The inset shows T_{th} against g_f .

$\langle XX \rangle$. It turns out that all of these local observables show coherent oscillations with twice the renormalized phonon frequency, ω_0^r . This can be understood as follows. Let us suppose that each local phonon oscillates as $X(t) \sim \cos(\omega_0^r t)$. Since the present interaction quench does not induce any phonon distortion $\langle X \rangle(t) \equiv 0$ and does not discriminate the direction of the lattice distortion ($X > 0$ or $X < 0$), the statistical distribution for the lattice displacement, $F(X, t)$, should be even in X . Hence only the symmetric dynamics is allowed and $2\omega_0^r$ -oscillations are observed. Provided that the phonon dynamics affects the electronic states through $F(X)$, it is natural to also expect oscillations of the other quantities with frequency $2\omega_0^r$.

The oscillations are damped as time evolves as seen in Fig. 4.1 and its amplitude becomes very small before $t = 60$ in all the cases shown here. When the system is fully thermalized, expectation values of observables should approach those of the equilibrium state with T_{th} , which increases with g_f , see inset of Fig. 4.2(d). For instance, the thermal kinetic energy should approach

$$E_{\text{kin,th}} = \frac{-v}{N} \sum_{\langle i,j \rangle, \sigma} \frac{\text{Tr} e^{-\mathcal{H}_f/T_{\text{th}}} (c_{i,\sigma}^\dagger c_{j,\sigma} + \text{h.c.})}{\text{Tr} e^{-\mathcal{H}_f/T_{\text{th}}}}. \quad (4.2)$$

In Fig. 4.1, we show with dashed lines the estimated thermal values at T_{th} for each observable.

We can see that once the oscillations are well damped ($t \gtrsim 60$), the local observables are already very close to the thermal values. In particular, the centers of the oscillation of $E_{\text{kin}} + \omega_0 N_{\text{ph}}$, $\langle X(n_{\uparrow} + n_{\downarrow}) \rangle$ and $\langle XX \rangle$ correspond to their respective thermal values from a very early stage of the relaxation dynamics. However, we note that this does not necessarily mean that the system is fully thermalized, as we shall see below.

Momentum distribution function

Here, we investigate the evolution of the momentum distribution function for the electrons, $n(\epsilon_{\mathbf{k}}, t) = -iG_{\mathbf{k}}^<(t, t)$ [Fig. 4.2, Fig. 4.3, Fig. 4.4, Fig. 4.5] as well as its jump, $\Delta n(t)$, at $\epsilon = 0$ [Fig. 4.2 (d)]. Since we start from $T = 0$ and $g = 0$, we have $\Delta n(0) = 1$. One can see a whole view in Fig. 4.2 and realize that the jump does not immediately disappear after the quench, but decreases gradually. As in the case of the Hubbard model [109, 110], $\Delta n(t)$ vanishes faster when the el-ph coupling g_f is increased. However, in the case of the Holstein model, $\Delta n(t)$ as well as $n(\epsilon_{\mathbf{k}}, t)$ for each $\epsilon_{\mathbf{k}}$ exhibit oscillations, see Fig. 4.2 (d) and Fig. 4.5.

Here we claim, as a key finding in the present investigation, that there are two qualitatively different types of relaxation behaviors in the Holstein model in the weakly to moderately correlated metal (prior to the bipolaron transition). The first type of relaxation dynamics is realized in the weaker coupling regime ($g_f \lesssim 0.5$), where the long-time relaxation process is dominated by the electrons. In this regime, oscillations originated from phonons are damped in both the local quantities and $n(\epsilon_{\mathbf{k}}, t)$ before $n(\epsilon_{\mathbf{k}}, t)$ is well thermalized. In more detail, the local quantities (in particular $E_{\text{kin}} + E_{\text{ph}}$, $\langle nX \rangle$ and $\langle XX \rangle$) are essentially thermalized after the damping of oscillation, Fig. 4.1, while the momentum distribution around the Fermi level represented by $\Delta n(t)$ is not fully thermalized, see Fig. 4.2 (d) and the result for $t = 59.6$ in Fig. 4.3. We note that the relaxation time strongly depends on the energy ϵ . The electron relaxation is fast when $\epsilon \gtrsim \omega_0^r$, while the relaxation is slow for $\epsilon \lesssim \omega_0^r$, see Fig. 4.3 and Fig. 4.5(a). This behavior is similar to the results in Ref. [97] analyzed without the phonon dynamics. These behaviors remind us of the prethermalization phenomena observed in a quench problem for the Hubbard model [109, 110], where local (momentum integrated) quantities quickly approach their thermal values, while momentum dependent quantities, such as $n(\epsilon, t)$, remain clearly nonthermal. However, we note that we do not observe a clear plateau-like structure in $n(\epsilon_{\mathbf{k}}, t)$ unlike in the Hubbard model. These behaviors are key characters in the relaxation behavior of the Holstein model in the sufficiently weak-coupling regime.

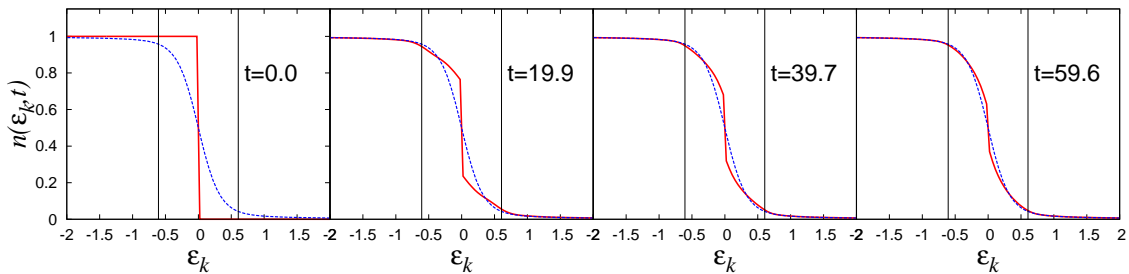


Figure 4.3: Time evolution of the electron momentum distribution function, $n(\epsilon, t)$, for $g_f = 0.35$ in the weaker-coupling regime. Dotted lines are the expected thermal distribution function, and vertical lines indicates $|\epsilon| = \omega_0^r$.

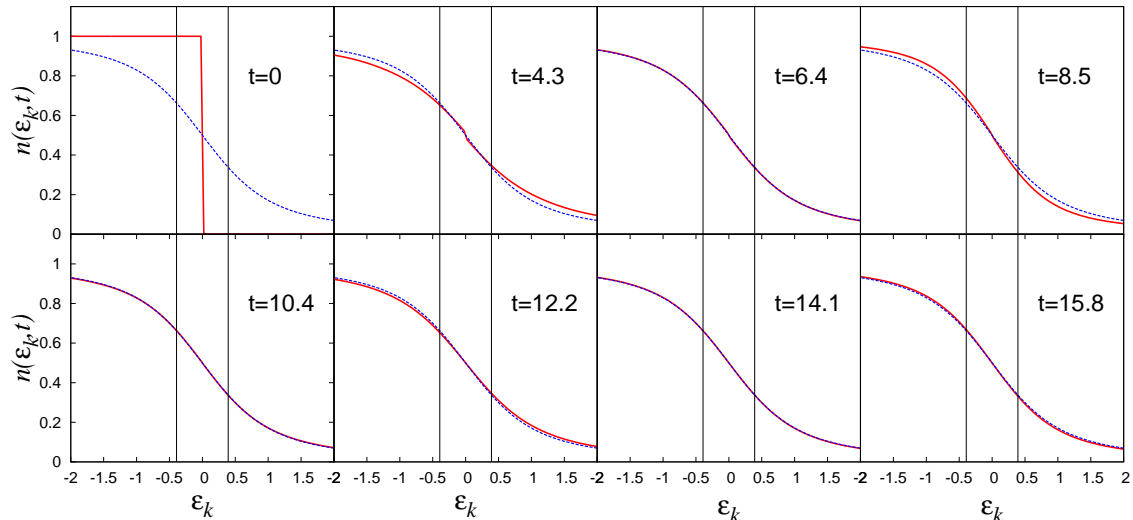


Figure 4.4: Temporal evolution of the electron momentum distribution function, $n(\epsilon, t)$, for $g_f = 0.65$ in the stronger-coupling regime. Dotted lines are the expected thermal distribution function, and vertical lines indicates $|\epsilon| = \omega_0^r$. $t = 6.4, 10.4, 14.1$ are the special times where $E_{\text{kin}}(t) = E_{\text{kin,th}}$

The second type of relaxation appears in the stronger-coupling regime ($g_f \gtrsim 0.5$, but before the bipolaronic transition), where the phonon dynamics turns out to dominate the long-time dynamics. Here we explain the character of the dynamics in this regime looking at $g_f = 0.65$, as an example. There we find that $\Delta n(t)$ vanishes [Fig. 4.2 (d), Fig. 4.4] before the oscillations of the momentum-integrated observables are damped (Fig. 4.1). Associated with this, the distribution function quickly approaches its thermal value, but it continues to oscillate around its thermal value as shown in Fig. 4.4. Once these oscillations are fully damped, $n(\epsilon, t)$ as well as local quantities reach respective thermal values. We also note in Fig. 4.4 that, interestingly, $n(\epsilon, \tilde{t})$ becomes almost indistinguishable from the thermalized distribution (dashed line, almost overlapping) after $\Delta n(t)$ has become small enough. Here \tilde{t} stands for those times at which $E_{\text{kin}}(\tilde{t}) = E_{\text{kin,th}}$ [Eq. (4.2)] is realized. As will be discussed later, the damping of the oscillation turns out to be related to the lifetime of phonons and the phonon self-energy. Therefore, phonons, rather than electrons, govern the long-time relaxation in this regime.

We note that the change from the electron-dominated to the phonon-dominated thermalization is not discontinuous but smooth. Hence this is a crossover phenomenon and we call it a “thermalization crossover”. In the present setup the crossover between these two different relaxation processes occurs around $g_f \sim 0.5$, where the oscillations and $\Delta n(t)$ vanish on similar time scales.

Now we comment on the relation between the present result and the phenomenological two-temperature model [142]. In this model, it is assumed that in the relaxation dynamics the electron sector and the phonon sector respectively are kept in temporal (quasi-)thermal states with different temperatures because of el-el Coulomb interactions and anharmonic phonon couplings. Then, through el-ph couplings these sectors exchange energies, and the whole system reaches the fully thermalized state. First of all, we have to note that the present situation is different from those in the two-temperature model, since in the latter it is assumed that the

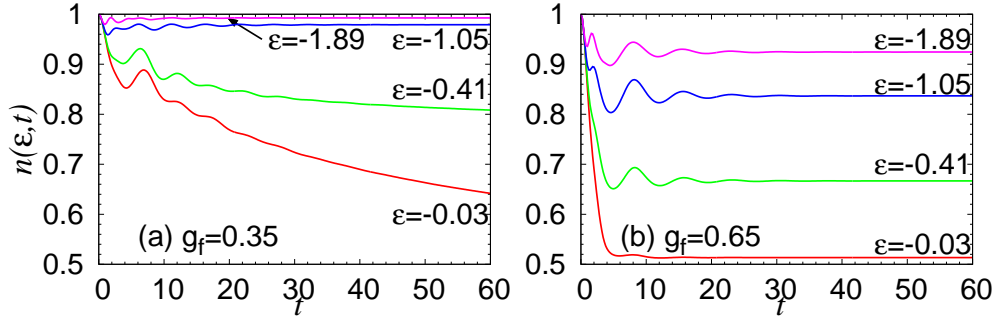


Figure 4.5: Temporal evolution of $n(\epsilon, t)$ for several values of ϵ for $g_f = 0.35$ (a) or 0.65 (b).

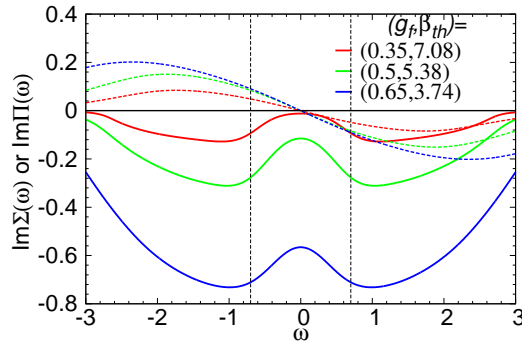


Figure 4.6: Imaginary parts of the phonon self-energy (dashed lines) and that of the electron self-energy (solid lines) in equilibrium at T_{th} for various values of g_f . The vertical lines indicate $|\omega| = \omega_0$.

electron degrees of freedom thermalize quickly due to the Coulomb interaction. This effect is not considered in the Holstein model studied here. Still, it is worthwhile to consider the relation between them. As for the first type of relation observed in the weaker-coupling regime, the relaxation time of $n(\epsilon, t)$ strongly depends on ϵ , and it would not be appropriate to describe this with a single decay rate as in the two-temperature model. Moreover, in this situation it would be difficult to define a meaningful effective temperature for the electron part, since the shape of $n(\epsilon, t)$ is far from that of thermal ones before full thermalization. As for the second type of relaxation in stronger-coupling regime, the long-time behavior is dominated by damped oscillations. Since the two-temperature model predicts no oscillations but a monotonic relaxation to the thermal value, it is not proper to describe this situation. Hence we conclude that neither of the two-relaxation processes presented here cannot be described by the conventional two temperature model.

Damping rates and self-energies

Here we discuss the relation between the different relaxation rates of physical quantities (E_{kin} , $\Delta n(t)$, $n(\epsilon, t)$...) and the g -dependence of the electron (Σ) and phonon (Π) self-energies. Firstly, we plot the imaginary parts of the electron self-energy and the phonon self-energy in the expected thermal state ($T = T_{th}$) for various vales of g_f in Fig. 4.6. One can find that the imaginary part

4.1. THERMALIZATION CROSSOVER IN NORMAL STATES

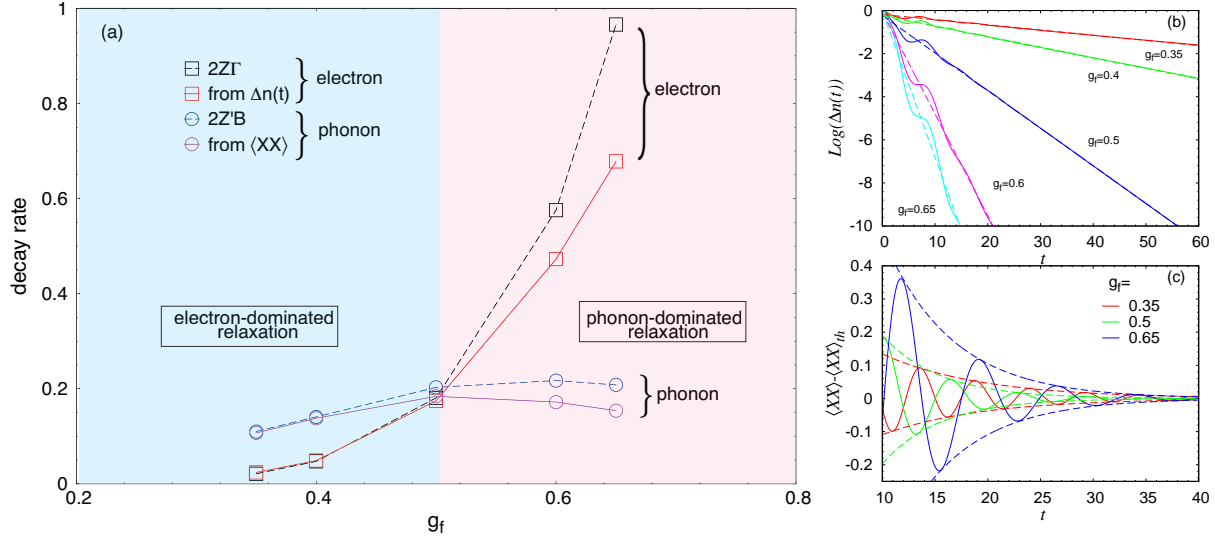


Figure 4.7: (a) Electron and phonon decay rates (\propto inverse relaxation times) against the electron-phonon coupling g_f . (b) Temporal evolution of the jump, $\Delta n(t)$, in the electron momentum distribution on a logarithmic scale for various values of g_f . Dashed lines are exponential fits. (c) Temporal evolution of the phonon displacement, $\langle XX \rangle - \langle XX \rangle_{\text{th}}$. The dashed lines represent exponential fits to the envelopes of the oscillating curves.

of electron self-energy, $|\text{Im}\Sigma|$, shows relatively small value in the energy range $|\omega| < \omega_0^r$, which becomes clearer at lower temperatures. This structure in the self-energy can be explained from the fact that electron (hole)-like quasiparticles cannot emit (absorb) phonons in this energy window because the final state after phonon emission (absorption) is already well occupied at low enough temperatures. This picture qualitatively explains the different relaxation time scales of $n(\epsilon, t)$ for different ϵ observed in the weaker-coupling regime, illustrated in Fig. 4.3 and Fig. 4.5(a). In addition, when g_f becomes larger T_{th} increases. This should make the energetically blocking effect less efficient and hence such an ϵ -dependent relaxation becomes less obvious. This is consistent with the behavior in the stronger-coupling regime illustrated in Fig. 4.4 and Fig. 4.5(b).

Now we consider the lifetime of a single electron quasiparticle in more detail. When the quasiparticle picture is valid, the electron self-energy in the small ω regime is expressed as

$$\Sigma^R(\omega) = (1 - 1/Z)\omega - i\Gamma + O(\omega^2), \quad (4.3)$$

where Z is the quasiparticle residue. From this, one finds that a quasiparticle with momentum \mathbf{k} has a renormalized energy $\epsilon_{\mathbf{k}}^r \equiv Z\epsilon_{\mathbf{k}}$ with a lifetime of $(2Z\Gamma)^{-1}$ at low-energies.

The quasiparticle lifetime of phonons can also be extracted from the self-energy of phonons in a similar way. We expand the phonon self-energy around $\omega = 0$ to obtain

$$\Pi^R(\omega) = A - iB\frac{\omega}{\omega_0} + C\frac{\omega^2}{\omega_0^2} + O(\omega^3), \quad (4.4)$$

where A , B and C are coefficients and the dressed phonon Green's function becomes

$$D^R(\omega) \simeq \frac{2Z'\omega_0}{(\omega - \omega'_0 + iZ'B)(\omega + \omega'_0 + iZ'B) + Z'^2B^2}, \quad (4.5)$$

where $\omega'_0 = Z'\omega_0(1 + A/\omega_0)^{1/2}$ with $Z' = (1 - 2C/\omega_0)^{-1}$. Here ω'_0 serves as an approximate peak position of the phonon spectral function, i.e. ω_0^r . We note that the second term (Z'^2B^2) in the denominator of $D^R(\omega)$ (Eq. 4.5) can be neglected if $B \ll \omega'_0$. This is because the absolute value of the first term in the denominator is more than $\sim O(B\omega'_0)$, which is much larger than the second term $\sim O(B^2)$. These arguments lead that $D^R(t)$ decays with a damping rate $Z'B$, which is confirmed by directly observing the damping of $D^R(t)$ in the interaction regime considered. In addition, when we think of the retarded part of the Green's function of a single phonon, $-i\langle T_c a(t)a^\dagger(t') \rangle$, it has the same poles as those for D^R . Hence the lifetime of a phonon quasi-particle can be identified with $(2Z'B)^{-1}$.

In Figure 4.7(a), we plot the quasiparticle lifetimes for an electron ($2Z\Gamma$) and a phonon ($2Z'B$), which we evaluate from the equilibrium self-energies against g_f at corresponding T_{th} . The two lifetimes cross with each other around $g_f = 0.5$ with $2Z\Gamma < 2Z'B$ for $g_f < 0.5$, while $2Z\Gamma > 2Z'B$ for $g_f > 0.5$. Hence as long as the quasiparticle picture is valid, an electron quasiparticle created around the Fermi level decays more slowly than a phonon quasiparticle for $g_f < 0.5$, while the situation is reversed for $g_f > 0.5$.

In Fig. 4.7(a), we also show the electron decay rate extracted from $\Delta n(t)$ by exponential fitting as shown in Fig. 4.7(b). Here we use the data from $t = 0$ up to $t = 60$ or up to $\Delta n(t) = 10^{-4}$. The decay rate increases with g_f . It turns out that the value of $2Z\Gamma$ explains well the dependence of the decay rate of $\Delta n(t)$ on g_f . More precisely, in the smaller- g_f regime the discrepancy is very small, while $2Z\Gamma$ tends to overestimate the exponent of $\Delta n(t)$ in the larger- g_f regime. On the other hand, it turns out that the phonon decay rate $2Z'B$ manifests itself in the damping of oscillations in E_{kin} , $\langle Xn \rangle$, $\langle XX \rangle$ and $\langle a^\dagger a \rangle$. As an example, the oscillation of $\langle XX \rangle - \langle XX \rangle_{\text{th}}$ is displayed in Fig. 4.7(c). The envelopes are fitted with exponentials, and the corresponding decay rates are plotted in Fig. 4.7(a). We have confirmed that the oscillations for other quantities (E_{kin} , $\langle Xn \rangle$ and $\langle a^\dagger a \rangle$) have almost the same damping rates. Figure 4.7(a) tells that $2Z'B$ indeed provides a good explanation for the damping rates of the oscillations. To be more precise, while the agreement with $2Z'B$ is very good for $g_f \lesssim 0.5$, the quasiparticle lifetime from the phonon self-energy tends to overestimate the damping rate of the oscillations as we increase g_f .

The above analysis indicates that the different dependence of the electron and phonon lifetimes on the electron-phonon coupling g_f explains the two different relaxation regimes: In the weaker-coupling regime, the phonon oscillations are damped before electron's $n(\epsilon, t)$ thermalizes, which reflects that the lifetime for a phonon is shorter than that for an electron (electron-dominated thermalization). In the stronger-coupling regime, on the other hand, the electron lifetime is shorter than the phonon lifetime (Fig. 4.7(a)). Reflecting this, $\Delta n(t)$ vanishes quickly and the momentum distribution approaches to its thermal value quickly. However, since the phonons are still in the process of relaxation, the electrons are forced to move with them (phonon-dominated thermalization). We note that the manifestation of quasiparticle lifetimes in the quench dynamics is not trivial, since in quasiparticle lifetimes only one particle is excited while the quench problem particles more than one are excited at the same time.

Non-equilibrium spectral functions

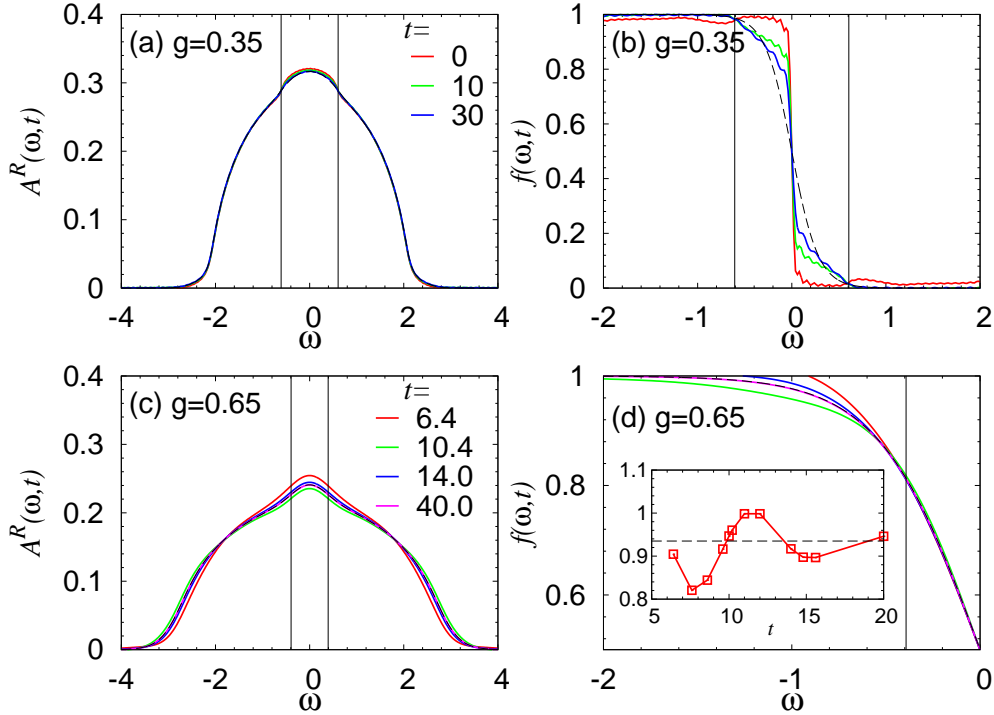


Figure 4.8: Nonequilibrium spectral function, $A^R(\omega, t)$, at different t for $g_f = 0.35$ (a) or 0.65 (c), and nonequilibrium distribution function $f(\omega, t)$ for $g_f = 0.35$ (b) or 0.65 (d). The dashed curves represent the thermal A^R and distribution functions. Vertical lines in each panel indicate ω_0^r in equilibrium at T_{th} for each value of g_f . The inset in (d) plots the time evolution of $\frac{\partial f(\omega, t)}{\partial \omega}|_{\omega=0}$, where the dotted line indicates the thermal value.

Here we discuss how these qualitatively different relaxation processes show up in the non-equilibrium spectral function and distribution function. One can extend the definition of the electron spectral function A^R and occupied spectral function $A^<$ to non-equilibrium situations as

$$A^{R,<}(\omega, t) = \mp \frac{1}{\pi} \text{Im} \int_t^\infty dt' e^{i\omega(t'-t)} G_{\text{loc}}^{R,<}(t', t), \quad (4.6)$$

where $-$ is for R and $+$ is for $<$. Then the non-equilibrium distribution function is defined as $f(\omega, t) \equiv A^<(\omega, t)/A^R(\omega, t)$. $A^R(\omega, t)$ and $f(\omega, t)$ at different times are shown in Fig. 4.8. The result for $g_f = 0.35$ in the electron-dominated regime is shown in Fig. 4.8(a,b). First, we note that a peak structure of A^R around ω_0 at $t = 0$ indicates the difference from the spectrum of the free state. This is attributed to the fact that $A^R(\omega, t)$ includes information on later times than t , see Eq. 4.6. A characteristic feature in the relaxation of $A^R(\omega, t)$ and $f(\omega, t)$ is that for $\omega \gtrsim \omega_0^r$ they thermalize quickly while for $\omega \lesssim \omega_0^r$ the relaxation is slow and gradual. We note that a similar behavior is pointed out in a previous work on the photoexcited Holstein model [98]. The small wiggles in Fig. 4.8 (b) are Fourier cutoff artifacts.

The results for $g_f = 0.65$ in the phonon-dominated regime is shown in Fig. 4.8(c,d). Here we pick up the special times at which $E_{\text{kin}} = E_{\text{kin,th}}$ is realized. Even though the momentum distributions are indistinguishable from the thermal ones at these times, it turns out that both $A^R(\omega, t)$ and $f(\omega, t)$ are different from the thermal curves. This discrepancy comes from the fact that the latter quantities are not determined by instantaneous temporal information unlike the former quantity. In the inset of panel (d), $\frac{\partial f(\omega, t)}{\partial \omega}|_{\omega=0}$ is shown. The oscillation in the slope means the oscillation of $f(\omega, t)$ near $\omega = 0$ around its thermal value. These observations suggest that in the phonon-dominated regime $A^R(\omega, t)$ and $f(\omega, t)$ oscillate around their thermal values both in the energy range $|\omega| \gtrsim \omega_0^r$ and $|\omega| \lesssim \omega_0^r$. After this oscillation is fully damped, thermalization of A^R and $f(\omega, t)$ is achieved (see the result for $t = 40$).

4.1.3 Interaction quench: Results of DMFT + unrenormalized Migdal approximation

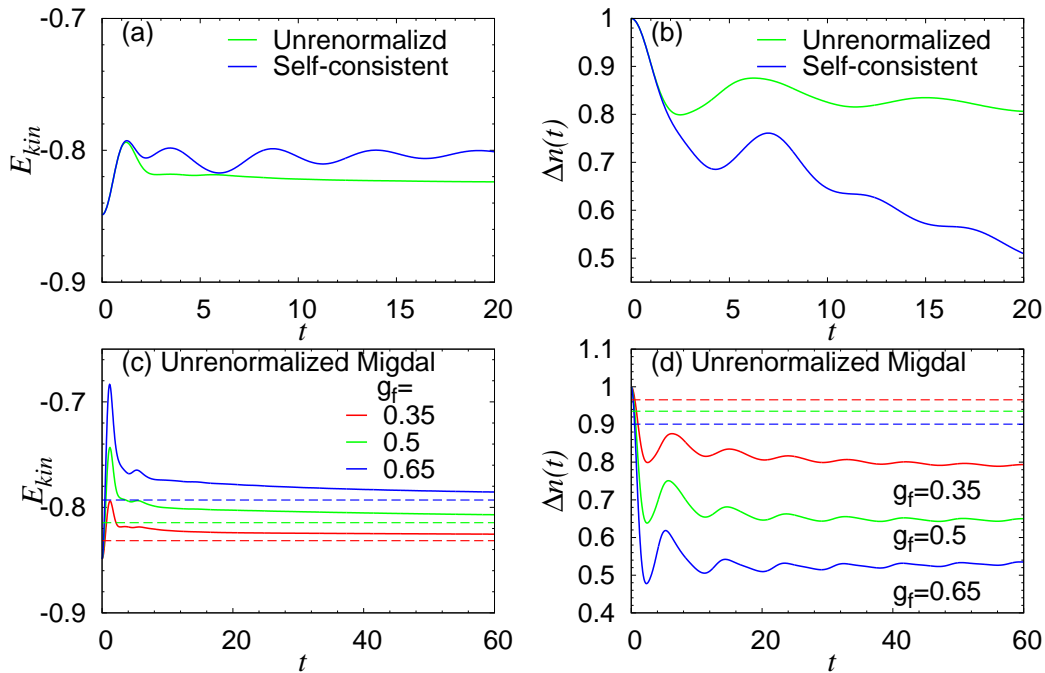


Figure 4.9: Comparison of the dynamics in the unrenormalized Migdal and the self-consistent Migdal approximations for (a) the kinetic energy and (b) $\Delta n(t)$. Temporal evolution of (c) E_{kin} and (d) $\Delta n(t)$ within the unrenormalized Migdal approximation for various g_f . Horizontal dashed lines indicate the thermal values at $T = 0$.

For comparison, here we study the same quench problem with the unrenormalized Migdal approximation in order to make clear the effect of the phonon dynamics. First of all, we note that, since the phonon is assumed to stay in equilibrium in this approximation from the outset, the thermalization crossover does not occur. In Fig. 4.9, we show the time evolution of $\Delta n(t)$ and $E_{\text{kin}}(t)$. It turns out that the unrenormalized Migdal and the self-consistent Migdal show the same dynamics at very short times. However after a certain period, they start to deviate and end up with very different relaxation dynamics. One striking difference from the results of

4.1. THERMALIZATION CROSSOVER IN NORMAL STATES

the self-consistent Migdal approximation is the quick disappearance of the oscillations in local quantities within $t < 10$, see Fig. 4.1(a)(c). Then $E_{\text{kin}}(t)$ slowly approaches a steady value in the long-time limit. Here we note that, as discussed in Ref. [117], it is expected that phonons act as a heat bath for electrons, which are cooled down to the temperature of the initial equilibrium phonons. Indeed, our results are consistent with the relaxation towards the equilibrium with the initial temperature (i.e., $T = 0$ here). In Fig. 4.1(c), we see that $E_{\text{kin}}(t)$ gradually relax to the thermal values at $T = 0$ for various g_f , which is also the case with another local quantity, $\langle Xn \rangle$. The results for $\Delta n(t)$ within the unrenormalized Migdal are shown in Fig. 4.10(d). $\Delta n(t)$ starts to decrease after the quench, but it remains finite for a long time, which behavior is different from the results of the self-consistent Migdal approximation [Fig. 4.2(d)]. The fact that $\Delta n(t)$ does not vanish is consistent with the expectation that the phonons in the unrenormalized Migdal effectively act as a heat bath with $T = 0$. However, we have to note that $\Delta n(t)$ is still far from the expected thermal value for $T = 0$ even at $t = 60$, which indicates that the cooling rate is very low. We can understand this as follows. In the $T = 0$ equilibrium state, we have $\text{Im}\Sigma(\omega) \propto \omega^2$ for the Fermi liquid. Hence the decay rate for $\Delta n(t)$ is expected to become very small as the system approaches the equilibrium state at $T = 0$.

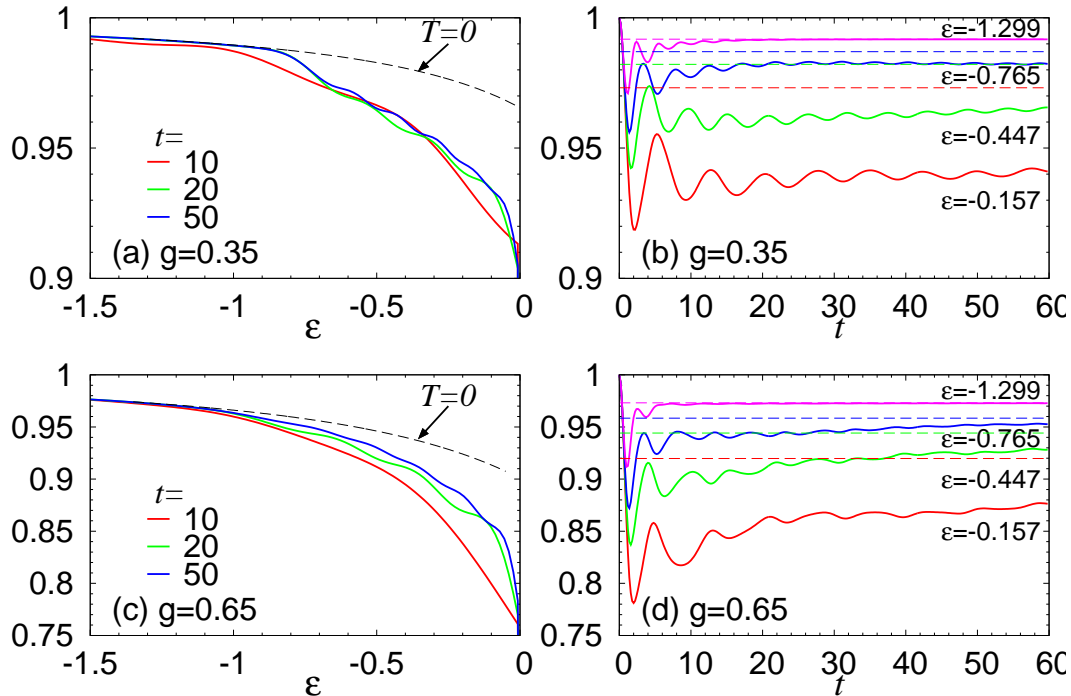


Figure 4.10: $n(\epsilon, t)$ at various times for (a) $g_f = 0.35$ and (c) $g_f = 0.65$. Dashed curves indicate the equilibrium values at $T = 0$. The temporal evolution for $n(\epsilon, t)$ of various values of ϵ for (b) $g_f = 0.35$ and (d) $g_f = 0.65$.

Now, let us take a closer look at the momentum distribution function. Figure 4.10 shows the dynamics of $n(\epsilon, t)$ in more detail. For both $g = 0.35$ and $g = 0.65$, the distribution at large $|\epsilon|$ relaxes fast to the equilibrium value at $T = 0$, while the distribution for small $|\epsilon|$ relaxes slowly. This aspect is consistent with the prediction of the self-consistent Migdal approximation and the previous simulations of a pumped Holstein model [96], and the structure of the self-energy.

However, strictly speaking, we find that the energy window exhibiting a slow relaxation in $n(\epsilon, t)$ is larger than the window $-\omega_0 < \epsilon < \omega_0$ predicted by the self-energy analysis. We consider that this originates from several reasons. Firstly, if we increase the el-ph interaction the quasiparticle renormalization increases and quasiparticle with a momentum \mathbf{k} has smaller energy than its bare value $\epsilon_{\mathbf{k}}$. Secondly, after the quench, many quasiparticles are excited in the energy range $-\omega_0 < \omega < \omega_0$, so that quasiparticles with energy $|\omega| > |\omega_0|$ can decay less easily. In addition, compared to the results of the self-consistent Migdal approximation, $n(\epsilon, t)$ shows more pronounced oscillations with a different frequency for each ϵ , see Fig. 4.10(b)(d). These oscillations lead to the complicated structure of $n(\epsilon, t)$ shown in Fig. 4.10(a)(c). Here, we can attribute the fast damping of the oscillations in E_{kin} to the dephasing of the oscillation in the momentum distribution at each momentum. We note that this is a scenario different from the damping in the self-consistent Migdal approximation, where the oscillations of the electrons are tied to the dynamics of the phonons and its damping is related to the quasiparticle lifetime of a phonon. These comparisons between the unrenormalized Migdal and the self-consistent Migdal imply that the feedback from the non-equilibrium phonon dynamics to electrons leads to a qualitatively very different dynamics. Therefore, we conclude that the unrenormalized Migdal approximation cannot properly describe the evolution of isolated systems. However, we note that it may be possible to use the approximation in order to phenomenologically express electrons coupled to a heat bath (open system), as in Refs. [117, 118].

4.2 Collective excitations in strongly-coupled superconductors

4.2.1 Background: Collective amplitude mode in superconductors

Non-equilibrium dynamics enables us to gain access to new phenomena and information that are hard to reach in equilibrium. As an interesting example, Shimano's group [17, 18] has recently succeeded for the first time in observing the amplitude Higgs mode in conventional phonon-mediated superconductors with pump-probe experiments using a strong THz laser. Since the amplitude Higgs mode does not couple with the electromagnetic field in the linear-response regime, observation of the mode was limited [32–35, 48] to the special case when SC coexists with a charge density wave before Shimano's experiment. From the theoretical point of view, the collective modes in superconductors have been attracting interests for a long time [32, 37–50, 99, 100]. Most of the theoretical works have been based on the mean-field dynamics (the BCS dynamics). One important consequence of these theories is the coincidence of the energy of the amplitude Higgs mode (ω_{H}) and the SC gap ($2\Delta_{\text{SC}}$). This relation suppresses the relaxation channel of the collective amplitude mode to Bogoliubov quasiparticles, and ends up with a power law ($\sim 1/\sqrt{t}$) decay of the mode. This relatively slow decay helps the accessibility of the mode in the pump-probe experiment.

On the other hand, as far as we know, studies of collective amplitude modes beyond the mean-field picture are limited to recent works [99, 100], and the nature of the modes in the strongly-coupled phonon-mediated SCs remains to be revealed. Here, we note that so-called strong-coupling conventional superconductors correspond to cases of $\lambda_{\text{eff}} \sim 1$, where λ_{eff} is the

dimensionless el-ph coupling. It is defined as

$$\lambda_{\text{eff}} \equiv 2 \int_0^\infty d\omega \frac{\alpha^2 F(\omega)}{\omega}, \quad (4.7a)$$

$$\alpha^2 F(\omega) = N(0)g^2 B(\omega), \quad (4.7b)$$

where $N(0)$ is the DOS at the Fermi level, $B(\omega) = -\frac{1}{\pi} \text{Im}D^R(\omega)$ and we obtain $\lambda_{\text{eff}} = N(0)g^2 D^M(i\nu_n = 0)$. Here the superscript M indicates the Matsubara component. In the strongly-coupled regime¹, the system is described by the Migdal-Eliashberg theory [13–15]. There, in order to evaluate a susceptibility, one usually needs to solve the Bethe-Salpeter equation that includes a frequency-dependent irreducible vertex, which contrast with the BCS analysis, where we can analytically solve the equation. In addition, we need to perform a numerical analytic continuation for information for real times and real frequencies, which would be a bottleneck in the direct evaluation of the Bethe-Salpeter equation. However, NbN, which is used in Shimoano’s experiment, has relatively a large dimensionless el-ph coupling $\lambda_{\text{eff}} \gtrsim 1$ and belongs to the strong-coupling regime [157–160]. In addition, we can expect that further pump-probe experiments will reveal properties of collective modes in a wide range of materials. Hence it is important to provide theoretical understanding or predictions about collective excitations in strongly-coupled SCs.

Based on this background, the purpose of this section is to reveal properties of collective amplitude modes in strongly-coupled phonon-mediated SCs. In particular, we want to understand the fate of the relation between ω_H and $2\Delta_{\text{SC}}$ as the electron-phonon coupling is increased, effects of the phonon dynamics on the amplitude Higgs mode, possibility of new collective excitations and the decay of the amplitude Higgs mode. In order to do this, we directly simulate the non-equilibrium dynamics after external perturbations using the framework of the non-equilibrium DMFT. By taking small enough external fields we can evaluate linear susceptibilities without solving the Bethe-Salpeter equation and performing a numerical analytic continuation.

We note that Kemper et al [99,100] have studied the amplitude Higgs modes in the strongly-coupled SC by simulating time evolution after shining a laser. There, they employ the unrenormalized Migdal approximation, which assumes that phonons are always in equilibrium despite electrons being out of equilibrium, and discuss accessibility of the mode with time-resolved angle-resolved photoemission spectroscopy (ARPES). However, they do not answer none of the questions we have raised above. In the following, we investigate collective modes with DMFT+self-consistent Migdal approximation in Sec. 4.2.2 to 4.2.4, while in Sec. 4.2.5 we use the fixed-phonon picture, i.e. DMFT+unrenormalized Migdal approximation, in order to extract effects of the quasiparticle lifetime on decay of the amplitude Higgs mode. We focus on the strongly-coupled superconductors with $1 \lesssim \lambda_{\text{eff}} \lesssim 2$ described by the half-filled Holstein model, see Appendix. B.2. Strictly speaking, if we allow the possibility of CO, it is more favorable than SC at half-filling, as we have discussed in the previous chapter. However, if the lattice has frustration such as the next-nearest neighbor hopping on the Bethe lattice, CO is suppressed and the present treatment is justified [25]. Therefore, in this section, we are considering such a situation. Before we proceed, we again note that the self-consistent Migdal approximation becomes quantitatively accurate when ω_0 is small enough compared to the electron bandwidth.

¹We note that the meaning of ”strong” is different from Sec. 3. In the context of conventional superconductors, the strongly-coupled regime is characterized by the strength of renormalized phonon-mediated attractive interaction, and it is located before the bipolaronic transition.

Here we focus on a relatively high phonon frequency in this section, i.e., $\omega_0 = 0.4$ because of the limit of the computational time and the memory of the machine used. However, we consider that results discussed here with the self-consistent Migdal approximation should be qualitatively correct, because it is still small compared to the electron bandwidth $W = 4$, and that the discussions are applicable to cases with lower phonon frequencies. Indeed, we have confirmed that a choice of lower phonon frequency $\omega_0 = 0.2$ shows the same general features and discussions involved do not change, although the study for these cases is less systematic since the calculation is much more demanding.

4.2.2 Dynamical pair susceptibility and collective modes

In order to study collective excitations involving amplitude oscillations of the SC order parameter, we evaluate the dynamical pair susceptibility,

$$\chi_{\text{pair}}(t - t') = -i\theta(t - t')\langle [B_0(t), B_0(t')] \rangle, \quad (4.8)$$

with $B_0 = \sum_i (c_{i\uparrow}^\dagger c_{i\downarrow}^\dagger + c_{i\downarrow} c_{i\uparrow})$. In order to do this, we apply an external perturbation expressed as $H'(t) = d_f \delta(t) \sum_i (c_{i\uparrow}^\dagger c_{i\downarrow}^\dagger + c_{i\downarrow} c_{i\uparrow})$ with small enough d_f (for the linear-response regime to be valid), and follow the subsequent dynamics with the non-equilibrium DMFT and the self-consistent Migdal approximation as an impurity solver. Diagrammatic expression for the dynamical pair susceptibility evaluated in this way will be discussed in the next section.

In Fig. 4.11 we display $\chi_{0,\text{pair}}(t)$, which is obtained by the Wick expansion and taking account only of the bubble diagram along with $\chi_{\text{pair}}(t)$. The result shows that $\chi_{\text{pair}}(t)$ exhibits long-lived oscillations, while $\chi_{0,\text{pair}}(t)$ damps very quickly on a time scale of $1/W$ and becomes featureless. Since $\chi_{0,\text{pair}}$ only includes contribution from single-particle excitations, the oscillations in $\chi_{\text{pair}}(t)$ are originated from collective excitations. An important point is that the oscillations in $\chi_{\text{pair}}(t)$ cannot be explained by a single mode unlike in the BCS and unrenormalized Migdal dynamics, and this tendency becomes clearer as the el-ph coupling is increased. In order to understand the energy scale of the collective modes, we compare, in Fig. 4.11 (c) (d), $-\text{Im}\chi_{\text{pair}}(\omega)$, $-\text{Im}\chi_{0,\text{pair}}(\omega)$, the electron spectrum $A(\omega) = -\frac{1}{\pi}G^R(\omega)$ and the phonon spectrum $B(\omega) = -\frac{1}{\pi}D^R(\omega)$. Here we evaluate $\chi_{\text{pair}}(\omega)$ as $\int_0^{t_{\text{max}}} dt \chi_{\text{pair}}(t) e^{i\omega t}$ with $t_{\text{max}} = 200$ and the wiggles in $-\text{Im}\chi_{\text{pair}}(\omega)$ originate from this finite range of the Fourier transformation. We have checked that the main peaks in $-\text{Im}\chi_{\text{pair}}(\omega)$ stay almost at the same positions with $t_{\text{max}} = 300$ and do not affect the following discussions. Before we discuss $-\text{Im}\chi_{\text{pair}}(\omega)$, we have to note several properties about $A(\omega)$ and $B(\omega)$. First, as a consequence of the strong el-ph coupling the jump in $A(\omega)$ at the gap becomes slightly smoothed. Therefore, in the present study, we define the gap size by the energy where $A(\Delta_{\text{SC}}) = N(0)$ with $N(0)$ the density of states for free electrons at $\omega = 0$ and its uncertainty is estimated by the peak position of $A(\omega)$ and the position where $A(\omega) = N(0)/2$. Secondly, our results show that when the renormalized phonon frequency is comparable to the SC gap, the strong el-ph coupling leads to complicated renormalized phonon spectra in SC. This is illustrated in Fig. 4.12, where we show detailed temperature dependence of the phonon spectrum. Here we define the renormalized phonon frequency ω_r as the position of the dominant peak in the phonon spectra (colored arrows in Fig. 4.12). In the SC phase, as the SC gap develops, the spectral weight in the low-energy regime is strongly suppressed, a sharp peak develops below the SC gap and the phonon spectra becomes highly asymmetric, see the red and black curves in Fig. 4.11(c)(d) for example. On the other hand, in

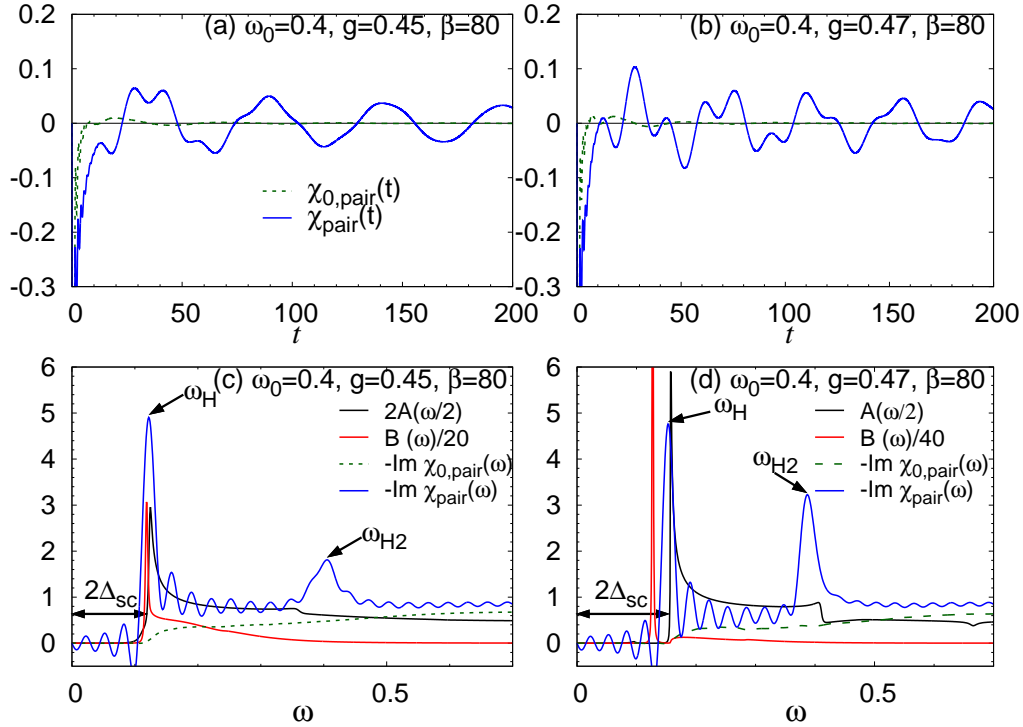


Figure 4.11: (a)(b) Dynamical pair susceptibility against t evaluated with the full dynamics in the Migdal approximation [$\chi_{\text{pair}}(t)$] and with the bubble diagrams [$\chi_{0,\text{pair}}(t)$] for $g = 0.45, \beta = 80$ ($\lambda_{\text{eff}} = 1.38$) (a) and $g = 0.47, \beta = 80$ ($\lambda_{\text{eff}} = 1.89$) (b). (c)(d) Comparison of the electron spectrum $A(\omega/2)$, the phonon spectrum $B(\omega)$, $-\text{Im}\chi_{0,\text{pair}}^R(\omega)$ and $-\text{Im}\chi_{\text{pair}}^R(\omega)$ for $g = 0.45, \beta = 80$ (c) and $g = 0.47, \beta = 80$ (d). $\chi_{\text{pair}}(\omega)$ and $\chi_{0,\text{pair}}(\omega)$ evaluated from the data at $t \in [0, 200]$. The factor of 2 in $A(\omega/2)$ facilitates a comparison between $2\Delta_{\text{SC}}$ and ω_{H} .

the normal state ($\beta = 30$), the phonon spectra exhibit an almost symmetric structure around a peak that is softened by the el-ph coupling from ω_0 [30, 114]. This phenomenon has indeed been observed in some real strongly-coupled SCs [161–165] and theoretically explained as an effect of the phonon self-energy [166] (*phonon anomaly*). In particular, the suppression of the phonon spectrum in the low-energy regime is attributed to the fact that scattering of phonons with quasi-particles is energetically suppressed below the SC gap.

It turns out that the oscillations in $\chi_{\text{pair}}(t)$ come from two different modes at ω_{H} and $\omega_{\text{H}2}$ ($\omega_{\text{H}} < \omega_{\text{H}2}$), see $-\text{Im}\chi_{\text{pair}}(\omega)$. The lower peak is always located around the SC gap ($2\Delta_{\text{SC}}$) and remains there as we approach the BCS regime, see the inset of Fig. 4.13(b). Therefore, this lower mode is identified as the amplitude Higgs mode in the strongly-coupled SC. In other words, we have shown that the BCS relation of

$$\omega_{\text{H}} = 2\Delta_{\text{SC}} \quad (4.9)$$

is valid to a good approximation even when the el-ph coupling is strong and the phonon energy is comparable to the SC gap. One important consequence of this relation is that the damping channel to quasi-particles remains small, especially, at lower temperatures, where the gap edge is sharp and the quasi-particle excitation is lower-bounded at Δ_{SC} . Here we note that when we

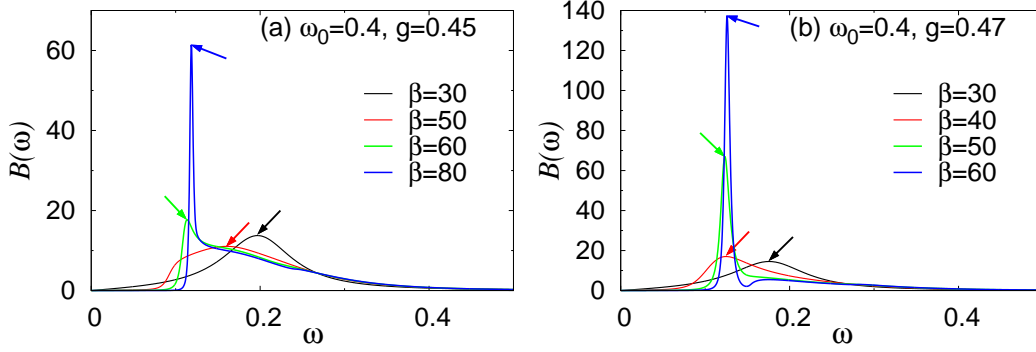


Figure 4.12: Phonon spectrum at various temperatures for $\omega_0 = 0.4$, $g = 0.45$ (a) and $\omega_0 = 0.4$, $g = 0.47$ (b). Arrows indicate the peak positions (ω_r). In both cases, the system is in the normal phase at $\beta = 30$, while in the SC phase at other temperatures.

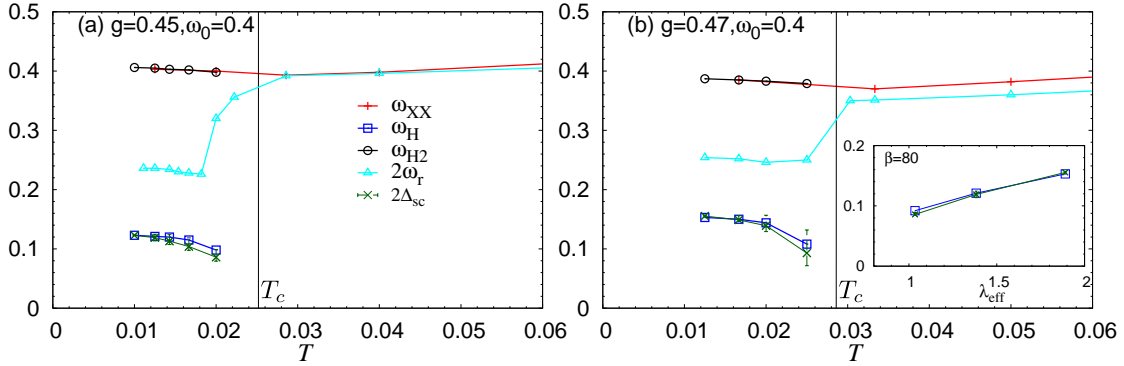


Figure 4.13: Characteristic energies against temperature (T) at $g = 0.45, \omega_0 = 0.4$ (a) or $g = 0.47, \omega_0 = 0.4$ (b). Here ω_{XX} means a frequency of coherent oscillation in the response of $\langle XX \rangle$ after a small hopping quench. Vertical black lines indicate T_c . The inset shows the el-ph coupling dependence of the Higgs mode and the SC gap at $\beta = 80$ against λ_{eff} , which is the dimensionless coupling constant.

get closer to T_c , the edge becomes more smoothed, and the suppression of the damping channel becomes weaker. Such effects will be discussed in Sec. 4.2.5. We also note that the depletion of the phonon spectral weight in the low-energy regime (phonon anomaly) also suppresses the possible damping channel from the Higgs mode into two phonons.

The higher peak found here, on the other hand, is a new collective amplitude mode which is not included in the dynamics of BCS or the unrenormalized Migdal approximation [99, 100]. Therefore, we can conclude that the phonon dynamics should be the origin of the new collective mode involving amplitude oscillation. However, ω_{H2} does not have a simple relation with the renormalized phonon frequency ω_r .

In order to obtain a full picture for different energy scales and clarify relation among them, we summarize them against the temperature in Fig. 4.13. First, we note that this plot shows that the relation, $\omega_H \simeq 2\Delta_{SC}$, is robust in the strongly-coupled SC for the whole region of T studied here. Secondly, it turns out that, even though ω_{H2} does not manifest itself in the dynamical pair susceptibility, it shows up in other susceptibilities and continues to exist in the normal states. In Fig. 4.13, we also display ω_{XX} , the frequency of coherent oscillations in the

response of $\langle XX \rangle$ after a small hopping quench. As can be seen, ω_{XX} coincides with ω_{H2} . Hence this mode intertwines the phonon dynamics and the SC order parameter in SC, but is not a special mode accompanying the symmetry breaking. With decreasing temperature, this mode shows softening in the normal state and hardening in SC. If we compare this mode with the renormalized phonon frequency (ω_r), it turns out that ω_{H2} and $2\omega_r$ agree well in the normal state with not too strong el-ph coupling. On the other hand, in SC, deviation between these two quantities becomes significant.

Now the questions are (1) the origin of the discrepancy between ω_{H2} and $2\omega_r$ in SC, and (2) effects of the dynamics of phonons on the amplitude Higgs mode. In the next section, we discuss these issues considering the diagrammatic expression for χ_{pair} derived from the direct simulation with DMFT + self-consistent Migdal approximation.

4.2.3 Diagrammatic analysis

In order to answer the questions above, we analyze the diagrammatic expression for χ_{pair} in the present calculation (DMFT+ self-consistent Migdal approximation) as well as its relation to the susceptibility in the fixed-phonon pictures (DMFT+ unrenormalized Migdal approximation). For the dynamical pair susceptibility, we need to evaluate the response of Green's functions against modulation of the pair potential, $F_{\text{ex}}(t)$. Hence we want to know the quantity,

$$\hat{\Lambda}_{\mathbf{k}}(\nu, \nu'; \nu'') \equiv \left. \frac{\delta_{\mathcal{C}}[\hat{G}_{\mathbf{k}}(\nu, \nu')]}{\delta_{\mathcal{C}}[F_{\text{ex}}(\nu'')]} \right|_{F_{\text{ex}}(t)=0}. \quad (4.10)$$

Here we use ν for representing a point on the KB contour, $\hat{\cdot}$ means a 2×2 matrix in the Nambu formalism, \mathbf{k} is a momentum and $\frac{\delta_{\mathcal{C}}[\cdot]}{\delta_{\mathcal{C}}[\cdot]}$ is the functional derivative on the KB contour.

First we evaluate the corresponding quantity for the free Green's function, $\hat{G}_{0,\mathbf{k}}$. The Green's function satisfies

$$\int_{\mathcal{C}} d\nu_1 [i\partial_{\nu} \hat{I} - \xi_{\mathbf{k}} \hat{\sigma}_3 + F_{\text{ex}}(\nu) \hat{\sigma}_1] \delta_{\mathcal{C}}(\nu, \nu_1) \hat{G}_{0,\mathbf{k}}(\nu_1, \nu') = \delta_{\mathcal{C}}(\nu, \nu') \hat{I}, \quad (4.11)$$

which leads to, with a functional derivative,

$$\hat{\Lambda}_{0,\mathbf{k}}(\nu, \nu'; \nu'') = \hat{G}_{0,\mathbf{k}}(\nu, \nu'') \hat{\sigma}_1 \hat{G}_{0,\mathbf{k}}(\nu'', \nu'). \quad (4.12)$$

Now, we turn to evaluate $\hat{\Lambda}_{\mathbf{k}}$ with interactions. In order to do this, we introduce a vertex part ($\hat{\Gamma}_{\mathbf{k}}$) as

$$\hat{\Lambda}_{\mathbf{k}}(\nu, \nu'; \nu'') = \int_{\mathcal{C}} d\nu_1 d\nu_2 \hat{G}_{\mathbf{k}}(\nu, \nu_1) \hat{\Gamma}_{\mathbf{k}}(\nu_1, \nu_2; \nu'') \hat{G}_{\mathbf{k}}(\nu_2, \nu'). \quad (4.13)$$

Hence for the free system, $\hat{\Gamma}_{\mathbf{k}}(\nu, \nu'; \nu'') = \hat{\Gamma}^0(\nu, \nu'; \nu'') \equiv \hat{\sigma}_1 \delta_{\mathcal{C}}(\nu'', \nu) \delta_{\mathcal{C}}(\nu', \nu)$. In the following, we assume the self-energy is of a DMFT type (independent of momentum). A functional

derivative of the Dyson equation at a momentum \mathbf{k} leads to

$$\begin{aligned} \hat{\Lambda}_{\mathbf{k}}(\nu, \nu'; \nu'') &= \hat{\Lambda}_{0, \mathbf{k}}(\nu, \nu'; \nu'') + \int_{\mathcal{C}} d\nu_1 d\nu_2 \hat{\Lambda}_{0, \mathbf{k}}(\nu, \nu_1; \nu'') \hat{\Sigma}(\nu_1, \nu_2) \hat{G}_{\mathbf{k}}(\nu_2, \nu') \\ &+ \int_{\mathcal{C}} d\nu_1 d\nu_2 \hat{G}_{0, \mathbf{k}}(\nu, \nu_1) \left. \frac{\delta_{\mathcal{C}}[\hat{\Sigma}(\nu_1, \nu_2)]}{\delta_{\mathcal{C}}[F_{\text{ex}}(\nu'')]} \right|_{F_{\text{ex}}=0} \hat{G}_{\mathbf{k}}(\nu_2, \nu') \\ &+ \int_{\mathcal{C}} d\nu_1 d\nu_2 \hat{G}_{0, \mathbf{k}}(\nu, \nu_1) \hat{\Sigma}(\nu_1, \nu_2) \hat{\Lambda}_{\mathbf{k}}(\nu_2, \nu'; \nu''). \end{aligned} \quad (4.14)$$

From Eq. 4.13, 4.14 and the Dyson equation, we obtain an equation for the vertex part,

$$\hat{\Gamma}_{\mathbf{k}}(\nu, \nu'; \nu'') = \hat{\Gamma}^0(\nu, \nu'; \nu'') + \left. \frac{\delta_{\mathcal{C}}[\hat{\Sigma}(\nu, \nu')]}{\delta_{\mathcal{C}}[F_{\text{ex}}(\nu'')]} \right|_{F_{\text{ex}}=0}. \quad (4.15)$$

Hence the vertex does not depend on \mathbf{k} , either. Since in the diagrammatic approximations the expression for the self-energy is known, we can evaluate $\frac{\delta_{\mathcal{C}}[\hat{\Sigma}(\nu, \nu')]}{\delta_{\mathcal{C}}[F_{\text{ex}}(\nu'')]}$ explicitly. In our case, the diagrammatic expressions for the vertex part are as displayed in Fig. 4.14 (b) for the unrenormalized Migdal approximation and (c) for the self-consistent Migdal approximation as will be shown in the following. Main difference between these two approximations is the third and the fourth diagrams in Fig. 4.14(c).

The expression for the dynamical pair susceptibility is,

$$\begin{aligned} \chi_{\text{pair}}(\nu, \nu') &= \left. \frac{\delta_{\mathcal{C}}[-i \text{tr}\{\hat{\sigma}_1 \hat{G}_{\text{loc}}(\nu, \nu + 0_c^+)\}]}{\delta_{\mathcal{C}}[F_{\text{ex}}(\nu')]} \right|_{F_{\text{ex}}=0} = -i \text{tr} \left[\hat{\sigma}_1 \frac{1}{N} \sum_{\mathbf{k}} \hat{\Lambda}_{\mathbf{k}}(\nu, \nu + 0_c^+; \nu') \right] \\ &= -i \int_{\mathcal{C}} d\nu_1 d\nu_2 \text{tr} \left[\sigma_1 \frac{1}{N} \sum_{\mathbf{k}} \hat{G}_{\mathbf{k}}(\nu, \nu_1) \hat{\Gamma}(\nu_1, \nu_2; \nu') \hat{G}_{\mathbf{k}}(\nu_2, \nu + 0_c^+) \right]. \end{aligned} \quad (4.16)$$

The diagrammatic expression for $\chi_{\text{pair}}(\nu, \nu')$ is shown in 4.14 (a). Now let us evaluate the vertex Γ for each approximation.

1. The unrenormalized Migdal approximation (uMig):

The self-energy of electron is expressed as

$$\hat{\Sigma}^{\text{uMig}}(\nu, \nu') = ig^2 D_0(\nu, \nu') \frac{1}{N} \sum_{\mathbf{k}} \hat{\sigma}_3 \hat{G}_{\mathbf{k}}(\nu, \nu') \hat{\sigma}_3. \quad (4.17)$$

Then we have

$$\left. \frac{\delta_{\mathcal{C}}[\hat{\Sigma}(\nu, \nu')]}{\delta_{\mathcal{C}}[F_{\text{ex}}(\nu'')]} \right|_{F_{\text{ex}}=0} = ig^2 D_0(\nu, \nu') \frac{1}{N} \sum_{\mathbf{k}} \int_{\mathcal{C}} d\nu_1 d\nu_2 \hat{\sigma}_3 \hat{G}_{\mathbf{k}}(\nu, \nu_1) \hat{\Gamma}(\nu_1, \nu_2; \nu'') \hat{G}_{\mathbf{k}}(\nu_2, \nu') \hat{\sigma}_3, \quad (4.18)$$

hence

$$\begin{aligned} \hat{\Gamma}(\nu, \nu'; \nu'') &= \hat{\Gamma}^0(\nu, \nu'; \nu'') \\ &+ ig^2 D_0(\nu, \nu') \frac{1}{N} \sum_{\mathbf{k}} \int_{\mathcal{C}} d\nu_1 d\nu_2 \hat{\sigma}_3 \hat{G}_{\mathbf{k}}(\nu, \nu_1) \hat{\Gamma}(\nu_1, \nu_2; \nu'') \hat{G}_{\mathbf{k}}(\nu_2, \nu') \hat{\sigma}_3. \end{aligned} \quad (4.19)$$

This equation is represented in Fig. 4.14(b).

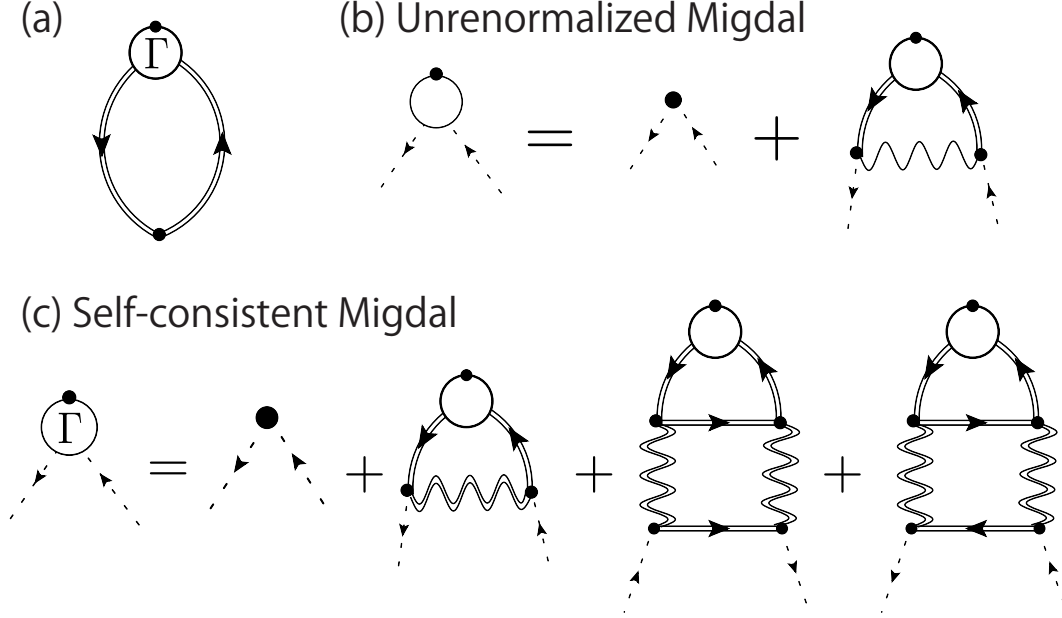


Figure 4.14: Diagrammatic expressions in the Nambu formalism. Open circles represent $\hat{\Gamma}$, while solid circles $\hat{\sigma}_1$ (bare vertex). (a) The dynamical pair susceptibility, (b) the vertex in the unrenormalized Migdal approximation, and (c) the vertex in the Migdal approximation.

2. The self-consistent Migdal approximation (sMig):

The electron self-energy (Σ) and phonon self-energy (Π) are expressed as

$$\hat{\Sigma}^{\text{sMig}}(\nu, \nu') = ig^2 D_{\text{loc}}(\nu, \nu') \frac{1}{N} \sum_{\mathbf{k}} \hat{\sigma}_3 \hat{G}_{\mathbf{k}}(\nu, \nu') \hat{\sigma}_3, \quad (4.20)$$

$$\Pi^{\text{sMig}}(\nu, \nu') = -ig^2 \text{tr}[\hat{\sigma}_3 \hat{G}_{\text{loc}}(\nu, \nu') \hat{\sigma}_3 \hat{G}_{\text{loc}}(\nu', \nu)]. \quad (4.21)$$

From this, we obtain

$$\begin{aligned} \frac{\delta_{\mathcal{C}}[\hat{\Sigma}(\nu, \nu')]}{\delta_{\mathcal{C}}[F_{\text{ex}}(\nu'')]} &= ig^2 D_{\text{loc}}(\nu, \nu') \frac{1}{N} \sum_{\mathbf{k}} \int_{\mathcal{C}} d\nu_1 d\nu_2 \hat{\sigma}_3 \hat{G}_{\mathbf{k}}(\nu, \nu_1) \hat{\Gamma}(\nu_1, \nu_2; \nu'') \hat{G}_{\mathbf{k}}(\nu_2, \nu') \hat{\sigma}_3 \\ &\quad + ig^2 \Omega(\nu, \nu'; \nu'') \hat{\sigma}_3 \hat{G}_{\text{loc}}(\nu, \nu') \hat{\sigma}_3, \end{aligned} \quad (4.22)$$

where we have defined

$$\Omega(\nu, \nu'; \nu'') \equiv \frac{\delta_{\mathcal{C}}[D_{\text{loc}}(\nu, \nu')]}{\delta_{\mathcal{C}}[F_{\text{ex}}(\nu'')]} \quad (4.23)$$

Now we introduce

$$\Theta(\nu, \nu'; \nu'') \equiv \int_{\mathcal{C}} d\nu_1 d\nu_2 D_{\text{loc}}^{-1}(\nu, \nu_1) \Omega(\nu_1, \nu_2; \nu'') D_{\text{loc}}^{-1}(\nu_2, \nu'). \quad (4.24)$$

From the Dyson equation for the phonon Green's function and through the same procedure

as for Λ , it turns out that

$$\begin{aligned}
 \Theta(\nu, \nu'; \nu'') &= \frac{\delta_{\mathcal{C}}[\Pi(\nu, \nu')]}{\delta_{\mathcal{C}}[F_{\text{ex}}(\nu'')]} \\
 &= -ig^2 \text{tr}[\hat{\sigma}_3 \frac{1}{N} \sum_{\mathbf{k}} \int_{\mathcal{C}} d\nu_1 d\nu_2 \hat{G}_{\mathbf{k}}(\nu, \nu_1) \hat{\Gamma}(\nu_1, \nu_2; \nu'') \hat{G}_{\mathbf{k}}(\nu_2, \nu') \hat{\sigma}_3 \hat{G}_{\text{loc}}(\nu', \nu)] \\
 &\quad - ig^2 \text{tr}[\hat{\sigma}_3 \hat{G}_{\text{loc}}(\nu, \nu') \hat{\sigma}_3 \frac{1}{N} \sum_{\mathbf{k}} \int_{\mathcal{C}} d\nu_1 d\nu_2 \hat{G}_{\mathbf{k}}(\nu', \nu_1) \hat{\Gamma}(\nu_1, \nu_2; \nu'') \hat{G}_{\mathbf{k}}(\nu_2, \nu)]. \quad (4.25)
 \end{aligned}$$

Then final expression for the vertex function becomes

$$\begin{aligned}
 \hat{\Gamma}(\nu, \nu'; \nu'') &= \hat{\sigma}_1 \delta_{\mathcal{C}}(\nu'', \nu) \delta_{\mathcal{C}}(\nu'', \nu') \\
 &\quad + ig^2 D(\nu, \nu') \frac{1}{N} \sum_{\mathbf{k}} \int_{\mathcal{C}} d\nu_1 d\nu_2 \hat{\sigma}_3 \hat{G}_{\mathbf{k}}(\nu, \nu_1) \hat{\Gamma}(\nu_1, \nu_2; \nu'') \hat{G}_{\mathbf{k}}(\nu_2, \nu') \hat{\sigma}_3 \\
 &\quad + g^4 \hat{\sigma}_3 \hat{G}_{\text{loc}}(\nu, \nu') \hat{\sigma}_3 \int_{\mathcal{C}} d\nu_3 d\nu_4 D_{\text{loc}}(\nu, \nu_3) D_{\text{loc}}(\nu_4, \nu') \\
 &\quad \times \{ \text{tr}[\hat{\sigma}_3 \frac{1}{N} \sum_{\mathbf{k}} \int_{\mathcal{C}} d\nu_1 d\nu_2 \hat{G}_{\mathbf{k}}(\nu_3, \nu_1) \hat{\Gamma}(\nu_1, \nu_2; \nu'') \hat{G}_{\mathbf{k}}(\nu_2, \nu_4) \hat{\sigma}_3 \hat{G}_{\text{loc}}(\nu_4, \nu_3)] \\
 &\quad + \text{tr}[\hat{\sigma}_3 \hat{G}_{\text{loc}}(\nu_3, \nu_4) \hat{\sigma}_3 \frac{1}{N} \sum_{\mathbf{k}} \int_{\mathcal{C}} d\nu_1 d\nu_2 \hat{G}_{\mathbf{k}}(\nu_4, \nu_1) \hat{\Gamma}(\nu_1, \nu_2; \nu'') \hat{G}_{\mathbf{k}}(\nu_2, \nu_3)] \}. \quad (4.26)
 \end{aligned}$$

This equation is represented in Fig. 4.14(c).

Comparing the expressions for the vertex in these approximations, one finds that the 3rd and 4th diagrams in Fig. 4.14(c) can be interpreted as an effect of non-equilibrium dynamics of phonons, since within the fixed-phonon picture (Fig. 4.14(b)) these diagrams are absent. We also note that the vertex of the BCS dynamics, which does not take account of the phonon dynamics, is obtained by replacing the phonon propagator in Fig. 4.14(b) with the BCS interaction. To decompose various contributions, we evaluate certain subsets of the diagrams for χ_{pair} . The first set is $\chi_{\text{el-ladder}}$ in Fig. 4.16 (a). This has the same diagrammatic structure as those for the pair susceptibility from the BCS and for the unrenormalized Migdal approximation, Fig. 4.14(b). Hence we can regard $\chi_{\text{el-ladder}}$ as the contribution without phonon dynamics. Indeed, we can evaluate $\chi_{\text{el-ladder}}$ from time evolution with

$$\hat{\Sigma}(\nu, \nu') = ig^2 D_{\text{loc,eq}}(\nu, \nu') \frac{1}{N} \sum_{\mathbf{k}} \hat{\sigma}_3 \hat{G}_{\mathbf{k}}(\nu, \nu') \hat{\sigma}_3, \quad (4.27a)$$

$$\Pi(\nu, \nu') = -ig^2 \text{tr}[\hat{\sigma}_3 \hat{G}_{\text{loc,eq}}(\nu, \nu') \hat{\sigma}_3 \hat{G}_{\text{loc,eq}}(\nu', \nu)]. \quad (4.27b)$$

Here, "eq" indicates that they are fixed in equilibrium. Therefore, with this dynamics, we take into account the phonon renormalization from the el-ph coupling but we do not take into its dynamics out of equilibrium.

On the other hand, by eliminating the 2nd diagram in the vertex in Fig. 4.14(c), we obtain a set of diagrams for the pair susceptibility, i.e. $\chi_{\text{ph-ladder}}$ in Fig. 4.16(b), which represents the contribution of the phonon dynamics through the 3rd and 4th diagrams in Fig. 4.14(c). This

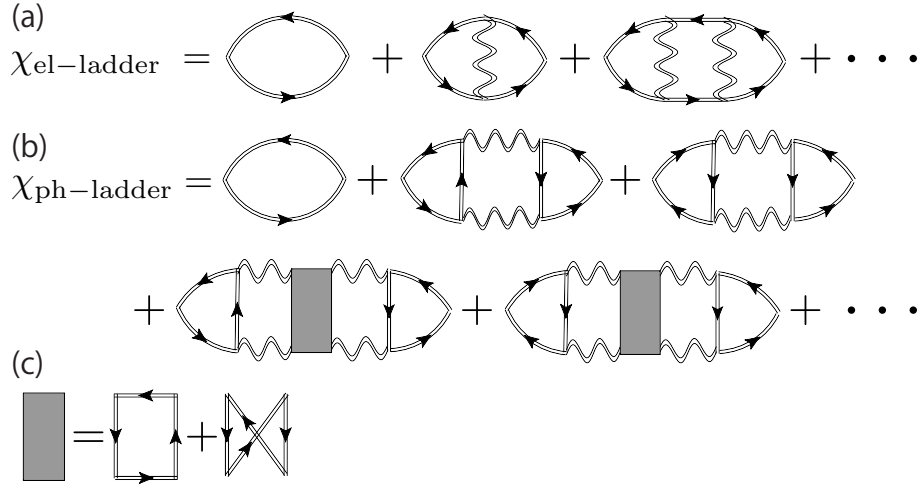


Figure 4.15: Diagrammatic expression for (a) $\chi_{\text{el-ladder}}$, (b) $\chi_{\text{ph-ladder}}$ and (c) the electron-mediated phonon-phonon interaction.

diagram can be evaluated by considering dynamics described by

$$\hat{\Sigma}(\nu, \nu') = ig^2 D_{\text{loc}}(\nu, \nu') \frac{1}{N} \sum_{\mathbf{k}} \hat{\sigma}_3 \hat{G}_{\text{eq}, \mathbf{k}}(\nu, \nu') \hat{\sigma}_3, \quad (4.28a)$$

$$\Pi(\nu, \nu') = -ig^2 \text{tr}[\hat{\sigma}_3 \hat{G}_{\text{loc}}(\nu, \nu') \hat{\sigma}_3 \hat{G}_{\text{loc}}(\nu', \nu)]. \quad (4.28b)$$

In Fig. 4.16, we show the comparison among χ_{pair} , $\chi_{\text{el-ladder}}$ and $\chi_{\text{ph-ladder}}$ against t (a) and ω (b). It turns out that each of $\chi_{\text{el-ladder}}(t)$ and $\chi_{\text{ph-ladder}}(t)$ shows oscillations with a single characteristic frequency, where their Fourier transformation shows that these frequencies agree well with ω_{H} and ω_{H2} , respectively. Hence ω_{H} and ω_{H2} are mainly determined by the process represented by $\chi_{\text{el-ladder}}$ and $\chi_{\text{ph-ladder}}$, respectively.

As for the question(1), we first note that the 2nd and 3rd diagrams for $\chi_{\text{ph-ladder}}$ are expected to give rise to $2\omega_r$ -oscillation due to the two parallel phonon propagators in them. This indicates that in SC the effect of the *electron mediated effective interaction between phonons* (the shaded box in Fig. 4.16(c)) becomes more significant than in the normal state, and pushes up the energy of the collective mode to ω_{H2} above $2\omega_r$. We note that even in the normal states we can observe the discrepancy between ω_{H2} and $2\omega_r$ increases as we increase the el-ph coupling g , which can again be attributed to the phonon-phonon interaction. However, the effect is small compared to that in SC.

Let us discuss this issue in more detail. First, the expected $2\omega_r$ -oscillation from the effect of the 2nd and 3rd diagrams for $\chi_{\text{ph-ladder}}$ can be confirmed by considering another susceptibility which is easier to access. We note that a direct evaluation of these diagrams in $\chi_{\text{ph-ladder}}$ is numerically very demanding. Here we focus on

$$\kappa^R(t) \equiv -i\theta(t) \langle [XX(t), B_0] \rangle \quad (4.29)$$

(response of XX against the external pair field). This quantity is evaluated from $\Omega(t, t'; t'')$ defined in Eq. 4.23. We evaluate a sub-set of diagrams, $\kappa_{\text{ph-ladder}}$, corresponding to $\chi_{\text{ph-ladder}}$, from the dynamics described by Eq. 4.28. In Fig. 4.17(c) we show the diagrammatic expression

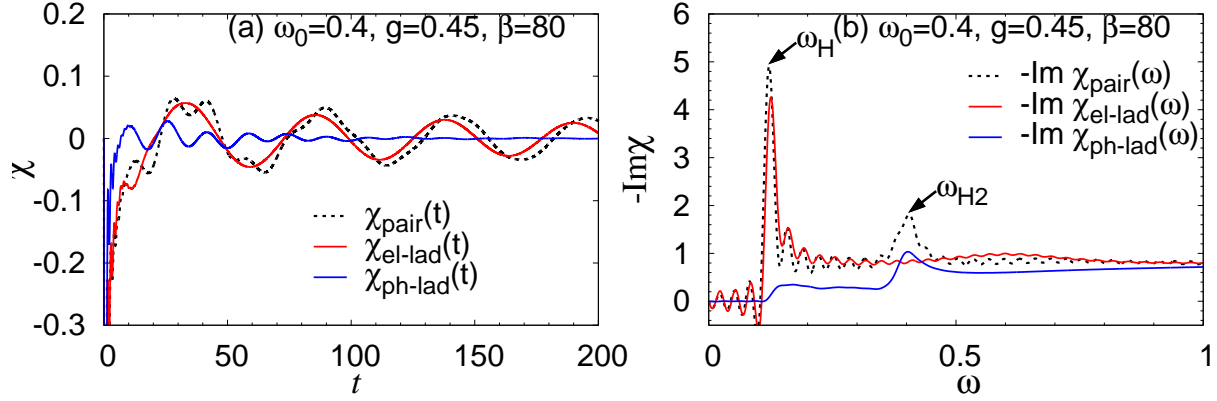


Figure 4.16: (a) Comparison of $\chi(t)$ evaluated for different diagrams for $g = 0.45, \omega_0 = 0.4, \beta = 80$. (b) Comparison of $-\text{Im}\chi(\omega)$ evaluated for different diagrams for $g = 0.45, \omega_0 = 0.4, \beta = 80$.

for $\kappa_{\text{ph-ladder}}$. From the expression one can see that the 1st diagram in $\kappa_{\text{ph-ladder}}$ corresponds to the 2nd and 3rd ones in $\chi_{\text{ph-ladder}}$. In the following, we express the contribution from the first diagram in Fig. 4.17(c) as $\kappa_{\text{ph-lowest}}$. Fig. 4.17(a)(b) show the comparison of $\kappa(\omega)$ from the full dynamics in the self-consistent Migdal approximation, $\kappa_{\text{ph-lowest}}(\omega)$, $\kappa_{\text{ph-ladder}}(\omega)$ and the phonon spectrum $B(\omega)$. Again, we choose $t_{\text{max}} = 200$. From the figure, we find that $\kappa_{\text{ph-lowest}}(\omega)$ indeed shows a peak at $2\omega_r$, which is different from $\omega_{\text{H}2}$. However, once we take into account the effect of the ph-ph interaction in $\kappa_{\text{ph-ladder}}(\omega)$, there emerges a peak around $\omega_{\text{H}2}$ as in the analysis of the dynamical pair susceptibility.

Now we consider the origin of the different effects of the ph-ph interaction in SC and in normal states. The expression for the ph-ph interaction on the KB contour, Fig. 4.16(c), is

$$I_{\text{ph}}(\nu_1, \nu_2, \nu_3, \nu_4) \equiv \frac{g^4}{N} \sum_{\mathbf{k}} \{ \text{tr}[\hat{\sigma}_3 \hat{G}_{\text{loc}}(\nu_1, \nu_2) \hat{\sigma}_3 \hat{G}_{\mathbf{k}}(\nu_2, \nu_4) \hat{\sigma}_3 \hat{G}_{\text{loc}}(\nu_4, \nu_3) \hat{\sigma}_3 \hat{G}_{\mathbf{k}}(\nu_3, \nu_1)] \\ + \text{tr}[\hat{\sigma}_3 \hat{G}_{\text{loc}}(\nu_1, \nu_2) \hat{\sigma}_3 \hat{G}_{\mathbf{k}}(\nu_2, \nu_3) \hat{\sigma}_3 \hat{G}_{\text{loc}}(\nu_3, \nu_4) \hat{\sigma}_3 \hat{G}_{\mathbf{k}}(\nu_4, \nu_1)] \}. \quad (4.30)$$

Here we focus on the Matsubara components,

$$I_{\text{ph}}^{\text{M}}(\tau_1, \tau_2, \tau_3) \equiv \frac{g^4}{N} \sum_{\mathbf{k}} \{ \text{tr}[\hat{\sigma}_3 \hat{G}_{\text{loc}}(\tau_1 - \tau_2) \hat{\sigma}_3 \hat{G}_{\mathbf{k}}(\tau_2) \hat{\sigma}_3 \hat{G}_{\text{loc}}(-\tau_3) \hat{\sigma}_3 \hat{G}_{\mathbf{k}}(\tau_3 - \tau_1)] \\ + \text{tr}[\hat{\sigma}_3 \hat{G}_{\text{loc}}(\tau_1 - \tau_2) \hat{\sigma}_3 \hat{G}_{\mathbf{k}}(\tau_2 - \tau_3) \hat{\sigma}_3 \hat{G}_{\text{loc}}(\tau_3) \hat{\sigma}_3 \hat{G}_{\mathbf{k}}(-\tau_1)] \}, \quad (4.31)$$

$$I_{\text{ph}}^{\text{M}}(i\nu_{n_1}, i\nu_{n_2}, i\nu_{n_3}) = \int_0^\beta d\tau_1 d\tau_2 d\tau_3 e^{i\nu_{n_1}\tau_1} e^{i\nu_{n_2}\tau_2} e^{i\nu_{n_3}\tau_3} I_{\text{ph}}^{\text{M}}(\tau_1, \tau_2, \tau_3), \quad (4.32)$$

where $\nu_{n_\alpha} = 2n_\alpha\pi/\beta$.

In order to understand different effects of the ph-ph interaction in the SC phase and the normal phase, we evaluate $I_{\text{ph}}^{\text{M}}(i\nu_{n_1}, i\nu_{n_2}, i\nu_{n_3})$ from the Green's function for a free system and the BCS Green's function. The former represents the normal state and the latter the SC state. We consider the attractive interaction (the attractive Hubbard model on the Bethe lattice)

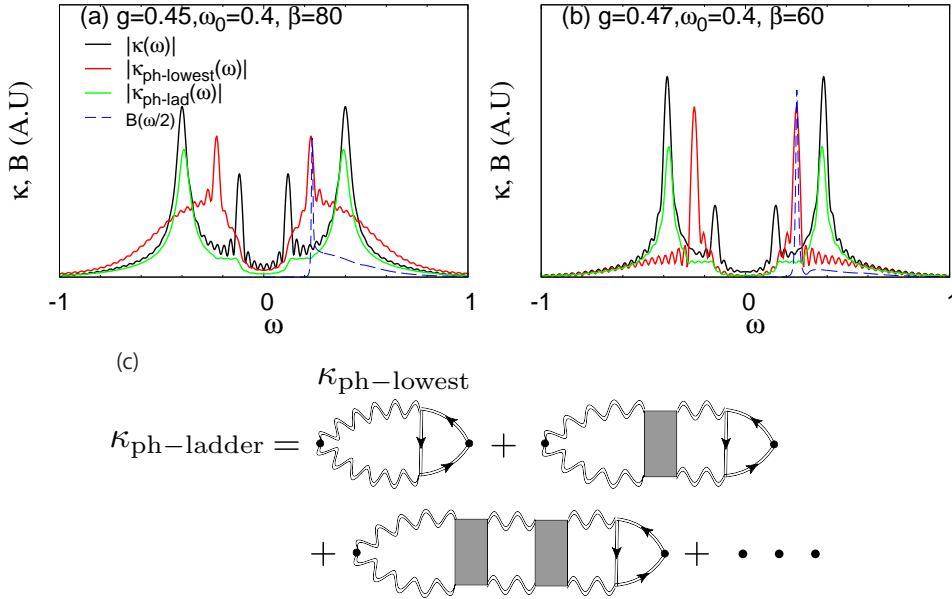


Figure 4.17: (a)(b) Comparison of $\kappa^R(\omega)$ evaluated from different sets of diagrams along with the phonon spectrum, $B(\omega)$, for $g = 0.45$, $\omega_0 = 0.4$, $\beta = 80$ (a) or $g = 0.47$, $\omega_0 = 0.4$, $\beta = 60$ (b). (c) Diagrammatic expression for $\kappa_{\text{ph-ladder}}$ and $\kappa_{\text{ph-lowest}}$.

with $U = -1$ at $\beta = 400$, where the SC gap Δ_{BCS} is 0.128. In Fig. 4.18, we show the results for the normal and SC states. First we note that $I_{\text{ph}}^{\text{M}}(i\nu_{n_1}, i\nu_{n_2}, i\nu_{n_3})$ is real. In the normal state, the ph-ph interaction ($I_{\text{ph}}^{\text{M}}(i\nu_{n_1}, i\nu_{n_2}, i\nu_{n_3})$) strongly depends on the Matsubara frequency and has a clear sign change. On the other hand, in the SC phase, there is a drastic change from the normal state. Namely, in the frequency regime comparable to the SC gap, the frequency dependence becomes much weaker and the sign change disappears. This lets us to approximate $I_{\text{ph}}^{\text{M}}(i\nu_{n_1}, i\nu_{n_2}, i\nu_{n_3})$ by a constant in the SC state to understand its effect. From a comparison with diagrams that appear in the perturbation expansion of a simple phonon model with an anharmonic term, $H_{\text{eff,ph}} = \omega_{\text{ph}} a^\dagger a + IX^4$, it turns out that an approximate constant $I_{\text{ph}}^{\text{M}}(i\nu_{n_1}, i\nu_{n_2}, i\nu_{n_3})$ corresponds to the case of $I > 0$. Since the anharmonic term makes the potential steeper, the frequency of the coherent oscillations increases for $I > 0$. This consideration is indeed consistent with our observation of hardening from $2\omega_r$ to $\omega_{\text{H}2}$ in the SC phase. In the normal state, it is expected that the cancellation from the sign change in the frequency dependence reduces this effect.

As for effects of phonon dynamics on the amplitude Higgs mode (the question(2)), even though the response without phonon dynamics mainly sets the energy scale of the Higgs mode, there does exist an effect from the phonon dynamics. This effect appears as the difference in the phase of the Higgs oscillation in $\chi_{\text{pair}}(t)$ and $\chi_{\text{el-ladder}}(t)$, where the latter tends to slightly overestimate ω_{H} than the former by several percent, see Fig. 4.16. This difference can be attributed to the rest of the diagrams in χ_{pair} besides those in $\chi_{\text{el-ladder}}$ and $\chi_{\text{ph-ladder}}$. These diagrams hybridize fermion ladders and phonon ladders, and the decrease of ω_{H} from that in $\chi_{\text{el-ladder}}$ can be understood as an effect of the hybridization between the Higgs mode

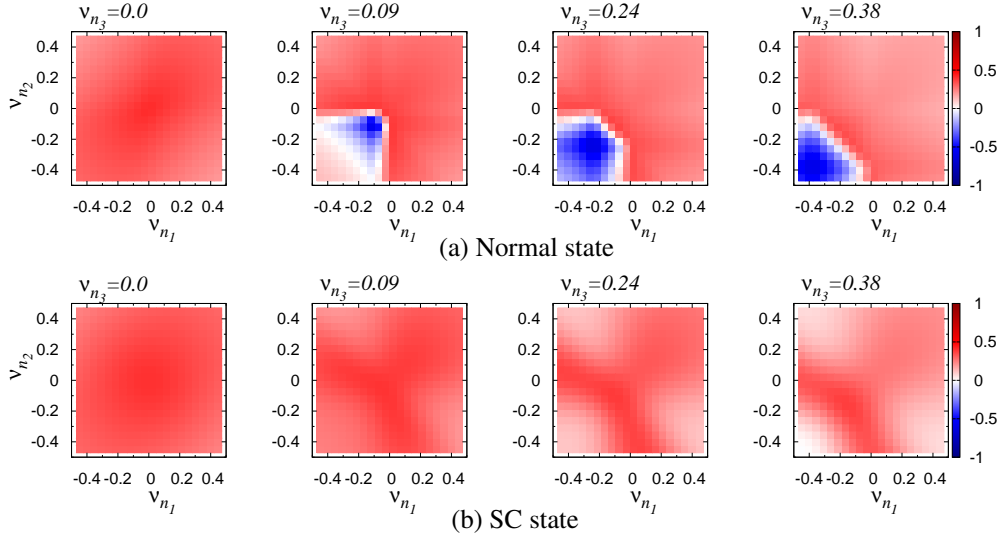


Figure 4.18: (a) $I_{\text{ph}}^{\text{M}}(i\nu_{n_1}, i\nu_{n_2}, i\nu_{n_3})/g^4$ for various values of ν_{n_3} in the normal state evaluated with the Green's function for a free case. (b) $I_{\text{ph}}^{\text{M}}(i\nu_{n_1}, i\nu_{n_2}, i\nu_{n_3})/g^4$ in the SC state evaluated with the BCS Green's function for an attractive $U = -1$. The temperature is $1/\beta = 1/400$ in both cases.

in $\chi_{\text{el-ladder}}$ and the phonon-origin mode in $\chi_{\text{ph-ladder}}$.

4.2.4 Experimental accessibility

Let us now discuss accessibility of the collective modes with the pump-probe experiments. As an observable, we focus on the dynamics of the spectral function that can be observed in the time-resolved photoemission spectroscopy (PES) [167],

$$A_{\text{PES}}(t_{\text{probe}}, \omega) \equiv \frac{1}{\pi} \text{Im} \int dt \int dt' s(t - t_{\text{probe}}) s(t' - t_{\text{probe}}) e^{i\omega(t-t')} G_{\text{loc}}^<(t, t'). \quad (4.33)$$

Here $s(t)$ is the form of the probe pulse and we use a gaussian, $s(t) = \frac{1}{\sqrt{2\pi}\sigma_{\text{probe}}} \exp(-\frac{t^2}{2\sigma_{\text{probe}}^2}) \theta(t_c - |t|)$, with a sufficient large cutoff time t_c to save the calculation cost. As for the pump of the system, we consider the modulation of the hopping parameter,

$$v(t) = v_0 + \delta v \exp \left[-\frac{(t - t_{\text{pump}})^2}{2\sigma_{\text{pump}}^2} \right], \quad (4.34)$$

where σ_{pump} and t_{pump} stand for the width and the center of the pump pulse, respectively. We note that this type of pump can be effectively realized with a strong and high frequency laser [168]. We also note that the same effect can be expected from light-induced lattice distortions [12, 51, 100]. With this setup, we focus on the linear-response of $A_{\text{PES}}(t_{\text{probe}}, \omega)$ against δv . To this end, we define a function,

$$A'_{\text{PES}}(t_{\text{probe}}, \omega; t_{\text{pump}}, \sigma_{\text{pump}}) \equiv \lim_{\delta v \rightarrow 0} \frac{A_{\text{PES}}(t_{\text{probe}}, \omega; t_{\text{pump}}, \sigma_{\text{pump}}, \delta v) - A_{\text{PES}}(t_{\text{probe}}, \omega; t_{\text{pump}}, \sigma_{\text{pump}}, 0)}{\delta v} \quad (4.35)$$

4.2. COLLECTIVE EXCITATIONS IN STRONGLY-COUPLED SUPERCONDUCTORS

where $A_{\text{PES}}(t_{\text{probe}}, \omega; t_{\text{pump}}, \sigma_{\text{pump}}, \delta v)$ represents the spectrum after pumping the system with the pulse characterized by $t_{\text{pump}}, \sigma_{\text{pump}}, \delta v$. In the following we fix the pump condition as $t_{\text{pump}} = 5.0$ and $\sigma_{\text{pump}} = 1.0$ and change the probe condition. In order to study how $A'_{\text{PES}}(t_{\text{probe}}, \omega; t_{\text{pump}}, \sigma_{\text{pump}})$ changes along t_{probe} , we make a Fourier transformation focusing on $[t_c, t_{\text{max}} - t_c]$ as

$$A'_{\text{PES}}(\omega_t, \omega; t_{\text{pump}}, \sigma_{\text{pump}}) \equiv \int_{t_c}^{t_{\text{max}} - t_c} dt A_{\text{PES}}(t, \omega; t_{\text{pump}}, \sigma_{\text{pump}}) e^{i\omega_t t}. \quad (4.36)$$

Results are shown in Fig. 4.19 and Fig. 4.20. Significant signals can be observed in a wide energy range for $\omega \lesssim 0$. We note that, as can be seen from the expression for $A_{\text{PES}}(t_{\text{probe}}, \omega)$, we have worse resolution for the time evolution while the resolution for ω increases with increasing the width of the probe pulse. $|A'_{\text{PES}}(\omega_t, \omega; 5.0, 1.0)|$ exhibits two peaks against ω_t at ω_H and ω_{H2} . Hence our calculation predicts that the collective excitation can be observed with pump-probe experiments as oscillations in PES spectra in a wide range of ω , especially near the band edge ($\omega \sim W/2 = 2$ here) and the gap edge ($\omega \sim \Delta_{\text{SC}} = 0.06 \sim 0.08$ here).

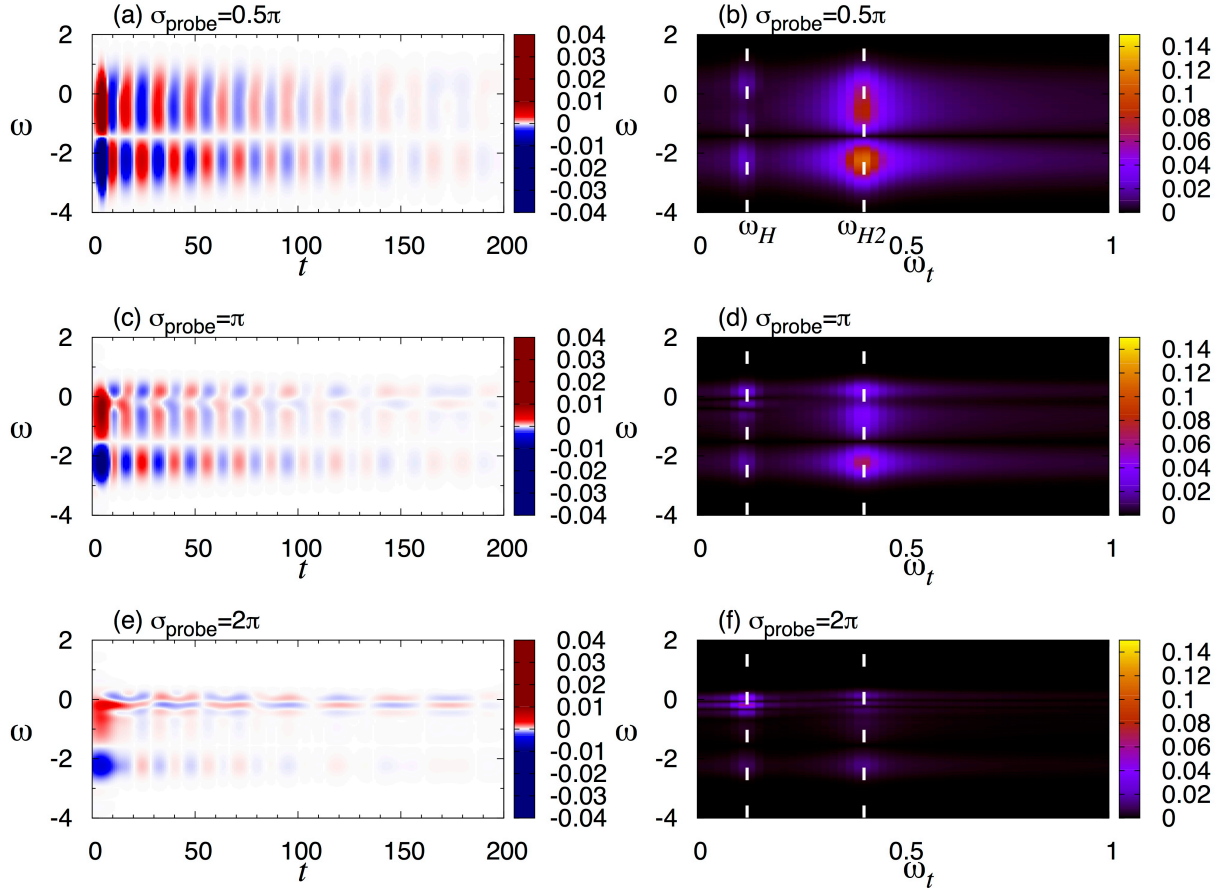


Figure 4.19: (a)(c)(e) $A'_{\text{PES}}(t, \omega; 5.0, 1.0)$ against t and ω for various values of σ_{probe} at $g = 0.45, \omega_0 = 0.4, \beta = 80$. (b)(d)(f) $|A'_{\text{PES}}(\omega_t, \omega; 5.0, 1.0)|$ against t and ω for various values of σ_{probe} at $g = 0.45, \omega_0 = 0.4, \beta = 80$ with $t_c = 25$. The white vertical lines in (b)(d)(f) indicate ω_H and ω_{H2} .

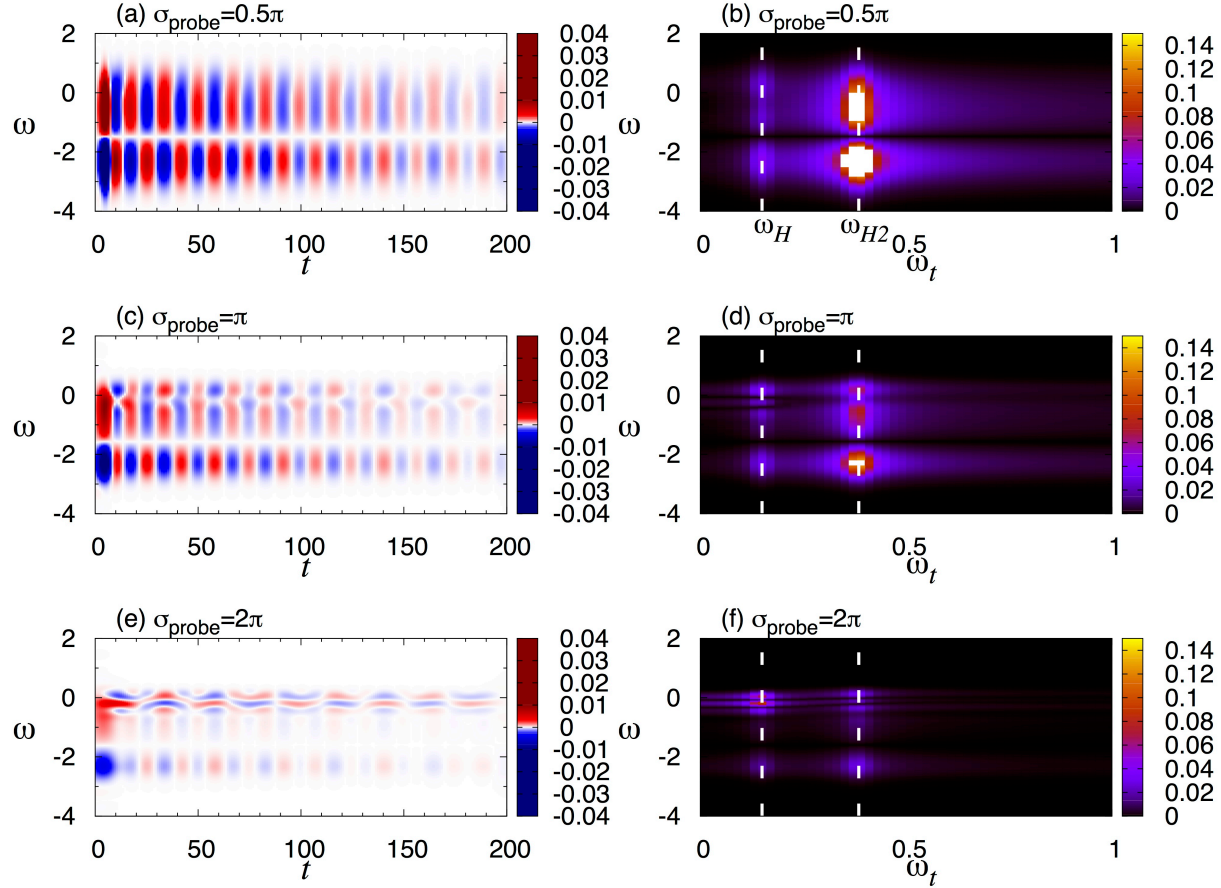


Figure 4.20: A plot similar to Fig. 4.19 for g increased from 0.45 to 0.47 and β changed from 80 to 60.

4.2.5 Decay of the amplitude Higgs mode: Effect of quasiparticle lifetime

In the conventional analyses based on the BCS theory, the amplitude Higgs mode decay to the quasi-particles with an infinite lifetime. Here, we study effects of a finite electron quasiparticle lifetime from strong el-ph couplings on the decay of the amplitude Higgs mode. In order to extract the effects only, in this section, we do not consider the phonon dynamics or decay to phonons and assume that phonons are always in equilibrium due to some couplings with other (bath) degrees of freedom (open systems). This picture is implemented by the unrenormalized Migdal approximation. This analysis predicts a crossover of the decay of the amplitude Higgs mode from a power law to an exponential law. This feature is outside the BCS theory.

As is pointed out above, the expression for the dynamical pair susceptibility in the unrenormalized Migdal approximation has the same structure as in the BCS theory [33], except that the interaction includes the retardation effect. Since we are considering open systems we do not

need to confine ourselves to the phonon of the Holstein type, i.e.,

$$D_0^R(\omega) = \frac{2\omega_0}{(\omega + i0^+)^2 - \omega_0^2}, \quad (4.37)$$

$$B_0(\omega) = -\frac{1}{\pi} \text{Im} D_0^R(\omega) = \delta(\omega - \omega_0) - \delta(\omega + \omega_0).$$

We can also think of phonons with a finite lifetime, which phenomenologically represents the case in which the phonons have coupling to degrees of freedom outside the system and energy can dissipate into them so that the phonon part stays in equilibrium. Here the phonon part can be expressed as

$$D_0^R(\omega, \Gamma) = \frac{2\omega_0}{(\omega + i\Gamma)^2 - \omega_0^2}, \quad (4.38)$$

$$B_0(\omega, \Gamma) = \frac{1}{\pi} \frac{\Gamma}{(\omega - \omega_0)^2 + \Gamma^2} - \frac{1}{\pi} \frac{\Gamma}{(\omega + \omega_0)^2 + \Gamma^2}, \quad (4.39)$$

where Γ ($\in \mathbb{R}$) represents the lifetime of the phonon. We note that other components of Green's functions (lesser, greater etc) are connected to the retarded part by the fluctuation-dissipation theorem [26]. In the following, we employ phonons with non-zero lifetime.

First, we study the damping of oscillations in the dynamical pair susceptibility. We note that this quantity represents how the amplitude of the order parameter evolves after a small external field of the pair potential (small d_f). We discuss the results comparing them with the BCS dynamics. In order to see how the amplitude mode decays here we employ two types of fitting curves,

$$F_1(t) = a \exp(b t) + c \sin(\omega t + d)/(t - t_0)^e, \quad (4.40)$$

$$F_2(t) = a \exp(b t) + c \sin(\omega t + d) \exp(e t), \quad (4.41)$$

where a, b, c, d, e and ω are fitting parameters. The former describes a power-law decay, while the latter is an exponential decay. We define t_0 as the center of a pump field concerned.

Since we want to make clear the difference from the BCS dynamics, we first show the dynamical pair susceptibility evaluated from it in Fig. 4.21, with the fitting form of Eq. 4.40 with $t_0 = 0$. It turns out that the fitting works very well from the first oscillation, and that the exponent is 0.5 as the previous works pointed out for various types of excitations [38, 42, 44]. We note that this behavior is realized even when the temperature is close to T_c , see the inset and panel (b) in Fig. 4.21.

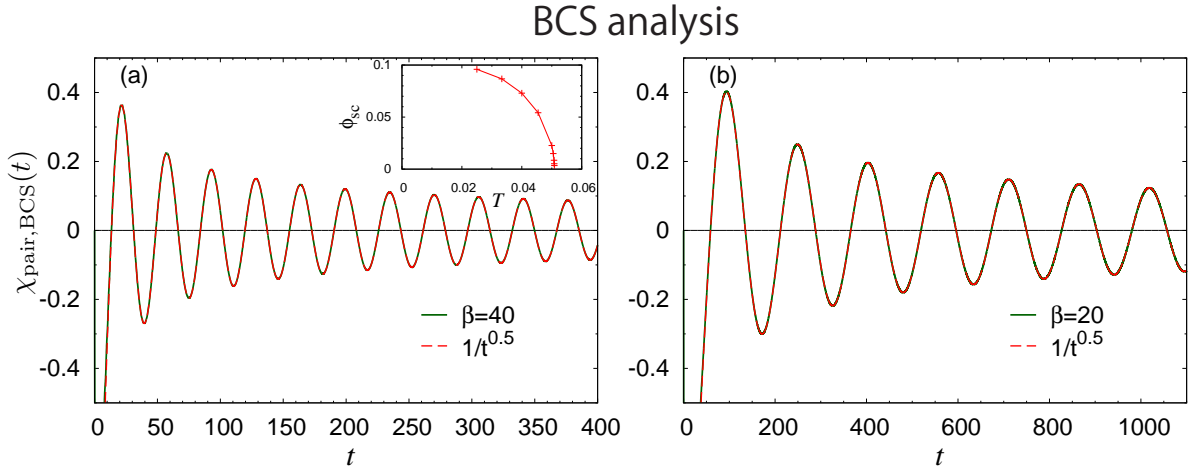


Figure 4.21: $\chi_{\text{pair,BCS}}(t)$ for $\lambda = 0.9$ at $\beta = 40$ (a) or $\beta = 20$ (b). Dashed lines represent the result of the fitting with the form of Eq. 4.40. Inset in (a) is the temperature dependence of the order parameter.

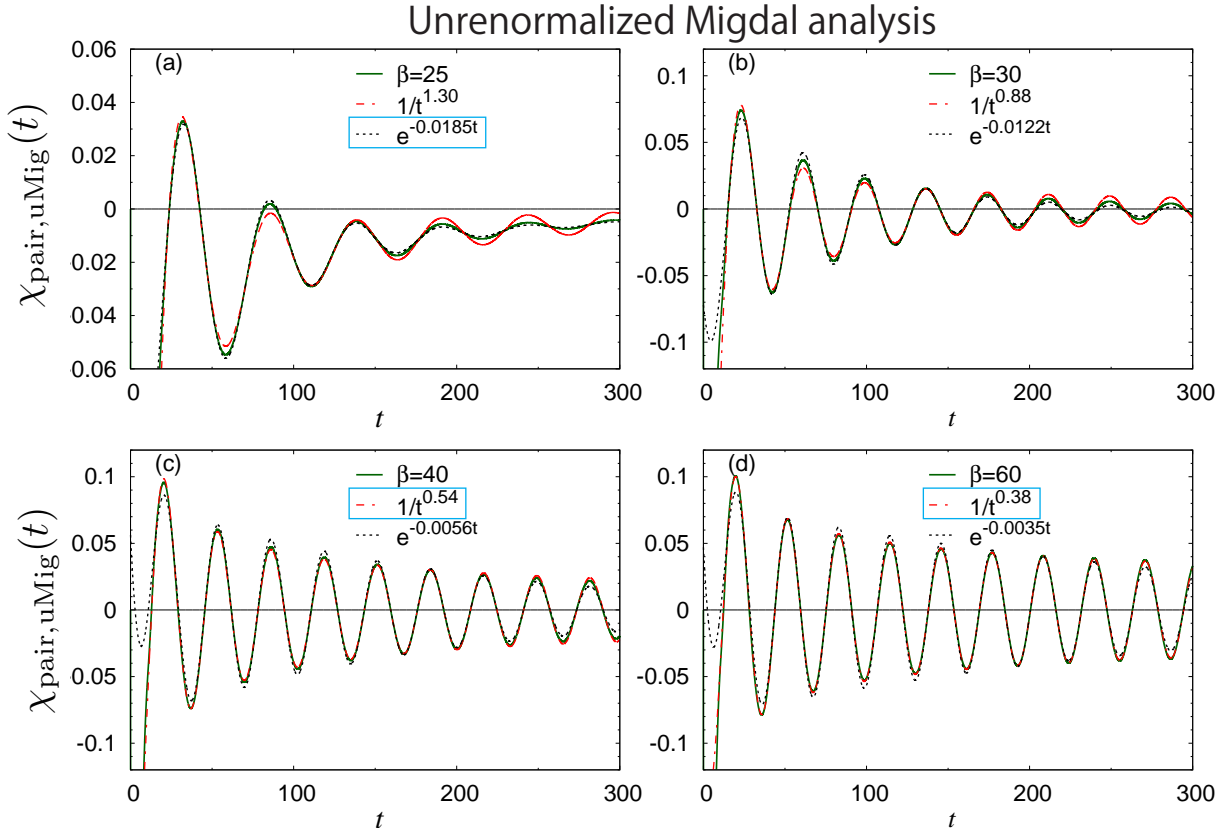


Figure 4.22: $\chi_{\text{pair,uMig}}(t)$ for $\omega_0 = 0.4$, $g = 0.9$, $\gamma = 0.1$ ($\lambda_{\text{eff}} \simeq 1.2$) at various temperatures. Power-law and exponential fits are also plotted, where the one marked with a rectangle indicates a better fit.

Now, we move onto the results with the unrenormalized Migdal approximation (phonons

in equilibrium). In Fig. 4.22, we show the pair susceptibility in this scheme, $\chi_{\text{pair,uMig}}(t)$, and fitting curves with $t_0 = 0$. We note that we could not find converged solutions of Eq. 4.40 with "FindFit" in Mathematica when we regard t_0 as a fitting parameter, but choice of t_0 turns out to be not so relevant. The result indicates a crossover between different decay laws with the temperature. When the temperature is much lower than T_c , the power-law fitting is better than the exponential one, see Fig. 4.22(c)(d). The exponent increases and the decay becomes faster with increasing temperature. Our analysis shows a smaller exponent than the BCS value (0.5) in the low-temperature regime, see Fig. 4.22(d). When the temperature is close to T_c , we have a better fit to the exponential decay as shown in Fig. 4.22(a). In between these regimes, the decay of the amplitude mode cannot be well described either with the power law or the exponential law.

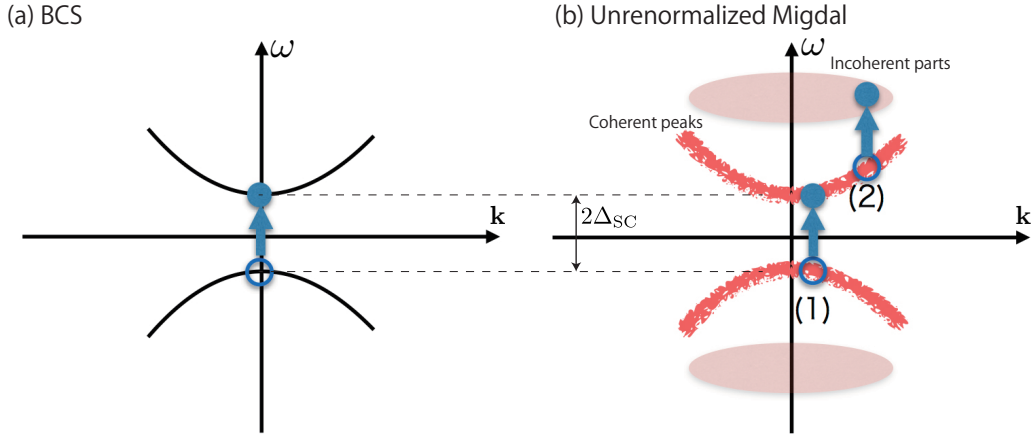


Figure 4.23: Schematic picture for the difference between BCS and unrenormalized Migdal about the decay process of the amplitude mode. An arrow indicates an excitation process from an initial state of an electron (empty circle) and a final state (filled circle). Black curves in the panel (a) express the quasi-particle dispersion with an infinite lifetime, while red thick curves in the panel (b) illustrate the dispersion of the quasi-particles with a finite lifetime. Pink ovals in the panel (b) show incoherent parts.

In the BCS theory, because of the relation $\omega_H = 2\Delta_{\text{SC}}$ and the fact that the lifetime of a quasiparticle is infinite, the relaxation channel of the amplitude mode ($\mathbf{q} = 0$) is limited to the quasiparticle excitations just at $|\mathbf{k}| = k_F$, see Fig. 4.23(a). On the other hand, the unrenormalized Migdal approximation can take into account the lifetime of the quasiparticles and incoherent parts. Therefore, it becomes possible for the amplitude Higgs mode to decay to a quasiparticle excitation from the lower band away from the Fermi surface ((1) in Fig. 4.23(b)) and to a quasiparticle excitation to incoherent parts ((2) in Fig. 4.23(b)). Since the quasiparticle lifetime decreases with increasing temperature and the latter channel needs thermally excited quasiparticles above the Fermi energy, these decay processes of the amplitude mode are expected to become larger close to T_c .

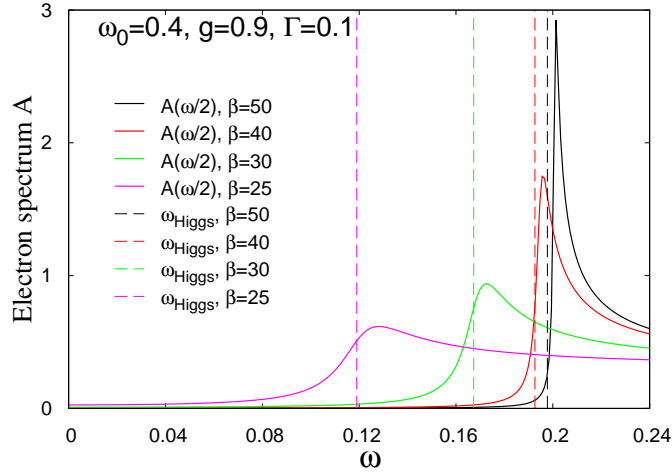


Figure 4.24: Comparison between the electron spectrum $A(\omega/2)$ and ω_{Higgs} for $\omega_0 = 0.4, g = 0.9, \gamma = 0.1$ ($\lambda_{\text{eff}} \simeq 1.2$) at various temperatures.

The former effect is indeed demonstrated in the temperature dependence of the electron spectrum, $A(\omega)$. In Fig. 4.24, we show $A(\omega)$ and the Higgs frequency derived from the fitting for various T . The gap edge becomes smoothed as we increase T , and, at the same time, the Higgs frequency is always located at the smoothed edge, i.e. $\omega_{\text{H}} \simeq 2\Delta_{\text{SC}}$. Hence we consider that near T_c possible relaxation channels of the amplitude Higgs mode increase due to the finite quasi-particle lifetimes from the strong el-ph coupling and that this leads to its exponential decay as we have observed above. We also note that we have observed smaller exponents of the power-law decay at low-temperatures compared to the BCS value at least for several oscillations. With decreasing temperatures, the SC edge becomes shaper, and, strictly speaking, the Higgs frequency is slightly below $2\Delta_{\text{SC}}$. This condition leads to the suppression of available quasiparticle states for the relaxation of the Higgs mode. We note that, to speak of extremes, if the collective mode is completely below the gap, there is no relaxation to quasiparticles and the mode is undamped. The present case is considered to be a middle situation of the BCS situation and the extreme situation.

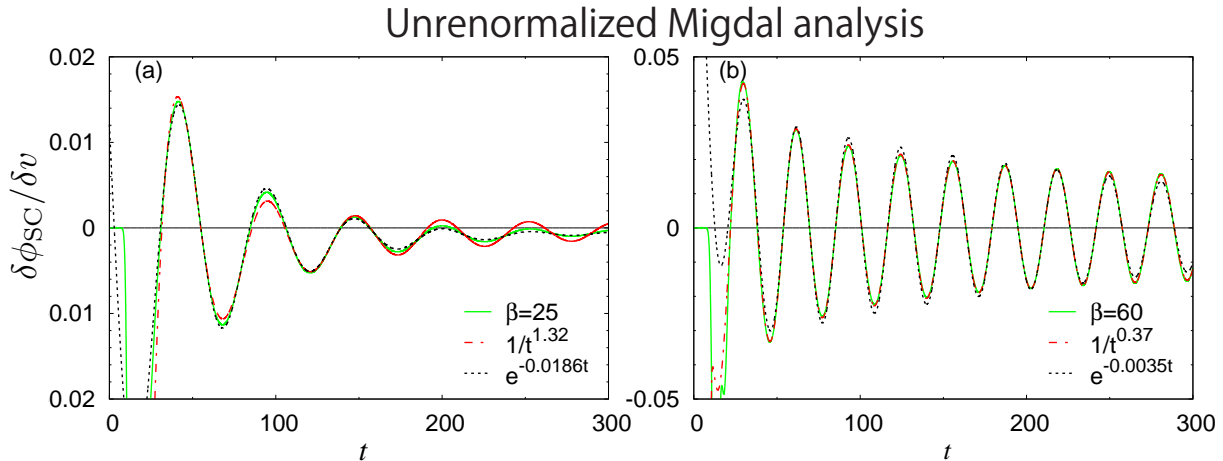


Figure 4.25: $\delta\phi(t)/\delta v$ at $\omega_0 = 0.4, g = 0.9, \gamma = 0.1$ ($\lambda_{\text{eff}} \simeq 1.2$) at various temperatures. The pump pulse has $t_{\text{pump}} = 10.0, \sigma_{\text{pump}} = 1.0$.

4.3. CONCLUSION OF THIS CHAPTER

In addition, we emphasize that the decay of the amplitude mode discussed above does not depend on the pump protocol. To demonstrate this we employ the hopping modulation as a different pump protocol, $v(t) = v + \delta v \exp(-\frac{(t-t_{\text{pump}})^2}{2\sigma_{\text{pump}}^2})$. Since we choose $t_{\text{pump}} = 10$, we fix $t_0 = 10$ for the fitting Eq. 4.40. The result is shown in Fig. 4.25. Again, we observe that at low enough temperatures the power-law decay is better and that when T is close to T_c the exponential decay is better. In addition, the exponents derived from fitting are consistent with those from the first excitation protocol, Fig. 4.22.

Finally, we point out that the crossover behavior of the decay of the Higgs oscillations from the power-law at low temperatures to the exponential-law near T_c is experimentally reported in NbN [169]. Even though we need to consider effects of impurities for real materials, our analysis indicates that the strong el-ph coupling is enough to explain such a behavior.

4.3 Conclusion of this chapter

In this chapter, we have studied the dynamical properties of the Holstein model applying the framework of the non-equilibrium DMFT combined with the self-consistent Migdal approximation, which is a conserving approximation and includes the dynamics of phonons through the phonon self-energy.

In the former part of this chapter, Sec. 4.1, we have studied the relaxation dynamics after a sudden change of the el-ph coupling. One important message in this study is that there occurs a crossover in the qualitative nature of the relaxation dynamics as we change the quenched electron-phonon coupling g_f within the moderately correlated metallic regime, which we call “a thermalization crossover”, see Fig 4.26. Namely, the smaller- g_f region exhibits a fast damping of

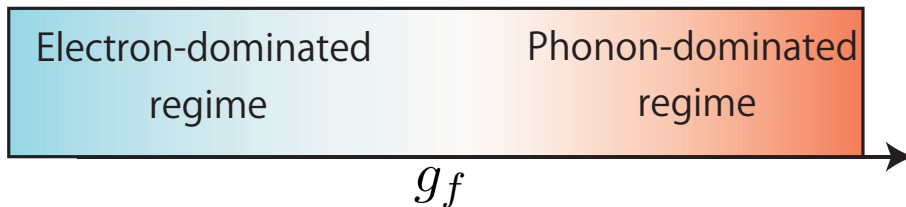


Figure 4.26: Thermalization crossover.

the oscillations originating from the phonon dynamics, with the momentum-summed quantities approaching the thermal values quickly, while the momentum distribution of the electrons exhibits a much slower relaxation (electron-dominated relaxation). The second region corresponds to larger g_f , but still before the phase transition to the bipolaronic phase. In this regime, the momentum distribution quickly approaches its thermal value with quick disappearance of the jump in the momentum distribution. However the phonon oscillations damp more slowly and the momentum distribution as well as local quantities oscillate around their thermal values (phonon-dominated relaxation). We have revealed that the relaxation time scales can be explained in terms of quasiparticle lifetimes for electrons and phonons and that the crossover in the relaxation behavior originates from a different g_f -dependence of the electron and phonon self-energies. We have also made clear the difference from the relaxation described with the unrenormalized Migdal approximation, where phonons are fixed in equilibrium [30, 96–98].

In the latter part of this chapter, Sec. 4.2, we have applied our method to investigated the

properties of collective amplitude modes in strongly-coupled SCs. We have revealed that the BCS relation between the SC gap and the Higgs energy is robust beyond the BCS regime. In addition, we have shown that there appears a second collective amplitude mode involving the phonon dynamics and the electron-mediated phonon-phonon interaction. Then we have predicted that both collective modes should be observed as oscillations in the time-resolved PES spectrum in a wide energy range after a pump with a strong laser. We have also discussed that the finite quasi-particle lifetime from the strong el-ph coupling leads to a crossover of the damping of the amplitude mode from a power law at low-temperatures to an exponential law around T_c .

Chapter 5

Concluding remarks

5.1 Summary of the thesis: Equilibrium and non-equilibrium

In this thesis, we have investigated the Holstein and Holstein-Hubbard models with the framework of the dynamical mean-field theory (DMFT) in order to study effects of the electron-phonon (el-ph) coupling in and out of equilibrium. Let us summarize the main new findings obtained in the present thesis.

Equilibrium

·Competition between antiferromagnetism and charge order (Sec. 3.1, Ref. [28,29])

Using DMFT with the hybridization-expansion continuous-time quantum Monte Carlo (CT-QMC), we have determined the finite temperature phase diagrams of the half-filled Holstein-Hubbard model around $U_{\text{eff}} (= U - \lambda) = 0$ and have studied competition of different orders. When U and λ are small the paramagnetic metallic (PM) phase appears between the antiferromagnetic (AF) and charge ordered (CO) phases, while the paramagnetic insulating (PI) phase appears when U and λ are large. When the temperature is low enough, the PM and PI phases are separated by a hysteretic region emerging just along $U_{\text{eff}} = 0$, where AF and CO directly compete and have a first-order phase transition. The PM regime widens with increasing the phonon frequency and temperature. In addition, we have introduced three different simplified descriptions (the Hubbard model, the static mean-field theory and the polaron picture) and discussed their reliability.

·Supersolid in the Holstein model (Sec. 3.2, Ref. [27])

We have studied competition among different orders in the Holstein model away from half-filling using DMFT with the hybridization-expansion CT-QMC. While perturbation theories predict absence of microscopic coexistence of CO and SC, or a supersolid (SS) phase, in the weak- and strong-coupling regimes, the analysis with DMFT+CT-QMC has revealed that the SS phase emerges in the intermediate-coupling regime, which is characterized by a peak in the T_c dome and a metal-insulator crossover above T_c . The boundary of the SS phase is of second order, which indicates an appearance of a QCP between SS and SC in the $T \rightarrow 0$ limit. The QCP is characterized by a kink (maximum) in the superfluid density and a reentrant behavior (higher symmetry with decreasing temperature) around it. We have pointed out that the origin of

5.2. FUTURE PERSPECTIVES: HOW DO WE CONNECT INSIGHTS OBTAINED IN THIS THESIS?

the stable SS phase in the intermediate-coupling regime is longer-range exchange interactions beyond the nearest neighbor coming from high-order processes in the bipolaron picture.

Out of equilibrium

· *New impurity solver for non-equilibrium el-ph problems (Sec. 2.3.5, Ref. [30, 31])*

We have developed the self-consistent Migdal approximation for non-equilibrium impurity problems, which is used to solve the effective impurity problem in the non-equilibrium DMFT for the Holstein model. In contrast with the unrenormalized Migdal approximation, which is previously used, this method can deal with dynamics of phonons, is a conserving approximation, and hence is suitable for describing dynamics of an isolated system.

· *Thermalization crossover (Sec. 4.1, Ref. [30])*

We have applied DMFT+ self-consistent Migdal approximation to reveal relaxation dynamics of the Holstein model in normal states after a sudden change of the el-ph coupling. We have found that qualitative character of the relaxation process changes as the quenched el-ph coupling (g_f) is varied within the metallic regime. In the smaller- g_f regime, oscillations in physical quantities damp before the electron momentum distribution reaches its thermal behavior, while in the larger- g_f regime, the electron momentum distribution quickly approaches its thermal behavior before the oscillations are fully damped. We have discussed that this crossover is attributed to the different dependence on the el-ph coupling between the electron and phonon self-energies. We have also shown that the unrenormalized Migdal approximation describes a totally different type of relaxation process with phonons effectively acting as a heat bath (an open system).

· *Amplitude modes in strongly-coupled SC (Sec. 4.2, Ref. [31])*

We have studied properties of collective amplitude modes in the strongly-coupled phonon-mediated SC in the Holstein model. Avoiding direct evaluation of the Bethe-Salpeter equation, we have calculated the dynamical pair susceptibility by direct simulations of the dynamics using DMFT+self-consistent Migdal approximation. We have found that the frequency of the Higgs amplitude mode agrees well with the superconducting gap even beyond the BCS regime. Besides the Higgs mode, we have unraveled another collective mode involving the dynamics of both the phonons and the superconducting order parameter. The frequency of this mode, higher than twice the renormalized phonon frequency in the superconducting phase, is shown to reflect a strong *electron-mediated phonon-phonon interaction*. Then, we have predicted that both types of collective excitations can be detected from time-resolved PES spectra after a strong laser pump. We have also argued that the finite quasi-particle lifetime from the strong el-ph coupling leads to a crossover of the decay of the Higgs mode from a power law to an exponential law.

5.2 Future perspectives: How do we connect insights obtained in this thesis?

In this thesis, we have discussed both equilibrium and non-equilibrium situations. This is motivated by the following reasons. Firstly, we need to understand equilibrium situations before we study transient non-equilibrium dynamics, since the former is the starting point. Secondly, a

region with competition of different phases is promising for drastic optical control of properties of the system. Hence we consider that equilibrium information about the competition is important to find interesting phenomena out of equilibrium. Thirdly, in periodically driven systems, some effects of external fields can be interpreted as time-independent change of values of parameters in the Hamiltonian.

However, we have to confess that we have not investigated competition among different orders out of equilibrium in this thesis. This is because of the limitation of proper impurity solvers for the Holstein model and Holstein-Hubbard models. In equilibrium, as we have performed, there are many powerful impurity solvers which let us operate detailed studies of these models. On the other hand, when it comes to non-equilibrium cases, solvers are very limited. Numerically exact Quantum Monte Carlo impurity solvers suffer from a dynamical sign problem so that one cannot reach long times. For the Holstein-Hubbard model, at the present time, only solvers based on a non-crossing approximation exist [101, 102, 170]. However, reliability of these solvers around the boundary between CO and AF remains to be clarified. In addition, it turns out that the self-consistent Migdal approximation shows an unphysical first-order phase transition for the CO state, Fig. 5.1(b), which makes us skeptical to use this method to study the competition between the CO and SC states. Hence **development of more sophisticated impurity solvers is necessary** to study competition of different orders out of equilibrium within the DMFT framework.

One promising strategy for the competition of CO and SC in the Holstein model is inclusion of the lowest-order vertex correction to the self-energy, see Fig. 5.1(a). We have checked that the second-order character of the CO transition recovers, see Fig. 5.1(b). Implementation of the improved approximation for non-equilibrium problems remains yet to be done, and a study in this direction is under way. In addition, we note that reducing the dynamical sign problem in QMC solvers is also an interesting direction. Such possibility has been proposed in a recent work [171], and it is worth considering application of their strategy to DMFT in order to rigorously study various situations including competition of orders.

In the following, we list up other future problems.

·Application of non-equilibrium DMFT to more realistic situations

So far applications of the non-equilibrium DMFT are limited to simple models such as the Hubbard model and the Holstein model. On the other hand, the equilibrium DMFT has been successful in revealing properties of various strongly-correlated materials when combined with the density functional theory (DFT). Even though there already exists the time-dependent DFT, it would be useful to develop a time-dependent DFT+DMFT in order to understand non-equilibrium properties of strongly-correlated materials.

·Extensions of the formalism

The DMFT formalism cannot take into account the momentum dependence of the self-energy. In equilibrium, many kinds of extensions of the DMFT framework have been developed in order to take into account the momentum dependence such as the dynamical cluster approximation, cellular DMFT and DMFT+fluctuation-exchange approximation [172–175]. In particular, such extensions are essential to describe unconventional superconductors. As for non-equilibrium situations, such extensions are still limited to the non-equilibrium dynamical cluster approxi-

5.2. FUTURE PERSPECTIVES: HOW DO WE CONNECT INSIGHTS OBTAINED IN THIS THESIS?

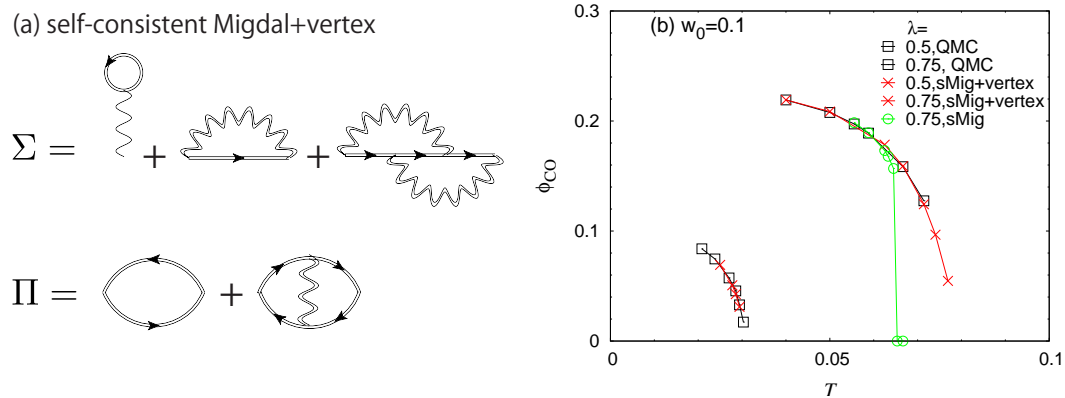


Figure 5.1: (a) Diagrams for the electron self-energy (Σ) and the phonon self-energy (Π) in the approximate impurity solver with the lowest order vertex correction (sMig+vertex). (b) Transition temperatures for CO evaluated with QMC, sMig and sMig+vertex impurity solvers for $\omega_0 = 0.1$.

mation [176, 177]. Further development of new frameworks and their application should give new insight into recent various experiments about unconventional superconductors.

Appendix A

Equilibrium part

A.1 CT-QMC

A.1.1 Evaluation of ω_{ph}

Here we prove the expression for $\omega_{\text{ph}}(\theta)$ Eq. 2.57. We use an equation,

$$\begin{aligned} \exp(\hat{c}) \exp(\hat{d}) &= \exp\left(\hat{c} + \hat{d} + \frac{1}{2}[\hat{c}, \hat{d}]\right) \\ \text{with } [\hat{c}, [\hat{c}, \hat{d}]] &= [\hat{d}, [\hat{c}, \hat{d}]] = 0, \end{aligned} \quad (\text{A.1})$$

where \hat{c} and \hat{d} are some operators. Applying this to phonon creation and annihilation operators, we obtain

$$\begin{aligned} \exp(\gamma a^\dagger + \gamma' a) &= \exp(\gamma a^\dagger) \exp(\gamma' a) \exp\left(\frac{1}{2}\gamma\gamma'\right) \\ &= \exp(\gamma' a) \exp(\gamma a^\dagger) \exp\left(-\frac{1}{2}\gamma\gamma'\right). \end{aligned} \quad (\text{A.2})$$

With this relation, we transform ω_{ph} , with $\gamma = \frac{\lambda}{\omega_0}$,

$$\begin{aligned} &\text{Tr}_a \left[e^{\beta\omega_0 a^\dagger a} e^{s_{2n}\gamma(e^{\omega_0\tau_{2n}} a^\dagger - e^{-\omega_0\tau_{2n}} a)} e^{s_{2n-1}\gamma(e^{\omega_0\tau_{2n-1}} a^\dagger - e^{-\omega_0\tau_{2n-1}} a)} \dots \right] \\ &= e^{n\gamma^2} \text{Tr}_a \left[e^{\beta\omega_0 a^\dagger a} e^{-s_{2n}\gamma e^{-\omega_0\tau_{2n}} a} e^{s_{2n}\gamma e^{\omega_0\tau_{2n}} a^\dagger} e^{-s_{2n-1}\gamma e^{-\omega_0\tau_{2n}} a} e^{s_{2n-1}\gamma e^{\omega_0\tau_{2n-1}} a^\dagger} \dots \right] \\ &= e^{n\gamma^2} \exp\left[\gamma^2 \sum_{i>j} s_i s_j e^{\omega_0\tau_i} e^{-\omega_0\tau_j}\right] \text{Tr}_a \left[e^{-\beta\omega_0 a^\dagger a} e^{(-\sum_{i=1}^{2n} s_i \gamma e^{-\omega_0\tau_i}) a} e^{(\sum_{i=1}^{2n} s_i \gamma e^{\omega_0\tau_i}) a^\dagger} \right] \end{aligned} \quad (\text{A.3})$$

A.1. CT-QMC

On the other hand, $\text{Tr}_a[e^{-\beta\omega_0 a^\dagger a} e^{\Gamma a} e^{\Gamma' a^\dagger}]$ is evaluated with coherent states of phonons, $|\phi\rangle$, as

$$\begin{aligned}
& \text{Tr}_a[e^{-\beta\omega_0 a^\dagger a} e^{\Gamma a} e^{\Gamma' a^\dagger}] \\
&= \int d[\phi\bar{\phi}] e^{-|\phi|^2} \sum_n \langle n| e^{-\beta\omega_0 a^\dagger a} e^{\Gamma a} |\phi\rangle \langle\phi| e^{\Gamma' a^\dagger} |n\rangle \\
&= \int d[\phi\bar{\phi}] e^{-|\phi|^2} \langle\phi| e^{\Gamma'\bar{\phi}} e^{\bar{\phi}\phi e^{-\beta\omega_0}} e^{\Gamma\phi} |\phi\rangle \\
&= \int d[\phi\bar{\phi}] e^{-(1-e^{-\beta\omega_0})(\bar{\phi}-\frac{\Gamma}{1-e^{-\beta\omega_0}})(\phi-\frac{\Gamma'}{1-e^{-\beta\omega_0}})} e^{\frac{\Gamma\Gamma'}{1-e^{-\beta\omega_0}}} \\
&= Z_a e^{\frac{\Gamma\Gamma'}{1-e^{-\beta\omega_0}}}.
\end{aligned} \tag{A.4}$$

Here, we have used $\langle\phi| e^{-\beta\omega_0 a^\dagger a} |\phi'\rangle = e^{\bar{\phi}\phi' e^{-\beta\omega_0}}$ and $\hat{1} = \int d[\bar{\phi}, \phi] e^{-|\phi|^2} |\phi\rangle \langle\phi|$. Combining these two equations and arranging the results, we obtain Eq. 2.57.

A.1.2 Derivation of the expression for g and f

In order to prove Eq. 2.64, we introduce new configurations, $\underline{\theta} = [\{\tau_1^\uparrow \cdots \tau_{n_\uparrow}^\uparrow\}, \{\tau_1^\downarrow \cdots \tau_{n_\downarrow}^\downarrow\}; \{\tau_1^{\prime\uparrow} \cdots \tau_{n_\uparrow}^{\prime\uparrow}\}, \{\tau_1^{\prime\downarrow} \cdots \tau_{n_\downarrow}^{\prime\downarrow}\}]$, which does not care about the order of time in each $\{\}$. This new configuration space is an extended version of the configuration space we introduced in Sec. 2.2.3, where in each $\{\}$, τ 's are time-ordered. The weight $\underline{\omega}_\theta$ is

$$\underline{\omega}_\theta = \frac{1}{(n_\uparrow!)^2 (n_\downarrow!)^2} \omega_\theta, \tag{A.5}$$

where θ denotes the configuration we obtain rearrange $\underline{\theta}$ so that each $\{\tau \cdots \tau\}$ is time-ordered.

First, it can be shown that

$$g(\tau_0) = \int_0^\beta d\tau \int_0^\beta d\tau' \frac{1}{\beta} \Delta(\tau_0, \tau - \tau') g(\tau - \tau'). \tag{A.6}$$

Next, define a new configuration, $\tilde{\underline{\theta}} = [\{\tau, \tau_1^\uparrow \cdots \tau_{n_\uparrow}^\uparrow\}, \{\tau_1^\downarrow \cdots \tau_{n_\downarrow}^\downarrow\}; \{\tau', \tau_1^{\prime\uparrow} \cdots \tau_{n_\uparrow}^{\prime\uparrow}\}, \{\tau_1^{\prime\downarrow} \cdots \tau_{n_\downarrow}^{\prime\downarrow}\}]$

form θ . Its time ordered one is represented as $\tilde{\theta}$. Now, we set

$$\omega_{\theta}^{c_{\uparrow}(\tau)c_{\uparrow}^{\dagger}(\tau')} = Z_{\text{bath}} \text{Tr}_{\text{loc}} \left\{ e^{-\beta H_{\text{loc}}} \mathcal{T} \left[c_{\uparrow}(\tau) c_{\uparrow}^{\dagger}(\tau') c_{\uparrow}(\tau_{n_{\uparrow}}^{\uparrow}) c_{\uparrow}^{\dagger}(\tau_{n_{\uparrow}}^{\prime\uparrow}) \cdots c_{\uparrow}(\tau_1^{\uparrow}) c_{\uparrow}^{\dagger}(\tau_1^{\prime\uparrow}) \right. \right. \\ \left. \left. \times c_{\downarrow}^{\dagger}(\tau_{n_{\downarrow}}^{\prime\downarrow}) c_{\downarrow}(\tau_{n_{\downarrow}}^{\downarrow}) \cdots c_{\downarrow}^{\dagger}(\tau_1^{\prime\downarrow}) c_{\downarrow}(\tau_1^{\downarrow}) \right] \right\} \quad (\text{A.7})$$

$$\begin{aligned} & \times \det M^{-1}(\{\tau_1^{\uparrow} \cdots \tau_{n_{\uparrow}}^{\uparrow}\}, \{\tau_1^{\prime\downarrow} \cdots \tau_{n_{\downarrow}}^{\prime\downarrow}\}; \{\tau_1^{\prime\uparrow} \cdots \tau_{n_{\uparrow}}^{\prime\uparrow}\}, \{\tau_1^{\downarrow} \cdots \tau_{n_{\downarrow}}^{\downarrow}\}) (d\tau)^{2n_{\uparrow}+2n_{\downarrow}}, \\ g(\tau - \tau') &= \frac{1}{Z} \sum_{\theta} \omega_{\theta}^{c_{\uparrow}(\tau)c_{\uparrow}^{\dagger}(\tau')} \\ &= \frac{1}{Z} \sum_{\theta} \omega_{\tilde{\theta}} \frac{\omega_{\theta}^{c_{\uparrow}(\tau)c_{\uparrow}^{\dagger}(\tau')}}{\omega_{\tilde{\theta}}} \\ &= \frac{1}{Z} \sum_{\theta} \omega_{\tilde{\theta}} \frac{[(n_{\uparrow} + 1)!]^2 [n_{\downarrow}]^2}{d\tau^2} \\ & \times \frac{\det M^{-1}(\{\tau_1^{\uparrow} \cdots \tau_{n_{\uparrow}}^{\uparrow}\}, \{\tau_1^{\prime\downarrow} \cdots \tau_{n_{\downarrow}}^{\prime\downarrow}\}; \{\tau_1^{\prime\uparrow} \cdots \tau_{n_{\uparrow}}^{\prime\uparrow}\}, \{\tau_1^{\downarrow} \cdots \tau_{n_{\downarrow}}^{\downarrow}\})}{\det M^{-1}(\{\tau, \tau_1^{\uparrow} \cdots \tau_{n_{\uparrow}}^{\uparrow}\}, \{\tau_1^{\prime\downarrow} \cdots \tau_{n_{\downarrow}}^{\prime\downarrow}\}; \{\tau', \tau_1^{\prime\uparrow} \cdots \tau_{n_{\uparrow}}^{\prime\uparrow}\}, \{\tau_1^{\downarrow} \cdots \tau_{n_{\downarrow}}^{\downarrow}\})} \quad (\text{A.8}) \\ &= \frac{1}{Z} \sum_{\theta} \omega_{\tilde{\theta}} \frac{1}{(d\tau)^2} \left(\sum_{i,j=1}^{n_{\uparrow}+1} \delta_{\tau, \tau_i} \delta_{\tau', \tau'_j} M_{\tilde{\theta}, j, i} \right) \\ &= \frac{1}{Z} \sum_{\tilde{\theta}} \omega_{\tilde{\theta}} \frac{1}{(d\tau)^2} \left(\sum_{i,j=1}^{n_{\uparrow}+1} \delta_{\tau, \tau_i} \delta_{\tau', \tau'_j} M_{\tilde{\theta}, j, i} \right), \\ &= \frac{1}{Z} \sum_{\theta'} \omega_{\theta'} \frac{1}{(d\tau)^2} \left(\sum_{i,j=1}^{n'_{\uparrow}} \delta_{\tau, \tau_i} \delta_{\tau', \tau'_j} M_{\theta', j, i} \right). \end{aligned}$$

Here θ' does not need to include τ, τ' unlike $\tilde{\theta}$. Combining the last part of the above equation and Eq. A.6, we have

$$g(\tau_0) = \frac{1}{Z} \sum_{\theta'} \sum_{i,j=1}^{n'_{\uparrow}} \frac{1}{\beta} \frac{\Delta_{\tau_0, \tau_i - \tau'_j}}{d\tau} M_{\theta', j, i} \omega_{\theta'}, \quad (\text{A.9})$$

where $\frac{\Delta_{\tau_0, \tau_i - \tau'_j}}{d\tau}$ is $\Delta(\tau_0, \tau - \tau')$ in the desecrate representation. The proof for f is almost the same as that for g .

A.2 Perturbative approaches for the Holstein model

Here we concretely explain the perturbative approaches used in Sec. 3.2.

Weak coupling

As a representative of weak-coupling perturbation theories, in Sec. 3.2.2, we have shown the results of the iterative perturbation theory (IPT) [123]. This is a diagrammatic expansion up to second order of λ in terms of the Weiss field \mathcal{G}_0 in the effective impurity problem. This approximation has been originally considered for the Hubbard model [25], and in Ref. [123] they have extended it to normal phases in the Holstein model. Here, we further extend this

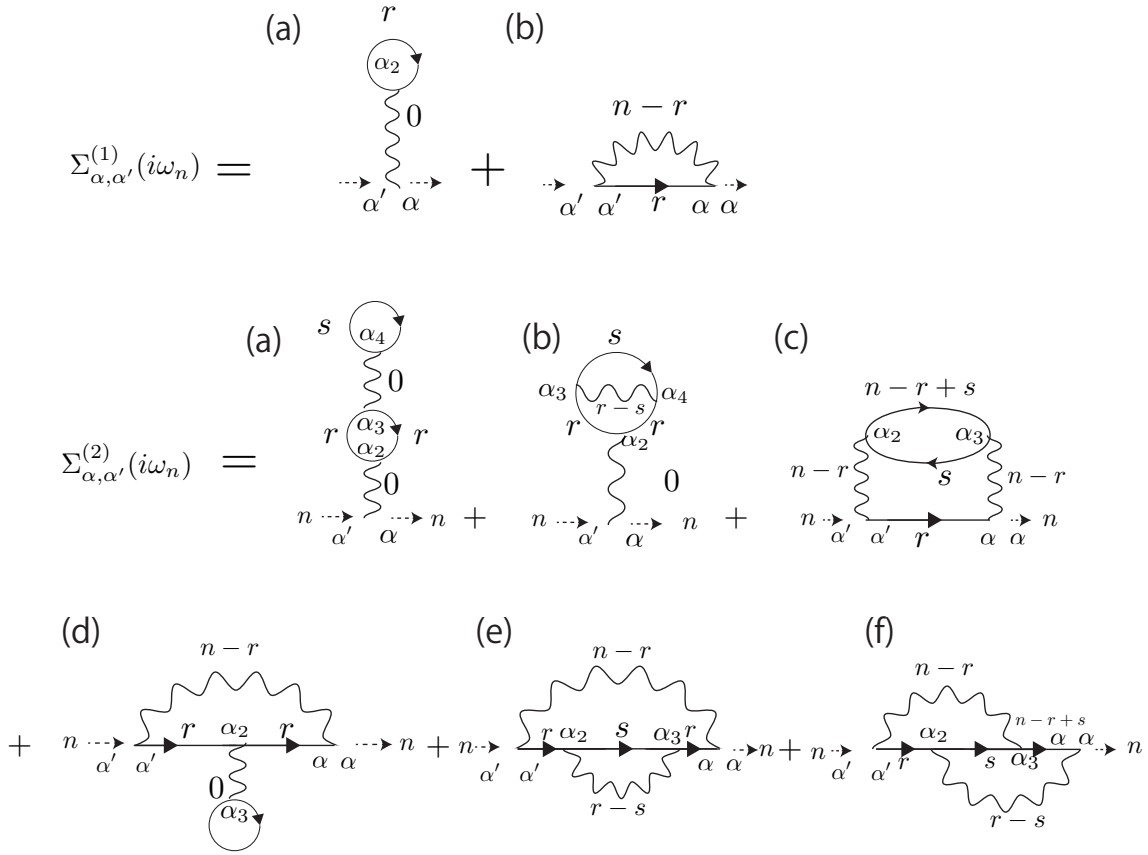


Figure A.1: Self-energy of IPT in the Nambu formalism. $\Sigma^{(1)}$ is the first order term of λ , while $\Sigma^{(2)}$ is the second order term.

perturbation theory so that we can deal with CO and SC in the Holstein model. Diagrammatic expression for the self-energy in IPT is illustrated in Fig. A.1. Explicitly, the first order part against $\lambda = 2g^2/\omega_0$ is

$$\begin{aligned}
\Sigma_{\alpha,\alpha'}^{(1)}(i\omega_n) &= \Sigma_{\alpha,\alpha'}^{(1,a)}(i\omega_n) + \Sigma_{\alpha,\alpha'}^{(1,b)}(i\omega_n) \\
&= \delta_{\alpha,\alpha'} \sigma_\alpha^3 g^2 \sum_{\alpha_2,r} D_0(i\nu_{n=0}) \mathcal{G}_{0,\alpha_2,\alpha_2}(i\omega_r) \sigma_{\alpha_2}^3 - g^2 \sigma_\alpha^3 \sigma_{\alpha'}^3 \frac{1}{\beta} \sum_r \mathcal{G}_{0,\alpha,\alpha'}(i\omega_r) D_0(i\nu_{n-r}),
\end{aligned} \tag{A.10}$$

where $\sigma^3 = [1, -1]$ and $\alpha, \alpha' = 1, 2$ are the Nambu index.

The second order part against λ is

$$\begin{aligned}
 \Sigma_{\alpha,\alpha'}^{(2)}(i\omega_n) &= \Sigma_{\alpha,\alpha'}^{(2,a)}(i\omega_n) + \Sigma_{\alpha,\alpha'}^{(2,b)}(i\omega_n) + \Sigma_{\alpha,\alpha'}^{(2,c)}(i\omega_n) + \Sigma_{\alpha,\alpha'}^{(2,d)}(i\omega_n) + \Sigma_{\alpha,\alpha'}^{(2,e)}(i\omega_n) + \Sigma_{\alpha,\alpha'}^{(2,f)}(i\omega_n) \\
 &= (-)^4 \delta_{\alpha,\alpha'} \sigma_\alpha^3 g^4 D_0(i\nu_0) \left(\frac{1}{\beta} \sum_{r,\alpha_2,\alpha_3} \mathcal{G}_{0,\alpha_3,\alpha_2}(i\omega_r) \mathcal{G}_{0,\alpha_2,\alpha_3}(i\omega_r) \sigma_{\alpha_2}^3 \sigma_{\alpha_3}^3 \right) D_0(i\nu_0) \left(\frac{1}{\beta} \sum_{s,\alpha_4} \mathcal{G}_{0,\alpha_4,\alpha_4}(i\omega_s) \sigma_{\alpha_4}^3 \right) \\
 &+ (-)^3 \delta_{\alpha,\alpha'} \sigma_\alpha^3 g^4 D_0(i\nu_0) \left(\frac{1}{\beta^2} \sum_{r,s,\alpha_2,\alpha_3,\alpha_4} \mathcal{G}_{0,\alpha_3,\alpha_2}(i\omega_r) \mathcal{G}_{0,\alpha_2,\alpha_4}(i\omega_r) D_0(i\nu_{r-s}) \mathcal{G}_{0,\alpha_4,\alpha_3}(i\omega_s) \sigma_{\alpha_2}^3 \sigma_{\alpha_3}^3 \sigma_{\alpha_4}^3 \right) \\
 &+ (-)^3 \sigma_\alpha^3 \sigma_{\alpha'}^3 g^4 \frac{1}{\beta^2} \sum_{r,s,\alpha_2,\alpha_3} \mathcal{G}_{0,\alpha,\alpha'}(i\omega_r) \mathcal{G}_{0,\alpha_2,\alpha_3}(i\omega_s) \mathcal{G}_{0,\alpha_3,\alpha_2}(i\omega_{n-r+s}) D_0(i\nu_{n-r}) D_0(i\nu_{n-r}) \sigma_{\alpha_2}^3 \sigma_{\alpha_3}^3 \\
 &+ (-)^3 \sigma_\alpha^3 \sigma_{\alpha'}^3 g^4 \frac{1}{\beta} \sum_{r,\alpha_2} \mathcal{G}_{0,\alpha_2,\alpha'}(i\omega_r) \mathcal{G}_{0,\alpha,\alpha_2}(i\omega_r) D_0(i\nu_{n-r}) D_0(i\nu_0) \sigma_{\alpha_2}^3 \left(\frac{1}{\beta} \sum_{s,\alpha_3} \mathcal{G}_{0,\alpha_3,\alpha_3}(i\omega_s) \sigma_{\alpha_3}^3 \right) \\
 &+ (-)^2 \sigma_\alpha^3 \sigma_{\alpha'}^3 g^4 \frac{1}{\beta^2} \sum_{r,s,\alpha_2,\alpha_3} \mathcal{G}_{0,\alpha_2,\alpha'}(i\omega_r) \mathcal{G}_{0,\alpha,\alpha_3}(i\omega_r) D_0(i\nu_{n-r}) D_0(i\nu_{r-s}) \mathcal{G}_{0,\alpha_3,\alpha_2}(i\omega_s) \sigma_{\alpha_2}^3 \sigma_{\alpha_3}^3 \\
 &+ (-)^2 \sigma_\alpha^3 \sigma_{\alpha'}^3 g^4 \frac{1}{\beta^2} \sum_{r,s,\alpha_2,\alpha_3} \mathcal{G}_{0,\alpha_2,\alpha'}(i\omega_r) D_0(i\nu_{n-r}) \mathcal{G}_{0,\alpha_3,\alpha_2}(i\omega_s) \mathcal{G}_{0,\alpha,\alpha_3}(i\omega_{n-r+s}) D_0(i\nu_{r-s}) \sigma_{\alpha_2}^3 \sigma_{\alpha_3}^3.
 \end{aligned} \tag{A.11}$$

We have used this approximate impurity solver in the DMFT iteration loop illustrated in Sec. 2.2.1.

Strong coupling

When the strength of the effective attractive interaction mediated by phonons, λ , is strong, two electrons are bound into a composite particle, i.e., a bipolaron. There, we can construct effective models for bipolarons with the perturbation theory against v/λ , where v is the hopping parameter [63, 122]. Briefly speaking, the procedure is the following [122]. First let Q_0 the subspace that contains all of the degenerate ground states of the unperturbed Hamiltonian H_0 , which we take the part expect the kinetic part of electrons (T), and E_0 the energy of the ground states. Q is the subspace that consists of eigen states of the perturbed Hamiltonian $H = H + T$ that continuously connected to Q_0 . We set P_0 the projection to Q_0 and P the projection to Q . Now, the eigenvalue equation $(H - E)|E\rangle = 0$ can be projected to Q_0 , which leads to $P_0(H - E)PP_0|E\rangle = 0$. This equation means that we need to find eigen values and states of the effective Hamiltonian on Q_0 ,

$$H_{\text{eff}} = (P_0PP_0)^{-\frac{1}{2}} P_0HPP_0(P_0PP_0)^{-\frac{1}{2}}. \tag{A.12}$$

Here

$$(P_0PP_0)^{-\frac{1}{2}} = P_0 + \sum_{n=1}^{\infty} \frac{(2n-1)!!}{(2n)!!} [P_0(P_0 - P)P_0]^n, \tag{A.13}$$

and

$$P = P_0 - \sum_{n=1}^{\infty} \sum_{k_1+k_2+\dots+k_{n+1}=n, k_i \geq 0} R^{k_1} T R^{k_2} T \dots T R^{k_{n+1}}, \tag{A.14}$$

with

$$R^0 \equiv -P_0, \quad R^k \equiv [(1 - P_0)/(E_0 - H_0)]^k \quad (k \neq 0). \quad (\text{A.15})$$

Now we expand H_{eff} against T to obtain for the second order (the lowest order),

$$H^{(2)} = P_0 T \frac{1 - P_0}{E_0 - H_0} T P_0, \quad (\text{A.16})$$

and for the fourth order

$$\begin{aligned} H^{(4)} = & P_0 T \frac{1 - P_0}{E_0 - H_0} T \frac{1 - P_0}{E_0 - H_0} T \frac{1 - P_0}{E_0 - H_0} T P_0 \\ & - \frac{1}{2} \left[P_0 T \frac{1 - P_0}{(E_0 - H_0)^2} T P_0 T \frac{1 - P_0}{E_0 - H_0} T P_0 + P_0 T \frac{1 - P_0}{E_0 - H_0} T P_0 T \frac{1 - P_0}{(E_0 - H_0)^2} T P_0 \right]. \end{aligned} \quad (\text{A.17})$$

In Sec. 3.2.2 we have shown the expression of the lowest order expansion (the second order of v/λ). Following the above procedure, we expand the Holstein model on the Bethe lattice up to fourth-order in v/λ to obtain additional terms,

$$\begin{aligned} H^{(4)} = & \frac{1}{2} \sum'_{i,j,k} \left[-\frac{j'_{a,\perp}}{2} (S_i^+ S_j^- + S_i^- S_j^+ + S_k^+ S_j^- + S_k^- S_j^+) - j_{a,\parallel} (S_i^z S_j^z + S_k^z S_j^z) \right. \\ & \left. + \frac{j'_{b,\perp}}{2} (S_i^+ S_k^- + S_i^- S_k^+) + (j_{a,\parallel} + j_{b,\parallel}) S_i^z S_k^z \right], \end{aligned} \quad (\text{A.18})$$

where the prime in the summation means that i, j , and k are all different but j is a nearest-neighbor site for both i and k . The first two terms are correction to the nearest-neighbor exchange interactions in Eq. 3.12. The last two terms are the next-nearest neighbor exchange interactions expressed in Eq. 3.18.

Explicit expressions for the exchange interactions are

$$\begin{aligned} j'_{a,\perp} = & \frac{4v_{i,j}^2 v_{j,k}^2}{\lambda^3} \gamma^3 e^{-2\gamma} \left[\int_0^1 dx \int_0^1 dy \int_0^1 dz (xyz)^{\gamma-1} \right. \\ & \times \left(\exp\left\{ \frac{1}{2} \gamma [x - y + z - 2z(x - y) - xyz] \right\} + \exp\left\{ \frac{1}{2} \gamma [x - y - z(x + y)] \right\} \right) \\ & + 2 \int_0^1 dx \int_0^1 dy (xy)^{\gamma-1} e^{\gamma(x-y)} \sum_{m=1}^{\infty} \frac{(\gamma/2)^m (1-x)^m (1+y)^m}{m!m} \\ & \left. + \int_0^1 dx \int_0^1 dy (xy)^{\gamma-1} e^{\gamma(x-y)} (\ln x + \ln y) \right], \end{aligned} \quad (\text{A.19})$$

$$\begin{aligned} j'_{b,\perp} = & -\frac{4v_{i,j}^2 v_{j,k}^2}{\lambda^3} \gamma^3 e^{-2\gamma} \left[\int_0^1 dx \int_0^1 dy \int_0^1 dz (xyz)^{\gamma-1} \exp\left\{ \frac{1}{2} \gamma [x + y + z - 2z(x + y) + xyz] \right\} \right. \\ & + 2 \int_0^1 dx \int_0^1 dy (xy)^{\gamma-1} e^{-\gamma(x+y)} \sum_{m=1}^{\infty} \frac{(\gamma/2)^m (1+x)^m (1+y)^m}{m!m} \\ & \left. + 2 \int_0^1 dx \int_0^1 dy (xy)^{\gamma-1} e^{-\gamma(x+y)} \ln x \right], \end{aligned} \quad (\text{A.20})$$

$$\begin{aligned}
 j'_{a,\parallel} = & -\frac{4v_{i,j}^2 v_{j,k}^2}{\lambda^3} \gamma^3 e^{-2\gamma} \left[\int_0^1 dx \int_0^1 dy \int_0^1 dz (xyz)^{\gamma-1} (\exp\{\frac{1}{2}\gamma[-x-y+z+2z(x+y)+xyz]\} \right. \\
 & + \exp\{\frac{1}{2}\gamma[-x-y+2z+z(x+y)+2xyz]\}) \\
 & + 2 \int_0^1 dx \int_0^1 dy (xy)^{\gamma-1} e^{\gamma(x+y)} \sum_{m=1}^{\infty} \frac{(\gamma/2)^m (1-x)^m (1-y)^m}{m!m} \\
 & \left. + 2 \int_0^1 dx \int_0^1 dy (xy)^{\gamma-1} e^{\gamma(x+y)} \ln x \right], \tag{A.21}
 \end{aligned}$$

$$j'_{b,\parallel} = \frac{4v_{i,j}^2 v_{j,k}^2}{\lambda^3} \gamma^3 e^{-2\gamma} \int_0^1 dx \int_0^1 dy \int_0^1 dz (xyz)^{\gamma-1} \exp\{\frac{1}{2}\gamma[x+y+2z-z(x+y)+2xyz]\}. \tag{A.22}$$

Here we set $\gamma = \lambda/\omega_0 = 2g^2/\omega_0^2$. We note that $v_{i,j}$ scales as v/\sqrt{z} and the number of the next-nearest neighbors is z^2 , where z is the coordination number of the Bethe lattice.

A.3 Superconductivity in the Holstein-Hubbard model

In the main part of the thesis, we have discussed competition of different orders. On the other hand, it is also important to understand how superconducting states behave when ω_0 , λ and/or U are comparable to the electronic bandwidth. Indeed, this type of condition is considered to be realized in carbon based superconductors such as alkali-doped C_{60} superconductors and recent reported aromatic superconductors. In addition, Cavalleri's group has reported a light-induced superconductivity in an alkali-doped C_{60} compound [22] and its origin is under investigation [178]. However, it is usually difficult to analyze such unconventional parameter regime systematically because of lack of rigorous and appropriate treatments. The DMFT+CT-QMC method for ordered phases in the Holstein-Hubbard, which we newly extended in Sec. 2.2.3 and is numerically exact in the infinite special dimensions, is a suitable method for this aim. In this appendix, we reveal effects of the retardation and the Coulomb repulsion on the s-wave SC state, show the polaron picture, which we introduce in Sec. 3.1.2, is helpful for qualitative understanding the effects of retardation and the Coulomb interaction, and discuss its quantitative reliability. The results are published in Ref. [27, 28].

Our investigation is focused on $U_{\text{eff}} < 0$ regime at half-filling, and we make a constraint on the Green's function, $G_{11}(\tau) = G_{11}(\beta - \tau) = G_{22}(\tau) = G_{22}(\beta - \tau)$, in order to suppress the AF and CO phases and only allow the SC phase as an ordered phase. Strictly speaking, if we allow both CO and SC orders in the self-consistency loop, CO dominates over SC on a bipartite lattice. However, if the system has a frustration (e.g. induced by a second-neighbor hopping on a bipartite lattice), CO and AF are suppressed and our treatment is justified [24]. In the following, we study the transition temperature, the superconducting order parameter and the SC gap in the one-particle spectral function.

First we show the effect of the retardation and the Coulomb interaction on the structure of the anomalous Green's function. In Fig. A.2(a), we plot normal and anomalous Green's functions on the imaginary-time axis. While the diagonal Green's function is negative and symmetric (at half-filling), the off-diagonal Green's function is antisymmetric about $\tau/\beta = 0.5$.

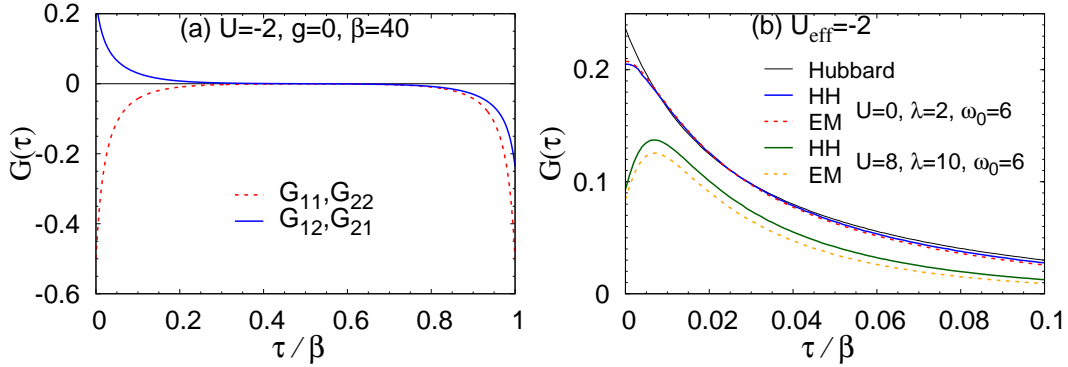


Figure A.2: (a) Typical behavior of Green's functions on the imaginary time axis, here for $U = -2$, $g = 0$, and $\beta = 40$. (b) A close-up of the anomalous Green's function for various λ and U with fixed $U_{\text{eff}} (= U - \lambda) = -2$ ($\omega_0 = 6$ and $\beta = 40$). 'HH' means the Green's function is computed from the HH model, while 'EM' means that it is obtained with the effective model.

These characters are common to other parameters. In Fig. A.2(b), we compare the short-time behavior of the anomalous Green's functions for different sets of parameter values: without retardation (Hubbard model with $U = -2$), with only a retarded attractive interaction ($U = 0$ and $\omega_0 > 0$) and with both retardation and Coulomb repulsion. In all three cases, $U_{\text{eff}} = -2$, $\omega_0 = 6$ and $T = 0.025$. The anomalous Green's function has its maximum at $\tau = 0$ without the retardation. When we introduce a retarded attractive interaction without U , the position of the maximum remains at $\tau = 0$, but the initial peak is rounded off. If we switch on a $U > 0$, the peak position starts to shift to $\tau > 0$. This behavior indicates that when electrons form pairs, they tend to avoid the instantaneous repulsive interaction U while exploiting the retarded attractive interaction.

These behaviors can be well explained with the effective polaron model, Eq. 3.9. In order to evaluate Green's functions from the effective model, we first consider the LF transformation as

$$\begin{aligned} G_\sigma(\tau) &= -\langle T_\tau c_\sigma(\tau) c_\sigma^\dagger(0) \rangle_H \\ &= -\langle T_\tau e^{-\frac{g}{\omega_0}(a^\dagger(\tau) - a(\tau))} c_\sigma(\tau) e^{\frac{g}{\omega_0}(a^\dagger(0) - a(0))} c_\sigma^\dagger(0) \rangle_{H_{\text{LF}}}. \end{aligned} \quad (\text{A.23})$$

Now we make an approximation and separate the phonon dynamics and the polaron dynamics. Namely we treat the whole system as if its Hamiltonian is $H_{\text{eff}} + H_{\text{ph}}$ [179]. This leads to

$$G_\sigma(\tau) \approx -\langle T_\tau c_\sigma(\tau) c_\sigma^\dagger(0) \rangle_{H_{\text{eff}}} \cdot \langle T_\tau e^{-\frac{g}{\omega_0}(a^\dagger(\tau) - a(\tau))} e^{\frac{g}{\omega_0}(a^\dagger(0) - a(0))} \rangle_{H_{\text{ph}}}, \quad (\text{A.24})$$

where $H_{\text{ph}} = \omega_0 \sum_i a_i^\dagger a_i$. As for the anomalous part we obtain

$$G_{12}(\tau) \approx -\langle T_\tau c_\uparrow(\tau) c_\downarrow(0) \rangle_{H_{\text{eff}}} \cdot \langle T_\tau e^{-\frac{g}{\omega_0}(a^\dagger(\tau) - a(\tau))} e^{-\frac{g}{\omega_0}(a^\dagger(0) - a(0))} \rangle_{H_{\text{ph}}}. \quad (\text{A.25})$$

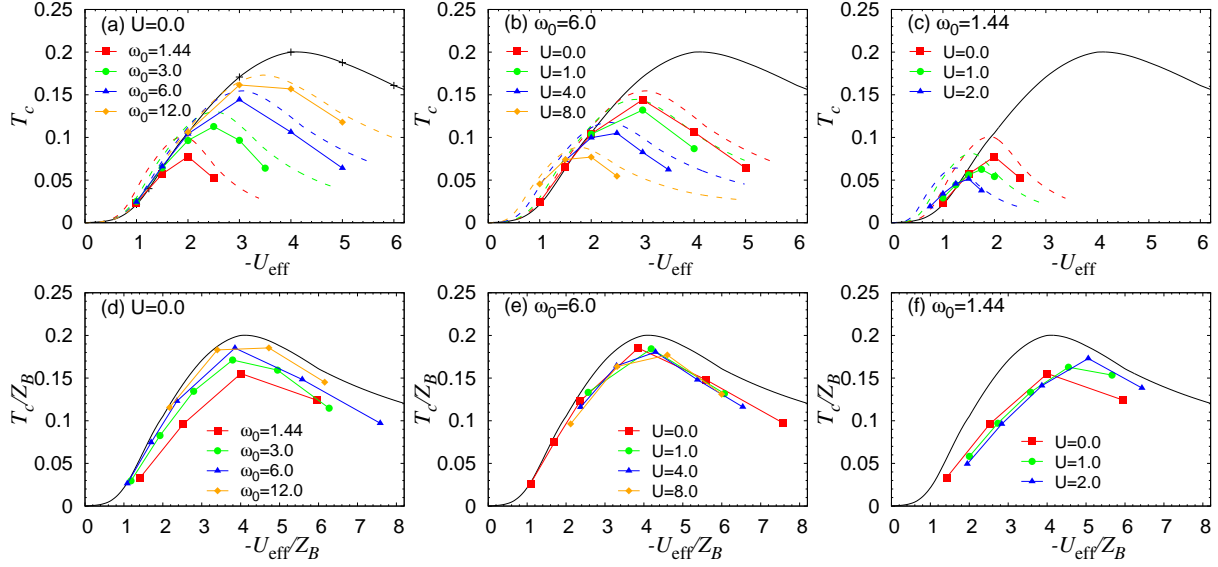


Figure A.3: (a)(b)(c) T_c against $-U_{\text{eff}}$ for various sets of parameter values. Solid symbols represent results of DMFT+QMC analysis. (a) shows the dependence on ω_0 for $U = 0$. The lines connecting symbols are guides for the eye. (b) and (c) show the phase diagram when U is switched on with a fixed value of $\omega_0 = 6$ (b), or $\omega_0 = 1.44$ (c). (d)(e)(f) The phase diagram plotted for rescaled parameters: $\tilde{U}_{\text{eff}} \equiv U_{\text{eff}}/Z_B$ and $\tilde{T} \equiv T/Z_B$. (d) shows the result for various values of ω_0 at $U = 0$. (e) and (f) show the result when U is switched on with a fixed $\omega_0 = 6$ (e), or $\omega_0 = 1.44$ (f). Crosses in (a) show the results for the attractive Hubbard model with $-U_{\text{eff}}$, and the black curve in each panel indicates the corresponding T_c . The color dashed curves show the results from the effective model.

The expression for the phonon factor is

$$\begin{aligned} & \langle T_\tau e^{-s\frac{g}{\omega_0}(a^\dagger(\tau)-a(\tau))} e^{-s'\frac{g}{\omega_0}(a^\dagger(0)-a(0))} \rangle_{H_{\text{ph}}} \\ & = \exp\left\{-\frac{g^2/\omega_0^2}{e^{\beta\omega_0}-1} [(e^{\omega_0\beta}+1) + ss'(e^{\omega_0(\beta-\tau)} + e^{\omega_0\tau})]\right\}, \end{aligned} \quad (\text{A.26})$$

where $s, s' = \pm 1$ and $0 \leq \tau \leq \beta$.

The Green's functions evaluated from the effective model are also shown in Fig. A.2(b). The results reproduce that they become rounded and a shift of the peak by the introduction of the retardation and U . These structures come from the phonon part, Eq. A.26, which increases with τ near $\tau = 0$ and becomes steeper with U for a fixed U_{eff} .

Now, we study the effect of the retardation and the Coulomb interaction in the transition temperature (T_c). Fig. A.3 shows T_c as a function of $-U_{\text{eff}}$ for various conditions. In all cases, T_c rises with $-U_{\text{eff}}$ in the small U_{eff} regime, while decreases in the large- U_{eff} regime. Hence there is a T_c dome, signifying a BCS-BEC crossover. The large- U_{eff} regime is characterized by the condensation of bipolarons, which are electron pairs bound by the phonon-mediated retarded attractive interaction. Panel (a) illustrates the effect of the retardation (controlled by ω_0) on the SC phase for the case $U = 0$, i.e. the Holstein model. As ω_0 decreases, the peak position of T_c shifts to the small- $|U_{\text{eff}}|$ regime and the height of the peak decreases. We also note that

T_c in the small- $|U_{\text{eff}}|$ regime is rather well described with that of the attractive Hubbard model (the antiadiabatic limit with λ and U fixed) with the interaction U_{eff} . This behavior is different from that of CO in the Holstein model [68, 79]. In the latter case the shift of the T_c dome with ω_0 also occurs but the height of the T_c peak does not show a significant change. In addition, the transition temperature of CO significantly increases in the weak-coupling regime when U_{eff} is fixed and ω_0 decreases [68, 79]. This difference between SC and CO in the weak-coupling region can be explained by considering the strength of relevant interactions. The driving force of SC is the attractive interaction between electrons with opposite spins. On the other hand, for CO, the phonon-mediated interaction between electrons with the same spin is also relevant, as can be understood from a mean-field analysis in the adiabatic limit discussed in Sec. 3.1.2. When the phonon frequency is reduced, the lattice movement takes more time and an electron feels more the attraction from other electrons with the same spin through the phonon distortion. Because of this additional attraction from electrons with the same spin, T_c increases in the CO case as ω_0 decreases, while SC cannot take this advantage.

The effect of the Coulomb repulsion is illustrated in Fig. A.3(b) and (c). The peak position shifts to the small- $|U_{\text{eff}}|$ regime and its height decreases as U increases. We note that this time the antiadiabatic picture as the Hubbard model with U_{eff} cannot necessarily well describe T_c , see e. g. $U = 8$ in panel (b) or $U = 2$ in panel (c).

Let us now examine the above properties in terms of the effective polaron model (Eq. 3.9), which is the Hubbard model with a renormalized hopping parameter (reduced by the factor Z_B) and the interaction U_{eff} . The prediction of the model is shown as color curves in Fig. A.3. It turns out that it provides qualitatively good description of the dependence of T_c on ω_0 , U , and λ , although it always overestimates T_c in the region investigated. If we increase U or decrease ω_0 with U_{eff} fixed, $Z_B = \exp(-\frac{\lambda}{2\omega_0})$ increases since $\lambda = U - U_{\text{eff}}$. This renormalization for the polaron band leads to an enhancement of $U_{\text{eff}}/Z_B W$, which means that the system is moved toward the strong-coupling regime of the Hubbard model. This explains the peak shift of T_c toward smaller $|U_{\text{eff}}|$. We note that the effective polaron model also shows that the deviation from the attractive Hubbard model increases in the weak-coupling regime with larger U , see for example the color dashed lines for $U = 8$ in Fig. A.3(b) or $U = 2$ in Fig. A.3(c). This phenomenon is originated from that the shape of T_c in the attractive Hubbard model is convex in the weak-coupling (BCS) regime. In this regime, the enhancement of the correlation due to the renormalization of the hopping parameter by Z_B leads to deviations from the attractive Hubbard model if we do not rescale the U_{eff} -axis. Now one may wonder why the deviation from the attractive Hubbard model with $U = 0$ (Fig. A.3 (a)) is not so clear, although the effective model also predicts the deviation from the attractive Hubbard model. This may be because we need smaller ω_0 to realize a given value of Z_B and U_{eff} when $U = 0$ than when $U > 0$, while the effective model becomes less reliable for smaller ω_0 . Related to this, we comment on the relation between the present work and conventional analyses for small phonon frequencies. Here we have shown that the effective model provides a good picture for describing the effect of the retardation and the effect of the Coulomb interaction when ω_0 is comparable to or larger than the bandwidth of the bare electrons. On the other hand, when ω_0 is much smaller than W , the present picture should become incorrect. Instead, the Migdal theorem becomes appropriate [13] and the effect of the Coulomb interaction should be described in terms of the reduced Coulomb interaction, μ^* [112, 180, 181]. Because of numerical difficulties we cannot investigate crossover between these two pictures, but it would be worthwhile to study such crossover in future.

Now we briefly mention the quantitative accuracy of the effective model for the transition

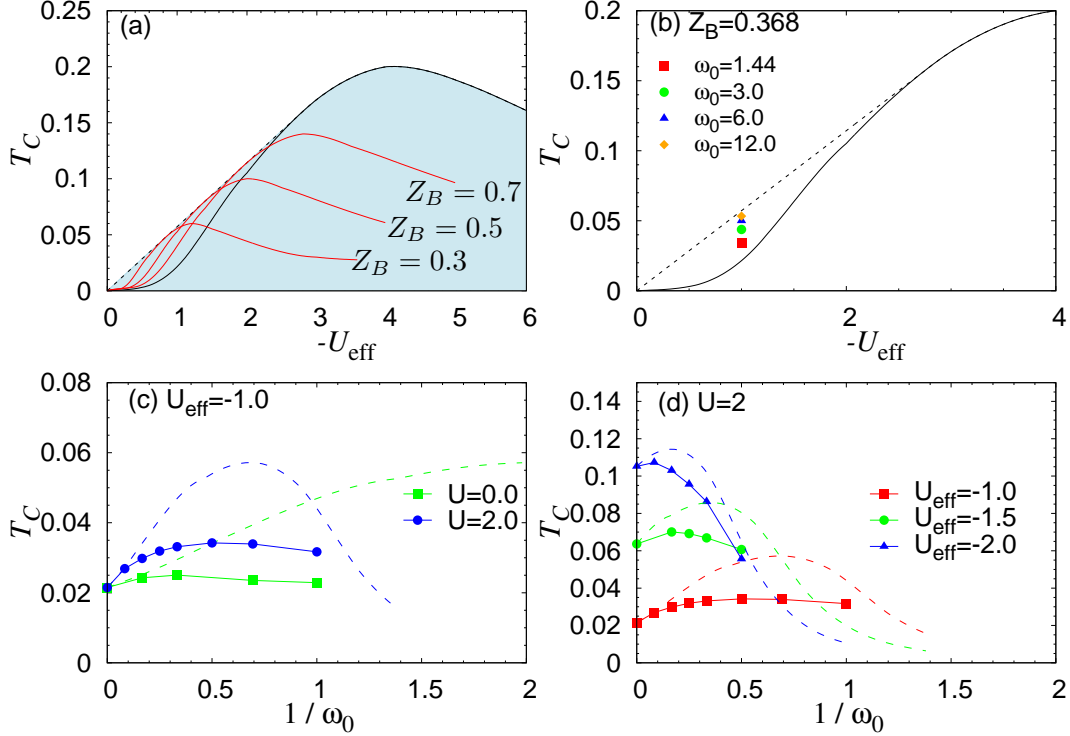


Figure A.4: (a) Possible area (shaded) for the SC phase in the Holstein-Hubbard model, defined by the envelope of the T_c curves (red) for various values of Z_B . The black solid curve represents the behavior in the attractive Hubbard model with $-U_{\text{eff}}$, while the dashed line the envelope of the curves when Z_B is varied. (b) T_c vs $-U_{\text{eff}}$ for various values of ω_0 , plotted here for $U_{\text{eff}} = -1$, $Z_B = U_{\text{eff}}/U_0$. (c)(d) Dependence of the transition temperature against $1/\omega_0$ for various indicated conditions. The colored dashed curves are the prediction from the effective polaron model.

temperature. If the effective model reproduces the Holstein-Hubbard model results accurately, the phase diagram in the space of $\tilde{T} \equiv T/Z_B$ and $\tilde{U}_{\text{eff}} \equiv U_{\text{eff}}/Z_B$ should coincide with that of the attractive Hubbard model. We replot our numerical data in terms of \tilde{U}_{eff} and \tilde{T} in Fig. A.3(d)(e)(f), which cover the range $2 \lesssim |\tilde{U}_{\text{eff}}| \lesssim 6$. For $U = 0$ (retardation effect only), the deviation decreases from $\delta T_c = |T_c - T_{c,\text{eff}}|/T_c \leq 0.25$ for $\omega_0 = 4$ to $\delta T_c \leq 0.1$ for $\omega_0 = 12$. As expected, the reliability of the effective model becomes better as ω_0 increases (Fig. A.3 (d)). The dependence of δT_c on U_{eff} is relatively small at $\omega_0 \geq 4$. On the other hand, if $\omega_0 \leq 2$, the reliability of the effective model strongly depends on U_{eff} , as shown in Fig. A.3(d). As for the effect of U , we find that δT_c slightly, but systematically, increases with increasing U at least in the weak-coupling regime (Fig. A.3 (e) and (f)), and at $\omega_0 = 4$, $\delta T_c \leq 0.25$ up to $U = 4$. We note that the effective model is quantitatively accurate up to larger values of U for larger ω_0 .

Now we discuss the consequences from the effective polaron model. Firstly, the effective model predicts the possible region of the superconducting state in the Holstein-Hubbard model on the plane of T and $-U_{\text{eff}}$, see the shaded area in Fig. A.4(a). The T_c curves for various values of Z_B form a homologous series of phase boundaries of the attractive Hubbard model as is shown

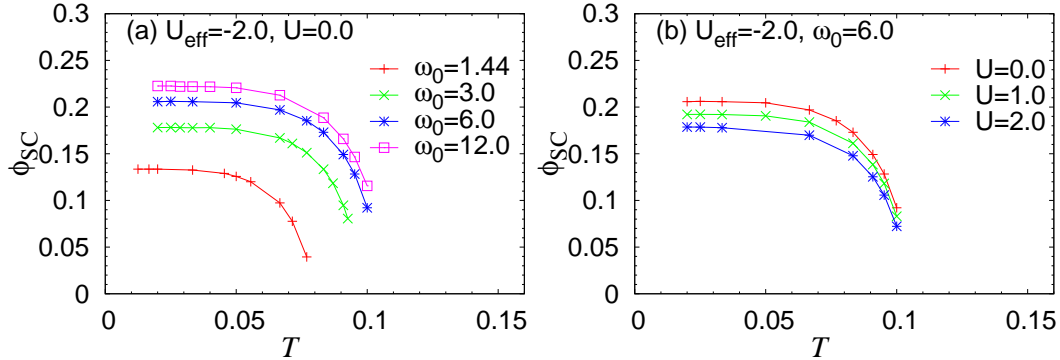


Figure A.5: Temperature dependence of the superconducting order parameter ($\Phi_{\text{SC}}(T)$) for $U_{\text{eff}} = -2, U = 0$ with various values of ω_0 (a), or for $U_{\text{eff}} = -2, \omega_0 = 6$ with various values of U (b).

in red curves in Fig. A.4. These curves set the boundary of the shaded area, which linearly rises from the origin and becomes a tangent to the T_c curve of the attractive Hubbard model (black solid curve in Fig. A.4) at $U_{\text{eff}} = U_0 \simeq -2.72$. This structure comes from the fact that in the weak-coupling the phase boundary of the Hubbard model is convex and that in the BCS-BEC crossover regime it becomes upward convex. Now the question is how meaningful this is. From the construction of the polaron model, we expect that the T_c curves in the effective model are realized in the anitadiabatic limit with U_{eff} and Z_B fixed. We can numerically confirm that the boundary of the blue area is indeed obtained by fixing U_{eff} and $Z_B = U_{\text{eff}}/U_0$ and taking the limit $\omega_0 \rightarrow \infty$, see Fig. A.4 (b). Hence the shaded region should be realized and the SC region is larger than the simple Hubbard model. Within our study of cases with ω_0 comparable to W , the effective model always overestimates the transition temperature. Therefore, we may be able to expect that the superconducting phase of the Holstein-Hubbard model is confined within the blue area. However, since the effective model becomes worse in the adiabatic regime, this prediction may be invalidated in a low-temperature regime.

Secondly, the effective model predicts a *negative isotope effect*. Usually, g and ω_0 in the HH model scale as $g \sim M^{-1/4}$ and $\omega_0 \sim M^{-1/2}$, where M is the mass of atoms. On the other hand, λ and U are expected not to change. Within the effective polaron model, this corresponds to the case where the band is further renormalized with heavier atoms, i.e. Z_B decreases. As can be seen in Fig. A.4 (a), when $|U_{\text{eff}}| < U_0$ the transition temperature enhances as a function of $1/\omega_0$ around $1/\omega_0 = 0$, while for $|U_{\text{eff}}| > U_0$ it monotonically decreases. Although the region and the strength of the negative isotope effect is overestimated by the effective model, direct calculation for the HH model confirms the existence of the negative isotope effect with the phonon frequency comparable to the bandwidth, see Fig. A.4 (c)(d).

Now let us discuss properties below T_c . First, we consider temperature dependence of the SC order parameter, $\Phi_{\text{SC}}(T)$. In Fig. A.5(a) we fix $U = 0, U_{\text{eff}} = -2$ and change the value of ω_0 in order to study the effect of the retardation. In Fig. A.5(b) we fix $\omega_0 = 6, U_{\text{eff}} = -2$ and change U in order to study the effect the Coulomb interaction. In both cases, Φ_{SC} increases monotonically below T_c and saturates with decreasing temperature. Both of the retardation and the Coulomb repulsion U decrease $\Phi_{\text{SC}}(T)$ as can be seen in panels (a) and (b).

Next we focus on the saturation value of Φ_{SC} in the limit of $T \rightarrow 0$. In Fig. A.6 (a), we show

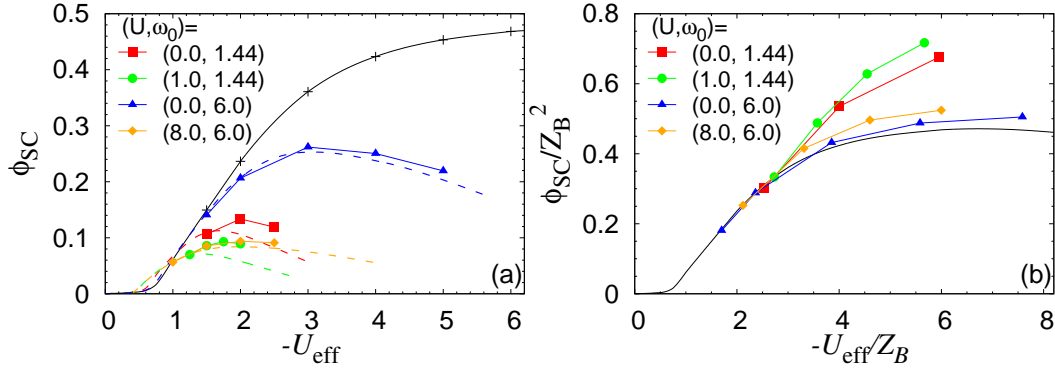


Figure A.6: The superconducting order parameter in the limit of $T \rightarrow 0$ ($\Phi_{SC}(T \rightarrow 0)$). Solid symbols are results of DMFT+QMC analysis. Panel (a) plots the result against $-U_{eff}$ for various sets of parameter values. The crosses are $\Phi_{SC}(T \rightarrow 0)$ for the attractive Hubbard model, and the black curve is an interpolation. The color dashed curves show the results from the effective model, and open symbols on these lines should be compared with the solid symbols with the same shape. Panel (b) plots the results on rescaled axes: $\tilde{U}_{eff} \equiv U_{eff}/Z_B$ and $\tilde{\Phi} \equiv \Phi/Z_B^2$.

$\Phi_{SC}(T \rightarrow 0)$ as a function of $-U_{eff}$. We find that $\Phi_{SC}(T \rightarrow 0)$ shows a peak as a function of $-U_{eff}$ for finite ω_0 . We note that this is different from the behavior of the attractive Hubbard model where $\Phi_{SC}(T \rightarrow 0)$ saturates at 0.5 in the strong-coupling limit [107]. In addition, the peak position shifts to smaller $|U_{eff}|$ with increasing the retardation (decreasing ω_0) or with increasing the Coulomb interaction U . We also note that $\Phi_{SC}(T \rightarrow 0)$ decreases as we decrease ω_0 or increase U in the region investigated ($-U_{eff} \gtrsim 1.5$), see Fig. A.5.

We now consider how the effective model works for this quantity. Let us express the order parameter of SC in the HH model at (T, U, U_{eff}, Z_B) as $\Phi_{SC}(T, U, U_{eff}, Z_B)$. Within the effective model, the order parameter is expressed as

$$\begin{aligned} \Phi_{SC}(T, U, U_{eff}, Z_B) &= \langle e^{-2\frac{g}{\omega_0}(b^\dagger - b)} c_\downarrow c_\uparrow \rangle_{H_{LF}} \\ &\approx \langle 0 | e^{-2\frac{g}{\omega_0}(b^\dagger - b)} | 0 \rangle \langle c_\downarrow c_\uparrow \rangle_{H_{eff}} = Z_B^2 \Phi_0(T/Z_B, U_{eff}/Z_B) \\ &\equiv \Phi_{eff}[T, Z_B, U_{eff}], \end{aligned} \quad (\text{A.27})$$

where we have defined $\Phi_{0,SC}(T, U)$ as the order parameter for the Hubbard model with unrenormalized hopping v and interaction U at temperature T .

It turns out that these behaviors are qualitatively well described by the effective polaron model, whose results are shown as the color curves in Fig. A.6(a). In the effective model, what saturates at large U_{eff} with $\omega_0 \neq \infty$ is the condensation density of pairs of polarons, which can be expressed as $\langle c_\downarrow c_\uparrow \rangle_{LF}$ after the Lang-Firsov transformation. On the other hand, Φ_{SC} is the order parameter defined for electrons, and the correction from the phonon dressing is expressed as Z_B^2 in Eq. A.27. This correction becomes large as the electron-phonon coupling becomes strong, which is the origin of the peak in $\Phi_{SC}(T \rightarrow 0)$. Hence the dome structure of $\Phi_{SC}(T \rightarrow 0)$ in the Holstein-Hubbard model can be attributed to the enhancement of the phonon dressing with increasing $|U_{eff}|$.

In order to assess quantitative reliability of the effective polaron model about the superconducting order parameter, we rescale in Fig. A.6(b) the axis of Fig. A.6(a) as $\tilde{U}_{eff} \equiv U_{eff}/Z_B$ and

$\tilde{\Phi} \equiv \Phi/Z_B^2$. Here we again focus on the range $2 \lesssim |\tilde{U}_{\text{eff}}| \lesssim 6$. It turns out that, the rescaled curve underestimates $\Phi_{\text{SC}}(T \rightarrow 0)$ for large enough $|\tilde{U}_{\text{eff}}|$. On the other hand, for smaller $|\tilde{U}_{\text{eff}}|$ ($\lesssim 2.5$), the effective model becomes better. A larger U gives a larger underestimation in the strong $|\tilde{U}_{\text{eff}}|$ regime. We have $\delta\Phi \equiv |(\Phi_{\text{SC}}(T \rightarrow 0) - \Phi_{\text{eff}}(T \rightarrow 0))|/\Phi_{\text{SC}}(T \rightarrow 0) \leq 0.2$ for $\omega_0 \gtrsim 4$ at $U = 0$. As for the effect of U , we find $\delta\Phi \leq 0.2$ up to $U = 6$ at $\omega_0 = 4$. The effective model is quantitatively accurate up to larger U for larger ω_0 .

Now we discuss the SC gap in the spectral function and its relation with the transition temperature. We first note that within DMFT the self-energy is momentum independent and expressed as

$$\hat{\Sigma}(i\omega_n) = \begin{bmatrix} \Sigma(i\omega_n) & S(i\omega_n) \\ S(i\omega_n) & -\Sigma^*(i\omega_n) \end{bmatrix}, \quad (\text{A.28})$$

where Σ represents the normal self-energy while S is the anomalous one. The lattice Green's function at a momentum \mathbf{k} is

$$\begin{aligned} \hat{G}(\mathbf{k}, i\omega_n) &= \begin{bmatrix} G_{11}(\mathbf{k}, i\omega_n) & G_{12}(\mathbf{k}, i\omega_n) \\ G_{21}(\mathbf{k}, i\omega_n) & G_{22}(\mathbf{k}, i\omega_n) \end{bmatrix} \\ &= [G^0(\mathbf{k}, i\omega_n)^{-1} - \Sigma(i\omega_n)]^2 + |S(i\omega_n)|^2]^{-1} \begin{bmatrix} G^0(-\mathbf{k}, -i\omega_n)^{-1} - \Sigma(-i\omega_n) & -S(i\omega_n) \\ -S(i\omega_n) & -G^0(\mathbf{k}, i\omega_n)^{-1} + \Sigma(i\omega_n) \end{bmatrix}. \end{aligned} \quad (\text{A.29})$$

Here $G^0(\mathbf{k}, i\omega_n) = i\omega_n - (\epsilon_{\mathbf{k}} - \mu)$ is the bare lattice Green's function and $\epsilon_{\mathbf{k}}$ is the dispersion relation for the bare electrons.

Now we evaluate the spectral gap in the following manner. First let us imagine that we have made an analytic continuation ($i\omega_n \rightarrow \omega + i0^+$) to obtain the self-energy on the real frequency axis. If the contribution to the self-energy from the terms higher-order in ω than $\mathcal{O}(\omega)$ can be neglected, the spectral gap in the single-particle spectrum is evaluated by $zS(\omega = 0)$. Here $z \equiv [1 - \partial\Sigma(\omega)/\partial\omega|_{\omega=0}]^{-1}$ is the quasiparticle weight.

When the quasiparticle picture is good, the self-energies for small $|\omega_n|$ can be expanded as

$$\Sigma(i\omega_n) = \Sigma^{(0)} + i\omega_n \Sigma^{(1)} + \mathcal{O}((i\omega_n)^2), \quad (\text{A.30})$$

$$S(i\omega_n) = S(\omega = 0) + \mathcal{O}((i\omega_n)^2), \quad (\text{A.31})$$

where $\Sigma^{(0)} \equiv \Sigma(\omega = 0)$, $\Sigma^{(1)} \equiv \partial\Sigma(\omega)/\partial\omega|_{\omega=0}$. Then one can evaluate z and $S(\omega = 0)$ using self-energies on the Matsubara axis. One can approximate the quasiparticle weight z as $Z \equiv [1 - \text{Im}\Sigma(\omega_{n=0})/\omega_{n=0}]^{-1}$ and $S(\omega = 0)$ as $S^{(0)} \equiv [9S(\omega_{n=0}) - S(\omega_{n=1})]/8$. With this approximation, the gap in the excitation spectrum is evaluated as

$$\Delta_{\text{SC}} \equiv ZS^{(0)}. \quad (\text{A.32})$$

This expression provides a rough estimate of the spectral gap. Here, we have to note that this approximation, which uses the information around $\omega = 0$, is justified in the weak-coupling regime and when the gap is small enough. When U_{eff} becomes larger, there is no guarantee that the approximation is valid. However, it turns out that the gap estimated in this way is adequate even in the strong-coupling regime, judging from the comparison with a previous work for the Hubbard model [182].

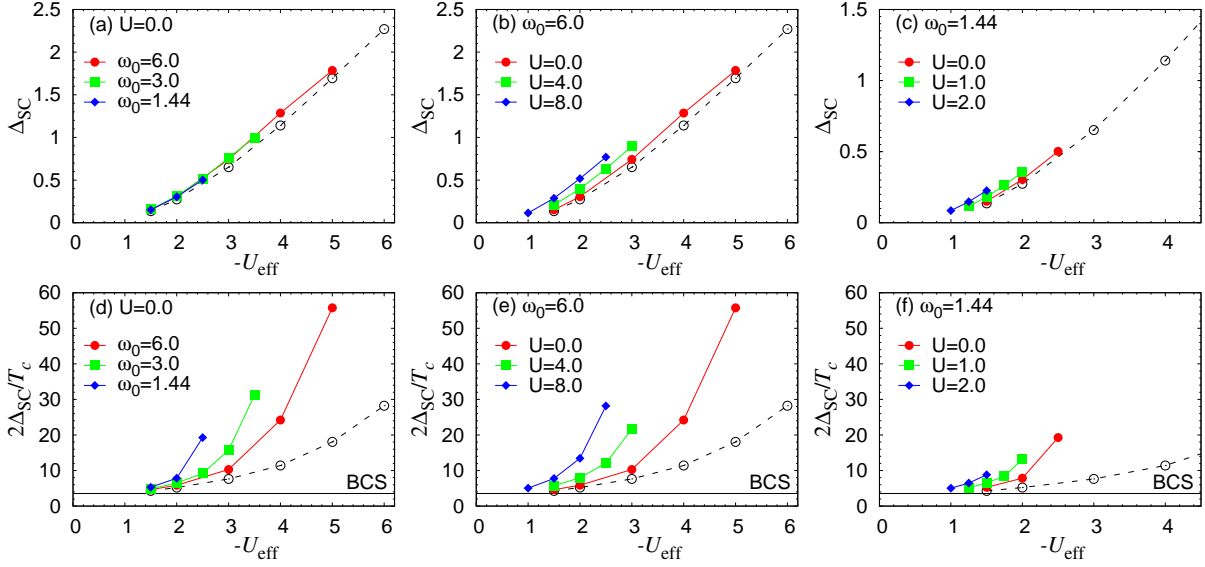


Figure A.7: (a)(b)(c) The energy-gap parameter $\Delta_{\text{SC}} (= \Delta_{\text{SC}}(T \rightarrow 0))$ against $-U_{\text{eff}}$ for various sets of parameters. (a) is for various values of ω_0 at $U = 0$, and (b) (c) are the results when U is switched on with a fixed $\omega_0 = 6$ (b), or $\omega_0 = 1.44$ (c). (d)(e)(f) The ratio of the energy-gap parameter to the transition temperature ($2\Delta_{\text{SC}}(T \rightarrow 0)/T_c$) against $-U_{\text{eff}}$. The horizontal blue line indicates the BCS value $2\Delta/T_c = 3.528$. (d) shows the result for various values of ω_0 at $U = 0$. (e) and (f) are the result with finite U and fixed $\omega_0 = 6$ (e), or $\omega_0 = 1.44$ (f). Empty circles along the dashed line show the results for the attractive Hubbard model with $-U_{\text{eff}}$ for each panel. Note the different scale of horizontal and vertical axes in panel (c)(f) from the rest.

In Fig. A.7(a)(b)(c), we display the gap, Δ_{SC} , estimated as described above in the limit of $T \rightarrow 0$ against U_{eff} . Δ_{SC} monotonically increases with $|U_{\text{eff}}|$ in all cases. When ω_0 is changed with $U = 0$, the dependence on ω_0 is small, see Fig. A.7(a). On the other hand, with ω_0 and $|U_{\text{eff}}|$ fixed, the gap increases with U , see Fig. A.7(b)(c).

In Fig. A.7(d)(e)(f), we show $2\Delta_{\text{SC}}(T \rightarrow 0)/T_c$, which is 3.528 in the BCS theory. Hence deviation of $2\Delta_{\text{SC}}(T \rightarrow 0)/T_c$ from 3.528 is a good measure for the deviation from the BCS theory. The quantity significantly increases monotonically with $|U_{\text{eff}}|$. In the opposite limit of $|U_{\text{eff}}| \rightarrow 0$, $2\Delta_{\text{SC}}/T_c$ approaches the BCS value in all cases, which is consistent with the prediction from the effective polaron model. Now, let us take a closer look at the effect of the retardation and the Coulomb interaction on $2\Delta_{\text{SC}}(T \rightarrow 0)/T_c$. In Fig. A.7(d) for $U = 0$, we find that $2\Delta_{\text{SC}}/T_c$ grows with $|U_{\text{eff}}|$ faster for smaller ω_0 . In other words, the region where the BCS theory works decreases with decreasing the phonon frequency. Figure A.7(e) and (f) exhibit the effect of the Coulomb interaction U . They tell that $2\Delta_{\text{SC}}/T_c$ grows faster for larger U . This suggests that, even though both T_c and Δ_{SC} increase with U at each $|U_{\text{eff}}|$ in the small $|U_{\text{eff}}|$ regime (see Fig. A.3 for T_c), the latter increases faster. To sum up, the retardation and the Coulomb interaction both lead to deviations from the BCS theory, and the deviation is larger for larger $|U_{\text{eff}}|$. We note that these findings are again consistent with the prediction from the effective polaron model, where the retardation and the Coulomb interaction lead to smaller Z_B

A.3. SUPERCONDUCTIVITY IN THE HOLSTEIN-HUBBARD MODEL

and the relative strength of the effective instantaneous interaction $U_{\text{eff}}/Z_{\text{B}}W$ becomes larger.

Appendix B

Non-equilibrium part

B.1 Volterra equations for Dyson equations

Here we explain how to numerically solve Dyson equations, Eqs. 2.96, 2.99, 2.102, 2.105, for the retarded (R), left-mixing ($\bar{}$) and lesser parts ($<$), taking the most complicated case Eq. 2.105 as an example.

First of all, these equations belong to so-called Volterra equations [26],

$$y(t) = q(t) + \int_{t'}^t d\bar{t} K(t, \bar{t}) y(\bar{t}), \quad (\text{B.1a})$$

$$\frac{d}{dt} y(t) = q(t) + p(t) y(t) + \int_{t'}^t d\bar{t} K(t, \bar{t}) y(\bar{t}), \quad (\text{B.1b})$$

$$\frac{d^2}{dt^2} y(t) = q(t) + p(t) y(t) + \int_{t'}^t d\bar{t} K(t, \bar{t}) y(\bar{t}), \quad (\text{B.1c})$$

where t' can be 0 or nonzero. In particular, three equations in Eq. 2.105 correspond to Eq. B.1c. The situation we consider is that the self-energies, $\Pi(\Sigma)$, the free parts, $D_0(G_0, \mathcal{G}_0)$, and the Matsubara components, $D^M(G^M)$, are given. We note that, since $K(t, \bar{t})$ in Eq. B.1c for the lesser part needs the information of R and $\bar{}$ we need to solve the equations for R and $\bar{}$ before the lesser part.

Now, we explain how to solve Eq. B.1c. If we put $\frac{d}{dt} y(t) = z(t)$,

$$\frac{d}{dt} y(t) = z(t), \quad (\text{B.2})$$

$$\frac{d}{dt} z(t) = q(t) + p(t) y(t) + \int_{t'}^t d\bar{t} K(t, \bar{t}) y(\bar{t}). \quad (\text{B.3})$$

We assume that we have value of $y(t), z(t)$ on t_i ($i = 0, 1, \dots, n-1$), then we obtain

$$y(t_n) - y(t_{n-1}) \approx \Delta t \sum_{i=m}^{n-1} (W_{n,m}^i - W_{n-1,m}^i) y'(t_i) + \Delta t W_{n,m}^n y'(t_n), \quad (\text{B.4})$$

$$z(t_n) - z(t_{n-1}) \approx \Delta t \sum_{i=m}^{n-1} (W_{n,m}^i - W_{n-1,m}^i) z'(t_i) + \Delta t W_{n,m}^n z'(t_n), \quad (\text{B.5})$$

B.2. DIMENSIONLESS ELECTRON-PHONON COUPLING

where we take $t_m = t'$. Here we approximate a integral as

$$\int_{t_m}^{t_n} d\bar{t} f(\bar{t}) \approx \Delta t \sum_{i=m}^n W_{n,m}^i f(t_i), \quad (\text{B.6})$$

and in the 2nd order approximation we take

$$W_{n,m}^i = \begin{cases} 0.5 & i=n \text{ or } i=m \\ 1 & \text{otherwise} \end{cases}. \quad (\text{B.7})$$

Since

$$\begin{aligned} z'(t_n) &\approx q(t_n) + p(t_n)y(t_n) + \Delta t \sum_{i=m}^n W_{n,m}^i K(t_n, t_i)y(t_i) \\ &= (p(t_n) + \Delta t W_{n,m}^n K(t_n, t_n))y(t_n) + q(t_n) + \Delta t \sum_{i=m}^{n-1} W_{n,m}^i K(t_n, t_i)y(t_i), \end{aligned} \quad (\text{B.8})$$

we need to solve the following equation to obtain $y(t_n), z(t_n)$ with the given value of $y(t_i), z(t_i)$ for $i < n$,

$$y(t_n) - \Delta t W_{n,m}^n z(t_n) \approx y(t_{n-1}) + \Delta t \sum_{i=m}^{n-1} (W_{n,m}^i - W_{n-1,m}^i) z(t_i), \quad (\text{B.9})$$

$$\begin{aligned} z(t_n) - \Delta t W_{n,m}^n [p(t_n) + \Delta t W_{n,m}^n K(t_n, t_n)]y(t_n) &\approx z(t_{n-1}) + \Delta t \sum_{i=m}^{n-1} (W_{n,m}^i - W_{n-1,m}^i) z'(t_i) \\ &+ \Delta t W_{n,m}^n [q(t_n) + \Delta t \sum_{i=m}^{n-1} W_{n,m}^i K(t_n, t_i)y(t_i)]. \end{aligned} \quad (\text{B.10})$$

B.2 Dimensionless electron-phonon coupling

The dimensionless el-ph coupling λ_{eff} , which is defined in Eq. 4.7, for the parameters employed in the thesis is show in Fig. B.1. In all cases, the temperature dependence is weak.

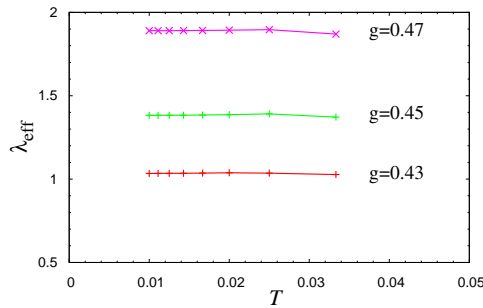


Figure B.1: Dimensionless el-ph coupling λ_{eff} used in this thesis. $\omega_0 = 0.4$ for all cases.

B.3 Implementation of the pulse field

The Dyson equations involved in the DMFT solution of the Holstein model with the pair potential, $H_{\text{ex}}(t) = F_{\text{ex}}(t) \sum_i (c_{i\uparrow}^\dagger c_{i\downarrow}^\dagger + c_{i\downarrow} c_{i\uparrow})$, are

$$D_{\text{loc}}(\nu, \nu') = D_0(\nu, \nu') + [D_0 * \Pi * D_{\text{loc}}](\nu, \nu'), \quad (\text{B.11a})$$

$$\begin{bmatrix} i\partial_\nu + \mu & -F_{\text{ex}}(\nu) \\ -F_{\text{ex}}(\nu) & i\partial_\nu - \mu \end{bmatrix} \hat{G}_{\text{loc}}(\nu, \nu') - [(\hat{\Sigma} + \hat{\Delta}) * \hat{G}_{\text{loc}}](\nu, \nu') = \hat{I}\delta_{\mathcal{C}}(\nu, \nu'), \quad (\text{B.11b})$$

$$\begin{bmatrix} i\partial_\nu + \mu & -F_{\text{ex}}(\nu) \\ -F_{\text{ex}}(\nu) & i\partial_\nu - \mu \end{bmatrix} \hat{\mathcal{G}}_0(\nu, \nu') - [\hat{\Delta} * \hat{\mathcal{G}}_0](\nu, \nu') = \hat{I}\delta_{\mathcal{C}}(\nu, \nu'). \quad (\text{B.11c})$$

Here, as in the main part, $D_{\text{loc}}(\nu, \nu') = -2i\langle T_{\mathcal{C}} X_i(\nu) X_i(\nu') \rangle = D_{\text{imp}}(\nu, \nu')$, $\hat{G}_{\text{loc}}(\nu, \nu') = -i\langle T_{\mathcal{C}} \Psi_i(\nu) \Psi_i^\dagger(\nu') \rangle = \hat{G}_{\text{imp}}(\nu, \nu')$, \mathcal{G}_0 is the Weiss Green's function, and $\hat{\Delta}(\nu, \nu')$ is the hybridization function. $\hat{\Sigma}(\nu, \nu')$ ($\Pi(\nu, \nu')$) is the momentum-independent electron (phonon) self-energy, which is equivalent that of the effective impurity problem. When we take $F_{\text{ex}}(t) = d_f \delta(t)$, one finds from the above Dyson equations that the effect of the external field leads to a jump in \mathcal{G}_0 and \hat{G} around $t = 0$:

$$G_{\alpha\beta}^R(0^+, 0^+) = -i\delta_{\alpha,\beta}, \quad (\text{B.12a})$$

$$\hat{G}^\neg(0^+, \tau') = \hat{M}\hat{G}^\neg(0^-, \tau'), \quad (\text{B.12b})$$

$$\hat{G}^<(0^+, 0^+) = \hat{M}\hat{G}^<(0^-, 0^-)\hat{M}^\dagger, \quad (\text{B.12c})$$

where we have defined the matrix \hat{M} ,

$$\hat{M} \equiv \frac{1}{1 + \frac{d_f^2}{4}} \begin{bmatrix} 1 - \frac{d_f^2}{4} & -id_f \\ -id_f & 1 - \frac{d_f^2}{4} \end{bmatrix}. \quad (\text{B.13})$$

The expressions for the discontinuity of the Weiss Green's functions are obtained by replacing G with \mathcal{G}_0 in Eq. B.12. On the other hand, the phonon Green's function (D) is continuous there.

Bibliography

- [1] A. Albuquerque, F. Alet, P. Corboz, P. Dayal, A. Feiguin, S. Fuchs, L. Gamper, E. Gull, S. Grtler, A. Honecker, R. Igarashi, M. Krner, A. Kozhevnikov, A. Luchli, S. Manmana, M. Matsumoto, I. McCulloch, F. Michel, R. Noack, G. Pawowski, L. Pollet, T. Pruschke, U. Schollwck, S. Todo, S. Trebst, M. Troyer, P. Werner, and S. Wessel, “The {ALPS} project release 1.3: Open-source software for strongly correlated systems,” *Journal of Magnetism and Magnetic Materials*, vol. 310, no. 2, Part 2, pp. 1187 – 1193, 2007. Proceedings of the 17th International Conference on MagnetismThe International Conference on Magnetism.
- [2] B. Bauer, L. D. Carr, H. G. Evertz, A. Feiguin, J. Freire, S. Fuchs, L. Gamper, J. Gukelberger, E. Gull, S. Guertler, A. Hehn, R. Igarashi, S. V. Isakov, D. Koop, P. N. Ma, P. Mates, H. Matsuo, O. Parcollet, G. Pawowski, J. D. Picon, L. Pollet, E. Santos, V. W. Scarola, U. Schollwck, C. Silva, B. Surer, S. Todo, S. Trebst, M. Troyer, M. L. Wall, P. Werner, and S. Wessel, “The alps project release 2.0: open source software for strongly correlated systems,” *Journal of Statistical Mechanics: Theory and Experiment*, vol. 2011, no. 05, p. P05001, 2011.
- [3] O. Gunnarsson, “Superconductivity in fullerenes,” *Rev. Mod. Phys.*, vol. 69, pp. 575–606, Apr 1997.
- [4] Y. Takabayashi, A. Y. Ganin, P. Jegli, D. Aron, T. Takano, Y. Iwasa, Y. Ohishi, M. Takata, N. Takeshita, K. Prassides, and M. J. Rosseinsky, “The disorder-free non-bcs superconductor cs_3c_{60} emerges from an antiferromagnetic insulator parent state,” *Science*, vol. 323, no. 5921, pp. 1585–1590, 2009.
- [5] M. Capone, M. Fabrizio, C. Castellani, and E. Tosatti, “*Colloquium* : Modeling the unconventional superconducting properties of expanded $A_3\text{c}_{60}$ fullerenes,” *Rev. Mod. Phys.*, vol. 81, pp. 943–958, Jun 2009.
- [6] Y. Nomura, K. Nakamura, and R. Arita, “*Ab initio* derivation of electronic low-energy models for c_{60} and aromatic compounds,” *Phys. Rev. B*, vol. 85, p. 155452, Apr 2012.
- [7] Y. Nomura, S. Sakai, M. Capone, and R. Arita, “Unified understanding of superconductivity and mott transition in alkali-doped fullerenes from first principles,” *Science Advances*, vol. 1, no. 7, 2015.
- [8] R. Mitsuhashi, Y. Suzuki, Y. Yamanari, H. Mitamura, T. Kambe, N. Ikeda, H. Okamoto, A. Fujiwara, M. Yamaji, N. Kawasaki, Y. Maniwa, and Y. Kubozono, “Superconductivity in alkali-metal-doped picene.,” *Nature*, vol. 464, pp. 76–9, Mar. 2010.

- [9] T. Kato, T. Kambe, and Y. Kubozono, “Strong intramolecular electron-phonon coupling in the negatively charged aromatic superconductor picene,” *Phys. Rev. Lett.*, vol. 107, p. 077001, Aug 2011.
- [10] Y. Kubozono, H. Mitamura, X. Lee, X. He, Y. Yamanari, Y. Takahashi, Y. Suzuki, Y. Kaji, R. Eguchi, K. Akaike, T. Kambe, H. Okamoto, A. Fujiwara, T. Kato, T. Kosugi, and H. Aoki, “Metal-intercalated aromatic hydrocarbons: a new class of carbon-based superconductors,” *Physical chemistry chemical physics : PCCP*, vol. 13, pp. 16476–93, Oct. 2011.
- [11] T. Kosugi, T. Miyake, S. Ishibashi, R. Arita, and H. Aoki, “First-principles structural optimization and electronic structure of the superconductor picene for various potassium doping levels,” *Phys. Rev. B*, vol. 84, p. 214506, Dec 2011.
- [12] A. Subedi and L. Boeri, “Vibrational spectrum and electron-phonon coupling of doped solid picene from first principles,” *Phys. Rev. B*, vol. 84, p. 020508, Jul 2011.
- [13] A. B. Migdal, “Interaction between electrons and lattice vibrations in a normal metal,” *Sov. Phys. JETP*, vol. 7, p. 996, 1958.
- [14] G. M. Eliashberg, “Interactions between electrons and lattice vibrations in a superconductor,” *Sov. Phys. JETP*, vol. 11, p. 696, 1960.
- [15] G. M. Eliashberg, “Temperature green’s function for electrons in a superconductor,” *Sov. Phys. JETP*, vol. 12, no. 5, pp. 1000–1002, 1961.
- [16] A. Lanzara, P. V. Bogdanov, X. J. Zhou, S. a. Kellar, D. L. Feng, E. D. Lu, T. Yoshida, H. Eisaki, A. Fujimori, K. Kishio, J. I. Shimoyama, T. Noda, S. Uchida, Z. Hussain, and Z. X. Shen, “Evidence for ubiquitous strong electron-phonon coupling in high-temperature superconductors,” *Nature*, vol. 412, pp. 510–4, Aug. 2001.
- [17] R. Matsunaga, Y. I. Hamada, K. Makise, Y. Uzawa, H. Terai, Z. Wang, and R. Shimano, “Higgs amplitude mode in the bcs superconductors $\text{Nb}_{1-x}\text{Ti}_x\text{N}$ induced by terahertz pulse excitation,” *Phys. Rev. Lett.*, vol. 111, p. 057002, Jul 2013.
- [18] R. Matsunaga, N. Tsuji, H. Fujita, A. Sugioka, K. Makise, Y. Uzawa, H. Terai, Z. Wang, H. Aoki, and R. Shimano, “Light-induced collective pseudospin precession resonating with higgs mode in a superconductor,” *Science*, vol. 345, no. 6201, pp. 1145–1149, 2014.
- [19] D. Fausti, R. I. Tobey, N. Dean, S. Kaiser, A. Dienst, M. C. Hoffmann, S. Pyon, T. Takayama, H. Takagi, and A. Cavalleri, “Light-induced superconductivity in a stripe-ordered cuprate,” *Science*, vol. 331, no. 6014, pp. 189–191, 2011.
- [20] S. Kaiser, C. R. Hunt, D. Nicoletti, W. Hu, I. Gierz, H. Y. Liu, M. Le Tacon, T. Loew, D. Haug, B. Keimer, and A. Cavalleri, “Optically induced coherent transport far above T_c in underdoped $\text{YBa}_2\text{Cu}_3\text{O}_{6+\delta}$,” *Phys. Rev. B*, vol. 89, p. 184516, May 2014.
- [21] W. Hu, S. Kaiser, D. Nicoletti, and C. Hunt, “Optically enhanced coherent transport in $\text{YBa}_2\text{Cu}_3\text{O}_6$. 5 by ultrafast redistribution of interlayer coupling,” *Nature materials*, vol. 13, no. May, pp. 705–711, 2014.

BIBLIOGRAPHY

- [22] M. Mitrano, A. Cantaluppi, D. Nicoletti, S. Kaiser, A. Perucchi, S. Lupi, P. D. Pietro, D. Pontiroli, M. Ricc3, A. Subedi, S. R. Clark, D. Jaksch, and A. Cavalleri, “An optically stimulated superconducting-like phase in k_3c_{60} far above equilibrium t_c ,” *arXiv preprint arXiv:1505.04529*, vol. 1, pp. 1–40, 2015.
- [23] W. Metzner and D. Vollhardt, “Correlated lattice fermions in $d = \infty$ dimensions,” *Phys. Rev. Lett.*, vol. 62, pp. 324–327, Jan 1989.
- [24] A. Georges and G. Kotliar, “Hubbard model in infinite dimensions,” *Phys. Rev. B*, vol. 45, pp. 6479–6483, Mar 1992.
- [25] A. Georges, G. Kotliar, W. Krauth, and M. J. Rozenberg, “Dynamical mean-field theory of strongly correlated fermion systems and the limit of infinite dimensions,” *Rev. Mod. Phys.*, vol. 68, pp. 13–125, Jan 1996.
- [26] H. Aoki, N. Tsuji, M. Eckstein, M. Kollar, T. Oka, and P. Werner, “Nonequilibrium dynamical mean-field theory and its applications,” *Rev. Mod. Phys.*, vol. 86, pp. 779–837, Jun 2014.
- [27] Y. Murakami, P. Werner, N. Tsuji, and H. Aoki, “Supersolid phase accompanied by a quantum critical point in the intermediate coupling regime of the holstein model,” *Phys. Rev. Lett.*, vol. 113, p. 266404, Dec 2014.
- [28] Y. Murakami, P. Werner, N. Tsuji, and H. Aoki, “Ordered phases in the holstein-hubbard model: Interplay of strong coulomb interaction and electron-phonon coupling,” *Phys. Rev. B*, vol. 88, p. 125126, Sep 2013.
- [29] Y. Murakami, P. Werner, N. Tsuji, and H. Aoki, “Dynamical mean-field analysis of ordered phases in the half-filled Holstein-Hubbard model,” *JPS Conf. Proc.*, vol. 3, p. 016023, 2014.
- [30] Y. Murakami, P. Werner, N. Tsuji, and H. Aoki, “Interaction quench in the holstein model: Thermalization crossover from electron- to phonon-dominated relaxation,” *Phys. Rev. B*, vol. 91, p. 045128, Jan 2015.
- [31] Y. Murakami, P. Werner, N. Tsuji, and H. Aoki, “Multiple amplitude modes in strongly-coupled phonon-mediated superconductors,” *arXiv:1511.06105*, 2015.
- [32] P. B. Littlewood and C. M. Varma, “Gauge-invariant theory of the dynamical interaction of charge density waves and superconductivity,” *Phys. Rev. Lett.*, vol. 47, pp. 811–814, Sep 1981.
- [33] P. B. Littlewood and C. M. Varma, “Amplitude collective modes in superconductors and their coupling to charge-density waves,” *Phys. Rev. B*, vol. 26, pp. 4883–4893, Nov 1982.
- [34] R. Sooryakumar and M. V. Klein, “Raman scattering by superconducting-gap excitations and their coupling to charge-density waves,” *Phys. Rev. Lett.*, vol. 45, pp. 660–662, Aug 1980.

BIBLIOGRAPHY

- [35] M.-A. Méasson, Y. Gallais, M. Cazayous, B. Clair, P. Rodière, L. Cario, and A. Sacuto, “Amplitude higgs mode in the $2h - nbse_2$ superconductor,” *Phys. Rev. B*, vol. 89, p. 060503, Feb 2014.
- [36] T. Cea, C. Castellani, and L. Benfatto, “Non-linear optical effects and third-harmonic generation in superconductors: Cooper-pairs vs higgs mode contribution,” *arXiv:1512.02544*, 2015.
- [37] P. W. Anderson, “Random-phase approximation in the theory of superconductivity,” *Phys. Rev.*, vol. 112, pp. 1900–1916, Dec 1958.
- [38] A. Volkov and S. Kogan, “Collisionless relaxation of the energy gap in superconductors,” *Soviet Journal of Experimental and . . .*, vol. 38, no. 5, pp. 1018–1021, 1974.
- [39] I. Kulik, O. Entin-Wohlman, and R. Orbach, “Pair susceptibility and mode propagation in superconductors: A microscopic approach,” *Journal of Low Temperature Physics*, vol. 43, no. 5-6, pp. 591–620, 1981.
- [40] R. A. Barankov, L. S. Levitov, and B. Z. Spivak, “Collective rabi oscillations and solitons in a time-dependent bcs pairing problem,” *Phys. Rev. Lett.*, vol. 93, p. 160401, Oct 2004.
- [41] R. A. Barankov and L. S. Levitov, “Synchronization in the bcs pairing dynamics as a critical phenomenon,” *Phys. Rev. Lett.*, vol. 96, p. 230403, Jun 2006.
- [42] E. A. Yuzbashyan and M. Dzero, “Dynamical vanishing of the order parameter in a fermionic condensate,” *Phys. Rev. Lett.*, vol. 96, p. 230404, Jun 2006.
- [43] T. Papenkort, V. M. Axt, and T. Kuhn, “Coherent dynamics and pump-probe spectra of bcs superconductors,” *Phys. Rev. B*, vol. 76, p. 224522, Dec 2007.
- [44] T. Papenkort, T. Kuhn, and V. M. Axt, “Coherent control of the gap dynamics of bcs superconductors in the nonadiabatic regime,” *Phys. Rev. B*, vol. 78, p. 132505, Oct 2008.
- [45] A. P. Schnyder, D. Manske, and A. Avella, “Resonant generation of coherent phonons in a superconductor by ultrafast optical pump pulses,” *Phys. Rev. B*, vol. 84, p. 214513, Dec 2011.
- [46] H. Krull, D. Manske, G. S. Uhrig, and A. P. Schnyder, “Signatures of nonadiabatic bcs state dynamics in pump-probe conductivity,” *Phys. Rev. B*, vol. 90, p. 014515, Jul 2014.
- [47] N. Tsuji and H. Aoki, “Theory of anderson pseudospin resonance with higgs mode in superconductors,” *Phys. Rev. B*, vol. 92, p. 064508, Aug 2015.
- [48] T. Cea and L. Benfatto, “Nature and raman signatures of the higgs amplitude mode in the coexisting superconducting and charge-density-wave state,” *Phys. Rev. B*, vol. 90, p. 224515, Dec 2014.
- [49] T. Cea, C. Castellani, G. Seibold, and L. Benfatto, “Nonrelativistic dynamics of the amplitude (higgs) mode in superconductors,” *Phys. Rev. Lett.*, vol. 115, p. 157002, Oct 2015.

- [50] F. Peronaci, M. Schiró, and M. Capone, “Transient dynamics of d-wave superconductors after a sudden excitation,” *arXiv:1506.01409*, 2015.
- [51] M. Först, C. Manzoni, S. Kaiser, Y. Tomioka, Y. Tokura, R. Merlin, and a. Cavalleri, “Nonlinear phononics as an ultrafast route to lattice control,” *Nature Physics*, vol. 7, pp. 854–856, Aug. 2011.
- [52] A. Subedi, A. Cavalleri, and A. Georges, “Theory of nonlinear phononics for coherent light control of solids,” *Phys. Rev. B*, vol. 89, p. 220301, Jun 2014.
- [53] R. Mankowsky, a. Subedi, M. Först, S. O. Mariager, M. Chollet, H. T. Lemke, J. S. Robinson, J. M. Glowia, M. P. Minitti, a. Frano, M. Fechner, N. a. Spaldin, T. Loew, B. Keimer, a. Georges, and a. Cavalleri, “Nonlinear lattice dynamics as a basis for enhanced superconductivity in YBa₂Cu₃O_{6.5},” *Nature*, vol. 516, pp. 71–3, Dec. 2014.
- [54] M. Rini, R. Tobey, N. Dean, J. Itatani, Y. Tomioka, Y. Tokura, R. W. Schoenlein, and A. Cavalleri, “Control of the electronic phase of a manganite by mode-selective vibrational excitation,” *Nature*, vol. 449, pp. 72–4, Sept. 2007.
- [55] M. Först, R. I. Tobey, S. Wall, H. Bromberger, V. Khanna, A. L. Cavalieri, Y.-D. Chuang, W. S. Lee, R. Moore, W. F. Schlotter, J. J. Turner, O. Krupin, M. Trigo, H. Zheng, J. F. Mitchell, S. S. Dhesi, J. P. Hill, and A. Cavalleri, “Driving magnetic order in a manganite by ultrafast lattice excitation,” *Phys. Rev. B*, vol. 84, p. 241104, Dec 2011.
- [56] M. Frst, R. Mankowsky, H. Bromberger, D. Fritz, H. Lemke, D. Zhu, M. Chollet, Y. Tomioka, Y. Tokura, R. Merlin, J. Hill, S. Johnson, and A. Cavalleri, “Displacive lattice excitation through nonlinear phononics viewed by femtosecond x-ray diffraction,” *Solid State Communications*, vol. 169, pp. 24 – 27, 2013.
- [57] Y. Takada, “Superconductivity in the half-filled hubbard-holstein model in the antiadiabatic region,” *Journal of the Physical Society of Japan*, vol. 65, no. 6, pp. 1544–1547, 1996.
- [58] T. Hotta and Y. Takada, “Unconventional superconductivity in the hubbard-holstein model,” *Physica B: Condensed Matter*, vol. 230232, pp. 1037 – 1040, 1997. Proceedings of the International Conference on Strongly Correlated Electron Systems.
- [59] Y. Takada and A. Chatterjee, “Possibility of a metallic phase in the charge-density-wave spin-density-wave crossover region in the one-dimensional hubbard-holstein model at half filling,” *Phys. Rev. B*, vol. 67, p. 081102, Feb 2003.
- [60] M. Tezuka, R. Arita, and H. Aoki, “Density-matrix renormalization group study of pairing when electron-electron and electron-phonon interactions coexist: Effect of the electronic band structure,” *Phys. Rev. Lett.*, vol. 95, p. 226401, Nov 2005.
- [61] M. Tezuka, R. Arita, and H. Aoki, “Phase diagram for the one-dimensional hubbard-holstein model: A density-matrix renormalization group study,” *Phys. Rev. B*, vol. 76, p. 155114, Oct 2007.
- [62] H. Fehske, G. Hager, and E. Jeckelmann, “Metallicity in the half-filled holstein-hubbard model,” *EPL (Europhysics Letters)*, vol. 84, no. 5, p. 57001, 2008.

- [63] J. E. Hirsch and E. Fradkin, “Phase diagram of one-dimensional electron-phonon systems. ii. the molecular-crystal model,” *Phys. Rev. B*, vol. 27, pp. 4302–4316, Apr 1983.
- [64] J. E. Hirsch, “Phase diagram of the one-dimensional molecular-crystal model with coulomb interactions: Half-filled-band sector,” *Phys. Rev. B*, vol. 31, pp. 6022–6031, May 1985.
- [65] R. T. Clay and R. P. Hardikar, “Intermediate phase of the one dimensional half-filled hubbard-holstein model,” *Phys. Rev. Lett.*, vol. 95, p. 096401, Aug 2005.
- [66] E. A. Nowadnick, S. Johnston, B. Moritz, R. T. Scalettar, and T. P. Devereaux, “Competition between antiferromagnetic and charge-density-wave order in the half-filled hubbard-holstein model,” *Phys. Rev. Lett.*, vol. 109, p. 246404, Dec 2012.
- [67] P. Werner and A. J. Millis, “Efficient dynamical mean field simulation of the holstein-hubbard model,” *Phys. Rev. Lett.*, vol. 99, p. 146404, Oct 2007.
- [68] J. K. Freericks, M. Jarrell, and D. J. Scalapino, “Holstein model in infinite dimensions,” *Phys. Rev. B*, vol. 48, pp. 6302–6314, Sep 1993.
- [69] J. Bauer and A. C. Hewson, “Competition between antiferromagnetic and charge order in the hubbard-holstein model,” *Phys. Rev. B*, vol. 81, p. 235113, Jun 2010.
- [70] F. Marsiglio, “Pairing and charge-density-wave correlations in the holstein model at half-filling,” *Phys. Rev. B*, vol. 42, pp. 2416–2424, Aug 1990.
- [71] R. T. Scalettar, N. E. Bickers, and D. J. Scalapino, “Competition of pairing and peierls charge-density-wave correlations in a two-dimensional electron-phonon model,” *Phys. Rev. B*, vol. 40, pp. 197–200, Jul 1989.
- [72] R. M. Noack, D. J. Scalapino, and R. T. Scalettar, “Charge-density-wave and pairing susceptibilities in a two-dimensional electron-phonon model,” *Phys. Rev. Lett.*, vol. 66, pp. 778–781, Feb 1991.
- [73] R. M. Noack and D. J. Scalapino, “Green’s-function self-energies in the two-dimensional holstein model,” *Phys. Rev. B*, vol. 47, pp. 305–308, Jan 1993.
- [74] M. Vekić and S. R. White, “Gap formation in the density of states for the holstein model,” *Phys. Rev. B*, vol. 48, pp. 7643–7650, Sep 1993.
- [75] S. Kumar and J. van den Brink, “Charge ordering and magnetism in quarter-filled hubbard-holstein model,” *Phys. Rev. B*, vol. 78, p. 155123, Oct 2008.
- [76] E. Berger, P. Valášek, and W. von der Linden, “Two-dimensional hubbard-holstein model,” *Phys. Rev. B*, vol. 52, pp. 4806–4814, Aug 1995.
- [77] E. A. Nowadnick, S. Johnston, B. Moritz, and T. P. Devereaux, “Renormalization of spectra by phase competition in the half-filled hubbard-holstein model,” *Phys. Rev. B*, vol. 91, p. 165127, Apr 2015.
- [78] W. Koller, D. Meyer, Y. no, and A. C. Hewson, “First- and second-order phase transitions in the holstein-hubbard model,” *EPL (Europhysics Letters)*, vol. 66, no. 4, p. 559, 2004.

BIBLIOGRAPHY

- [79] J. K. Freericks, M. Jarrell, and D. J. Scalapino, “The electron-phonon problem in infinite dimensions,” *EPL (Europhysics Letters)*, vol. 25, no. 1, p. 37, 1994.
- [80] E. Kim and M. H. W. Chan, “Probable observation of a supersolid helium phase.,” *Nature*, vol. 427, pp. 225–7, Jan. 2004.
- [81] D. Y. Kim and M. H. W. Chan, “Absence of supersolidity in solid helium in porous vycor glass,” *Phys. Rev. Lett.*, vol. 109, p. 155301, Oct 2012.
- [82] P. Sengupta, L. P. Pryadko, F. Alet, M. Troyer, and G. Schmid, “Supersolids versus phase separation in two-dimensional lattice bosons,” *Phys. Rev. Lett.*, vol. 94, p. 207202, May 2005.
- [83] D. Yamamoto, I. Danshita, and C. A. R. Sá de Melo, “Dipolar bosons in triangular optical lattices: Quantum phase transitions and anomalous hysteresis,” *Phys. Rev. A*, vol. 85, p. 021601, Feb 2012.
- [84] P. Anders, P. Werner, M. Troyer, M. Sigrist, and L. Pollet, “From the cooper problem to canted supersolids in bose-fermi mixtures,” *Phys. Rev. Lett.*, vol. 109, p. 206401, Nov 2012.
- [85] K.-K. Ng and T. K. Lee, “Supersolid phase in spin dimer xxz systems under a magnetic field,” *Phys. Rev. Lett.*, vol. 97, p. 127204, Sep 2006.
- [86] P. Sengupta and C. D. Batista, “Field-induced supersolid phase in spin-one heisenberg models,” *Phys. Rev. Lett.*, vol. 98, p. 227201, May 2007.
- [87] N. Laflorencie and F. Mila, “Quantum and thermal transitions out of the supersolid phase of a 2d quantum antiferromagnet,” *Phys. Rev. Lett.*, vol. 99, p. 027202, Jul 2007.
- [88] D. Yamamoto and I. Danshita, “Magnon supersolid and anomalous hysteresis in spin dimers on a triangular lattice,” *Phys. Rev. B*, vol. 88, p. 014419, Jul 2013.
- [89] Y. Murakami, T. Oka, and H. Aoki, “Supersolid states in a spin system: Phase diagram and collective excitations,” *Phys. Rev. B*, vol. 88, p. 224404, Dec 2013.
- [90] J. Bauer, “Competing interactions and symmetry breaking in the hubbard-holstein model,” *EPL (Europhysics Letters)*, vol. 90, no. 2, p. 27002, 2010.
- [91] L. Vidmar, J. Bonča, M. Mierzejewski, P. Prelovšek, and S. A. Trugman, “Nonequilibrium dynamics of the holstein polaron driven by an external electric field,” *Phys. Rev. B*, vol. 83, p. 134301, Apr 2011.
- [92] D. Golež, J. Bonča, L. Vidmar, and S. A. Trugman, “Relaxation dynamics of the holstein polaron,” *Phys. Rev. Lett.*, vol. 109, p. 236402, Dec 2012.
- [93] D. Golež, J. Bonča, and L. Vidmar, “Dissociation of a hubbard-holstein bipolaron driven away from equilibrium by a constant electric field,” *Phys. Rev. B*, vol. 85, p. 144304, Apr 2012.
- [94] S. Sayyad and M. Eckstein, “Coexistence of excited polarons and metastable delocalized states in photoinduced metals,” *Phys. Rev. B*, vol. 91, p. 104301, Mar 2015.

BIBLIOGRAPHY

- [95] G. De Filippis, V. Cataudella, E. A. Nowadnick, T. P. Devereaux, A. S. Mishchenko, and N. Nagaosa, “Quantum dynamics of the hubbard-holstein model in equilibrium and nonequilibrium: Application to pump-probe phenomena,” *Phys. Rev. Lett.*, vol. 109, p. 176402, Oct 2012.
- [96] M. Sentef, A. F. Kemper, B. Moritz, J. K. Freericks, Z.-X. Shen, and T. P. Devereaux, “Examining electron-boson coupling using time-resolved spectroscopy,” *Phys. Rev. X*, vol. 3, p. 041033, Dec 2013.
- [97] A. F. Kemper, M. Sentef, B. Moritz, C. C. Kao, Z. X. Shen, J. K. Freericks, and T. P. Devereaux, “Mapping of unoccupied states and relevant bosonic modes via the time-dependent momentum distribution,” *Phys. Rev. B*, vol. 87, p. 235139, Jun 2013.
- [98] A. F. Kemper, M. A. Sentef, B. Moritz, J. K. Freericks, and T. P. Devereaux, “Effect of dynamical spectral weight redistribution on effective interactions in time-resolved spectroscopy,” *Phys. Rev. B*, vol. 90, p. 075126, Aug 2014.
- [99] A. F. Kemper, M. A. Sentef, B. Moritz, J. K. Freericks, and T. P. Devereaux, “Amplitude mode oscillations in pump-probe photoemission spectra of electron-phonon mediated superconductors,” *arXiv:1412.2762*, 2014.
- [100] M. A. Sentef, A. F. Kemper, A. Georges, and C. Kollath, “Theory of light-enhanced phonon-mediated superconductivity,” *arXiv:1505.07575*, 2015.
- [101] P. Werner and M. Eckstein, “Phonon-enhanced relaxation and excitation in the holstein-hubbard model,” *Phys. Rev. B*, vol. 88, p. 165108, Oct 2013.
- [102] P. Werner and M. Eckstein, “Field-induced polaron formation in the holstein-hubbard model,” *EPL (Europhysics Letters)*, vol. 109, no. 3, p. 37002, 2015.
- [103] H. Shiba, *Physics of Correlated Electrons*. Iwanami, 2001.
- [104] R. Bulla, “Zero temperature metal-insulator transition in the infinite-dimensional hubbard model,” *Phys. Rev. Lett.*, vol. 83, pp. 136–139, Jul 1999.
- [105] E. Gull, A. J. Millis, A. I. Lichtenstein, A. N. Rubtsov, M. Troyer, and P. Werner, “Continuous-time monte carlo methods for quantum impurity models,” *Rev. Mod. Phys.*, vol. 83, pp. 349–404, May 2011.
- [106] P. Werner, “Lecture notes for the workshop “simulating strongly correlated systems”: http://alps.comp-phys.org/mediawiki/index.php/cecama_school_2010,” 2010.
- [107] A. Koga and P. Werner, “Low-temperature properties of the infinite-dimensional attractive hubbard model,” *Phys. Rev. A*, vol. 84, p. 023638, Aug 2011.
- [108] P. Werner, T. Oka, and A. J. Millis, “Diagrammatic monte carlo simulation of nonequilibrium systems,” *Phys. Rev. B*, vol. 79, p. 035320, Jan 2009.
- [109] M. Eckstein, M. Kollar, and P. Werner, “Thermalization after an interaction quench in the hubbard model,” *Phys. Rev. Lett.*, vol. 103, p. 056403, Jul 2009.

BIBLIOGRAPHY

- [110] M. Eckstein, M. Kollar, and P. Werner, “Interaction quench in the hubbard model: Relaxation of the spectral function and the optical conductivity,” *Phys. Rev. B*, vol. 81, p. 115131, Mar 2010.
- [111] J. K. Freericks, “Conserving approximations for the attractive holstein and hubbard models,” *Phys. Rev. B*, vol. 50, pp. 403–417, Jul 1994.
- [112] J. Bauer, J. E. Han, and O. Gunnarsson, “Quantitative reliability study of the migdaliashberg theory for strong electron-phonon coupling in superconductors,” *Phys. Rev. B*, vol. 84, p. 184531, Nov 2011.
- [113] D. Meyer, A. C. Hewson, and R. Bulla, “Gap formation and soft phonon mode in the holstein model,” *Phys. Rev. Lett.*, vol. 89, p. 196401, Oct 2002.
- [114] W. Koller, D. Meyer, and A. C. Hewson, “Dynamic response functions for the holstein-hubbard model,” *Phys. Rev. B*, vol. 70, p. 155103, Oct 2004.
- [115] M. Capone and S. Ciuchi, “Polaron crossover and bipolaronic metal-insulator transition in the half-filled holstein model,” *Phys. Rev. Lett.*, vol. 91, p. 186405, Oct 2003.
- [116] J. Hague and N. d ’Ambrumenil, “Breakdown of migdaleliashberg theory viacatastrophic vertex divergence atlowphononfrequency,” *Journal of Low Temperature Physics*, vol. 151, no. 5-6, pp. 1149–1163, 2008.
- [117] M. Eckstein and P. Werner, “Photoinduced states in a mott insulator,” *Phys. Rev. Lett.*, vol. 110, p. 126401, Mar 2013.
- [118] M. Eckstein and P. Werner, “Dielectric breakdown of mott insulators doublon production and doublon heating,” *Journal of Physics: Conference Series*, vol. 427, no. 1, p. 012005, 2013.
- [119] R. P. Hardikar and R. T. Clay, “Phase diagram of the one-dimensional hubbard-holstein model at half and quarter filling,” *Phys. Rev. B*, vol. 75, p. 245103, Jun 2007.
- [120] M. Casula, P. Werner, L. Vaugier, F. Aryasetiawan, T. Miyake, A. J. Millis, and S. Biermann, “Low-energy models for correlated materials: Bandwidth renormalization from coulombic screening,” *Phys. Rev. Lett.*, vol. 109, p. 126408, Sep 2012.
- [121] T. Ohgoe and M. Imada, “Variational monte carlo method for electron-phonon coupled systems,” *Phys. Rev. B*, vol. 89, p. 195139, May 2014.
- [122] J. K. Freericks, “Strong-coupling expansions for the attractive holstein and hubbard models,” *Phys. Rev. B*, vol. 48, pp. 3881–3891, Aug 1993.
- [123] J. K. Freericks and M. Jarrell, “Iterated perturbation theory for the attractive holstein and hubbard models,” *Phys. Rev. B*, vol. 50, pp. 6939–6953, Sep 1994.
- [124] A. S. Alexandrov, J. Ranninger, and S. Robaszkiewicz, “Bipolaronic superconductivity: Thermodynamics, magnetic properties, and possibility of existence in real substances,” *Phys. Rev. B*, vol. 33, pp. 4526–4542, Apr 1986.

BIBLIOGRAPHY

- [125] H. Matsuda and T. Tsuneto, “Off-diagonal long-range order in solids,” *Progress of Theoretical Physics Supplement*, vol. 46, pp. 411–436, 1970.
- [126] A. Gabovich, A. Voitenko, and M. Ausloos, “Charge- and spin-density waves in existing superconductors: competition between cooper pairing and peierls or excitonic instabilities,” *Physics Reports*, vol. 367, no. 6, pp. 583 – 709, 2002.
- [127] K. Hashimoto, K. Cho, T. Shibauchi, S. Kasahara, Y. Mizukami, R. Katsumata, Y. Tsuruhara, T. Terashima, H. Ikeda, M. A. Tanatar, H. Kitano, N. Salovich, R. W. Giannetta, P. Walmsley, A. Carrington, R. Prozorov, and Y. Matsuda, “A sharp peak of the zero-temperature penetration depth at optimal composition in $\text{bafe}_2(\text{as}_{1-x}\text{px})_2$,” *Science*, vol. 336, no. 6088, pp. 1554–1557, 2012.
- [128] G. Ghiringhelli, M. Le Tacon, M. Minola, S. Blanco-Canosa, C. Mazzoli, N. B. Brookes, G. M. De Luca, A. Frano, D. G. Hawthorn, F. He, T. Loew, M. M. Sala, D. C. Peets, M. Salluzzo, E. Schierle, R. Sutarto, G. A. Sawatzky, E. Weschke, B. Keimer, and L. Braicovich, “Long-range incommensurate charge fluctuations in $(\text{y,nd})\text{ba}_2\text{cu}_3\text{o}_6+x$,” *Science*, vol. 337, no. 6096, pp. 821–825, 2012.
- [129] W. D. Wise, M. C. Boyer, K. Chatterjee, T. Kondo, T. Takeuchi, H. Ikuta, Y. Wang, and E. W. Hudson, “Charge-density-wave origin of cuprate checkerboard visualized by scanning tunnelling microscopy,” *Nature Physics*, vol. 4, pp. 696–699, July 2008.
- [130] I. M. Vishik, M. Hashimoto, R.-H. He, W.-S. Lee, F. Schmitt, D. Lu, R. G. Moore, C. Zhang, W. Meevasana, T. Sasagawa, S. Uchida, K. Fujita, S. Ishida, M. Ishikado, Y. Yoshida, H. Eisaki, Z. Hussain, T. P. Devereaux, and Z.-X. Shen, “Phase competition in trisected superconducting dome,” *Proceedings of the National Academy of Sciences*, vol. 109, no. 45, pp. 18332–18337, 2012.
- [131] C.-K. Chan, P. Werner, and A. J. Millis, “Magnetism and orbital ordering in an interacting three-band model: A dynamical mean-field study,” *Phys. Rev. B*, vol. 80, p. 235114, Dec 2009.
- [132] R. Peters and N. Kawakami, “Spin density waves in the hubbard model: A dmft approach,” *Phys. Rev. B*, vol. 89, p. 155134, Apr 2014.
- [133] N. Tsuji, M. Eckstein, and P. Werner, “Nonthermal antiferromagnetic order and nonequilibrium criticality in the hubbard model,” *Phys. Rev. Lett.*, vol. 110, p. 136404, Mar 2013.
- [134] G. Bilbro and W. L. McMillan, “Theoretical model of superconductivity and the martensitic transformation in a_{15} compounds,” *Phys. Rev. B*, vol. 14, pp. 1887–1892, Sep 1976.
- [135] S. Robaszkiewicz, R. Micnas, and K. A. Chao, “Thermodynamic properties of the extended hubbard model with strong intra-atomic attraction and an arbitrary electron density,” *Phys. Rev. B*, vol. 23, pp. 1447–1458, Feb 1981.
- [136] L.-F. m. c. Arsenault and A.-M. S. Tremblay, “Transport functions for hypercubic and bethe lattices,” *Phys. Rev. B*, vol. 88, p. 205109, Nov 2013.

BIBLIOGRAPHY

- [137] A. Toschi, M. Capone, and C. Castellani, “Energetic balance of the superconducting transition across the bcs⁻bose einstein crossover in the attractive hubbard model,” *Phys. Rev. B*, vol. 72, p. 235118, Dec 2005.
- [138] R. T. Scalettar, E. Y. Loh, J. E. Gubernatis, A. Moreo, S. R. White, D. J. Scalapino, R. L. Sugar, and E. Dagotto, “Phase diagram of the two-dimensional negative- U hubbard model,” *Phys. Rev. Lett.*, vol. 62, pp. 1407–1410, Mar 1989.
- [139] A. Moreo and D. J. Scalapino, “Two-dimensional negative- U hubbard model,” *Phys. Rev. Lett.*, vol. 66, pp. 946–948, Feb 1991.
- [140] R. Nourafkan, F. Marsiglio, and G. Kotliar, “Model of the electron-phonon interaction and optical conductivity of $\text{Ba}_{1-x}\text{K}_x\text{BiO}_3$ superconductors,” *Phys. Rev. Lett.*, vol. 109, p. 017001, Jul 2012.
- [141] Z. P. Yin, A. Kutepov, and G. Kotliar, “Correlation-enhanced electron-phonon coupling: Applications of gw and screened hybrid functional to bismuthates, chloronitrides, and other high- T_c superconductors,” *Phys. Rev. X*, vol. 3, p. 021011, May 2013.
- [142] P. B. Allen, “Theory of thermal relaxation of electrons in metals,” *Phys. Rev. Lett.*, vol. 59, pp. 1460–1463, Sep 1987.
- [143] R. H. M. Groeneveld, R. Sprik, and A. Lagendijk, “Femtosecond spectroscopy of electron-electron and electron-phonon energy relaxation in ag and au,” *Phys. Rev. B*, vol. 51, pp. 11433–11445, May 1995.
- [144] V. V. Kabanov and A. S. Alexandrov, “Electron relaxation in metals: Theory and exact analytical solutions,” *Phys. Rev. B*, vol. 78, p. 174514, Nov 2008.
- [145] K. Yonemitsu and N. Maeshima, “Coupling-dependent rate of energy transfer from photoexcited mott insulators to lattice vibrations,” *Phys. Rev. B*, vol. 79, p. 125118, Mar 2009.
- [146] H. Matsueda, S. Sota, T. Tohyama, and S. Maekawa, “Relaxation dynamics of photo-carriers in one-dimensional mott insulators coupled to phonons,” *Journal of the Physical Society of Japan*, vol. 81, no. 1, p. 013701, 2012.
- [147] J. Berges, S. Borsányi, and C. Wetterich, “Prethermalization,” *Phys. Rev. Lett.*, vol. 93, p. 142002, Sep 2004.
- [148] M. Moeckel and S. Kehrein, “Interaction quench in the hubbard model,” *Phys. Rev. Lett.*, vol. 100, p. 175702, May 2008.
- [149] M. Schiró and M. Fabrizio, “Time-dependent mean field theory for quench dynamics in correlated electron systems,” *Phys. Rev. Lett.*, vol. 105, p. 076401, Aug 2010.
- [150] M. Schiró and M. Fabrizio, “Quantum quenches in the hubbard model: Time-dependent mean-field theory and the role of quantum fluctuations,” *Phys. Rev. B*, vol. 83, p. 165105, Apr 2011.

BIBLIOGRAPHY

- [151] N. Tsuji and P. Werner, “Nonequilibrium dynamical mean-field theory based on weak-coupling perturbation expansions: Application to dynamical symmetry breaking in the hubbard model,” *Phys. Rev. B*, vol. 88, p. 165115, Oct 2013.
- [152] E. Pazy and A. Vardi, “Holstein model and peierls instability in one-dimensional boson-fermion lattice gases,” *Phys. Rev. A*, vol. 72, p. 033609, Sep 2005.
- [153] F. Herrera and R. V. Krems, “Tunable holstein model with cold polar molecules,” *Phys. Rev. A*, vol. 84, p. 051401, Nov 2011.
- [154] J. P. Hague and C. MacCormick, “Quantum simulation of electronphonon interactions in strongly deformable materials,” *New Journal of Physics*, vol. 14, no. 3, p. 033019, 2012.
- [155] M. Hohenadler, “Charge and spin correlations of a peierls insulator after a quench,” *Phys. Rev. B*, vol. 88, p. 064303, Aug 2013.
- [156] S. L. Johnson, P. Beaud, E. Vorobeva, C. J. Milne, E. D. Murray, S. Fahy, and G. Ingold, “Directly observing squeezed phonon states with femtosecond x-ray diffraction,” *Phys. Rev. Lett.*, vol. 102, p. 175503, Apr 2009.
- [157] K. E. Kihlstrom, R. W. Simon, and S. A. Wolf, “Tunneling $\alpha^2 f(\omega)$ from sputtered thin-film nbn,” *Phys. Rev. B*, vol. 32, pp. 1843–1845, Aug 1985.
- [158] S. D. Brorson, A. Kazeroonian, J. S. Moodera, D. W. Face, T. K. Cheng, E. P. Ippen, M. S. Dresselhaus, and G. Dresselhaus, “Femtosecond room-temperature measurement of the electron-phonon coupling constant γ in metallic superconductors,” *Phys. Rev. Lett.*, vol. 64, pp. 2172–2175, Apr 1990.
- [159] S. P. Chockalingam, M. Chand, J. Jesudasan, V. Tripathi, and P. Raychaudhuri, “Superconducting properties and hall effect of epitaxial nbn thin films,” *Phys. Rev. B*, vol. 77, p. 214503, Jun 2008.
- [160] M. Beck, M. Klammer, S. Lang, P. Leiderer, V. V. Kabanov, G. N. Gol’tsman, and J. Demsar, “Energy-gap dynamics of superconducting nbn thin films studied by time-resolved terahertz spectroscopy,” *Phys. Rev. Lett.*, vol. 107, p. 177007, Oct 2011.
- [161] J. D. Axe and G. Shirane, “Influence of the superconducting energy gap on phonon linewidths in nb₃sn,” *Phys. Rev. Lett.*, vol. 30, pp. 214–216, Feb 1973.
- [162] S. M. Shapiro, G. Shirane, and J. D. Axe, “Measurements of the electron-phonon interaction in nb by inelastic neutron scattering,” *Phys. Rev. B*, vol. 12, pp. 4899–4908, Dec 1975.
- [163] H. Kawano, H. Yoshizawa, H. Takeya, and K. Kadowaki, “Anomalous phonon scattering below t_c in yni₂¹¹b₂c,” *Phys. Rev. Lett.*, vol. 77, pp. 4628–4631, Nov 1996.
- [164] C. Stassis, M. Bullock, J. Zarestky, P. Canfield, A. I. Goldman, G. Shirane, and S. M. Shapiro, “Phonon mode coupling in superconducting luni₂b₂c,” *Phys. Rev. B*, vol. 55, pp. R8678–R8681, Apr 1997.

BIBLIOGRAPHY

- [165] F. Weber, A. Kreyssig, L. Pintschovius, R. Heid, W. Reichardt, D. Reznik, O. Stockert, and K. Hradil, “Direct observation of the superconducting gap in phonon spectra,” *Phys. Rev. Lett.*, vol. 101, p. 237002, Dec 2008.
- [166] P. B. Allen, V. N. Kostur, N. Takesue, and G. Shirane, “Neutron-scattering profile of $q \neq 0$ phonons in bcs superconductors,” *Phys. Rev. B*, vol. 56, pp. 5552–5558, Sep 1997.
- [167] J. K. Freericks, H. R. Krishnamurthy, and T. Pruschke, “Theoretical description of time-resolved photoemission spectroscopy: Application to pump-probe experiments,” *Phys. Rev. Lett.*, vol. 102, p. 136401, Mar 2009.
- [168] N. Tsuji, T. Oka, P. Werner, and H. Aoki, “Dynamical band flipping in fermionic lattice systems: An ac-field-driven change of the interaction from repulsive to attractive,” *Phys. Rev. Lett.*, vol. 106, p. 236401, Jun 2011.
- [169] R. Matsunaga *JPS meeting 2014 autumn 8pAD-7; JPS meeting 2015 spring 22aAA-5*.
- [170] D. Golež, M. Eckstein, and P. Werner, “Dynamics of screening in photodoped mott insulators,” *Phys. Rev. B*, vol. 92, p. 195123, Nov 2015.
- [171] G. Cohen, E. Gull, D. R. Reichman, and A. J. Millis, “Taming the dynamical sign problem in real-time evolution of quantum many-body problems,” *arXiv:1510.03534*, 2015.
- [172] M. H. Hettler, A. N. Tahvildar-Zadeh, M. Jarrell, T. Pruschke, and H. R. Krishnamurthy, “Nonlocal dynamical correlations of strongly interacting electron systems,” *Phys. Rev. B*, vol. 58, pp. R7475–R7479, Sep 1998.
- [173] G. Kotliar, S. Y. Savrasov, G. Pálsson, and G. Biroli, “Cellular dynamical mean field approach to strongly correlated systems,” *Phys. Rev. Lett.*, vol. 87, p. 186401, Oct 2001.
- [174] T. Maier, M. Jarrell, T. Pruschke, and M. H. Hettler, “Quantum cluster theories,” *Rev. Mod. Phys.*, vol. 77, pp. 1027–1080, Oct 2005.
- [175] M. Kitatani, N. Tsuji, and H. Aoki, “Flex+dmft approach to the d -wave superconducting phase diagram of the two-dimensional hubbard model,” *Phys. Rev. B*, vol. 92, p. 085104, Aug 2015.
- [176] N. Tsuji, P. Barmettler, H. Aoki, and P. Werner, “Nonequilibrium dynamical cluster theory,” *Phys. Rev. B*, vol. 90, p. 075117, Aug 2014.
- [177] M. Eckstein and P. Werner, “Ultra-fast photo-carrier relaxation in mott insulators with short-range spin correlations,” *arXiv:1410.3956*, 2014.
- [178] M. Knap, M. Babadi, G. Refael, I. Martin, and E. Demler, “Dynamical cooper pairing in non-equilibrium electron-phonon systems,” *arXiv:1511.07874*, 2015.
- [179] A. S. Alexandrov, *Theory of Superconductivity*. Bristol and Philadelphia, 2003.
- [180] P. Morel and P. W. Anderson, “Calculation of the superconducting state parameters with retarded electron-phonon interaction,” *Phys. Rev.*, vol. 125, pp. 1263–1271, Feb 1962.

BIBLIOGRAPHY

- [181] W. L. McMillan, “Transition temperature of strong-coupled superconductors,” *Phys. Rev.*, vol. 167, pp. 331–344, Mar 1968.
- [182] G. Sangiovanni, A. Toschi, E. Koch, K. Held, M. Capone, C. Castellani, O. Gunnarsson, S.-K. Mo, J. W. Allen, H.-D. Kim, A. Sekiyama, A. Yamasaki, S. Suga, and P. Metcalf, “Static versus dynamical mean-field theory of mott antiferromagnets,” *Phys. Rev. B*, vol. 73, p. 205121, May 2006.